

THESIS FOR THE DEGREE OF DOCTOR OF PHILOSOPHY

Fluidized bed combustion
– modeling and mixing

David Pallarès



Department of Energy and Environment
Division of Energy Technology
CHALMERS UNIVERSITY OF TECHNOLOGY

Göteborg (Sweden), 2008

Fluidized bed combustion – modeling and mixing

David Pallarès

ISBN 978-91-7385-142-8

© David Pallarès, 2008

Doktorsavhandlingar vid Chalmers Tekniska Högskola

Ny serie nr. 2823

ISSN 0346-718X

Department of Energy and Environment

Division of Energy Technology

Chalmers University of Technology

SE-41296 Göteborg (Sweden)



+46 31 7721000

Chalmers Reproservice

Göteborg (Sweden), 2008

Fluidized bed combustion – modeling and mixing

David Pallarès

Department of Energy and Environment
Division of Energy Technology
Chalmers University of Technology

Abstract

First demonstrated on industrial scale in 1976, fluidized bed combustion (FBC) rapidly became an established technology for solid fuel combustion with a current installed capacity of about 30 GW_e and power plants ranging from 10 to 460 MW_e. The widespread use of the FBC technology both under so-called circulating and bubbling conditions (*i.e.* with and without external recirculation of solids) is generally considered to be due to two main advantages with respect to other competing combustion technologies: the high fuel flexibility and possibilities of cost efficient reduction of SO_x and NO_x emissions. Yet, the relative lack of knowledge within some of the phenomena governing the process represents a major obstacle for the further development of the FBC technology.

Efficient scale-up and development of the FBC technology depends on the possibility to increase the knowledge on the main processes involved in FBC boilers. A combination of experimental work and formulation of mathematical models is important to increase the knowledge of the process. In this work, macroscopic submodels for key processes in FBC (fluid dynamics, combustion and heat transfer) are formulated based on experimental data. These submodels are then linked to form a comprehensive model for large-scale fluidized bed combustion which is compared to experimental data not used in the validation of the submodels. The submodels include treatment of important phenomena such as fluctuations in the gas phase, separate convective and radiative heat transfer accounting for absorption in the particle suspension, influence of the pressure drop across the gas distributor and corner effects in the solid phase. These phenomena were not included in previous comprehensive FBC models and are the focus of this thesis.

The comparison between the model and experimental data from large-scale fluidized bed boilers have been carried out for a wide range of data categories covering the solid phases (inert bed material and fuel), the gas phase and the temperature field. The modeled data generally shows good agreement with experimental data.

Although the model developed is primarily aimed at circulating fluidized bed boilers, its principles and formulation can also be applied to bubbling beds and gasifiers as well as new FBC technologies such as oxy-fuel or chemical looping combustion.

Keywords: Fluidized bed combustion; Modeling; Mixing

List of publications

This thesis is based on the work contained in the following papers, referred to by Roman numerals in the text.

- I Pallarès, D., Johnsson, F. 2006. "Macroscopic modelling of fluid dynamics in large-scale circulating fluidized beds". *Progress in Energy and Combustion Science*, 32 (5-6), pp. 539-569.
- II Pallarès, D., Johnsson, F. 2008. "Modeling of fuel mixing in fluidized bed combustors". Accepted for publication in *Chemical Engineering Science*.
- III Pallarès, D., Johnsson, F. 2008. "Macroscopic modeling of the gas phase in fluidized bed combustion". Submitted for publication.
- IV Pallarès, D., Johnsson, F. 2006. "A novel technique for particle tracking in cold 2-dimensional fluidized beds - simulating fuel dispersion". *Chemical Engineering Science*, 61 (8), pp. 2710-2720.
- V Pallarès, D., Díez, P., Johnsson, F. 2007. "Experimental analysis of fuel mixing patterns in a fluidized bed". *Proc. of the 12th Int. Conf. on Fluidization (Harrison, Canada)*.

Appendixes

- A Macroscopic modeling of heat transfer in circulating fluidized bed units.

David Pallarès is the principal author and investigator in all papers. Filip Johnsson has supervised the work in all papers and contributed to their writing. Pedro Díez carried out the experiments in Paper V.

The following papers have also been published during the course of the work but are not included in this thesis since their content either is outside the scope of the present work or partly overlaps with the papers included in it.

- Pallarès, D., Johnsson, F. 2008. "A comprehensive model of CFB combustion". *Proc. of the 9th Int. Conf. on Circulating Fluidized Beds (Hamburg, Germany)*.
- Pallarès, D., Johnsson, F. 2002. "Fluid dynamic modeling of CFB units". *Proc. of the 7th Int. Conf. on Circulating Fluidized Beds (Niagara Falls, Canada)*, pp. 387-394.
- Pallarès, D., Johansson, A., Johnsson, F. 2006. "Interpretation of dynamics of pressure measurements". *Proc. of the 19th Int. Conf. on Fluidized Bed Combustion (Vienna, Austria)*.
- Pallarès, D., Johnsson, F. 2007. "Modeling fuel mixing in a fluidized bed combustor". *Proc. of the 12th Int. Conf. on Fluidization (Harrison, Canada)*.
- Niklasson, F., Pallarès, D., Johnsson, F. 2006. "Biomass co-firing in a CFB boiler - the influence of fuel and bed properties on in-furnace gas-concentration profiles". *Proc. of the 19th Int. Conf. on Fluidized Bed Combustion (Vienna, Austria)*.
- Almendros-Ibáñez, J.-A., Pallarès, D., Johnsson, F., Santana, D. 2008. "A novel approach to characterize fluidized bed dynamics combining PIV and FEM". Submitted for publication in *AIChE Journal*.
- Almendros-Ibáñez, J.-A., Pallarès, D., Johnsson, F., Santana, D. 2008. "Porosity distribution around bubbles in a fluidized bed". Submitted for publication in *Powder Technology*.

Acknowledgements

Foremost, I wish to express my most sincere gratitude to my supervisor Professor Filip Johnsson for his skillful guidance throughout this and other works. His deep knowledge of the field of FBC combustion, together with his confidence on this work, provides a privileged ground which I deeply appreciate.

My gratitude must be extended to Associate Professor Henrik Thunman for the time and effort he has spent on valuable discussions which saved me by far more time and effort than otherwise would have been the case. Associate Professor Lars-Erik Åmand is acknowledged for his passion for the experimental field, which burns like no one else's and grants him the ability to provide almost any experimental data one can think of (and explanations for it).

Besides for wise advice, I am grateful to Professor Emeritus Bo Leckner specially for giving me the opportunity to regularly attend the highly rewarding workshops arranged by the Fluidized Bed Conversion group of the International Energy Agency, where this work has been presented and given further qualified feedback.

Very special thanks must go to Adjunct Professor Bengt-Åke Andersson for his strong trust in the embryo of what you hold in your hands and for giving it the chance to develop within a successful framework of collaboration with the manufacturing industry. It has been and will continue to be a pleasure to work with METSO Power Oy; their flexibility and understanding for the nature of academic research is highly appreciated and Mr. Marko Palonen is specially acknowledged in this sense.

Lennart Darell is thanked for always having a solution and a smile at hand for any difficulty encountered in the experimental field.

Coworkers at the Thermal and Fluid Engineering Department of University Carlos III (Madrid, Spain) and José Antonio Almendros-Ibáñez in special as well as Pedro-Antonio Díez are thanked for fruitful cooperation.

Financial support from the European Commission (under contract RFC-CR-03001), the Swedish Energy Agency and METSO Power Oy is acknowledged.

Highly-skilled surrounding, long field experience and funding have been a necessary but not sufficient condition for the implementation of this work. Thus, last but not least come the following acknowledgements:

The friendly and inspiring atmosphere at the division of Energy Technology has played an important role, and not only in pure academic terms: chats about weekend activities, movies, soccer, politics or life itself are a must to preserve some reasonable level of mental health during a work like this.

A time ago Göteborg became my new home, and some people managed to make it feel home too. These friends know who they are and how much I enjoy them.

My (increasing!) family at home in Barcelona has given me unconditional understanding and support for my move to Sweden, which I deeply value: moltes gràcies de debò. Friends I left there are also missed, even more now when distance confirmed them to be real ones (both day- and night-time).

It is nothing but a blessing to share life with my love and best friend Emma and her everlasting warmth and loyalty.

“All models are wrong.
Some are useful”.

- George Box, chemist and statistician

Table of contents

Chapter 1 - Introduction	1
1.1 <i>Scope: CFB boilers</i>	1
1.2 <i>Aim: Modeling and experimental work</i>	3
1.3 <i>Background: Macroscopic models</i>	4
 Chapter 2 - Submodels	6
2.1 <i>Governing phenomena in CFB combustion</i>	6
2.2 <i>Theory</i>	9
 Chapter 3 - Comprehensive Model	24
3.1 <i>Coupling of submodels</i>	24
3.2 <i>Computational flow scheme</i>	30
3.3 <i>Furnace mesh</i>	32
 Chapter 4 - Results	34
Chapter 5 - Further work	43
Chapter 6 - Conclusions	45
Notation	46
References	48

Chapter 1 - Introduction

1.1 Scope: CFB boilers

The focus of this thesis is on Circulating Fluidized Bed Combustion. The principle of a fluidized bed is that a bed of solid particles adopts a fluid-like behavior when a gas injected from below flows through it. A fluidized bed is known to provide a good gas-solids contact together with relatively high rates of solids and gas mixing. These properties have made fluidized beds a competitive technology in a wide variety of industrial sectors such as pharmaceuticals, metallurgy, material science, petrochemistry and, in the context of the present work, the energy sector.

For some applications, it is desirable to inject a relatively high gas flow to the fluidized bed reactor (generally called riser), which can lead to significant entrainment of bed material out of the riser through the exit duct. In such case, the entrained solids flow is separated from the gas flow by means of a cyclone and fed back into the riser through a particle seal system containing an auxiliary fluidized bed and a return duct. Depending on the magnitude of this externally recirculated solids flow, FB units can be divided into bubbling (BFB) and circulating (CFB) fluidized beds. Although a clear-cut value does not exist, FB units are considered to be operated under circulating conditions when a significant flux of externally recirculated solids is present (roughly above 0.5 kg/m^2). Otherwise, the bed is considered a BFB, also called stationary fluidized bed (SFB). The scope of this work is CFB boilers, *i.e.* CFB units used for combustion of solid fuels. Figure 1 illustrates a typical CFB boiler.

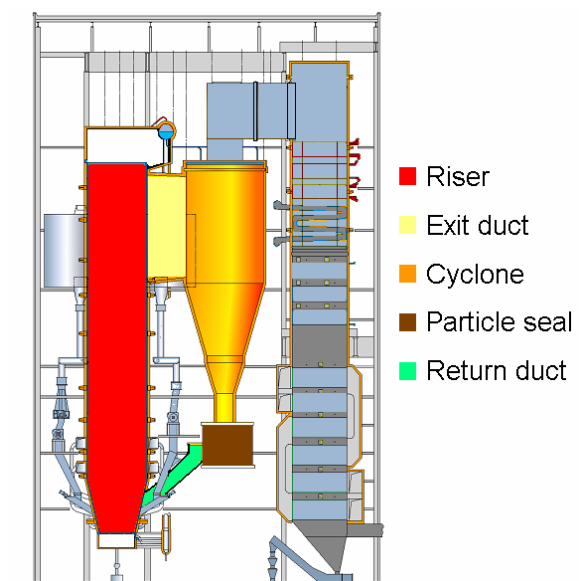


Figure 1: The 177 MW_{th} biomass-fired CFB boiler in Pori (Finland). Courtesy of Metso Power, manufacturer. The parts forming the circulating loop are identified.

While the basic principle of fluidization is common to all FB units, there are significant differences between large-scale and laboratory fluidized beds. Units of both these types can be found operating at bubbling as well as circulating conditions.

Large-scale FB units applied in combustion, which are in focus in this work, are generally characterized by:

- An aspect ratio of the riser ($H_{riser}/D_{eq, riser}$) lower than 10
- An aspect ratio of the settled bed ($H_{b, settled}/D_{eq, riser}$) lower than 1
- Bed material which belongs to group B in the Geldart classification

These characteristics give a flow and mixing pattern which significantly differs from that obtained in typical laboratory units (see e.g. Werther, 1993). Thus, application of data from laboratory units to large-scale units must be done with care and may not be appropriate at all.

Large-scale CFB units are used for the thermal conversion of solid fuels, i.e. combustion and gasification of coal, biomass, peat or solid waste. Fluidized bed combustion is widely used whereas FB gasification has not yet reached commercial status when it comes to difficult fuels such as biomass and waste. The focus of this work is on the use of large-scale CFB units in combustion.

One of the main advantages of FB combustion is its fuel flexibility and the ability to burn difficult fuels such as various biomass waste and other waste fuels. Thus, FB plants are not limited to one fuel type but can operate on different fuel types or co-firing a mix of fuels, depending on the availability and price of the fuels.

In addition, with the increasingly demanding regulations on emissions, FB combustion gives low emissions of both SO_x and NO_x . The high gas-solids contact in FB units facilitates in-bed SO_x capture by addition of a solid sorbent (limestone or dolomite) to the bed material, i.e. there is normally no need for scrubbers. In addition, the low and homogenous in-furnace temperature, around 850 °C, yields low emissions of NO_x (low thermal NO_x).

A problem with FB combustion is that there is significant lack of knowledge and understanding of the in-furnace processes which govern the combustion and, thus, are crucial for design and scale-up of the process, optimal operation of existing units and for preventing erosion of internals.

The first FB boilers were BFB units, with all bed material located in the furnace and combustion to a large extent taking place in the bed and in the lower part of the freeboard, especially when burning a low volatile fuel such as bituminous coal. Further development of the FB combustion technology resulted in CFB boilers which give an increased volumetric heat load as a result of the higher gas velocities. The external recirculation of solids for typical CFB boiler designs is between 0.5 and 20 kg/m²·s. In CFB boilers (see Figs 2a and 2b) combustion is distributed more homogeneously along the height of the furnace than in bubbling beds and heat extraction by means of internals in the return leg is also possible and often used in large boilers. At present, both BFB and CFB boilers are built, with BFB boilers applied for small- and medium-sized (10 to 50 MW_{th}) combined heat and power plants (including waste combustors) whereas CFB boilers are also applied as power boilers up to several hundreds of MW electric power (largest boiler is 465 MW_e).

Hupa (2005) estimates that the currently installed capacities of CFB and BFB boilers are 50 GW_{th} and 15 GW_{th}, respectively with the largest plants (single boiler) of 460 MW_e and 142 MW_e. There are ongoing feasibility studies for CFB capacities around 800 MW_e.



a)



b)

Figure 2: The world's largest (550 MW_{th}) biomass-fired CFB boiler in Alholmens Kraft (Finland).
a. Photo of plant (courtesy of Alholmens Kraft, plant owner)
b. Illustration of circulating loop (courtesy of Metso Power, manufacturer)

In future, new approaches to CFB combustion directed towards CO₂ capture such as oxy-fuel and chemical looping combustion are believed to play an increasingly important role in the development of CFB combustion technology.

1.2 Aim: Modeling and experimental work

Further development of the FBC technology requires an increased level of knowledge and understanding of key phenomena in the process, *i.e.* gas and solids mixing, fuel conversion and heat transfer. One way to increase understanding is a thorough combination of modeling and experimental work where modeling is validated against specific experimental data and thereafter applied to model a particular FB unit for comparison with corresponding experimental data. Successful development of models will then help to facilitate reliable design and scale-up of FB units.

The aim of this work is to develop such a modeling procedure combined with experimental work, with focus on key phenomena which are crucial for the process.

The phenomenon in focus for the experimental part of this work is the fuel mixing, described in Papers IV and V. This is investigated based on a novel method for particle tracking developed within the framework of this thesis. Fuel mixing is known to be a critical issue in the optimization of the performance of FBC units. However, there is a lack of knowledge on the phenomena governing fuel mixing, both in qualitative and quantitative terms.

Regarding the modeling part of this work, described in the following chapters and in Papers I to III, a model is developed with the aim to give a detailed 3-dimensional description of the steady-state combustion process in the circulating loop of a CFB unit at an affordable computational cost. This requires that fluid dynamics, heat transfer and combustion are all taken into account in the modeling.

Two main modeling approaches exist at present: macroscopic modeling and computational fluid dynamics (CFD).

Macroscopic modeling of multiphase flows has a semi-empirical character and therefore needs experimental data for its formulation and validation. Experimental data represents a critical point in the modeling in various ways: the measurements must be reliable and not too scarce and cover a wide range of operational conditions and geometries in order to make the model general at the same time that some data must be available for an independent validation of the model. Macroscopic modeling presents reasonably short computational times (from a few minutes to an hour or so).

CFD modeling is based on modeling from first principles, *i.e.* solving the transport equations for mass, momentum and energy in microscopic or mesoscopic scales. As far as FB units are concerned, CFD modeling can be divided into two sub-types depending on the how the particulate phase is modeled: multifluid and discrete element modeling. In multifluid modeling (also known as Eulerian modeling) the particulate phase is handled as a continuum while in discrete element modeling (also known as Lagrangian modeling) each individual particle is considered in the equation system. CFD modeling may be an important modeling tool for FB units in the future, but at present the long computational time (in the order of days to months), together with uncertain assumptions in modeling and inaccuracies in the results, make it still a tool under development, especially when aiming at including both fluid dynamics and reactions/combustion.

With the above concerns, and considering the aim set, the macroscopic approach is adopted for the modeling part of this thesis. It must be noted that even though the modeling is focused on CFB combustion, its theoretical ground makes it a valid basis also for the modeling of other large-scale FB processes, *i.e.* BFB combustion, BFB and CFB gasification and new FBC techniques with inherent CO₂ separation (such as oxy-fuel combustion and chemical looping combustion).

1.3 Background: Macroscopic models





A number of macroscopic models are available in literature for describing certain regions or phenomena in CFB boilers. However, so-called comprehensive models covering all the major phenomena (fluid dynamics, heat transfer and combustion) in the entire combustion space are scarce. Comprehensive models are built up by linking several validated local submodels into an overall model by means of proper boundary conditions and mass and energy balances. The main comprehensive macroscopic models for large-scale CFB units given in literature are listed in Table 1. All boiler manufacturers are known to have confidential in-house models which are more or less comprehensive but to a very large extent based on experimental data, becoming more of a correlation bank than a model.

While all models listed in Table 1 solve the coupling between their respective submodels by means of similar energy and population balances and sets of boundary conditions, the main differences are found in the dimensionality of the model and the choice of submodels.

So-called 1.5-dimensional models discretize the furnace in the axial direction, dividing each vertical layer in the freeboard into one core region and one wall region cell in order to account for the core-annulus flow pattern observed and explained

later on in connection to Fig. 3. This type of furnace discretization provides a more proper picture of the process than 1-dimensional models. Yet, a 1.5-dimensional model is not able to describe some of the crucial phenomena in CFB boilers, such as the horizontal fuel mixing and all events deriving from it.

Table 1: Macroscopic comprehensive models for CFB combustion.

Years	Developer	References	Dimensionality
- 1996	 International Energy Agency	Hannes (1996)	1.5-dimensional
1989 - present	 Technische Universität Hamburg-Harburg Hamburg University of Technology	Lücke (2003)*	3-dimensional
1998 - 2001	 Participants in EU Joule project	Zhang and Leckner (2001)	1.5-dimensional
2005 - present	 Chalmers University of Technology	This work	3-dimensional

* latest published full version

The present work contains submodels which give some phenomena a new approach or account for phenomena which were not included in previous models. Examples of these phenomena included in the modeling of this work are dynamic gas phase mixing, the coupling between fuel conversion and fuel mixing, the modeling of radiative heat flux in suspensions accounting for optical shadowing and consideration of corner effects in the solids flow. In addition, a wide range of experimental data has been used for validation of the submodels developed.

Chapter 2 - Submodels

2.1 Governing phenomena in CFB combustion

When operating a CFB boiler, primary air is injected from the bottom of the furnace where bed material (mostly sand-like particles) is contained. With this, the bed material is fluidized and a turbulent-like gas-solid flow with both dense solid emulsion and gas pockets is established in the bottom furnace region, providing good solids and gas mixing rates and gas-solids contact. These conditions constitute a favorable environment for combustion of solid fuels: fuel particles fed to the unit will spread over the cross section of the furnace (solids mixing) at the same time as the char is consumed in contact with oxygen in the primary air (gas-solid contact) and the volatiles released are combusted as they meet oxygen from the primary air (gas mixing).

Above the dense region formed in the bottom of the furnace, a splash zone is formed, provided a high enough furnace pressure drop. The splash zone is characterized by a strong back-mixing of solids in the form of solid clusters following a ballistic movement. These clusters are thrown up from the bed due to eruption of bubbles at the top of the bed.

Above the splash zone, solids are present in a more dispersed form and follow a core-annulus structure with upflow in the core region and downflow in the annular region at the furnace walls (so-called wall layers) with a net flow from the core to the wall layers. Secondary air injection (which represents an enhancement of the gas mixing) is generally introduced a few meters above the air distributor in order to reduce NO_x emissions and combust unburned volatile matter.

All gas and part of the solids reaching the top of the furnace flow into the cyclone (there might be more than one cyclone) through the exit duct, see Fig. 1. In the cyclone, high gas mixing makes any unburned volatiles and oxygen react. Also, gas and fine particles are removed from the circulating loop and directed towards the convection pass for heat extraction while most particles are separated from the gas flow and remain within the circulating loop. The solids captured by the cyclone, which contain a certain percentage of fuel particles, then flow down to a fluidized seal system in most CFB designs, as seen in Fig. 1. Thereafter the solids are fed back to the furnace through a return duct. Despite the fines leaving the cyclone with the gas flow, the solids inventory in the circulating loop can be maintained more or less constant due to the ashes fed with the fuel and controlled ash withdrawal.

Since the solid phase carries a large part of the total enthalpy flow in the circulating loop of a CFB unit, a high solids mixing will act as thermal flywheel and ensure a high

degree of homogeneity in the temperature field. Typically, about the same amount of heat is removed from the circulating loop as from the flue gas in the convection pass. With respect to the circulating loop, most of the heat extraction is through the waterwalls in the furnace, although in some designs there is a contribution from internals or waterwalls in the cyclone.

In the modeling of any process including several phenomena, it is a key task to identify the governing phenomena in order to establish corresponding submodels. To what extent this can be done depends on the focus and aim of the model and the complexity of the overall process. For the present work, phenomena considered to govern the process are listed and shortly described below, divided into three categories: fluid dynamics, combustion and heat transfer. Superscripts after each underlined item indicate the paper in this thesis where the phenomenon is addressed in detail.

Fluid dynamics

- The dense bed expansion^I, defined as the dependency of the time-averaged voidage of a dense bed (in the furnace and in particle seals, when applicable) with fluidization velocity, is a crucial phenomenon to account for in pressure or population balances since most of the solids in the unit are contained in the dense bed(s). In addition, the different pressure drop across the gas distributor between bubbling and circulating dense beds lead to different expansion behaviours which must be analyzed separately.
- The solids division between cluster and disperse phase in the freeboard^I allows the model to describe the two coexisting solid flow patterns in the freeboard of a CFB furnace: a cluster phase which originates from bubble bursts which follows a ballistic movement in the splash zone immediately above the dense bed surface and a disperse phase following a core-annulus flow structure in the upper freeboard. Proper description of solid flows in the freeboard is required for the modeling of the heat transfer, size segregation and net circulating flow.
- The lateral fuel mixing in the bottom region^{II,IV,V} (i.e. dense bed and splash zone) is a critical phenomenon in the design of large FB boilers since too low lateral mixing of fuel particles results in unbalanced local air-to-fuel ratios over the cross section of the furnace and inefficient operation of the unit. Consideration of the lateral fuel mixing allows calculation and analysis of horizontal heterogeneities in other variables, e.g. in temperature and gas species concentration.
- The continuously varying physical properties of the fuel particles^{II} as they dry, devolatilize and combust imply that *fresh* fuel particles behave in a much different way than those close to burn-out. These gradual changes in the flow of a fuel particle as conversion advances must be accounted for.
- The gas flow fluctuations^{III} originate from the bottom bed dynamics and strongly characterize the gas flow in the bottom region of the furnace. The fluctuating character of the gas flow is a key factor to describe combustion in the bottom region and gas mixing in the splash zone.
- The gas dispersion^{III} governs the gas flow in the upper freeboard and thereby combustion in this region by controlling the fate of oxygen. This phenomenon is enhanced by secondary air injections.

- The size segregation^I effect is observed along the height of the furnace, with coarser particles populating the bottom region and a decreasing averaged solids size with height, leading to that the solids inventory in the return leg consists of finer solids than in the furnace. This effect has a strong influence on the calculation of the solids distribution in the furnace and the net solids circulating flow in particular. The particle size distribution of the bed material is needed to account for size segregation.
- The so-called backflow effect^{I,II} describes which part of the solids reaching the level of the furnace exit will be entrained by the gas flow towards the cyclone and which part will join the solids downflow in the wall layers. This effect plays an important role in the calculation of both the net solids circulating flow and the locally increased solids downflow in the wall regions coupled to the furnace exit(s).
- The population balance in the return leg^I is a crucial term in the total population balance (some units work with most of their solids inventory located in the return leg). In this population balance, the solids contained in the existing fluidized solids column in the downcomer might be of importance and cannot be neglected.

Combustion

- The kinetics of the fuel particle conversion^{II} must be combined with the fuel mixing in order to model the distribution of moisture and volatile releases and of char combustion. These kinetics depend on a variety of parameters such as fuel properties and characteristics of the surrounding atmosphere.
- Based on experimental observations, in the bottom region of the furnace the gas division between throughflow and emulsion-only phase^{III} can be characterized by a high velocity oxygen-rich gas phase and a low velocity reducing gas phase (within the emulsion phase). When included in the modeling, this phase division gives a more accurate description of the real gas flow and thereby forms a basis for a more realistic ground for the formulation of the combustion model.

Heat transfer

- The convective and radiative components of the heat transfer^{App. A} differ in nature and need different modeling approaches. While the convective term is determined by particles and gas flow close to the heat transfer surface, radiation is more complex to handle in a fluidized bed since modeling must include treatment of the absorption of the particle suspension.
- The heat transfer to the fuel particles^{II} has a direct influence on the fuel conversion kinetics and need thus to be accounted for.

Thus, for successful modeling of CFB combustion the set of submodels chosen to form the comprehensive model need to account (individually or through their combination) for all of the above-listed phenomena.

2.2 Theory

This chapter summarizes the assumptions and expressions in the main submodels used in the present work. A more detailed description is available in the appended papers. The submodels are presented individually. The required inputs and the balances through which they are coupled into the comprehensive model are given in Chapter 3. The present chapter is structured in four sections: inert solids, fuel particles, gas phase and heat transfer.

Inert solids

Inert solids form typically more than 95% of the solids in the circulating loop and are thereby considered to govern the fluid dynamics of the solid phase. Submodels related to the fluid dynamics of the furnace can be divided into three regions with respect to the gas and solids flow: the dense (or bottom) bed, the splash zone and the transport zone, as illustrated in Fig. 3. The dense bed and the splash zone is here called *bottom region* while the splash and transport zone is called *freeboard*.

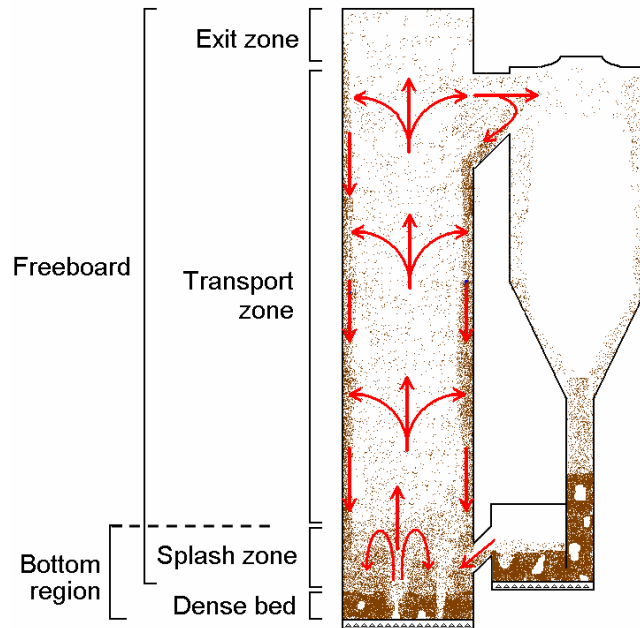


Figure 3: Representation of the solids distribution in the circulating loop. Arrows indicate the main solids flow pattern in the riser.

The presence of a dense bed is common to almost all CFB units and is mandatory in the formulation of the present model. Two phases with strong dynamics are usually considered in the dense bed: a bubble phase often regarded as solids-free and an emulsion phase containing solids and interstitial gas with a voidage which is usually assumed to be under minimum fluidization conditions, ε_{mf} . Thus, the dense bed voidage can be expressed as a weighted sum of the voidage of the two phases, *i.e.*,

$$\varepsilon = \delta + (1 - \delta) \cdot \varepsilon_{mf} \quad (1)$$

where δ is the volumetric fraction of the bubble phase.

The dense bed is taken as the region with a constant vertical pressure gradient on a time-averaged basis which, in addition, provides the time-averaged voidage, ε , in the dense bed according to the expression:

$$\frac{dP}{dh} = \rho_s \cdot g \cdot (1 - \varepsilon) \quad (2)$$

Thus, the time-averaged dense bed voidage can be measured relatively straightforward. The dense bed voidage has been the focus of several studies which have shown the voidage to depend on fluidization velocity (see Figs. 4a and 4b) and mean particle size. In addition, a dependency on the dense bed height (represented through the variable ΔP_{ref}) has also been found, but only for beds with gas distributors providing a low pressure drop (typical for CFB furnaces), as observed in Fig. 4b (see Svensson *et al.* (1996) for details).

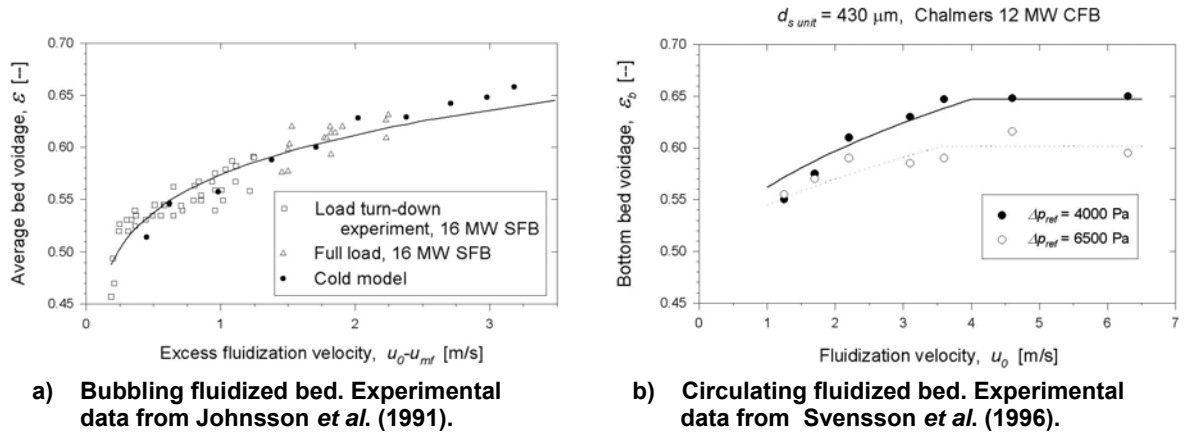


Figure 4: Dense bed expansion. Experimental data compared to model fit.

It is shown by Johnsson *et al.* (1991) that making use of a modified two phase flow theory accounting for gas throughflow and of the widely used expressions for the bubble size and rising velocity given by Clift and Grace (1977) and Darton *et al.* (1985), respectively, the volumetric bubble fraction can be expressed as:

$$\delta = \frac{1}{1 + \frac{1.3}{f} \cdot (u_0 - u_{mf})^{-0.8}} \quad (3)$$

where f is empirically correlated and which from a fit to experimental data from BFB (Johnsson *et al.*, 1991) becomes:

$$f_{BFB} = (0.26 + 0.7 \cdot e^{-3.3 \cdot d_s}) \cdot (0.15 + u_0 - u_{mf})^{-1/3} \quad (4)$$

This expression also holds for dense beds in the particle seals of CFB units, which use gas distributors with high pressure drop. Paper I presents a corresponding expression for bottom beds in CFB furnaces:

$$f_{CFB} = 0.31 + 0.13 \cdot u_0^{-1} - 16.6 \cdot d_s - 2.61 \cdot 10^{-5} \cdot \Delta p_{ref} \quad (5)$$

Thus, the voidage of a dense bed can be predicted by combining Eqs. 1, 3 and 4 or 5. A saturation value of the dense bed voidage in CFB units occurs at high fluidization velocities (see Fig. 4b) and a correlation for this value is given in Paper I.

As explained in Papers I and III, modeling of the freeboard solids flow can be made through a division of the solids flow into two phases: a cluster and a disperse phase. The cluster phase, present in both BFB and CFB units, is considered to be formed by particles ejected from the dense bed into the freeboard by means of bubble bursts. During these bursts, locally high gas velocities (this is known as the throughflow effect) eject into the freeboard particle clusters which would not be entrainable otherwise. The clusters follow a ballistic movement, *i.e.* after reaching a certain height, they fall back into the bed, as illustrated in Fig. 3. The cluster flow results in a strong back-mixing of solids yielding a strong gradient in vertical solids concentration gradient, following the expression:

$$\frac{dC_{cl}}{dh} = -a \cdot C_{cl} \quad (6)$$

This leads to an exponential vertical decay in cluster phase concentration. The decay constant a has been subject for several studies in both BFB and CFB units *e.g.* Kunii and Levenspiel (1991), Adánez *et al.* (1994) and Hiller (1995). In the present work, the expression given by Johnsson and Leckner (1995) is used:

$$a = 4 \cdot \frac{u_t}{u_g} \quad (7)$$

The expression for the cluster phase given in Eq. 6 has been widely used to describe the vertical solids concentration profile in the freeboard of BFB units as well as in CFB units. However, in the freeboard of CFB units there is also a so-called disperse phase. As illustrated in Fig. 3, particles in the disperse phase establish a core-annulus flow structure, flowing upwards in the core at the solids slip velocity with backmixing mainly at the furnace walls forming wall-layers with downward flowing solids. A representation of the solids in the freeboard as a sum of the cluster and disperse phase was introduced by Johnsson and Leckner (1995) which, in analogy to the cluster phase, represented the vertical concentration of the disperse phase in the core region as an exponential decay, *i.e.*:

$$\frac{dC_d}{dh} = -K \cdot C_d \quad (8)$$

The decay constant K was correlated by Johnsson and Leckner (1995) to:

$$K = \frac{0.23}{u_g - u_t} \quad (9)$$

Disperse phase particles join the wall layers downflow as they gradually disengage from the core region upflow. In the wall layers, which are relatively thin (several expressions for its thickness are available in Paper I) and thereby present a higher solids concentration than the core region. Measurements by Zhang *et al.* (1995)

indicate that particles in the wall layers flow downwards at roughly their terminal velocities, which suggests the assumption of stagnant gas in the wall layers.

In summary, both cluster and disperse phase populate the freeboard, with the bottom part dominated by the ballistic flow pattern of the cluster phase known as the splash zone while the upper freeboard mostly populated by the more dilute disperse phase is called transport zone or disperse zone. While the major part of the solids inventory (mass of solids) in the freeboard belongs to the cluster phase, the disperse phase dominates most of the extension of the freeboard and governs the net circulating solids flow. Consideration of both phases is a must for an accurate macroscopic description of the solids flow and concentration in the freeboard of CFB units. This can be seen from Fig. 5, where experimental data on solids concentration in a CFB freeboard is compared with results from several models considering only one solid phase and one model considering two solid phases. While one-phase models can predict the solids concentration in the freeboard of BFB units (splash zone dominates), Fig. 5 shows that such models are not able to provide a satisfactory prediction of the solids concentration in the freeboard of CFB boilers. Instead, two-phase modeling accounting for both cluster and disperse phase (solid line in Fig. 5) is required to the freeboard solids concentration in CFB units.

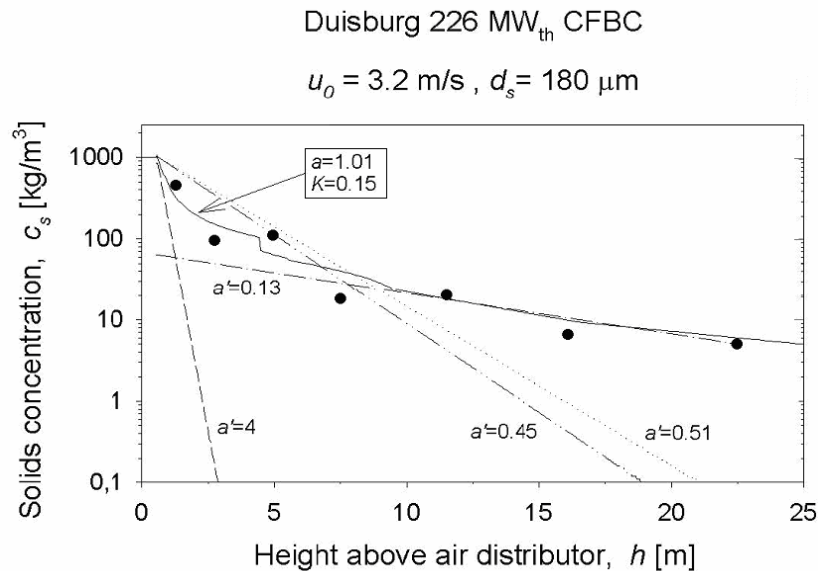


Figure 5: Vertical solids concentration profile. Comparison between one-phase models (dashed lines), a two-phase model (solid curve) and measurements (Werdermann, 1993).

The denomination *backflow effect* is given to the fact that only a fraction of the disperse phase core upflow reaching the furnace exit height follows the gas flow into the cyclone, while the rest is disengaged at the exit ducts (mainly at their entrances) and joins the wall layer downflow. Figure 6 shows experimentally measured values of the particle entrainment probability for different particle sizes under different operational conditions and in different large-scale CFB boilers. From these data, a correlation for the entrainment probability, p_{ent} , of a particle at the level of the exit of a furnace with a single exit duct is given in Paper I.

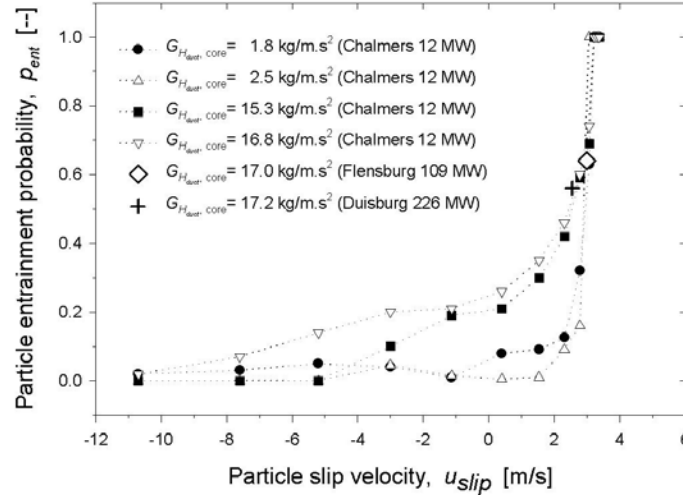


Figure 6: Entrainment probability of a particle at the exit height. Calculated from experimental data found in Werdermann (1993) and Amand *et al.* (1995).

Since values in Fig. 6 were sampled in CFB combustors with a single exit duct, an assumption has to be made in order to estimate the particle entrainment probability, p_{ent}' , in the general case of a furnace with n exit ducts. This is represented by the following expression:

$$p_{ent}' = 1 - (1 - p_{ent})^n \quad (10)$$

Accounting for the backflow effect gives a more accurate representation of the solids net circulating flow both in terms of magnitude and composition (note the dependency of the particle entrainment probability on particle size through the slip velocity, which yields a size segregation effect coupled to the backflow effect).

Fuel particles

Fuel particles follow the same fluid dynamical patterns expressed in the submodels for inert solids. However, two facts make modeling of fuel mixing significantly more complex than of inert bed material: the horizontal gradients in concentration and release of moisture and volatiles and the continuous change in physical properties of the fuel particles as they burn. Handling of these issues from a modeling point of view is outlined below and details are given in Paper II.

Horizontal heterogeneity of fuel concentration and moisture and volatile releases is due to the fact that the horizontal mixing rates of the fuel are limited compared to the kinetic rate for fuel conversion and release of moisture and volatiles. Thus, for a correct evaluation of the mixing, the mixing rate has to be compared with the kinetic rate of the process analyzed. This can be done defining a Damköhler number, which expressed in terms of characteristic times for the mixing (in $[s \cdot m^{-1}]$) and the kinetics (in $[s]$) becomes:

$$Da = \frac{\tau_{mix} \cdot L}{\tau_{kin}} \quad (11)$$

where L is the characteristic length of the system. Low values in Damköhler number indicate a fast mixing compared to the kinetics and thus a rather homogeneous

distribution of the phenomenon studied. Note that the same mixing and the kinetic rates might provide an homogeneous fuel distribution (*i.e.* low value of Da) in a given unit but an heterogeneous fuel distribution (*i.e.* high value of Da) in a larger one. An example of horizontal gradients coupled to the lateral fuel mixing is shown in Fig. 7 which plots two horizontal cuts of the simulated fuel concentration fields in the Chalmers CFB boiler. The same fuel (wood pellets) has been used for both simulations but a ten times higher fuel mixing coefficient, $D_{s,h}$, has been applied in the simulation shown in Fig. 7b, leading to a more homogeneous (and generally more desirable) fuel concentration field.

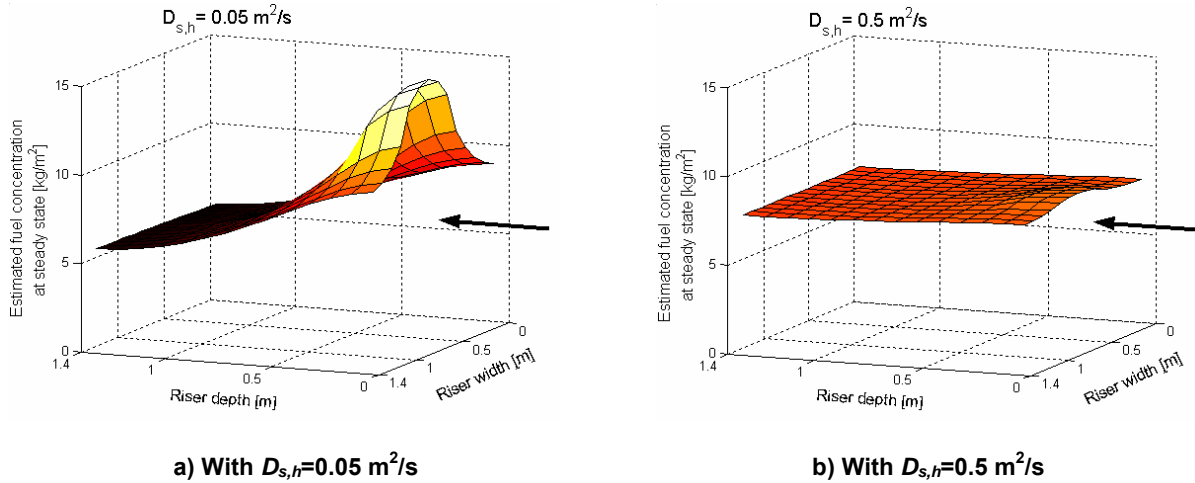


Figure 7: Simulated steady-state fuel concentrations over the cross section of the Chalmers CFB boiler for different values of the fuel mixing coefficient, $D_{s,h}$. Arrows indicate the fuel feeding location. Simulations obtained with the model described in Paper II in this thesis.

Measurements of the horizontal fuel dispersion rate in FB boilers are scarce. While measurements by Xiang *et al.* (1987) in a 100 MW_{th} BFB boiler under cold conditions and fluidization velocities below 1.3 m/s gave values of the fuel horizontal dispersion coefficient between 0.001 and 0.01 m²/s, experiments in the Chalmers 12 MW_{th} CFB given by Niklasson *et al.* (2002) with a fluidization velocity of 2.3 m/s under hot conditions gave values around 0.1 m²/s. However, experiments in cold units do not give exact quantitative information of the mixing pattern under operation but only of its magnitude.

In order to gain understanding of the fuel mixing process, an experimental method has been developed which by means of digital image analysis records the trajectory of a phosphorescent tracer particle (simulating a fuel particle) immersed in a cold 2-dimensional bed. With this, not only the qualitative flow pattern of the tracer can be studied but also the influence of several parameters on its mixing rate. This type of experimental work has been carried out in Papers IV (in a 0.4 m-wide cold unit) and V (in a 1.2 m-wide unit) and some of the main findings can be observed in Figs. 8 and 9. In both these figures the averaged velocity (vector plot) and the normalized concentration (color plot) fields of the tracer particle are superimposed.

The first observation to note, common to all runs carried out, is the existence of regions with relatively low tracer concentration and high upward velocities. These regions are more clearly defined in some runs than others and there are two such regions in the runs given in Figs. 8 and 9, located at about $x=20$ cm and $x=100$ cm

(easily seen in Figs 8a and 9a). Comparison with visual observation of video recordings shows that these regions correspond to the main bubble paths.

Studying the velocity plot, it can be seen that the tracer particle follows a flow pattern structured into horizontally-aligned vortices located around each of the above-mentioned main bubble paths (these vortices are indicated by arrows in Fig. 8b). The vortices can be seen as slice cuts of corresponding 3-dimensional toroidal structures around each main bubble path. Thus, the solids flow pattern is strongly coupled to the bubble flow. It is observed in other experiments that the amount of vortices is not a function of fluidization velocity but of dense bed height (the higher the dense bed, the lower the number of main bubble paths and, thereby, of flow vortices).

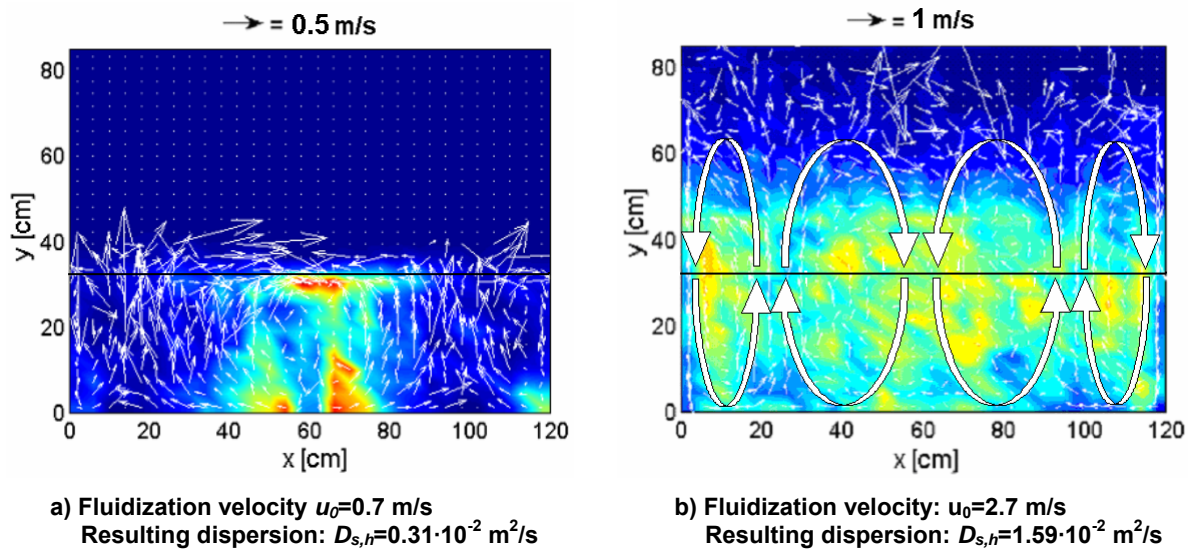


Figure 8: Normalized concentration [m⁻²] and velocity [m/s] of tracer particle with an increase in fluidization velocity. The horizontal line indicates the dense bed height ($Hb=0.33$ m). See Papers IV and V for similar results.

The results in Fig. 8 show a clear influence of the fluidization velocity on the mixing behavior of the tracer particle. While at low gas velocities (Fig. 8a) the tracer particle remains almost exclusively in a limited region of the bed (stagnation occurred for some time periods and had to be removed from the result data for a more clear representation), an increase in gas velocity (Fig. 8b) leads to a much higher mixing rate, revealed by the more homogeneous concentration field in Fig. 8b and higher magnitude of the velocity values (note the different vector plot scales used in Figs 8a and 8b). In quantitative terms, an increase from 0.7 to 2.7 m/s results in a fivefold increase in horizontal solids dispersion coefficient, $D_{s,h}$. This increase in solids mixing is found to be a general result of an increase in fluidization velocity, as long as a dense bed is maintained.

Another general observation from the experiments is the enhanced solids mixing provided by an increase in dense bed height. This can be observed from Fig. 9, where results from two runs at the same fluidization velocity but with different dense bed heights, 0.18 and 0.33 m, are shown. The higher bed gives a 40% higher horizontal solids dispersion coefficient and significantly higher values of the tracer velocity (note the difference in scale of the vector plots).

The influence of the tracer particle size and density on the horizontal mixing within representative ranges for fuel particles was also investigated and shown negligible in comparison to the influence on fluidization velocity and height of dense bed.

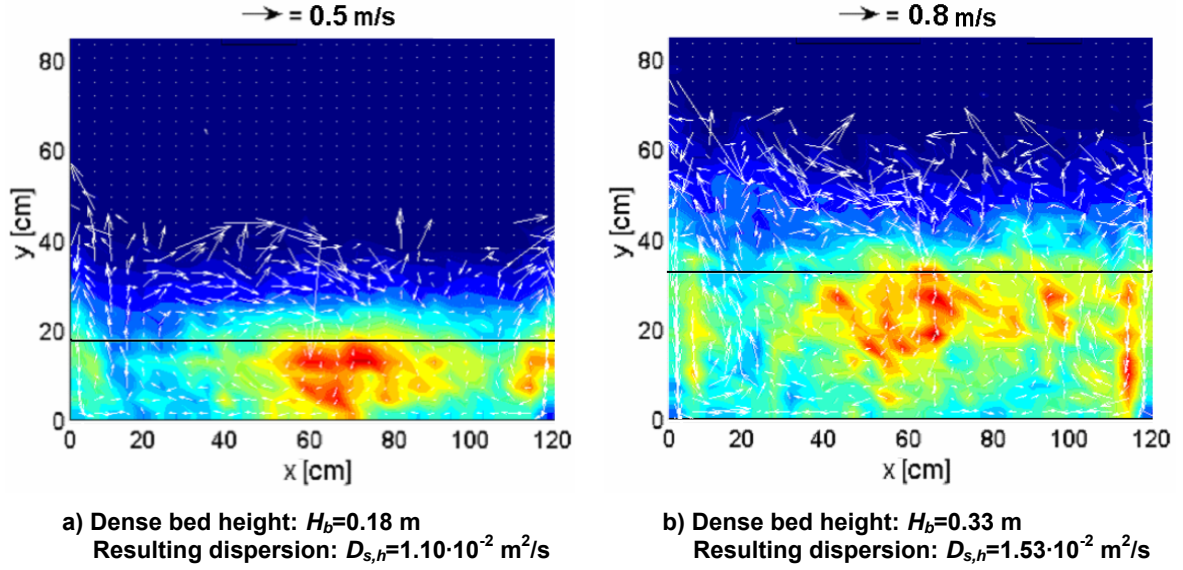


Figure 9: Normalized concentration [m^{-2}] and velocity [m/s] of tracer particle with an increase in dense bed height (indicated by horizontal line) at a fluidization velocity of $u_0=1.5 \text{ m/s}$. See Papers IV and V for similar results.

Finally, the pressure drop across the gas distributor was shown to give minor influence on the mixing provided a proper fluidization could be maintained. Despite this, low pressure drop might reduce the fuel-air contact, as shown in Paper V, negatively influencing the combustion process.

In summary, phenomena related to the inert bed material can be treated more or less satisfactorily with 1.5-dimensional models due to the rather homogeneous horizontal distribution of the bed material within the dense bed and the core region in the freeboard. It should be pointed out that the well-known heterogeneities in the wall layers (due to corner effects and the backflow effect) cannot be handled with 1.5-dimensional modeling. However, on the other hand, the horizontal gradients present in crucial parameters coupled to the horizontal mixing of the fuel phase (such as char concentration and moisture and volatile release rates) require a 3-dimensional analysis in order to provide a proper description of the process. In the present model, the horizontal mixing of fuel particles in the bottom region is modeled on a macroscopic scale by means of horizontal diffusion:

$$\frac{\partial C}{\partial t} = D_{s,h} \cdot \nabla^2 C + S \quad (12)$$

with the source term S including all of the following: fuel feed to the bottom region, i.e. fuel feeding ports, refeed of unburnt from the return leg, unburnt in the downflowing wall layers and, in form of negative values, the core fuel upflow leaving the bottom region.

In the transport zone, the core-to-annulus net solids flow also represents a lateral solids mixing mechanism. With respect to the axial direction, perfect fuel mixing is

assumed by the model in the dense bed while the freeboard is, as for inert particles, represented by Eqs 6 to 10.

In the return leg, fuel particles are assumed to be perfectly mixed with bed material and are thereby assigned the same residential time as that found for the inert particles.

Besides the consideration of the lateral mixing, modeling of the fuel mixing requires that the continuous change in physical properties (*i.e.* size and density) of the fuel particles as they burn is accounted for. This so that the corresponding changes in fluid dynamical behavior of the fuel particles can be described. Solid fuel in a boiler undergoes three potentially overlapping mechanisms: drying, devolatilization and char combustion. Under drying, the moisture release decreases the density of the fuel particle; analogously there is a further decrease in particle density during devolatilization due to the volatile matter released together with a certain shrinkage and, finally, char combustion can occur in two ways: through a shrink in size at approximately constant density or at constant particle size and with decreasing density. Neglecting the shrinkage due to devolatilization, the dynamical mass release rates of each of these three steps govern the size and density of the fuel particle under its conversion. As detailed in Paper II, these mass release rates can be described through the fuel conversion submodels by Thunman *et al.* (2004) for drying and devolatilization and by Field *et al.* (1967) for char combustion. The composition of the volatile matter released is calculated through an appropriate combination of energy and elementary mass balances and empirical ratios, as described in Thunman *et al.* (2001).

The submodel for drying and devolatilization is based on the description of the evolution of the temperature profile within the particle by solving the dimensionless energy equation given by Thunman *et al.* (2004):

$$\frac{1}{\xi^r} \frac{\partial}{\partial \xi} \left(\xi^r \frac{\partial \theta}{\partial \xi} \right) + c \cdot \frac{1}{\xi^r} \frac{\partial \theta}{\partial \xi} = 0 \quad (13)$$

The boundary conditions used in the solving process, expressed in non-dimensionless form, are:

$$T|_{r=\text{drying front}} = 100^\circ\text{C} \quad (14)$$

$$-\lambda_{\text{part}} \frac{\partial T}{\partial r} \bigg|_{r=\text{surface}} = h_{\text{eff}} \cdot (T|_{r=\text{surface}} - T_\infty) \quad (15)$$

where the effective heat transfer coefficient, h_{eff} , accounts for both convective and radiative heat. A main advantage of this submodel given by Thunman *et al.* (2004) is that it gives the existence of analytical expressions for the quasi-steady state solution of Eq. 13, providing a fast solving procedure for a wide variety of fuel particle geometries and compositions.

Concerning char combustion, a surface reaction process is most often established, for which the effective char combustion rate, R_{eff} , can be modeled according to Field *et al.* (1967) through a combination of the kinetic rate, R_{kin} (determined through

an Arrhenius-type correlation) and the mass transfer coefficient, k_m (determined through a Sherwood-type correlation):

$$R_{eff} = \frac{1}{\frac{1}{R_{kin}} + \frac{1}{k_m}} \quad (16)$$

Thus, the expression for char combustion (first order reaction is assumed) reads:

$$\frac{d m_C}{dt} = -\Omega \cdot R_{eff} \cdot A_{part} \cdot C_{O_2, \infty} \quad (17)$$

The satisfactory agreement of the fuel particle conversion submodel outlined can be seen in the comparison between in-house thermogravimetical experiments and modeled data shown in Fig. 10 for a wet coal particle. In this example, an overestimation of the drying and devolatilization rates is the reason for the slight overestimation of the modeled mass release in the initial time period. From measured data it is seen that the mass release coupled to drying and devolatilization dominates in the first 100 s and thereafter char combustion takes over. Finally, after 200 s, only the non-combustibles corresponding to the fuel ash content remain. From comparison with other modeling approaches, the present conversion submodel (Eqs 13 to 17) gives an agreement similar to that of discrete models but at a much lower computational cost.

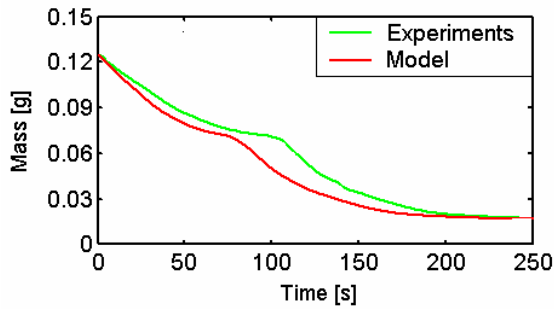


Figure 10: Coal particle conversion. Comparison between model results and in-house experiments (Thunman, 2005).

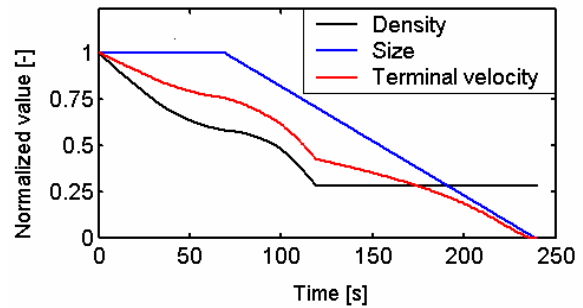


Figure 11: Coal particle conversion. Change in physical parameters as obtained from the model (Eqs 13 to 17).

Having modeled the dynamical mass release during drying, devolatilization and char combustion in a fuel particle, calculation of the change in particle size and apparent density is rather straightforward neglecting shrinking during drying and devolatilization, assuming char combustion to take place at the particle surface and ashes to leave the particle during char burn out. With this, the modeled particle size and apparent density corresponding to the same coal particle analyzed in Fig. 10 can be calculated and are shown (in normalized values) in Fig. 11. With these, the evolution of the terminal velocity of the fuel particle during its conversion can be easily calculated (for example through the expressions by Haider and Levenspiel, 1989) and is also plotted in Fig. 11. The continuous change in terminal velocity gives an idea on how different the fluidynamical behavior of a fuel particle can be, depending on its degree of conversion.

Finally, it should be noted that the drastic and sudden change in the fuel particle size entailed by fuel fragmentation plays an important role in both fuel conversion kinetics and fuel mixing. The comprehensive model presented here does not include a submodel for fragmentation (although such are available in literature, see e.g. Salatino and Massimilla, 1989, or Chirone *et al.*, 1991). Instead, this is an input which can be determined experimentally through fragmentation tests. A brief sensitivity analysis of the influence of fuel fragmentation on several fuel-related parameters is given in Paper II. The reason for not implementing a fuel fragmentation model is the further work needed in order to develop reliable fragmentation models which can be applied under boiler conditions.

Gas phase

A key feature of the present work is the modeling of the gas phase, described in detail in Paper III. The gas phase in a fluidized bed has a fluctuating character in terms of both flow magnitude and composition, as shown respectively by the oscillating pressure in the plenum (Sasic *et al.*, 2004) and fluctuations in zirconia cell measurements (Niklasson *et al.*, 2003). In addition, measurements show that both velocity and composition of the gas flow vary strongly in the bottom region of the furnace depending on whether the gas flows through the bubble phase (throughflow gas) or not (emulsion-only gas), as explained by Lyngfelt (1996).

However, neither a differentiation between throughflow and emulsion-only gas nor the flow fluctuations have been included in the macroscopic models of the gas phase given in literature. Instead, previous models have been limited to directly model time-averaged values which lead to a need for empirical fitting of the combustion kinetics. The present submodel divides the gas phase into a throughflow and an emulsion-only gas and models their respective flow fluctuations, which then govern the oxygen-fuel contact. This approach is based on the dynamical pressure balance presented in Paper III. To begin with, the rise of a bubble through the dense bed must be described. For this, there are expressions for bubble size and rise velocity available in literature (Clift and Grace, 1977, and Darton *et al.*, 1985). The pressure balance over a representative bed portion, L^* , at an arbitrary time step during the bubble rise is illustrated in Fig. 12, with the gas divided into two phases: throughflow and emulsion-only (orange and brown respectively). The pressure drops across the gas distributor and the dense bed solids are considered for each gas phase, yielding corresponding instantaneous gas fluxes (*i.e.* for gas flux in emulsion phase and in through flow phase).

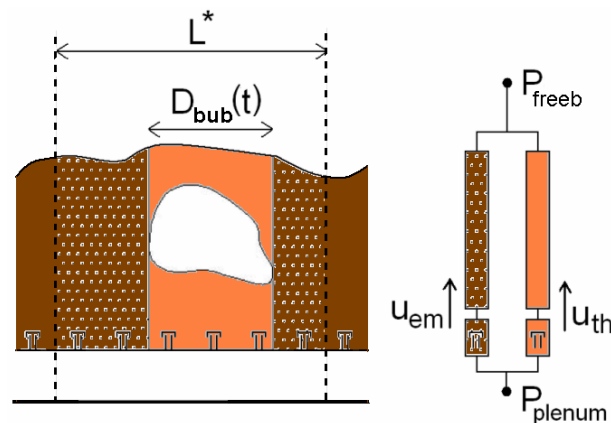


Figure 12: Scheme of the pressure balance for the two considered gas phases.

The calculated gas fluxes are combined with values of the combustible volatile flows and char concentration obtained from other submodels (details on the link between the models are given in Chapter 3) in order to compute the progress of combustion. As mentioned previously, the combustion rates do not need to be experimentally fitted in the present approach, and transport-controlled combustion (*i.e.* infinitely fast kinetics) can be assumed for the combustible volatile matter, while char combustion can be calculated by Eqs. 16 and 17. Thus, in each cell of the bed, the fluctuating flow of gas species calculated through the dynamical pressure balance can be combined with the outputs from the fuel mixing submodel in order to calculate how the combustion progresses. Modeled data showing the evolution of the oxygen consumption with height during a bubble cycle is shown in Fig. 13. This figure shows that, along the furnace centerline, at a height of 0.2 m above the gas distributor the oxygen is fully consumed in the emulsion-only gas phase at some point during the bubble cycle. Above this height, the time interval of flow without oxygen increases with height. During absence of oxygen, released volatile hydrocarbons will remain unburned and add to the gas flow, as observed in the dotted curve corresponding to $h=0.24$ m.

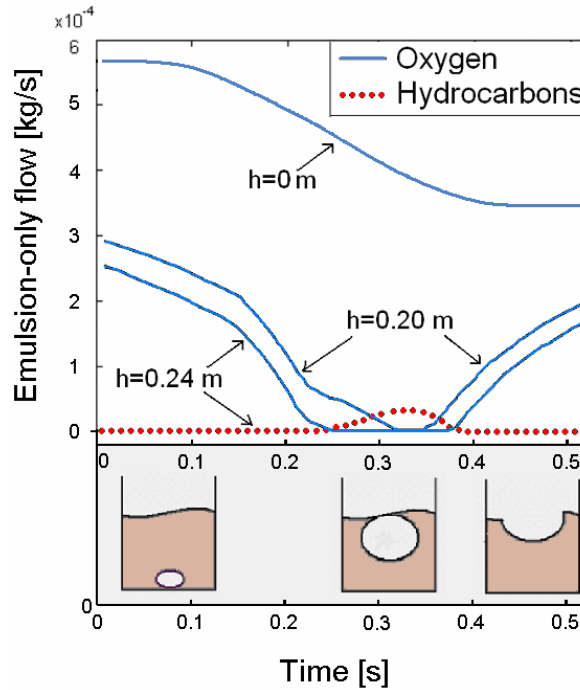


Figure 13: Modeled cell flow of gas species (oxygen and hydrocarbons) in the emulsion-only phase at different heights on the furnace centerline.

It is important to note that on a time-averaged basis the cell corresponding to a height of 0.24 m at the furnace centerline yields non-zero concentrations of both oxygen and hydrocarbons. Yet, coexistence of these is not allowed in the time-resolved modeling.

As a general result from the pressure balance illustrated by Fig. 12, gas fluxes (and thereby gas velocities) predicted for the throughflow are higher than those of the emulsion-only flow at any time step. In addition, the throughflow flows across a shorter emulsion path length, coming into contact with less fuel particles and thus experiencing lower oxygen consumption. Therefore, two types of gas phases are

present at the dense bed surface: a high velocity oxygen-rich (throughflow) phase and a low velocity oxygen-poor (emulsion-only) phase.

The velocity difference between gas phases, responsible for the bias observed in gas probe measurements in the bottom region of fluidized bed units, decreases with height in the splash zone. Also, the flow fluctuations within each gas phase are gradually damped along the splash zone. As a result, there is a significant gas backmixing in the splash zone which eventually leads to a rather constant (*i.e.* non-fluctuating) gas flow in the transport zone.

As stated above, measurements by Zhang *et al.* (1995) suggest a more or less stagnant gas flow within the wall layers of the transport region, supporting the assumption of gas flow in the core region only. Having this, horizontal dispersion of the gas in the core region of the transport zone is considered according to:

$$\frac{\partial G_i}{\partial t} = D_{g,h} \cdot \nabla^2 G_i \quad (18)$$

Gas species concentration, C_i , is usually the transported scalar in Eq. 18 instead of the gas species flux, G_i , used here. While the use of both variables leads to the same result under plug flow conditions, the use of the gas species flux is able to describe the flattening of heterogeneities in gas velocity field when such are present. Such heterogeneities are often present, mainly due to secondary air injections and have been measured by Kruse and Werther (1995). From several experimental studies available in literature on values for the gas horizontal dispersion coefficient, $D_{g,h}$, the Peclet number expression given in Kruse *et al.* (1995) is used:

$$Pe = \frac{u \cdot L_{riser}}{D_{g,h}} = 387 \quad (19)$$

In the cyclone perfect gas mixing is assumed, implying full combustion of any combustible volatiles remaining unburned, provided enough oxygen is available.

Finally, all gas leaving the particle seals is assumed to flow towards the riser through the solids recirculation ducts.

Heat transfer

In a fluidized bed boiler, heat is extracted from the solids and gas in the circulating loop and from the flue gas in the convective pass after the cyclone. With a given stack temperature for the flue gas, computation of the heat extraction from the convective pass is straightforward once the composition and temperature of the flue gas after the cyclone have been obtained from the comprehensive model. Thus, focus is set on the more complex modeling of the heat transfer in the circulating loop.

While the formulation of a heat balance is given in Chapter 3, the different terms in this modeling originate from the submodels explained in Chapter 2. With terms related to solids (including the fuel fraction) and gas flow available as output from other submodels, the heat transfer terms in the heat balance which describe the heat extraction are addressed in this section.

Heat is transferred to the heat exchanging surfaces through two mechanisms: convection and radiation. Simplified approaches estimating the heat transferred by the sum of these two phenomena exist, but a separate treatment of convection and radiation is desirable for a more accurate modeling of the heat transfer. This, since in the rather dilute upper freeboard, radiation from regions away from the heat transfer surfaces plays a more important role than in the bottom region. In the bottom region, the denser solids suspension density has a stronger absorption effect and gas and solids flowing near the heat transfer surfaces limit the influence of radiation from further away from the surfaces. Thus, heat transfer is expressed as:

$$q = q_{conv} + q_{rad} \quad (20)$$

where convective and radiative heat transfer from the gas-solid suspension to any surface are treated separately and each expressed in the classical form given by:

$$q = h \cdot A \cdot (T_{susp} - T_{surf}) \quad (21)$$

where the temperature of the gas-solid suspension must be taken as the local temperature close to the heat transfer surface in the case for convection and as some average over the surrounding in the case of radiation (\tilde{T} , which is explained below). In the present work, only heat transfer between the gas-solid suspension and the heat transfer surfaces is accounted for, *i.e.* heat transfer within the gas-solid suspension is neglected.

Breitholtz *et al.* (2001) managed to differentiate convection and radiation in their measurements and correlated the convective heat transfer coefficient to increase with the local solids concentration as:

$$h_{conv} = 25 \cdot C_{s, susp}^{0.58} \quad (22)$$

The radiation heat transfer coefficient between a suspension and a heat transfer surface reaches its maximum value when the suspension is free of solids, reading:

$$\hat{h}_{rad} = \frac{1}{\frac{1}{\varepsilon_{susp}} + \frac{1}{\varepsilon_{surf}} - 1} \cdot \sigma \cdot (\tilde{T}_{susp}^2 + T_{surf}^2) \cdot (\tilde{T}_{susp} + T_{surf}) \quad (23)$$

However, this coefficient decreases with the presence of solids in the suspension due to the shadowing effect of the suspended particles. In order to face this, Breitholtz *et al.* (2001) defined and correlated a radiative heat transfer efficiency as:

$$\eta_{rad} = \frac{h_{rad}}{\hat{h}_{rad}} = 0.86 - 0.14 * atg\left(\frac{\tilde{C}_{s, susp}}{2.6} - 1.6\right) \quad (24)$$

Note that suspension parameters (solids concentration and temperature) are averaged when used in expressions which concern radiative heat transfer such as Eqs. 23 and 24. This averaging stands for the fact that properties of the suspension which is not in the vicinity of the heat exchange surface can also play an important role in the radiative heat transfer. This is illustrated in Fig. 14, where the differential

weight of local values is represented by a continuous red line and the mesh grid at the level studied is drawn in green with the two figures illustrating typical conditions at low and high level in the freeboard (*i.e.* dilute and dense solids suspension, respectively).

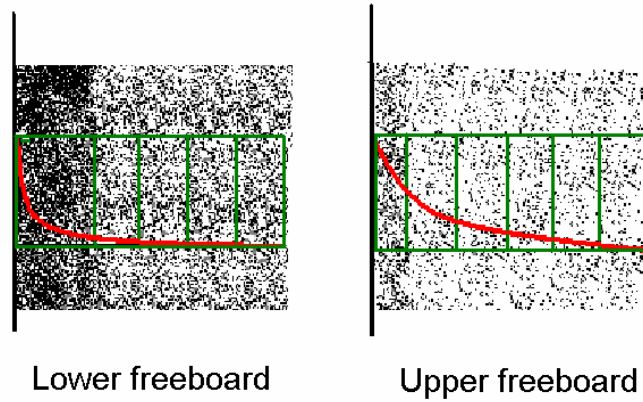


Figure 14: Weight of the local parameters in the Bouguer-averaging used in radiative heat modeling. The green lines represent a mesh at a certain level in the furnace, with the furnace wall (heat transfer surface) to the left.

As seen in Fig. 14, under dense flow conditions (such as in the lower level in the freeboard) the suspension close to the heat transfer surface (the wall to the left in this case) takes most of the area below the red curve representing the differential weight of radiation parameters. A different situation is encountered in dilute suspensions (upper freeboard positions), where cells also located relatively far away from the wall have a certain weight according to the red curve. The weighting curve is given by the Bouguer's law for radiative properties of solids suspensions (see *e.g.* Baskakov and Leckner, 1997, for an example on its use in fluidized bed units), which accounts for the absorption effect of solids in a suspension according to:

$$\alpha = 1 - \exp\left(-\frac{1.5 \cdot C_{v,s} \cdot L}{d_s}\right) \quad (25)$$

For simplicity reasons, calculation of the radiative heat from the suspension to the heat transfer surfaces in the circulating loop is limited in the sense that a certain cell is assumed to only transfer radiative heat to cells at the same height in the furnace. Details on the implementation of the Bouguer's law and other details on heat transfer modeling are given in Appendix A.

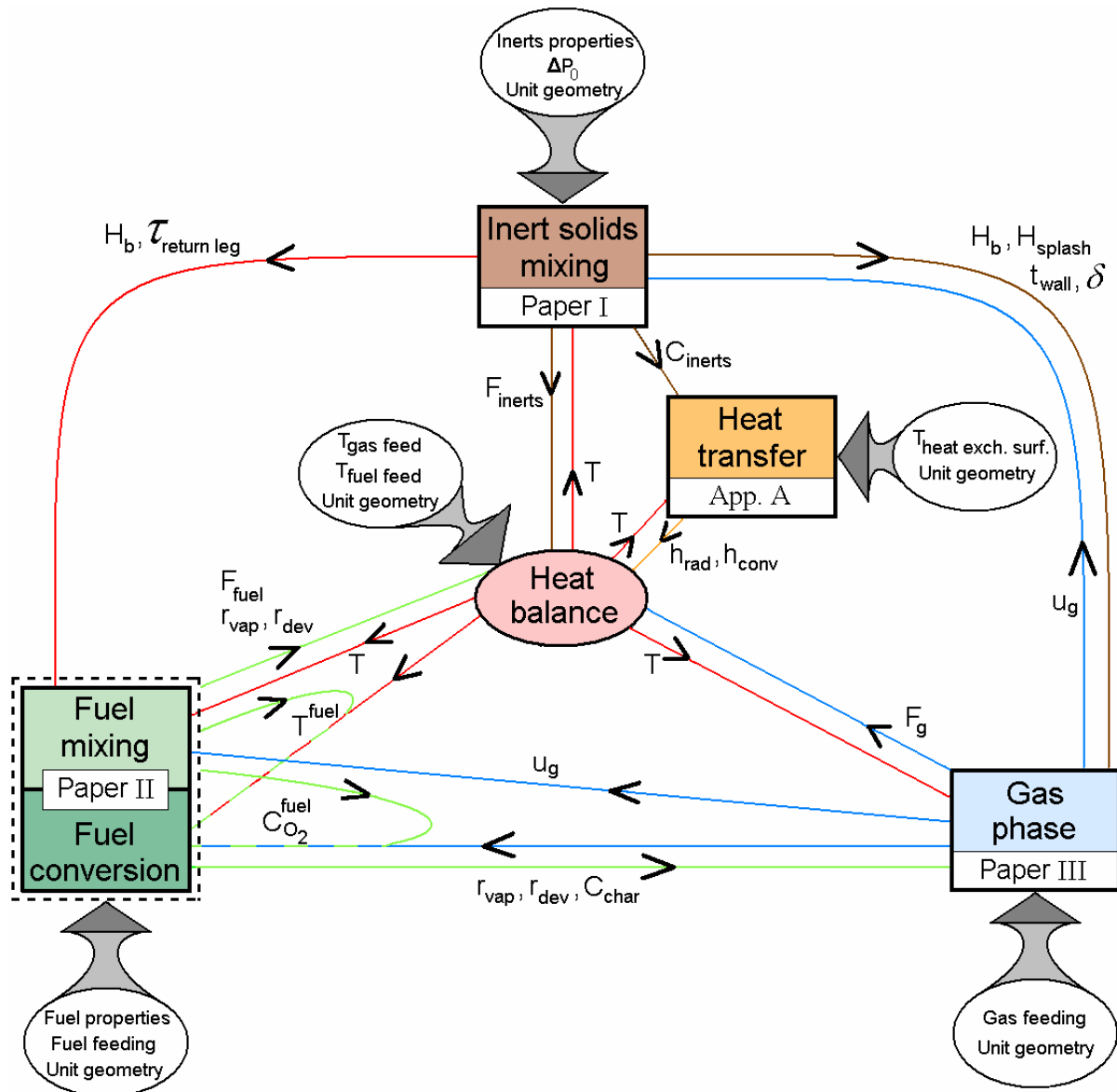
Chapter 3 – Comprehensive model

3.1 Coupling of submodels

The submodels summarized in Chapter 2 and given in Papers I, II and III and Appendix A can be linked in order to build a comprehensive model covering several fields in the process, *i.e.* fluid dynamics, combustion and heat transfer in the present case. The submodels presented need inputs which can be either external (if provided by the user of the model) or internal (if provided as outputs from other submodels or balances in the comprehensive model). A scheme of the coupling between submodels indicating the flow of internal and external inputs is given in Fig. 15. Pressure, population and heat balances are required for the solving procedure of the comprehensive model.

The external inputs required by the comprehensive model can be divided into four categories:

- Geometry of the circulating loop.
- Characterization of the fuel and gas feeding through fuel proximate and ultimate analyses, heating value, size, shape, temperature and feeding rate at each of the feeding ports, and gas composition and temperature at all injection locations. In addition, a fuel fragmentation pattern must also be provided to the model, although this is not a known variable (but defined as an input to provide transparency with respect to that this is an area where additional experimental work is required).
- Physical properties of the in-bed inert solids, namely the PSD, density and sphericity of each inert solid fraction considered in the bed material. As discussed above, the in-bed PSD is not known or easily measurable and its prediction (through implementation of submodels for attrition and size segregation in the cyclones and ash classifiers) should be included in further development of the present model.
- Operational conditions, which in the present model (and generally in practical operation) are the vertical pressure drop over the furnace (or part of it) and the temperature of the heat-extracting surfaces (which, for most cases, is the evaporation temperature at the steam pressure on the waterside).



C	Concentration field	Superscripts	
F	Flow field	fuel	Average experienced by fuel
H	Height		
h	Heat transfer coefficient	Subscripts	
r	Release rate field	char	Char fraction
t	Wall layer thickness	conv	Convective
T	Temperature field	dev	Devolatilization
u	Velocity field	fuel	Fuel
δ	Bubble fraction	g	Gas
τ	Residence time	inerts	Inert solid fraction
ΔP_0	Furnace pressure drop	rad	Radiative
		vap	Vaporization of fuel moisture

Figure 15: Data flow scheme used in the coupling of submodels. External inputs are indicated by the four white ellipses. Papers describing the different submodels are indicated.

Note that the submodel for fuel conversion has two inputs (the average oxygen concentration and temperature as experienced by the fuel particles) which are not direct outputs from any of the submodels but calculated by combination of outputs from other submodels.

The output of the overall model is a comprehensive set of data from the different submodels, but the most relevant results for evaluation and/or validation of the simulated process are generally the solids, gas and heat flow fields, the solids and gas concentration fields and the temperature field.

In the following, the formulation of the different balances in the solving process is given together with an outline of the strategy used to couple the fuel mixing and fuel conversion submodels.

Heat balance

As seen in Fig. 15, the heat balance in the present model provides the temperature field in the circulating loop given data on gas and solids flows, fuel releases (both drying and devolatilization are endothermic processes) and heat transfer coefficients.

Individual heat balances are performed over different elements (either mesh cells in the freeboard or regions considered to have perfect thermal mixing), providing an output temperature value to each of these elements and thereby forming a complete temperature field. In the present model, the bottom bed is assumed to be thermally perfectly mixed and therefore a single heat balance is formulated over the bottom bed. In the freeboard, individual heat balances are performed for each mesh element except for the region above the exit ducts towards the cyclone, which is treated as a single, thermally perfect mixed element. The return leg is divided into different regions assumed to be perfectly mixed, representing the cyclones and particle seals.

The heat balance for each element reads:

$$\sum_s \dot{h}_{s,in} + \sum_g \dot{h}_{g,in} = \sum_s \dot{h}_{s,out} + \sum_g \dot{h}_{g,out} + \dot{h}_{vap} + \dot{h}_{dev} + q_{conv} + q_{rad} \quad (26)$$

The terms can be easily identified in Eq. 26 representing the enthalpy flows coupled to the different solid fractions, s , and gas species, g , the heats of vaporization and devolatilization from the fuel-released moisture and volatiles and the transferred convective and radiative heat.

When applied to the different furnace regions considered in the model, the general form of the heat balance given in Eq. 26 takes different forms which are summarized below. For simplicity, only waterwalls have been considered as heat extraction surfaces in the model (although any internals can be treated in an analogous way).

The general formulation of the heat balance for any of the regions in the circulating loop which can be assumed to exhibit perfect thermal mixing, *region* (i.e. dense bed, exit zone, cyclones and particles seals), is expressed as:

$$\begin{aligned} \sum_s F_{s,in} \cdot h_s(T_{s,in}) + \sum_g F_{g,in} \cdot h_g(T_{g,in}) = \\ \sum_s F_{s,out} \cdot h_s(T_{region}) + \sum_g F_{g,out} \cdot h_g(T_{region}) \\ r_{vap} \cdot h_{vap} + r_{dev} \cdot h_{dev} + h_{conv} \cdot A_{surf} \cdot (T_{region} - T_{surf}) + h_{rad} \cdot A_{surf} \cdot (T_{region} - T_{surf}) \end{aligned} \quad (27)$$

Except for the temperature of the region studied to be solved, T_{region} , all data required by Eq. 27 are obtained from different submodels, as shown in Fig. 15.

In the dense bed, several solid streams need to be considered as inflows: the bottom wall layer solids downflow, the externally recirculated solids from the seal and the fuel fed to the bed, each at different temperatures. Solids leaving the dense bed are represented by the solids upflow in the bottom core region. In addition, a solids flow (an input in the current version of the model) of inerts and char leaves the dense bed at the dense bed temperature towards the ash classifier and reenters the bed at a higher temperature due to char combustion in the classifier.

The exit zone, the furnace region between the exit ducts and the furnace roof of the furnace, has the upflow in the top of the core region as inflow. The gas flow will leave towards the cyclone and the solids flow will split due to the backflow effect into a fraction entrained with the gas flow and a fraction internally recirculated through the wall layers.

In the cyclones and particle seals, identification of the solids in- and outflows is straightforward and thus is not described here.

For a core region cell both the gas and solids phase are assumed to enter the cell through its bottom face. If the cell studied is within the secondary air penetration area defined by the overall model inputs, secondary air is assumed to enter the cell at the injection temperature. The net transfer of solids from core to wall layer, F_{lat} , is assumed to be at the cell average temperature. No convective heat transfer term is considered for a core region cell. Finally, the radiative heat loss to the furnace wall applies a cell-dependent weighting coefficient, w' , as detailed in Appendix A.

$$\begin{aligned} \sum_s F_{s,bot} \cdot h_s(T_{bot}) + \sum_g F_{g,bot} \cdot h_g(T_{bot}) + \sum_g F_{g,inj} \cdot h_g(T_{inj}) = \\ \sum_s F_{s,top} \cdot h_s(T_{top}) + \sum_s F_{s,lat} \cdot h_s\left(\frac{T_{bot} + T_{top}}{2}\right) + \sum_g F_{g,top} \cdot h_g(T_{top}) + \quad (28) \\ r_{vap} \cdot h_{vap} + r_{dev} \cdot h_{dev} + w' \cdot h_{rad} \cdot A_{surf} \cdot \left(\left(\frac{T_{bot} + T_{top}}{2} \right) - T_{surf} \right) \end{aligned}$$

In the wall region, no gas flow is considered (this is also assumed for gaseous fuel releases and secondary gas injections). Downflowing solids enter the cells from the top face and are joined by the solids laterally transferred from the core region. In the lateral net solids flow from the core to the wall region each core cell is assigned a target wall cell to which the solids disengaged from the upflow flow into. Thus, each wall layer cell might have solids inflow from several core cells, with each inflow at the respective temperatures of the different core cells they originate from. Heat transfer to the waterwalls takes place by means of both convection and radiation. Thus, the heat balance in a wall layer cell reads:

$$\begin{aligned} \sum_s F_{s,top} \cdot h_s(T_{top}) + \sum_s F_{s,lat} \cdot h_s(T_{core\ cell}) = \\ \sum_s F_{s,bot} \cdot h_s(T_{bot}) + \quad (29) \\ h_{conv} \cdot A_{surf} \cdot \left(\left(\frac{T_{bot} + T_{top}}{2} \right) - T_{surf} \right) + w' \cdot h_{rad} \cdot A_{surf} \cdot \left(\left(\frac{T_{bot} + T_{top}}{2} \right) - T_{surf} \right) \end{aligned}$$

Pressure and population balances for the inert solids

The vertical pressure drop over the furnace (or part of it) is a usual operational parameter in FB units and is therefore treated in the present model as an external input to be provided by the user of the model (as listed above and shown in Fig. 15). It is an indicator of the amount of solids in the furnace and, thereby, of the dense bed height. Once a solids concentration field in the furnace is obtained, the pressure drop over the furnace can be easily calculated through axial integration:

$$\Delta P_0 = \sum_{h=0}^{H_{furnace}} \bar{C}_{s,h} \cdot g \cdot dz_h \quad (30)$$

where $\bar{C}_{s,h}$ is the cross-sectional average solids concentration at a certain height, h , and dz_h the height of the cells at that same height. Obviously, varying the summation height limits in Eq. 30 provides the pressure drop over the given height interval. Setting these summation limits to the heights corresponding to the recirculation ducts and the furnace exit ducts (see respectively P_{refeed} and P_{exit} in Fig. 16) gives the freeboard term in the pressure balance over the circulating loop as:

$$\Delta P_{freeboard} + \Delta P_{exit\ duct} + \Delta P_{cycl} + \Delta P_{dc} + \Delta P_{recirc\ duct} = 0 \quad (31)$$

Generally, the pressure drop over the recirculation duct is neglected compared to the other terms, *i.e.* P_{seal} and P_{refeed} in Fig. 16 are assumed equal. Models to estimate the pressure drops over the exit duct and the cyclone exist in literature (see Muschelknautz and Muschelknautz, 1991, and Rhodes and Geldart, 1987, respectively). With such a model and given a solids concentration field in the furnace, all terms in Eq. 31 can be either estimated or neglected except for the pressure drop over the downcomer, ΔP_{dc} , expressed as the difference between P_{dc} and P_{seal} in Fig. 16. This pressure drop is caused by the presence of the fluidized solids column (assumed to have the same voidage as that calculated for the particle seal) and is calculated from the pressure balance over the circulating loop by using Eq. 31.

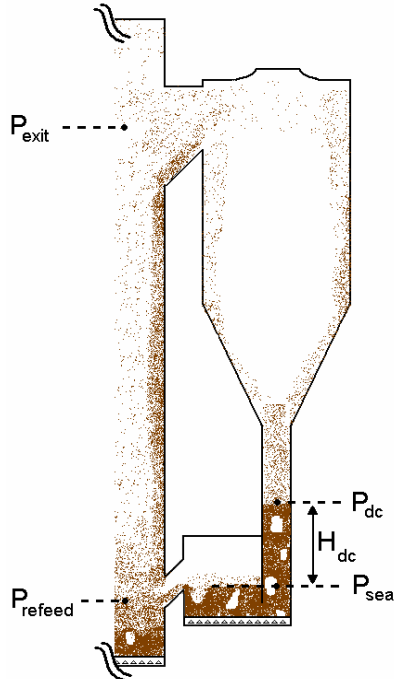


Figure 16: Key locations in the pressure balance over the circulating loop

From the calculated pressure drop across a solids column, the height of the column is easily estimated through:

$$H_{dc} = \frac{\Delta P_{dc}}{C_{s,dc} \cdot g} \quad (32)$$

Hereby, solids in the column formed in the downcomer (which might be an important term depending on the geometry of the unit and the operational conditions) can be calculated and taken into account in the formulation of a population balance over the circulating loop. Thus, formulation of a pressure balance is used to provide a value of the initially unknown term in the population balance.

Combined modeling of fuel mixing and conversion

A major difficulty encountered in the modeling of the fuel mixing is the continuously changing fluid dynamical behavior of the fuel particles as they burn, due to the variation in size and/or density. Thus solving the fuel mixing requires that the characteristics of the fuel conversion are accounted for and, as shown in Fig. 15, the two submodels of mixing and conversion must be combined in order to solve the fuel flow and concentration fields, as explained in Paper II.

An efficient way to work out this problem is based on the transient simulation of the behavior of a batch of fuel particles during the whole burnout time. The burn out time is discretized in several time steps for which the fuel particles present the corresponding values for the particle size and density provided by the fuel conversion model. With this, the fluid dynamics of the fuel fraction are solved at each time step applying the corresponding value for the fuel terminal velocity, providing the spatial distribution of the fuel concentration at any time step, $C_{fuel,t}$, originated by the fuel batch. This is illustrated by the first row in Fig. 17.

	$t=t_0$	$t=t_1$	$t=t_2$	$t=t_3$...	$t=t_{burn\ out}$	$t>t_{burn\ out}$
Fuel batch #1	$C_{fuel,0}$	$C_{fuel,1}$	$C_{fuel,2}$	$C_{fuel,3}$...	$C_{fuel,burn\ out}$	0
Fuel batch #2		$C_{fuel,0}$	$C_{fuel,1}$	$C_{fuel,2}$	$C_{fuel,3}$...	$C_{fuel,burn\ out}$
Fuel batch #3			$C_{fuel,0}$	$C_{fuel,1}$	$C_{fuel,2}$	$C_{fuel,3}$...
Fuel batch #4				$C_{fuel,0}$	$C_{fuel,1}$	$C_{fuel,2}$	$C_{fuel,3}$
...					$C_{fuel,0}$	$C_{fuel,1}$	$C_{fuel,2}$
...						$C_{fuel,0}$	$C_{fuel,1}$
...							$C_{fuel,0}$

Figure 17: Scheme applied to the calculation of the steady-state fuel concentration field

Having this, a continuous feeding of fuel can be simulated by a ‘continuous batch’ approach, in which further fuel batches are fed to the unit at each time step. This procedure is illustrated in Fig. 17, where the total fuel concentration at a certain time step is equal to the sum of the values in the corresponding column. Thus, note that a stationary concentration field is reached for the time steps after the burnout time of the fuel particles, with a value equal to the sum of all intermediate concentration values.

3.2 Computational flow scheme

The computational flow scheme required to solve the model is far from unique and can be done in many different ways. Yet, optimization of the computational flow scheme in order to minimize the computational time while ensuring a converging solution is a demanding task. Generally, several self-containing iterative loops are needed in the computation and sensitivity of each submodel is decisive for deciding which submodels occupy the inner iterations. Computational techniques have been adopted in the code in order to ensure and speed up convergence, such as dynamical tolerance values and relaxation factors, but are considered outside the scope of this manuscript. Thus, only a qualitative outline of the solving procedure of the comprehensive model is given in Fig. 18.

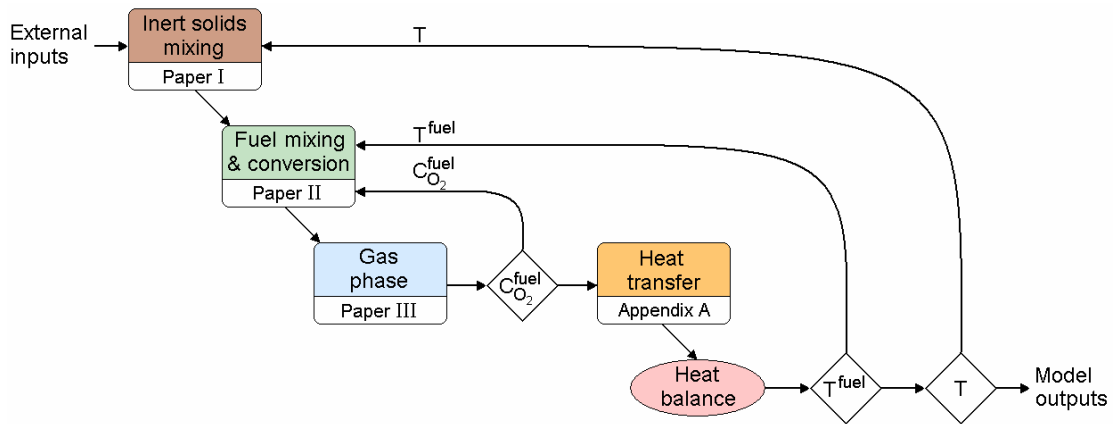


Figure 18: Solving procedure of the comprehensive model.
Papers describing the different submodels are indicated.

As seen in Fig. 18, there are three iterative structures at an inter-submodel level, with the convergence criteria for each of them being, respectively, the convergence of the average oxygen concentration and temperature experienced by the fuel and the temperature field in the circulating loop. While the internal computation of the submodels in Fig. 18 is straightforward from what is given in Chapter 2 and the respective papers dealing with each submodel, the internal computation of the submodel for the inert solids mixing and the heat balance have a higher complexity and are therefore explained further below.

Concerning the model for the inert solids mixing, its internal solving procedure is illustrated in Fig. 19. As seen, the dense bed and the cluster and disperse phase in the freeboard are first computed. This is done for each size interval of each solid fraction considered, with initial values for their dense bed PSD. From the resulting solids concentration field, the variable ΔP_{ref} is calculated by applying Eq. 30 between $h=0.14$ and 1.5 m (as specified in Paper I). The value obtained is used in Eq. 5 to estimate the dense bed voidage and this procedure is followed until a converging dense bed voidage is reached. In the midst iteration, the calculated operational pressure drop over the furnace is compared to the value provided as external input to the model, and the dense bed height is adjusted accordingly. After this, the pressure balance gives the height of the solids column in the downcomer, which can then be included in the population balance. Comparing the PSD of the calculated population

balance over the unit with that given as external input, the PSD in the dense bed to be used in the next iteration is chosen.

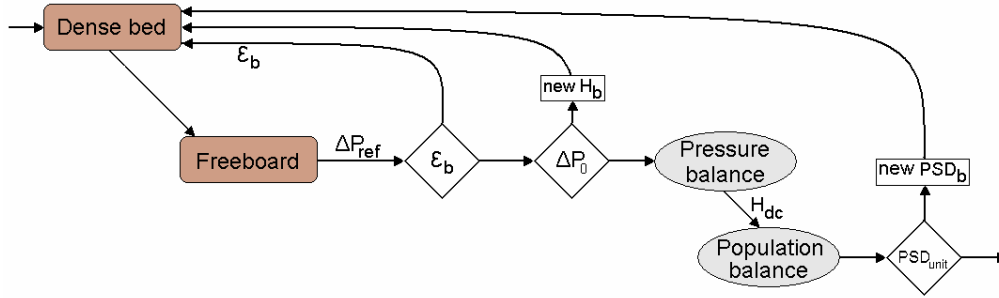


Figure 19: Solving procedure of the submodel for inert solids mixing

The solving procedure followed to couple the individual heat balances expressed by Eqs. 27 to 29 into the overall heat balance for the entire circulating loop seen in Figs 15 and 18 is illustrated in Fig. 20. The boxes in Fig. 20 referring to the core and wall cells represent all the individual mass balances formulated for each of these cells. For the core cells, the calculation starts with the heat balances of the bottom freeboard cells and continues upwards, while the opposite applies for the wall layer cells. Thus, while the *Core cells* and *Wall cells* boxes in Fig. 20 give temperature fields with as many values as cells evaluated, the other outputs are single scalars.

Two iterative processes constitute the solving scheme of the heat balance over the circulating loop. The inner iteration which is solved first gives the temperature field in the furnace and uses as convergence criterion the temperature of the wall layer downflow joining the dense bed.

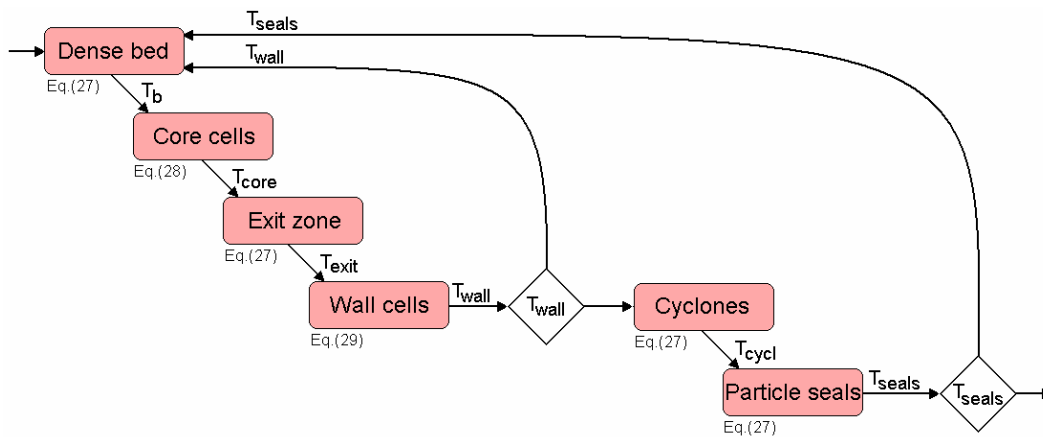


Figure 20: Solving procedure of the heat balance over the circulating loop.

After obtaining a converged furnace temperature field, heat balances in the elements of the return leg are formulated and the temperature of the solids externally recirculated to the dense bed (*i.e.* the temperature of the particle seals) is used as convergence criterion.

3.3 Furnace mesh

In order to enable a 3-dimensional analysis, the furnace is discretized by a mesh consisting of regular hexahedra. Finer meshing gives higher resolution in the results but also increased calculation time, so some compromise has to be adopted in the choice of the number of cells (calculations shown in this work have been performed with a number of cells in the order of 10^5).

For simplicity, all cells at a given height in the furnace have the same vertical extension, whereas the vertical extension varies with height in furnace. The mesh is generated so that the dense bed surface exactly coincides with the interface between two horizontal cell layers (note from Fig. 19 that the dense bed height is not fixed but varies during the computations, which implies that the mesh also needs to be regenerated during computation).

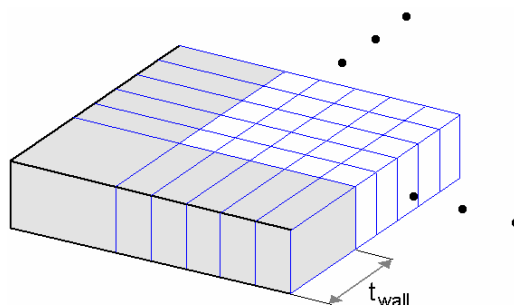


Figure 21: Meshing of the freeboard wall layers in the horizontal direction. Wall layer cells are gray-colored.

While the mesh is regular in the dense bed (cell sizes in the three dimensions can be chosen as input), the discretization of the freeboard is limited by the fact that no heterogeneities in the wall layers are accounted for in the direction normal to the furnace walls. Thus, at each height, the wall layer thickness becomes the size of the wall layer cells in the direction normal to the furnace walls, as shown in Fig. 21 for one of the furnace corners in an arbitrary horizontal cell layer (wall layer cells are gray-colored and core region cells are white).

In FB units, the splash zone presents a strong gradient in solids concentration and solids size and in fluctuating amplitude of the gas velocity, and its modeling is known to be critical for the correct performance of the overall modeling. To achieve a higher accuracy in this region, a refined mesh in the axial direction along the splash zone is used.

Finally, Fig. 22 exemplifies a representation of a fraction (10%) of cells from the mesh generated for the furnace of the 550 MW_{th} biomass-fired CFB boiler located in Alholmen (Finland).

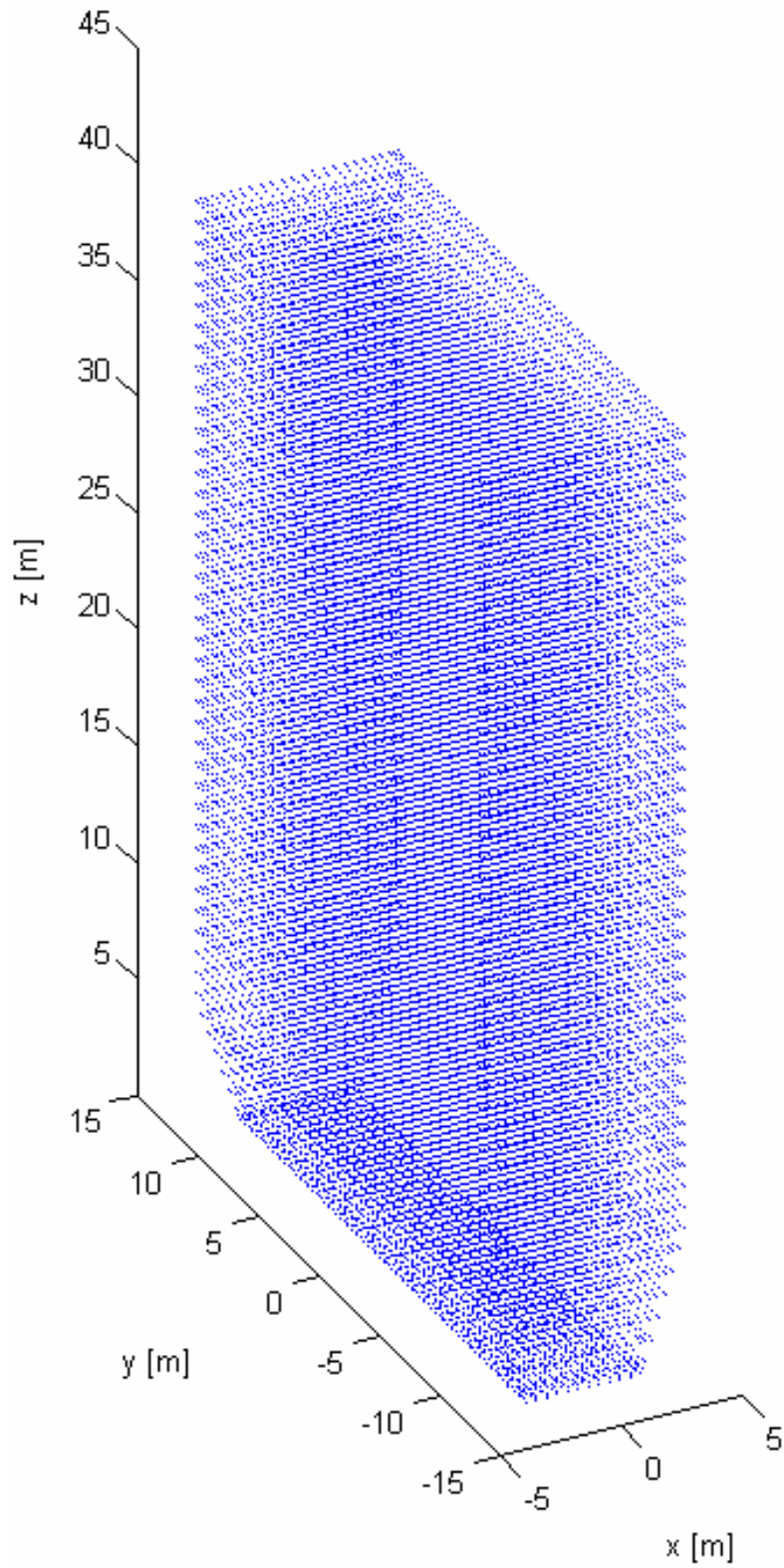


Figure 22: Mesh for the 550 MW_{th} biomass-fired CFB boiler in Alholmen (Finland). Only 10% of the nodes are plotted for better visualization. The total amount of cells is roughly $5 \cdot 10^5$.

Chapter 4 – Results

In order to illustrate its use and features, the comprehensive model presented above is applied to analyze the differences between combustion of high- and low-volatile content fuels in a CFB unit. Although fuel flexibility is one of the main advantages of fluidized bed combustion, the characteristics of the combustion process depend strongly on the fuel type. This makes the thorough analysis of combustion of different fuel types a must for the correct understanding of the process and thereafter for the optimization and scale up of the process.

Modeled data in this chapter are not compared to experimental data, but comparisons of modeled results with measurements in large-scale CFB boilers are available in Papers I, II and III.

Solid fuels can be classified according to the distribution of their combustible matter into volatile and char fields, given in the proximate analysis. The fuel types used in fluidized bed combustion sorted in descending char content (*i.e.* in ascending volatile content) read: coal, peat, biomass and waste. Here, for the sake of comparison, CFB combustion of a high-rank coal (anthracite) and biomass (wet, high-volatile wood chips) are selected for the model simulations. These fuels have been used in the experimental works by Lee *et al.* (2003) and Niklasson *et al.* (2007), respectively. Proximate and ultimate analyses and heating values for both fuel types are given in Table 2.

Table 2: Proximate and ultimate analyses and heating values of the two fuel types used in the simulations.

		Anthracite	Wood
as received	Moisture	3.2	34.9
	Volatiles	3.9	50.4
	Char	65.6	14.2
	Ash	27.3	0.5
dry ash-free	C	95.61	49.50
	H	1.11	6.21
	O	1.15	44.17
	N	0.60	0.10
	S	1.53	0.02
LHV [MJ/kg]	as received	22.02	11.38
	dry	22.82	18.57
	dry ash-free	31.78	18.72

Results

The boiler chosen for the simulations is the Chalmers CFB boiler, with a furnace height of 13.5 m which is schematized in Fig. 23. The single fuel feed point is located in the middle of the front wall at a height of 1.5 m and the secondary air injection ports used in the simulations are at both front and rear walls at a height of 2.1 m. The two sidewalls are waterwalls from 2.2 m above the distributor, with the remaining of the riser walls being refractory-lined. The bottom part cross section is 1.42×1.42 m, becoming 1.62×1.42 m as the side walls becomes bare membrane walls. Gases from the seal and the ash classifier enter the riser through the rear wall at 0.99 and 1.29 m above the primary gas distributor respectively. The furnace exit duct to the cyclone is placed in the rear wall, with its centerpoint at a height of 10.2 m above the air distributor. Further details on the geometry of the unit are given in Leckner *et al.* (1991). In the return leg, there is a heat exchanger in the seal system for increased flexibility by allowing control of the furnace temperature.

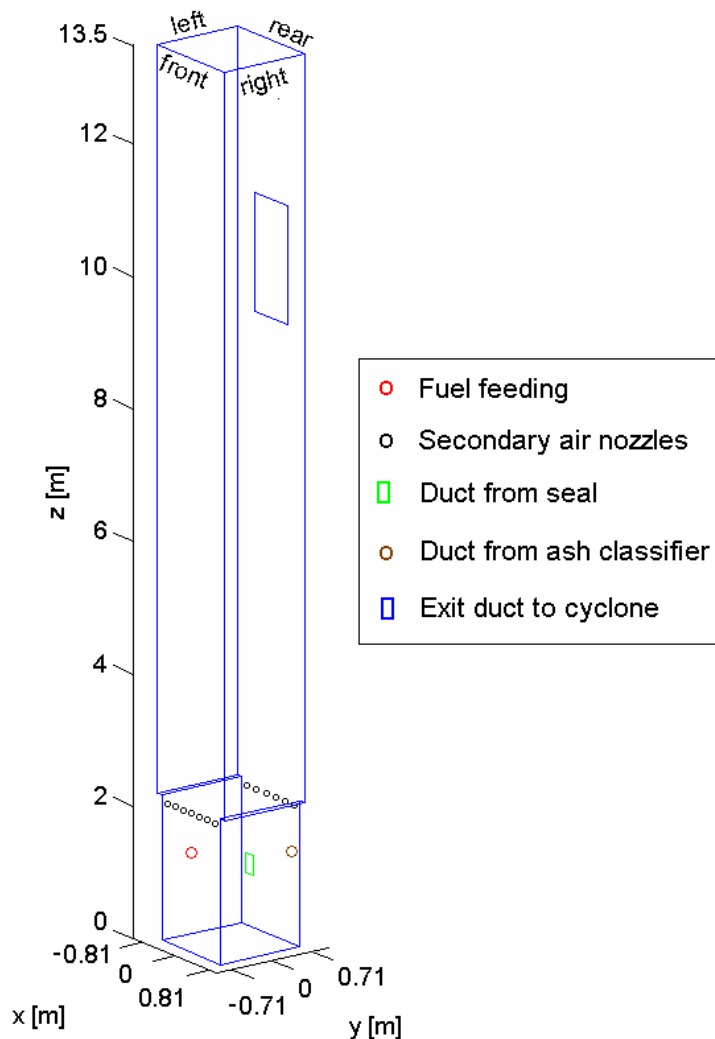


Figure 23: Illustration of the furnace of the Chalmers CFB boiler. The model covers the entire CFB loop, but only furnace is modeled 3-dimensionally.

The two fuel cases are simulated on the basis of a common heat power fed to the unit of 8 MW_{th} , at an air-to-fuel of 1.2. With the lower heating values given in Table 2, the respective fuel flows can be calculated (*i.e.* higher volumetric flow for the wood case, see Table 3).

Low-volatile fuels such as anthracite burn rather uniformly distributed over the furnace cross section (due to the relatively low kinetics of char combustion) and the fuel (char) is mostly present in the bottom region of the furnace (see Paper II). This makes it possible to operate the boiler with more or less all combustion air injected as primary air. Thus, no secondary air injection is applied in the simulations shown here for the anthracite case. On the other hand, high volatile fuels are known to be heterogeneously distributed over the furnace cross section. Introduction of secondary air helps enhancing the burnout of the volatiles by improving the gas mixing, *i.e.* breaking up the flow of so-called ghost bubbles (see Niklasson *et al.* (2003) for details on the ghost bubble phenomenon). The optimization of the flow magnitude and spatial distribution of the secondary air injections is often an issue of discussion, and for the present simulation of the wood case a 2^{ary} -to- 1^{ary} air-to-fuel of 0.57 has been chosen, with 13 active secondary air nozzles located at a height of 2.1 m (7 in the front wall and 6 in the rear wall).

Table 3: Main operational conditions used in the simulations.

		Anthracite	Wood
Heat power fed	MW _{th}	8	
Fuel feeding rate	kg/s	0.36	0.70
Air-to-fuel	-	1.2	
Fluidization velocity in furnace*	m/s	4.48	2.74
2^{ary} -to- 1^{ary} air ratio	-	0	0.57
Fluidization velocity in seal*	m/s	0.32	
Furnace pressure drop	Pa	9100	
Mean particle size	μm	348	
Solids density	kg/m ³	2600	
Dense bed aimed temperature	K	1173	1123
Waterside temperature	K	493	

* calculated at 1123 K

For a more straight-forward comparison between the two cases, the same air flow (0.17 kg/s) is supplied to the seal and the ash classifier in both cases. Also, the same inert bed material, furnace pressure drop and fluidization velocity in the seal are used in both cases.

Presence of internals and wing walls for controlling the furnace temperature is common in large CFB boilers. In the Chalmers CFB boiler, the dense bed temperature can be controlled through a heat exchanger located in the seal system. Thus, under operation, an aimed dense bed temperature can be approximated through the removal of more or less heat from the heat exchanger in the seal. The maximum temperature in the dense bed is obviously reached when no heat is removed from the seal system.

Finally, reactivity of anthracite char is much lower than that of wood. Furthermore, the char fed to the unit for the anthracite case is more than double than for the wood case. These (especially the difference in reactivity), make the char inventory in the unit become very high for anthracite (see Paper II for data on this). Having too high char concentrations in the unit implies a loss in combustion efficiency due to entrainment of char fines out of the circulating loop. In order to avoid this, the furnace is operated at a temperature above the usual 1123 K in order to speed up char combustion kinetics and thereby reduce the char inventory. Thus, the dense bed temperature is set to 1173 K. For the wood case, the standard dense bed temperature around 1123 K is set as target.

Besides the above-described operational parameters, the model needs the fragmentation pattern of each fuel type, the penetration of the secondary air gas jets and the solids flow through the ash classifier, which are not modeled. For simplicity, both anthracite and wood are assumed to fall apart in 8 pieces after 40 and 15 seconds respectively (this is arbitrarily chosen, but experiments have shown similar values). The difference in fragmentation time is due to the fact that coal fragmentation takes part mainly because of char combustion while wood fragmentation occurs primarily during devolatilization and thus earlier. The secondary air injection temperature is set to 493 K and the jet penetration in the furnace is assumed to be of 0.4 and 0.3 m in the normal and tangential directions to the wall respectively. A solids flow through the ash classifier of 1 kg/s is assumed.

With this, the model can provide the outputs for both cases considered. A selection of the modeled outputs is shown in Table 4 and commented below.

Table 4: Modeled values for a selection of key parameters.

		Anthracite	Wood
Dense bed height	m	0.39	0.54
Circulating net solids flux	kg/m²·s	33.2	2.6
Mean particle size in seal	μm	306	271
Temperature in furnace dense bed	K	1173	1111
Temperature in seal	K	1166	1143
Removed heat from seal	MW_{th}	0.76	0

With the same furnace pressure drop for both cases, a lower dense bed results for the case with higher fluidization velocity, *i.e.* the anthracite case. As a consequence of the higher fluidization velocity, the solids concentration in the freeboard for the anthracite case is higher than for the wood case, which results in a higher flux of externally recirculated solids observed in Table 4. Accordingly, since more of the coarse particles are entrained in the anthracite case, the mean particle size of the circulating solids, *i.e.* the mean particle size in the return leg, is larger.

According to the model, for the anthracite case the temperature in the dense bed of the furnace (where most combustion takes place) can in the Chalmers CFB boiler be adjusted to the targeted 1173 K by removing 0.76 MW_{th} from the seal, *i.e.* by cooling

down the externally recirculated solids to 1166 K before these solids are fed back to the furnace. For the anthracite case, the large char inventory in the unit (despite the high temperature at which the unit is operated) together with the high circulating solids flux (including char) makes char combustion in the seal high enough to consume all oxygen supplied with fluidization gas to the seal. Also in the ash classifier, all oxygen supplied is consumed.

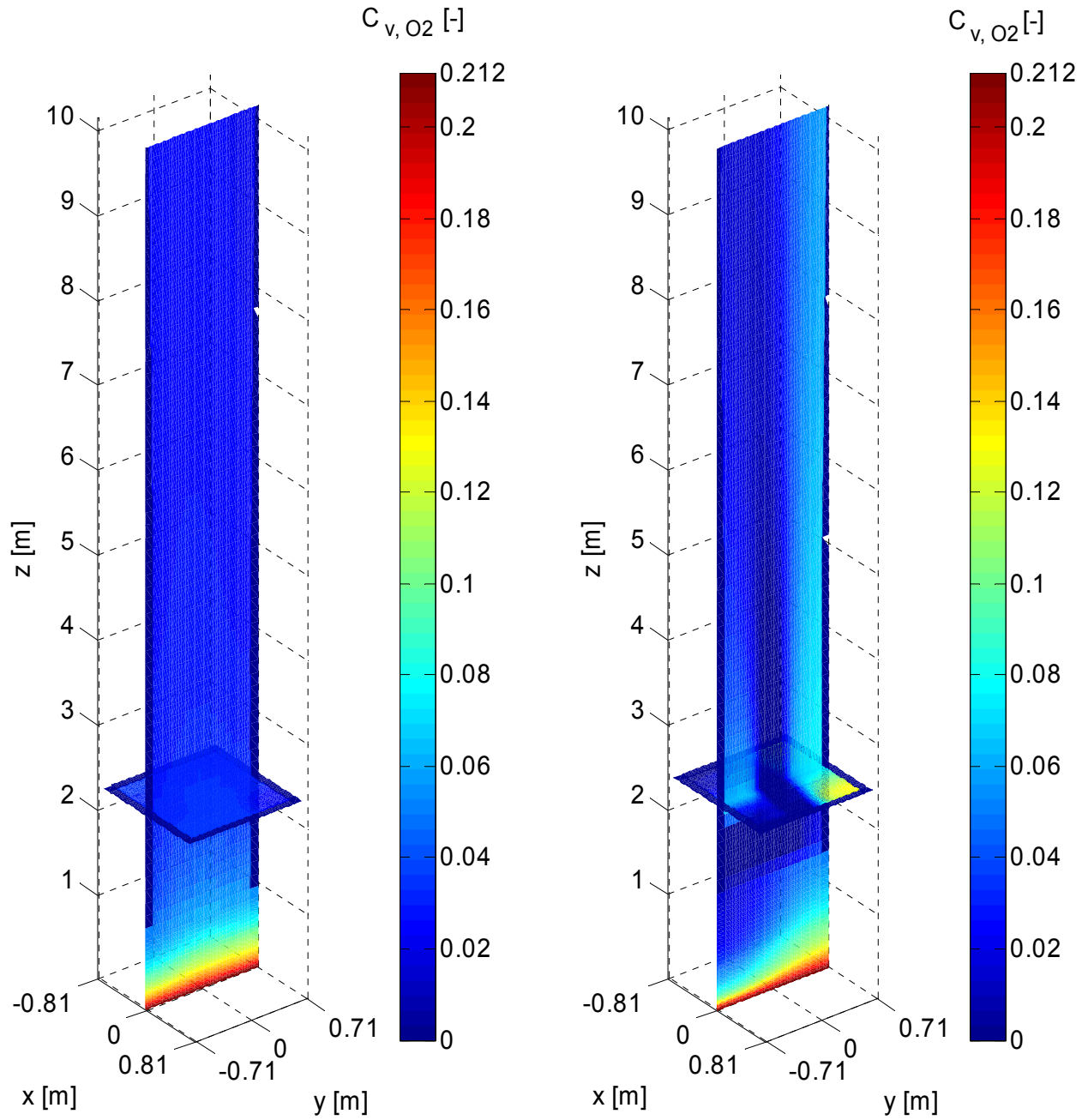
For the wood case, less combustion takes place in the dense bed and the targeted operational temperature of 1123 K for this region cannot be reached. A dense bed temperature of 1111 K is obtained from the model, with no heat removal from the seal system. This, despite the contribution of the externally recirculated solids at 1143 K coming from the seal (from which no heat is removed in this case). For this case, due to the low char inventory typical for high-volatile fuels, combustion in the seal and in the classifier is practically negligible.

Figure 24 shows the modeled distribution of oxygen concentration in the furnace for the two cases. For the anthracite case, the oxygen distribution in the horizontal direction is almost homogeneous at all heights in the furnace, with a sharp vertical decrease in the bottom region where most combustion occurs and a concentration around 3% at the exit height of the furnace. In contrary, the oxygen distribution for the wood case gives lateral heterogeneities already in the bottom region below the secondary air injections. This is due to the relatively fast kinetics of the devolatilization which, for this high-volatile fuel, implies a significant release of volatile matter concentrated close to the fuel feeding point and thereby resulting in higher oxygen consumption in this region. For the wood case, the limited amount of oxygen in the relatively low primary air flow leads to the prediction of a height interval immediately below the secondary air injections with strong reducing conditions. As can be seen from Fig. 24b in the horizontal slice cut placed directly above the secondary air injection, a larger part of the oxygen injected through the front wall is consumed compared to the rear wall-injected air. With the assumed jet penetration length of 0.4 m, the central region of the furnace gets oxygen depleted at the air injection height, although this effect disappears with height due to the horizontal gas dispersion in the freeboard (mixing of the secondary air further into the core region). Also, it should be observed that there is an increase in oxygen concentration due to the gas from the ash classifier injected close to the rear-right corner in the lower part of the furnace (see Fig. 23 for the exact location). A similar effect occurs with the gas from the seal, but this cannot be seen in Fig. 24b since this is located in a dead angle of the figure. With almost no char combustion in the seal or classifier for the wood case, the flue gas leaving these devices and injected to the riser is rich in oxygen. For the coal case the model predicts char combustion to occur also in both the seal and the ash classifier. Thus, injections of the (oxygen-free) flue gas from these devices into the riser do not represent any contribution to the oxygen flow, as seen in the horizontal slice in Fig. 24a.

Figure 25 gives the concentration fields for the combustible volatile matter for the two cases (note the different orders of magnitude of the plotted values). For both cases, the low Damköhler number for devolatilization in the horizontal direction leads to high release of volatile matter close to the fuel feeding point, which eventually build up regions of unburned volatiles (through the mechanism explained in relation to Fig. 13). For the anthracite case shown in Fig. 25a the negligible amount of volatiles is directly combusted. For the wood case, due to both the large mass flow of volatile matter fed into the unit with the fuel and the relatively low oxygen flow provided as

primary air, an important build up of combustible volatile matter occurs in the bottom region of the furnace, as seen in Fig. 25b. In the same figure, the horizontal heterogeneities of this volatile build up can also be observed. The higher concentration of combustible volatiles at the front wall than at the rear wall is the reason for the different levels of oxygen obtained above the secondary air injections in Fig. 24b. The model predicts a complete burnout of the volatiles in locations to which the secondary air jets reach, while some volatile matter remains unburned in the central part of the furnace. Obviously, results related to the injection of secondary air are sensible to the assumed penetration length and width of the secondary air, for which there is a notable lack of knowledge and experimental data. The remaining volatiles in the center part of the furnace cross section are consumed as gas mixes laterally on its way up through the freeboard. Note that with low enough values of the modeled horizontal gas dispersion coefficient, the lateral gas mixing could become slow enough to allow some of the unburned volatile matter to reach the cyclone.

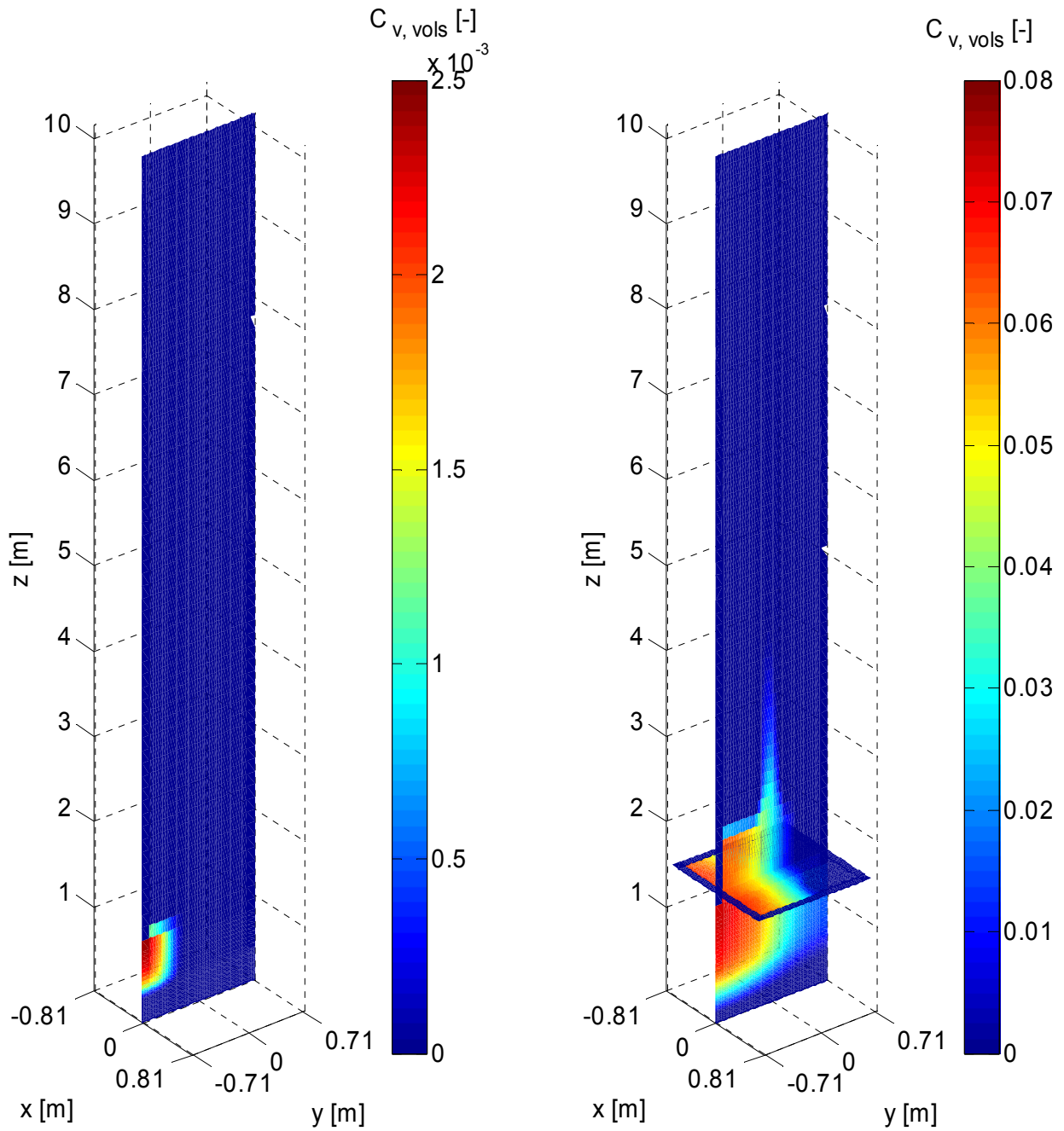
Finally, the furnace temperature fields for both cases are given in Fig. 26. Solids in a fluidized bed boiler act as thermal flywheel, with high values of the solids fluxes improving the homogeneity of the temperature field over the circulating loop. Thus, with the higher solids fluxes predicted for the anthracite case (see Table 4) the rather homogeneous temperature field observed for this case in Fig. 26a is consistent. As expected, the wood case presents heterogeneities in both the axial and lateral directions, as seen in Fig. 26b. For this case, a resulting dense bed temperature of 1111 K is obtained instead of the targeted temperature of 1123 K (as commented above), which increases with height in the splash zone mainly due to volatile combustion induced by the gas mixing in this region. At the air injection height, combustion of the volatile build up raises the temperature locally, with a predicted maximum value of 1255 K by the front wall. Concerning the air injection through the rear wall, excepting for a small region close to the furnace center, there is a balance between the heat produced by volatile combustion and that needed to heat up the air from injection temperature to surrounding temperature, and thus the temperature in the core region close to the rear wall is predicted to remain roughly unchanged. With the relatively dilute solids suspension in the freeboard for the wood case (mainly due to the lower primary velocity than in the coal case), heat radiation from the hot regions in the core to the waterwalls is significant and the temperature of the ascending solid-gas flow in the core region decreases gradually with height. Note the large temperature difference between solids downflowing by the front and the rear walls. This is due to that the downflow in the front wall is fed with solids coming from the locations with the highest temperatures in the core. From what is seen in Fig. 26b, an optimization of the process could be achieved by decreasing the air injection at the rear wall.



a) Anthracite case

b) Wood case

Figure 24: Modeled distribution of volumetric concentration in of O_2 in the furnace.



a) Anthracite case

b) Wood case

Figure 25: Modeled distribution of volumetric concentration of combustible volatiles in the furnace.

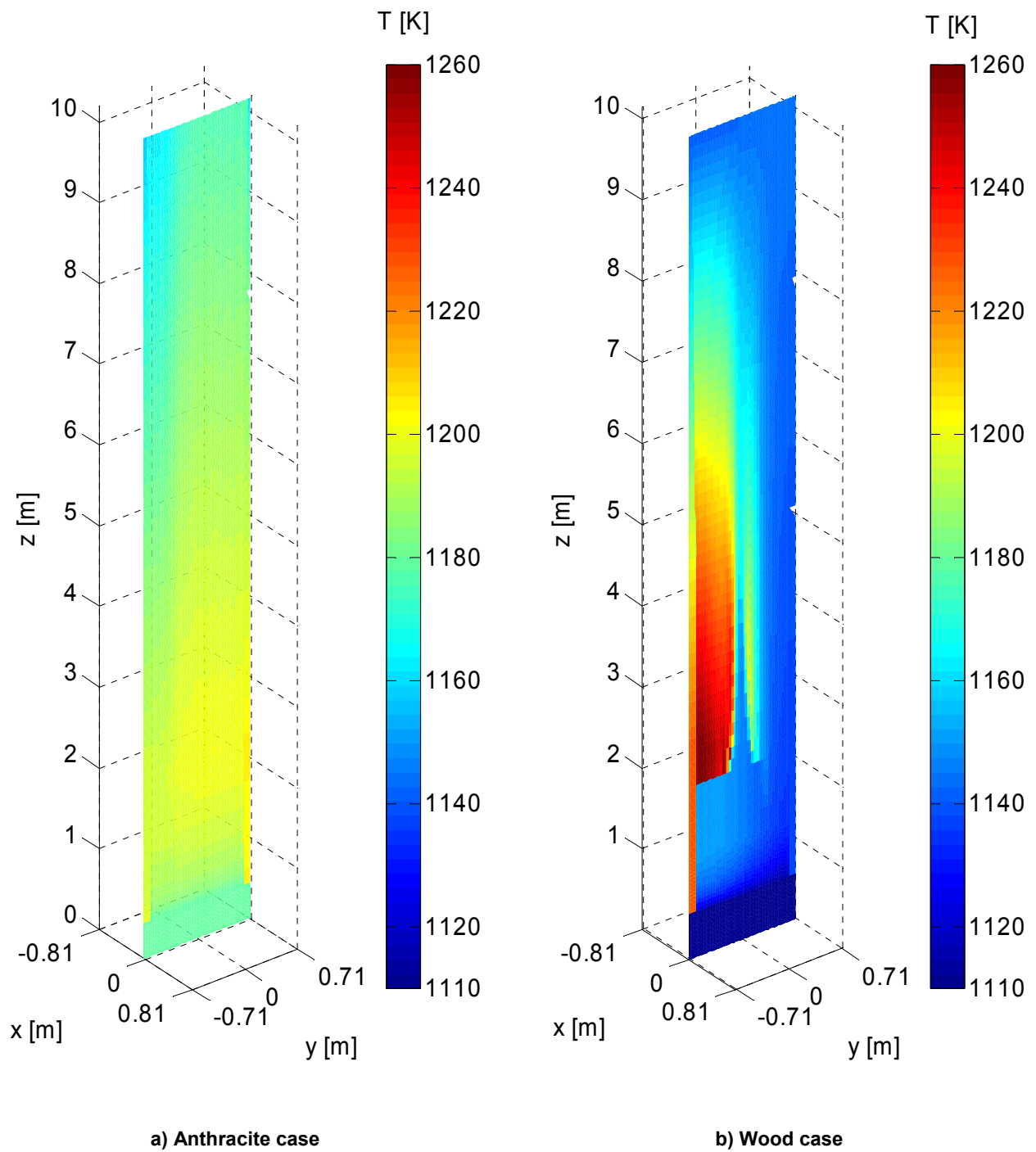


Figure 26: Modeled temperature field in the furnace.

Chapter 5 – Further work

Despite that the comprehensive model presented in this work is able to provide a rather accurate description of the major phenomena governing the operation of CFB boilers, potential improvements are planned to be implemented in the future development of the model. This includes also improved understanding of some of the underlying processes as expressed by the various submodels given in this work. A selection of possible improvements is listed and briefly commented below.

- In-bed particle size distribution. Currently, the particle size distribution (PSD) of the bed material is an input which the user of the model has to provide as input (although the internal solids size segregation is included). In practical operation this is not a known variable but results from a combination of several phenomena affecting the material fed to the unit, namely: attrition, bottom ash removal and cyclone separation efficiency. Proper description and combination of these processes through submodels will give a resulting in-bed PSD.

- NO_x and SO_x chemistry. The present model puts its focus on the main combustion reactions while those concerning sulphur capture and NO_x chemistry have not been included in the present version. Modeling of SO_x emissions obviously requires description of the mixing and kinetics of the sorbent, which should be carried out analogously to the modeling of the fuel fraction.

- Heat transfer within the gas-solid suspension. While at present only heat transfer from the gas-solid suspension to the heat transfer surfaces is considered in the circulating loop, heat transfer within the suspension itself is not accounted for. While this might not be of any major significance within the different fluid dynamical regions, heat transfer between these regions (e.g. between the core and annulus regions in the freeboard) might be significant under certain conditions.

- Lateral temperature gradients in the dense bed. The high axial solids mixing in the dense bed makes the assumption of perfect thermal mixing in the vertical direction in the dense bed a reasonable assumption. In relatively large units, however, the lateral mixing of solids (both inert and fuel fractions), and thereby of heat, is limited which might create regions of higher temperature in the dense bed close to the fuel feeding locations. Thus, modeling the solid flows within the dense bed would enable consideration of the temperature gradients in this region.

Finally, fuel fragmentation is not included in the modeling although models are available in literature. The complex nature of the fuel fragmentation phenomenon and its high sensibility on the fuel type and composition make experimental determination of the main fragmentation patterns a required activity before it is meaningful to implement a fragmentation submodel in the comprehensive model.

Chapter 6 – Conclusions

A model for the simulation of the combustion process in large-scale FB units has been presented, to a large extent based on the submodels and subprocesses given in the papers of this thesis. These submodels are combined with existing submodels in literature to a so-called comprehensive model for which the key features are presented above.

Most of the submodels developed in this work include innovative contents which enable the consideration of phenomena such as: the changing fluid dynamics of the fuel fraction as a function of the degree of conversion (including an experimental study on its mixing patterns), the fluctuating character of the gas flow, the existence of gas throughflow in the bottom region of the furnace, the influence of the pressure drop across the gas distributor, the corner effects in rectangular furnaces, the backflow effect and the separate modeling of radiative and convective heat transfer.

As a result, the modeled data show a good agreement with measurements carried out in several large-scale CFB boilers (including units which were not used to verify the submodels developed and used in this work).

Further work to improve the agreement and broaden the model targets is planned. The model addresses FB combustion, but should also be able to handle other FB applications such as FB oxy-fuel combustion, chemical looping combustion and FB gasification.

In addition, a novel method for 2-dimensional particle tracking has been introduced through an experimental study on the fuel mixing patterns. The mixing has been investigated with respect to its dependence on main operational parameters and physical properties of the fuel (tracer particle). A general structure in the flow pattern of horizontally-aligned vortices induced by the main bubble paths is observed for all cases. Increased dense bed height or fluidization velocity are found to enhance mixing both vertically and laterally, while size and density of the tracer particle only have a minor influence within the range of tracer particles studied (which correspond to the properties of typical fuel particles). As far as good fluidization is maintained, lowering the pressure drop across the gas distributor does not have any significant influence the solids mixing rate, but reduces the gas-solids contact.

Notation

Abbreviations

BFB	Bubbling fluidized bed
CFB	Circulating fluidized bed
FB	Fluidized bed

Greek letters

α	Absorption coefficient [-]	η	Efficiency [-]
δ	Bubble volumetric fraction [-]	ρ	Density [kg/m ³]
ε	Voidage [-]	σ	Stefan-Boltzmann ct. [J/K ⁴ m ² s]
θ	Dimensionless temperature [-]	τ	Residence time [s]
ξ	Dimensionless length [-]	Ω	Conversion factor [kg C/mole O ₂]
λ	Heat conductivity [W/m·K]		

Subscripts

b	Dense bed	mf	Minimum fluidization
bub	Bubble	mix	Mixing
cl	Cluster phase	rad	radiation
conv	Convection	riser	Riser
cycl	Cyclone	s	Solids
dc	Downcomer	settled	Settled bed
dev	Devolatilization	slip	Slip
disp	Disperse phase	surf	Surface
eff	Effective	susp	Suspension
em	Emulsion	t	Terminal
eq	Equivalent	th	Throughflow
freeb	Freeboard	vap	Vaporization
g	Gas	0	Primary
h	Horizontal	∞	Surrounding
kin	Kinetic		

Variables

A	Area [m^2]	c	Constant coefficient [-]
a	Decay constant [m^{-1}]	D	Dispersion coefficient [m^2/s]
C	Concentration [kg/m^3]	d	Particle size [m]
F	Flow [kg/s]	p	Pressure [Pa]
f	Empirical function	p_{ent}	Entrainment probability [-]
G	Flux [$\text{kg}/\text{m}^2\text{s}$]	q	Heat flow [W]
g	Gravity acceleration [m/s^2]	R	Rate [m/s]
h	Convective coefficient [$\text{W}/\text{m}^2\text{K}$]	r	Release rate [kg/s]
h	Height [m]	S	Source term [$\text{kg}/\text{m}^2\text{s}$]
h	Enthalpy [J]	T	Temperature [K]
K	Decay constant [m^{-1}]	t	Thickness [m]
k	Mass transfer coefficient [m/s]	u	Velocity [m/s]
L	Length [m]	w	Radiation cell coefficient [-]
m	Mass [kg]		

References

- Adánez, J., Gayán, P., García-Labiano, F., de Diego, L.F. 1994. "Axial voidage profiles in fast fluidized beds". *Powder Technology*, 81(3), pp.259-268.
- Baskakov, A.P., Leckner, B. 1997. "Radiative heat transfer in circulating fluidized bed furnaces". *Powder Technology*, 90(3), pp.213-218.
- Breitholtz, C., Leckner, B., Baskakov, A.P. 2001. "Wall average heat transfer in CFB boilers". *Powder Technology*, 120(1-2), pp.41-48.
- Chirone, R., Massimilla, L., Salatino, P. 1991. "Comminution of carbons in fluidized bed combustion". *Progress in Energy and Combustion Science*, 17 (4), pp.297-326.
- Clift, R., Grace, J.-R. 1985. "Fluidization". Davidson, Harrison and Clift Eds., Academic Press Inc., London (UK).
- Darton, R., LaNauze, R., Davidson, J., Harrison, D. 1977. "Bubble-growth due to coalescence in fluidized beds". *Transactions of the Institution of Chemical Engineers*, 55, pp.274-280.
- Field, M.A., Gill, D.W., Morgan, B.B., Hawksley, P.G.W. 1967. "Combustion of pulverized coal". The British Coal Utilization Research Association, Surrey (England).
- Haider, A., Levenspiel, O. 1989. "Drag coefficient and terminal velocity of spherical and nonspherical particles". *Powder Technology*, 58(1), pp.63-70.
- Hannes, J.-P. 1996. "Mathematical modelling of circulating fluidized bed combustion". *Ph.D. thesis*, Delft University of Technology. City-Print Verlag GmbH, Aachen (Germany). ISBN 3-88817-002-8.
- Hiller, R. 1995. "Mathematische Modellierung der kohleverbrennung in einer circofluid-wirbelschichtfeuerungen". *Ph.D. thesis*, University of Dortmund. Shaker Verlag, Dortmund, (Germany).
- Hupa, M. 2005. Lecture "Fluidized bed combustion" in lecture series "Options for energy recovery from municipal solid waste" at Politecnico di Milano.
- Johnsson, F., Andersson, S., Leckner, B. 1991. "Expansion of a freely bubbling fluidized bed". *Powder Technology*, 68(2), pp.117-23.
- Johnsson, F., Leckner, B. 1995. "Vertical Distribution of Solids in a CFB-Furnace". *Proc. of the 13th Int. Conf. on Fluidized Bed Combustion*, pp.671-679.
- Kruse, M., Werther, J. 1995. "2D gas and solids flow prediction in circulating fluidized beds based on suction probe and pressure profile measurements". *Chemical engineering and processing*, 34 (3), pp.185-203.
- Kruse, M., Schoenfelder, H., Werther, J. 1995. "Two-dimensional model for gas mixing in the upper dilute zone of a circulating fluidized bed". *Canadian Journal of Chemical Engineering*, 73(5), pp.620-634.
- Kunii, D., Levenspiel, O. 1991. "Fluidization Engineering". Butterworth-Heinemann Eds., Boston (USA). ISBN 978-0409902334.

- Leckner, B., Golriz, M.R., Zhang, W., Andersson, B.Å., Johnsson, F. 1991. "Boundary layers - first measurements in the 12 MW CFB research plant at Chalmers University". *Proc. of the 11th Int. Conf. on FBC* (Montreal, Canada), pp. 771–776.
- Lee, J.M., Kim, J.S., Kim, J.J. 2003. "Comminution characteristics of Korean anthracite in a CFB reactor". *Fuel*, 82, pp. 1349–1357.
- Lyngfelt, A., Åmand, L.-E., Leckner, B. 1996. "Progress of combustion in the furnace of a circulating fluidized bed boiler". *Proc. of the 26th Int. Symp. on Combustion* (Naples, Italy), pp.3253-3259.
- Lücke, K. 2003. "On the influence of mixing on the performance of large-scale atmospheric circulating fluidized bed combustors". *Ph.D. thesis*, Technical University of Hamburg-Harburg. ISBN 3-8322-1288-4.
- Muschelknautz, U., Muschelknautz, E. 1991. "Special design of inserts and short entrance ducts to recirculating cyclones". *Proc. of the 4th Int. Conf. on Circulating Fluidized Beds* (Pittsburgh, USA), pp.597-602.
- Niklasson, F., Thunman, H., Johnsson, F., Leckner, B. 2002. "Estimation of solids mixing in a fluidized bed combustor". *Industrial and Engineering Chemistry Research*, 41 (18), pp.4663-4673.
- Niklasson, F., Johnsson, F., Leckner, B. 2003. "Local air ratio measured by zirconia cell in a circulating fluidised bed furnace". *Chemical Engineering Journal*, 96(1-3), pp.145-155.
- Niklasson, F., Pallarès, D., Johnsson, F. 2007. "Biomass co-firing in a CFB boiler – The influences of fuel and bed properties on in-furnace gas-concentration profiles". *Proc. of the 19th Int. Conf. on Fluidized Bed Combustion* (Vienna, Austria).
- Rhodes, M.J., Geldart, D. 1987. "A model for the circulating fluidized bed". *Powder Technology*, 53(3), pp.155-162.
- Salatino, P., Massimilla, L. 1989. "A predictive model of carbon attrition in fluidized bed combustion and gasification of a graphite". *Chemical Engineering Science*, 44 (5), pp.1091-1099.
- Sasic, S., Johnsson, F., Leckner, B. 2004. "Interaction between a fluidized bed and its air-supply system: some observations". *Industrial and Engineering Chemistry Research*, 43(18), pp.5730-5737.
- Svensson, A., Johnsson, F., Leckner, B. 1996. "Bottom bed regimes in a circulating fluidized bed boiler". *International Journal of Multiphase Flow*, 22(6), pp.1187-1204.
- Thunman, H., Niklasson, F., Johnsson, F., Leckner, B. 2001 "Composition of volatile gases and thermochemical properties of wood for modeling of fixed or fluidized beds". *Energy and Fuels*, 15 (6), pp.1488-1497.
- Thunman, H., Davidsson, K., Leckner, B. 2004. "Separation of drying and devolatilization during conversion of solid fuels". *Combustion and flame*, 137 (1), pp.242-250.

- Thunman, H. 2005. Personal communication.
- Werdermann, C.C. 1993. "Feststoffbewegung und wärmeübergang in zirkulierenden wirbelschichten von kohlekraftwerken". Ph.D. thesis, Technical University of Hamburg-Harburg. Verlag Shaker, Aachen (Germany). ISBN 3-86111-327-9.
- Werther, J. 1993. "Fluid mechanics of large-scale CFB units". *Proc. of the 4th Int. Conf. on Circulating Fluidized Bed Technology*, pp.1-14.
- Xiang, Q., Huang, G., Ni, M., Cen, K., Tao, T. 1987. "Lateral dispersion of large coal particles in an industrial-scale fluidized bed combustor". *Proc. of the 9th Int. Conf. on Fluidized Bed Combustion* (Boston, USA). pp.546-553.
- Zhang, W., Johnsson, F., Leckner, B. 1995. "Fluid-dynamic boundary layers in CFB boilers". *Chemical Engineering Science*, 50(2), pp.201-10.
- Zhang, W., Leckner, B. 2001. "Process simulation of circulating fluidized beds with combustion/gasification of biomass". *Final report of project JOR3CT980306*, Non-Nuclear Energy Programme JOULE III, 4th EU framework.
- Åmand, L.-E., Lyngfelt, A., Karlsson, M., Leckner, B. 1995. "The reference case for coal at the 12 MW CFB-Boiler at Chalmers. Characterisation of the gas and particle phases in the combustion chamber". *Internal report A97-221*, Dept. of Energy Conversion, Chalmers University of Technology, Göteborg (Sweden).

Paper I

Pallarès, D., Johnsson, F. (2006)

"Macroscopic modelling of fluid dynamics in
large-scale circulating fluidized beds"

Progress in Energy and Combustion Science, 32 (5-6), pp. 539-569

Review

Macroscopic modelling of fluid dynamics in large-scale circulating fluidized beds

David Pallarès, Filip Johnsson*

Department of Energy and Environment, Energy Conversion, Chalmers University of Technology, SE 412 96 Göteborg, Sweden

Received 31 May 2005; accepted 13 February 2006

Abstract

Macroscopic (semi-empirical) models for fluid dynamics of circulating fluidized bed (CFB) units are presented, with emphasize on applications for conditions relevant to industrial units such as fluidized-bed combustors. In order to make a structured analysis of the models, the CFB unit is divided into 6 fluid dynamical zones, which have been shown to exhibit different fluid-dynamical behaviour (bottom bed, freeboard, exit zone, exit duct, cyclone and downcomer and particle seal). The paper summarizes the main basis and assumptions for each model together with major advantages and drawbacks. In addition, a practical example on how a selected set of these local models can be linked to an overall model of the fluid dynamics of the entire CFB loop is presented. It is shown that it is possible to reach good agreement between the overall model and experimental data from industrial units.

© 2006 Elsevier Ltd. All rights reserved.

Keywords: Circulating fluidized bed; Fluid dynamics; Modelling

Contents

1. Introduction	540
1.1. Scope: large-scale CFB units	540
1.2. Modeling of fluid dynamics in large-scale CFB units	543
1.3. The use of experimental data to verify models	544
2. Modeling of local CFB zones	544
2.1. Modeling of the bottom bed	545
2.2. Modeling of the freeboard	549
2.2.1. Terminal velocity	549
2.2.2. Wall-layer thickness	551
2.2.3. Gas flow	552
2.2.4. Solids concentration	552
2.2.5. Solid flows	554

Abbreviations: BFB, bubbling fluidized bed; CFB, circulating fluidized bed; CFBC, circulating fluidized bed combustor; CFBG, circulating fluidized bed gasifier; CFD, computational fluid dynamics; FCC, fluid catalytic cracking; HDCFB, high-density circulating fluidized bed; LDCFB, low-density circulating fluidized bed; SFB, stationary fluidized bed; PSD, particle size distribution

*Corresponding author. Tel.: +46 31 772 1449; fax: +46 31 722 3592.

E-mail address: filip.johnsson@me.chalmers.se (F. Johnsson).

2.3.	Modeling of the exit zone	555
2.3.1.	Backflow effect	556
2.3.2.	Solids concentration	557
2.4.	Modeling of the exit duct	557
2.5.	Modeling of the cyclone	558
2.6.	Modeling of the downcomer and particle seal	559
2.6.1.	Pressure balance	560
3.	Overall modeling of a CFB unit	561
3.1.	Practical example of an overall CFB model	562
4.	Closure	565
	Acknowledgements	566
	References	566

1. Introduction

As concluded by for instance Werther [1], circulating fluidized bed (CFB) units used in experimental investigations on CFB fluid dynamics given in literature can be divided into two types, depending on the aspect ratio (H_0/D_{eq}) of the riser

- (1) Tall and narrow units, with an aspect ratio of the order of 20 or higher.
- (2) Large units, with a lower aspect ratio typically less than 10.

The first type is used in investigations directed towards chemical engineering applications (such as fluid catalytic cracking, FCC) and typically operates at high solids net fluxes. The latter (here called *large CFB units*) is the scope of this review and corresponds to industrial-scale units with the purpose of producing heat, electricity, fuel-gas or combinations of these. For an introduction and overview of such fluidized bed systems see reviews by Anthony [2], and Leckner [3] for combustion systems and Longwell et al. [4] for a general review including both combustion and gasification systems (not only fluidized-bed systems).

Issangya et al. [5] give an overview of experimental investigations on CFB fluid dynamics concluding that “almost all reported CFB data are for low-density circulating fluidized bed (LDCFB) systems representative of CFB combustors” and therefore not applicable to the high-density fluidized beds (HDCFB) which are the scope of their work. The authors of this paper agree that the data to which Issangya et al. are referring are from investigations which may very well have had CFB combustors as application. However, as discussed previously (cf. [1,6,7]) much of this data are from experiments

in tall and narrow units, which together with the operational conditions applied in these units, make the results not applicable to CFB combustors.

During the last decades there has been an increase in the use of large CFB units for energy production, since the CFB technique has proved to be efficient, clean and with a high flexibility concerning type of fuel (e.g. wood, coal, municipal waste and mixtures of these), see e.g. [8]. Therefore, the development of models to simulate and predict the behaviour of such units is needed for design and scale-up purposes. Prediction of the flow is crucial in modeling heat transfer and combustion (mixing of fuel and combustion/gasification gas). The flow pattern in CFB gasifiers and combustors is similar since the overall riser geometry, fluidization conditions and properties of the solids used are similar. Thus, the same models should be able to describe the flow in both applications. Concerning combustion, circulating fluidized bed combustors (CFBC) have been built up to sizes of around 300 MW_{el} (e.g. the Gardanne and Turow plants, as described in [9,10], respectively), while gasifiers (CFBG) are still at a more developing stage and are about to reach values of 100 MW_{th} [11]. Combustors generally have a square or rectangular cross section and may partly have bare membrane tube walls, whereas the riser of a gasifier normally has a circular cross section with plane (isothermal) walls. Except for the presence of corner effects in the former type of units, the overall influence from the shape of cross section on the solids flow should be small, provided the riser has the characteristics listed in the next section.

1.1. Scope: large-scale CFB units

The first large-scale fluidized bed units were operated as stationary fluidized beds (SFB), i.e. at

Nomenclature		Superscripts	
a	decay factor of cluster phase (m^{-1})	d	PSD size interval index
A	area (m^2)	f	solid fraction index
A_0	gas-distributor area per nozzle (m^2)	<i>Subscripts</i>	
b	entrance width of exit duct (m)	b	bottom bed
C	solids concentration (kg/m^3)	bub	bubble
C_1, C_2	empirical constants	bub_∞	single bubble
C_{cycl}	empirical coefficient in cyclone model	$clust$	cluster phase
C_D	drag-force coefficient	$core$	core region
d	particle diameter (m)	$cycl$	cyclone
D	diameter (m)	dc	downcomer
f	empirical function	$disp$	disperse phase
F	solids mass flow (kg/s)	$duct$	exit duct
G	solids mass flux ($\text{kg}/\text{m}^2 \text{ s}$)	$emul$	emulsion phase
h	height (m)	eq	equivalent
H	height (m)	g	gas
H_0	riser height (m)	i	cell index
k	backflow ratio	lat	net lateral flow from core-to annulus
K	decay factor of disperse phase (m^{-1})	mb	minimum bubbling conditions
L	length (m)	mf	minimum fluidization conditions
m	mass (kg)	n	surrounding solids suspension
p	pressure (Pa)	net	net
p_0	(Δp_0) riser pressure drop (Pa)	p	particle
p_{entr}	particle entrainment probability	ref	riser height interval from 0.135 to 1.635 m above gas distributor
t	thickness (m)	$refeed$	riser interval between return leg and exit
u	velocity (m/s)	rel	relative
u_0	superficial fluidization gas velocity (m/s)	$retleg$	return leg
\dot{V}	gas volumetric flow (m^3/s)	s	solids
w	cloud settling velocity (m/s)	$seal$	particle seal
x	horizontal coordinate (m)	$settled$	settled (non-fluidized) bed
<i>Greek symbols</i>		$slip$	slip
γ	solids loading ratio at exit-duct inlet	sat	saturation value
δ	volumetric fraction	t	terminal
ε	voidage	tf	throughflow
ϕ	sphericity	vis	visible bubble flow
η	separation efficiency	$wall$	wall-layer (annulus) region
μ	dynamic viscosity (kg/ms)	<i>Dimensionless groups</i>	
v	rise velocity (m/s)	Ar	Archimedes number
ρ	density (kg/m^3)	Re	Reynolds number
ψ	dimensionless visible bubble flow		

fluidization velocities well below the terminal velocity of the bed material resulting in that the amount of solids entrained out from the riser can be neglected. Thus, there is no need for external recirculation of bed solids and the bed can be

maintained (stationary) as long as solid which are discharged from the unit (e.g. ash discharge) is replaced with fresh bed solids (fuel and/or inert solids). This type of bed is also known as bubbling fluidized bed (BFB). Under bubbling conditions,

bubbles rise through the bed and when erupting at the bed surface solids are thrown into the freeboard creating a so-called splash zone above the (time averaged) bottom bed surface. There is a pronounced decay in solids concentration up through the splash zone.

The CFB employs a higher gas velocity and/or finer bed solids than used in an SFB. More specifically, the gas velocity exceeds the terminal velocity of all or a significant part of the bed material, resulting in that solids are entrained out of the riser. To maintain the bed solids, the entrained solids must be recirculated back to the bed. This is done in the return leg, which consists of solids separation device (normally a cyclone), a dipleg and a particle seal connected to the riser with a duct pipe. The particle seal is used to maintain the pressure balance that prevents gas and solids from entering the return device. The particle seal is normally fluidized so that it forms a low-velocity SFB.¹ The fluidization air distributor of a CFB has a characteristic pressure–velocity curve designed for operation at higher gas velocities, thus providing a lower pressure drop than an SFB air distributor operating at the same gas flow rate. The bottom bed of a CFB is far more turbulent than in an SFB, with jet-formed gas voids (here called “exploding bubbles”) which can extend the whole way from the air distributor up to the bottom bed surface. As a result, there are occasions of by-pass (through flow) of gas (or combustion air) during eruption of these voids, facilitating a low-pressure path for the gas. The term exploding bubble was originally proposed by Fitzgerald [12] for bubbling beds but it was later found that the characteristics are similar in the bottom bed of a CFB (e.g. [13]). Consequently, a splash zone is present above the bed followed by a so-called transport zone with a dilute solids suspension that extends all the way up to the riser outlet. Solids concentration and solids size decrease with height in this zone, and at the top of the riser the mean particle size might differ strongly from that in the bottom bed due to solids size segregation. With a further increase in fluidization velocity (or lowering the total amount of solids in the CFB loop) the bottom bed disappears and the bed enters the pneumatic transport regime. Despite the importance of determining the conditions under which this

regime is established (i.e. when the transport velocity is reached will mainly depend on the PSD of the bed material, the fluidization velocity and the amount of bed material), such a mapping is not known to the authors. In addition, the transport velocity should also depend on the design of the CFB loop such as the height of the riser and the way the recirculation side of the unit is operated (e.g. to what degree the loop seal is fluidized), i.e. this makes it difficult to generalize the transport velocity only based on the above listed fluid dynamic parameters.

The present modeling review is restricted to large CFB units working at atmospheric pressure with a dense bottom bed present. Characteristics of such units are:

- A height to diameter (aspect) ratio of the riser (H_0/D_{eq}) of the order of or less than 10.
- A ratio of settled bed height (the bed formed if the solids are not fluidized) to riser diameter of less than 1 ($H_{b,settled}/D_{eq} < 1$).
- Fluidized solids belonging to group B in the Geldart classification (a brief summary of this classification is given below).
- A solids net flux typically ranging from 0.5 to 20 kg/m²s.

Primary operational parameters of the riser (with respect to fluid dynamics) are the riser pressure drop and the gas flows (i.e. fluidization velocity, secondary gas injection), whereas the solids net flux and the total inventory of solids are normally not known. The above-listed characteristics were shown [1,6,7] to give a flow pattern different from that of the well-investigated tall and narrow laboratory units directed towards chemical engineering applications. The latter type of units have a higher aspect ratio (H_0/D_{eq} typically ~ 20) and are normally run at a much higher solids net flux ($G_{s,net} \sim 50$ kg/m²s), i.e. are operated with finer (and often lighter) solids (d_s typically < 100 μ m) than CFBC and CFBG units.

The low aspect ratio of the riser in large CFB units results in a solids-flow profile developing up through the freeboard (above the bottom bed), i.e. the riser can be seen as an entrance zone with respect to the flow (both solids and gas). This gives a solids flux profile, which is fairly flat across the core region, but with pronounced wall layers formed by the solids backmixing at the riser walls [1,7]. Thus, a core/wall-layer structure is present. On the other hand, the above-mentioned tall and narrow risers

¹Instead of a particle seal a so-called *L*-valve could be used. Since the *L*-valve does not contain a fluidized bed it is difficult to combine with an external particle cooler.

exhibit a more developed solids flux profile, typically with a parabolic shape [14,15] depending on operational conditions. Although varying with the solids net flux and the fluidization velocity, these risers also show a more or less pronounced back-mixing at the riser walls forming a core-annular structure of the flow, but at high enough gas velocities there may even be up-flow of solids throughout the cross section (e.g. [16]).

The low $H_{b, \text{fixed}}/D_{eq}$ ratio (< 1) in large CFB units yields a non-slugging bed [13,17], whereas tall and narrow risers (with $H_{b, \text{fixed}}/D_{eq} > 1$) give a slugging bed [18]. As indicated above, the large CFB units considered in this review are operated with Geldart B solids according to the classification given by Geldart which is a classification of particles in four groups according to their fluidizing behaviour [19] (groups C, A, B and D in increasing size and density order). The classification is based on empirical observations and Geldart gave the classification in a $(\rho_s - \rho_g)$ vs. d_p diagram which was later developed by Grace [20] who draw the four groups in a dimensionless u_g vs. d_p diagram identifying different fluidization regimes. The Group B solids normally used in large CFB units for combustion and gasification consists of silica sand and/or primary ashes, and sorbent in the case of coal-fired units. However, depending on size distribution the bed solids also consists of certain fractions of Group A (fines generated by attrition) and Group D (relatively large fuel particles) solids. As will be shown below, the particle size distribution (PSD) is an essential feature of CFB units and must be included in any model in order to correctly describe the recirculation of bed solids as well as back-mixing of solids in the riser. Yet, when averaged quantities are to be calculated, the mean volume-to-surface diameter (also known as Sauter diameter) of the bed solids and the volume-averaged density are usually used.

Under CFB conditions with Geldart group B solids, a low H_b/D_{eq} ratio in combination with a low primary air-distributor pressure drop results in that a dense bubbling bed can be maintained also at high velocities with bubbles of a so-called exploding character [21]. Such flow results in large fluctuations in the overall gas flow with a high throughflow of gas in the bubbles, leading to high local gas velocities. Thus, the exchange of gas between the bubbles and the emulsion phase is low in relation to the gas flow through the bed. In combustors, this results in strongly reducing conditions in the bottom

bed. In addition, the gas flow becomes highly intermittent.

In laboratory risers operated with Group A solids, an increase in velocity from the slugging conditions results in a transition to a turbulent regime [22,23]. With Group B solids in this type of unit, the picture is less clear, but it was argued that an increase in velocity results in that transport conditions are reached [23], i.e. it is difficult or not possible to maintain a dense zone in the bottom region of narrow risers operated with Group B solids under circulating conditions [18].

In summary, the flow pattern of a large CFB unit differs significantly from that of tall and narrow laboratory CFB risers, so the abundant literature on the latter type of CFB units is seldom applicable for CFBC or CFBG.

1.2. Modeling of fluid dynamics in large-scale CFB units

Modeling of large CFB units can be divided into three main fields: fluid dynamics, chemistry (including formation of pollutant emissions), and heat balance (heat transfer). The relations between these three modeling fields are outlined in Fig. 1, where the thickness of the arrows corresponds to the sensitivity of the modeling field to the input represented by the arrow. As seen, all of the three modeling fields need some input parameters that are outputs from the other modeling fields. Modeling of the chemistry and the heat balance are sensitive to the values of the fluid dynamical parameters used as inputs. On the other hand, concerning fluid dynamics, most of the inputs needed are external operational parameters (known and adjustable under operation), whereas only a few are related to heat balance and chemistry (temperature profiles and internal gas generation, respectively). Under normal operating conditions, the fluid dynamics are not especially sensitive to the latter type, i.e. fluid dynamics can be reasonably well modelled by assuming typical values of those inputs. Despite the fluctuations observed in most fluidized-bed parameters even during steady-state operation, a time-averaged modeling approach is usually chosen to simplify the analysis. With respect to modeling CFB fluid dynamics, two types of models can be identified: macroscopic models (based on empirical and semi-empirical expressions) and models from first principles using computational fluid dynamics (CFD). At present, only the former type of models

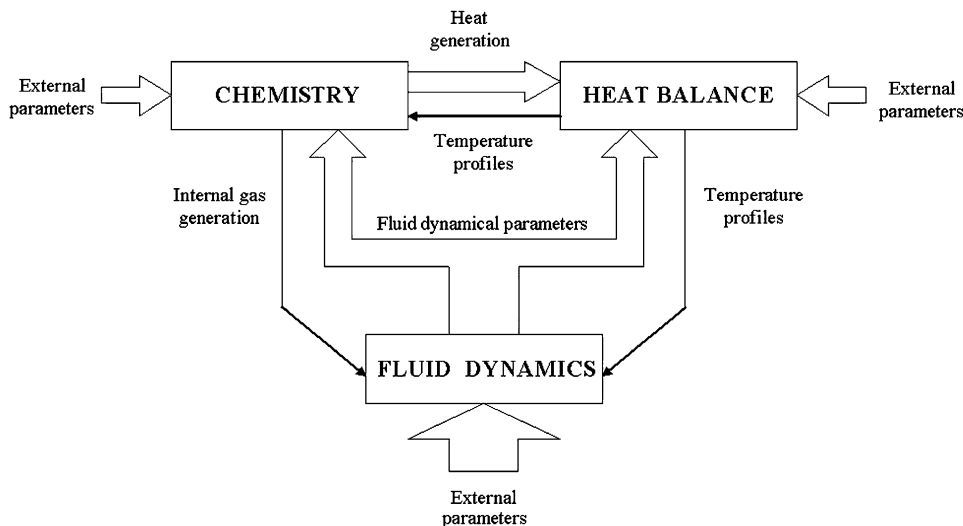


Fig. 1. Relationships between CFB modeling fields.

is practically applicable if aiming at both reasonable calculation times and agreement. Although the formulation of some critical terms in CFD modeling is still at a developing stage and computational times of the simulations are long, simulations from first-principle models will probably be the future modelling tool. Yet, inclusion of chemistry and heat transfer modelling with fluidized-bed two-phase flow in 3D CFD simulation will most likely require significant development before reliable results can be produced within reasonable calculation times. Thus, it can be assumed that there is a need for comprehensive semiempirical modelling of fluidized bed combustors and gasifiers—the topic of this paper—over at least the next decade.

1.3. The use of experimental data to verify models

The focus of this review is macroscopic modelling of CFBs, i.e. the modelling is of a semiempirical type. An obvious drawback with semiempirical models is that, since they are partly based on empirical data, it may be difficult to apply these under conditions different from those for which they were developed. The experimental data shown in this review is measured in full-scale units or cold models operated according to scaling relationships (e.g. such given by Glicksman [24]), i.e. transforming industrial conditions to ambient conditions. As indicated from the characteristics listed above, large cross sections are a key feature of CFB combustors

(not so much of gasifiers). In such large units—typically 100 MW or more—there is for obvious (practical) reasons little detailed experimental information on cross-sectional distribution of entities such as solids concentrations and gas velocities. The aim of this work is to gather all available information from large units and then use these data to compare modelling results in the way that, when possible, models are applied to units that were not included in the development of the models.

It should be mentioned that also cold models not operated according to scaling laws can be of great use when studying principal relationships between important parameters. Such experiments can be efficient when scanning over a broad range of operational parameters (e.g. from bubbling conditions at low velocity to transport conditions). Then, of course, only main trends are obtained and quantitative analyses will require full scale measurements or measurements in a scaled down unit operated according to the above-mentioned scaling relationships.

In summary, it is important to base macroscopic semi-empirical modeling on robust and high-quality experimental data obtained under conditions relevant for industrial units.

2. Modeling of local CFB zones

In order to organize the present review, the CFB loop is divided into six different zones, which, from

previous experiments, have been shown to exhibit different flow patterns and it is consequently assumed that these can be modelled separately (but linked by input/outputs between the zones). Therefore, each zone is analysed separately and this paper first presents the fluid dynamical models of each zone. The division in the different zones is shown in Fig. 2, i.e. the CFB unit is divided into a bottom bed, freeboard, exit zone, exit duct, cyclone and downcomer and particle seal.

This paper takes a selected set of models for each of the six zones and couples these in order to obtain an overall model for the entire CFB unit therefore making it possible to close the solids mass balance using solids with a size distribution. This coupling procedure must account for interactions between the zones (i.e. the zones are not independent in the overall model) and is described in Section 3.

2.1. Modeling of the bottom bed

In the lower part of a CFB unit, a bottom bed is formed provided enough bed material is present in the CFB loop. A CFB bottom bed consist of two phases: a dense (or emulsion) phase, formed by the bed particles and the interstitial gas flow between the particles, and a bubble phase, consisting of uprising gas bubbles assumed to be free of solids. In a strict sense, not all particles in the dense phase are

constantly fluidized as well as some solids will be present also in the bubble phase, but the above assumption should be reasonable for the solids typically used in CFBCs and CFBGs, strongly simplifying the analysis.

Fluidization of the bed material occurs when the fluidization gas velocity, u_0 , exceeds the minimum fluidization velocity, u_{mf} . Several expressions exist to calculate the Reynolds number at which fluidization is initiated. A widely used correlation is given by Wen and Yu [25]:

$$Re_{p,mf} = \sqrt{C_1^2 + C_2 Ar} - C_1, \quad (1)$$

where

$$Ar = \frac{d_p^3 \rho_g (\rho_s - \rho_g) g}{\mu_g^2}. \quad (2)$$

Grace [26] tabulated several pairs of values for C_1 and C_2 proposed in literature, and suggested the use of $C_1 = 27.2$ and $C_2 = 0.0408$. Thus, u_{mf} can easily be obtained through the Reynolds number expression:

$$u_{mf} = \frac{Re_{p,mf} \mu_g}{d_p \rho_g}. \quad (3)$$

And the voidage under minimum fluidization conditions is calculated by solving the equation derived from the Ergun equation [27]:

$$\frac{1.75}{\varepsilon_{mf}^3 \phi_s} Re_{p,mf}^2 + \frac{150(1 - \varepsilon_{mf})}{\varepsilon_{mf}^2 \phi_s^2} Re_{p,mf} = Ar. \quad (4)$$

Finally, once fluidized, the pressure drop over a vertical column of solids is obtained through:

$$\Delta p = (1 - \varepsilon)(\rho_s - \rho_g)gH. \quad (5)$$

A more detailed description of the pressure drop under homogenous (bubble-free) fluidization and for velocities below u_{mf} is given in [28,29]. However, for the solids of interest in the present modeling (Group B), there is no or little homogenous fluidization, i.e. it can be assumed that $u_{mf} = u_{mb}$. Gas bubbles, which are the main responsible for solids mixing in the bottom bed, appear in the bed when the fluidization velocity exceeds the minimum bubbling velocity, u_{mb} . Abrahamsen and Geldart [30] gave a correlation to determine the ratio u_{mb}/u_{mf} , which gives values close to 1 for particle belonging to Group B (typical for large CFB units) and Group D in the Geldart classification (see [19]).

Characterization of the properties of the gas bubbles is usually carried out by the set of

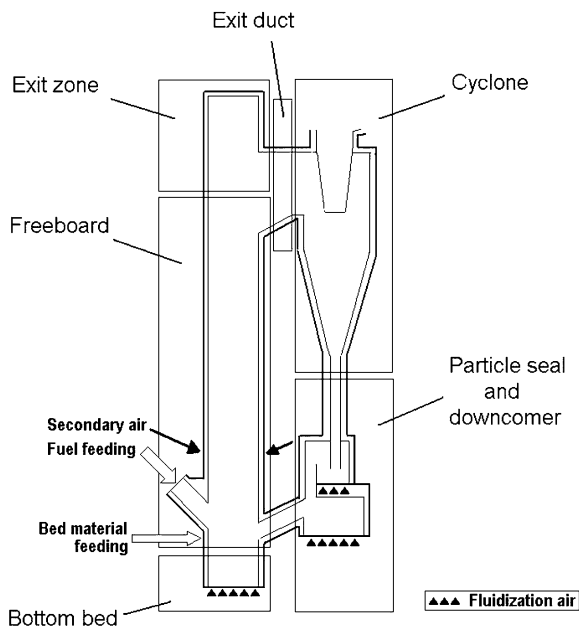


Fig. 2. The zone division used in the present model.

expressions briefly described below. Darton et al. [31] presented a model for determining the bubble size based on the assumption that bubbles only grow due to coalescence, which is assumed to occur after a bubble has travelled λ times its own diameter ($\lambda = 1.17$ in [31]), yielding:

$$D_{bub} = 0.54(u_0 - u_{mf})^{0.4}(h + 4\sqrt{A_0})^{0.8}g^{-0.2}. \quad (6)$$

Clift and Grace [32] summarized experimental data from several authors and correlated the rise velocity of an isolated bubble in a large bubbling fluidized bed:

$$v_{bub\infty} = 0.71\sqrt{gD_{bub}}. \quad (7)$$

The above-given velocity is often corrected by a term taking into account the presence of other bubbles and the increase in relative velocity between the rising bubble and the downflow of surrounding solids. Davidson and Harrison [33] give the following expression for the bubble velocity:

$$v_{bub} = u_{vis} + v_{bub\infty}. \quad (8)$$

However, the use of this expression is somewhat controversial and has been questioned in [34,35] and experimental bubble rise velocities have been successfully fitted to $v_{bub,\infty}$ instead of v_{bub} [36].

Since the above-mentioned expressions for estimation of bubble properties were obtained from experimental data measured at low fluidization velocities, care should be taken when applying these expressions to CFB modeling, where fluidization velocities are much higher.

For the non-slugging beds treated in this work, two types of behaviour were observed with respect to the time-averaged bottom bed voidage. The difference is related to the type of fluidized bed studied: stationary (SFB) or circulating (CFB). Most studies in literature on the bottom bed region concern SFB e.g. [37,38], while there is little detailed data on CFB bottom bed fluid dynamics e.g. [39,40]. SFB units are characterized by operating at lower fluidization velocities than CFB units, resulting in zero or very low net solids flux. CFB units have a lower pressure drop across the air-distributor than SFB at corresponding velocities. This is simply due to the fact that CFBs are operated at higher velocities than SFBs, but the affordable pressure drop is limited. As a consequence, CFBs cannot be operated under stable conditions (even fluidization) below a certain velocity. Although it follows the same principal behaviour, the relation between bed voidage and fluidization velocity (i.e. the bed

expansion curve) differs between the two types of units. Thus, in an intermediate range of primary-air velocities, corresponding to operation of an SFB at full load or a CFB at part-load, the rate of bed expansion differs between the two types of units. The bed expansion curve (bed voidage vs. superficial gas velocity) of a CFB unit [39] scatters more than the corresponding curve for an SFB [17]. This is believed to be due to that the lower air-distributor pressure drop of the CFB results in stronger interaction of the bed and the air-feed system (air-plenum, piping and fans) than in an SFB. As the velocity is increased, the CFB system reconfigures itself into a “new” system having a different interaction between the bed and the air-feed system (and the increase in bed expansion therefore does not follow a continuous curve). The influence of air-distributor pressure drop on fluidization behaviour is discussed in [21] and the interaction between the bottom bed dynamics (pressure fluctuations) and the air-feed system of a CFB is given in [41–44].

The bottom bed is defined as the extension of the linear part of the time-averaged vertical pressure-drop profile above the primary-air distributor. Thus,

$$\left[\frac{dp}{dh}\right]_b = const. \quad (9)$$

A linear pressure drop was confirmed under circulating [13] as well as under bubbling conditions [17] in units having the characteristics listed in Section 1.1. The expression for the time-averaged pressure drop is given by

$$\left[\frac{dp}{dh}\right]_b = -c_{sb}g = -\rho_{sb}(1 - \varepsilon_b)g. \quad (10)$$

Assumption of homogeneous mixing in the bottom bed does not allow a jetsam/flotsam segregation effect of the inert solids, provided the PSD is not too wide (see [45] for details on this effect). Thus, the averaged solids density within the bottom bed, ρ_{sb} , is generally assumed not to depend on height above the air distributor. Considering Eqs. (9) and (10), and assuming homogeneous mixing in the bottom bed, it can be concluded that

$$\frac{d\varepsilon_b}{dh} = 0. \quad (11)$$

With δ_{bub} being the bubble fraction, the bottom bed voidage can be written as

$$\varepsilon_b = \delta_{bub} + (1 - \delta_{bub})\varepsilon_{emul}. \quad (12)$$

In terms of superficial gas velocities, the total fluidization gas flow supplied to the bottom bed, u_0 , was originally divided into two terms by Toomey and Johnstone [46]: the flow in the emulsion phase, u_{emul} , and the visible bubble flow, u_{vis} . Toomey and Johnstone defined the flow in the emulsion phase as that required to fluidize the bed material, i.e. $u_{emul} = u_{mf}$, while they assumed all excess gas supplied to pass the bed as bubbles, i.e. $u_{vis} = u_0 - u_{mf}$. It was later proven that the two-phase flow theory overestimate the bed expansion and, as a consequence, the presence of a third term in the flow balance, the so-called throughflow, u_{tf} , was confirmed by several authors [47,48]. The throughflow is gas which flows mainly through the low-resistance gas passages in and between the bubbles. Thus, the gas flow in the bottom bed can be expressed by a modified two-phase flow model, which in terms of superficial gas velocities is written

$$u_0 = u_{mf} + u_{vis} + u_{tf}, \quad (13)$$

where the visible bubble flow is

$$u_{vis} = \delta_{bub} v_{bub}. \quad (14)$$

Measurements of the bubble fraction were carried out in a 2-dimensional bed by means of digital image analysis by Shen et al. [36]. These measurements show that with an increase in the supplied gas flow, u_0 , a decreasing proportion of the gas passes the bed as visible bubble flow, u_{vis} . Thus, the proportion of throughflow of the total gas flow supplied increases with an increase in fluidization velocity. However, despite the importance of this flow term, it remains unclear in which proportions the throughflow distributes itself between the emulsion and bubble phase, although this issue has been experimentally investigated in [32,49,50]. These three works conclude that the throughflow must be taken into account already at fluidization velocities just above the minimum fluidization velocity, leading to a higher interstitial velocity in the vicinity of bubbles than in bubble-free zones of the emulsion. In addition, the influence of the bottom bed regime on the gas flow distribution within the bed remains to a large extent unknown especially under conditions valid for industrial units (which yield bubbles far from “text book” bubbles), although Svensson et al. [39] showed that there is a strong dependence of the bottom bed expansion curve (bed voidage vs. velocity) on the pressure drop over the air distributor (and thereby also the bottom regime depends on air-distributor pressure drop).

Furthermore, the arrangement of the air feeding system was shown to strongly influence the bottom bed dynamics at low air distributor pressure drops [44]. The semi-empirical expressions (Eqs. (18)–(20)) given below have been obtained from experimental data sampled under single bubble and exploding bubble regimes, which are typical for the bottom bed of a CFB unit at low and high velocities, respectively. However, it should be noted that the data on which these expressions are based come from certain test units with particular air-distributor characteristic curves and air-feeding arrangements and, thus, data from other units, yet running under the same bottom bed regime, might differ from the expressions reported below.

In summary, the excess gas, $u_0 - u_{mf}$, is divided between u_{vis} and u_{tf} . The division between these flows can be given as a dimensionless visible bubble flow, ψ :

$$\psi = \frac{u_{vis}}{u_0 - u_{emul}} \quad (15)$$

which expresses the deviation from the original two-phase flow model. Grace and Clift [47] presented a large collection of experimental values of ψ (ranging from 0.06 to 1) under different fluidization conditions, indicating that the through flow strongly depends on operating conditions as well as the configuration of the fluidized bed and air feeding system (e.g. most likely air distributor pressure drop).

Werther and Wein [51] estimated ψ using a semi-empirical model for the bottom bed (later extended by Zijerveld et al. [52])

$$\psi = 1.45 Ar^{-0.18}. \quad (16)$$

However, outputs from this model result in a height-dependence in bottom bed voidage, which, as discussed above, is in disagreement with measurements (of time-averaged pressure drop).

A semi-empirical modeling of ψ was proposed by Johnsson et al. [17], for which

$$\psi = f(h + 4\sqrt{A_0})^{0.4} \quad (17)$$

with

$$f_{SFB} = [0.26 + 0.70 \times \exp(-3.3 d_{s,seal})] \times [0.15 + (u_0 - u_{mf})]^{-1/3}. \quad (18)$$

Based on CFB bed-expansion data (bed-pressure drop measurements) and the same assumptions as discussed below Pallarès and Johnsson [53] modified the correlation (Eq. (18)) for application

to CFB units

$$f_{CFB} = 0.3121 + 0.129 u_0^{-1} - 16.6 d_{s,b} - 2.61 \times 10^{-5} \Delta p_{ref}. \quad (19)$$

Once a model for ψ is chosen and applied, u_{vis} can be calculated from Eq. (15). Then, the bubble density is determined by combining Eqs. (14), (6), (7) and (10), and finally the bottom bed voidage is obtained from Eq. (12). The model by Johnsson et al. [17] gives a time-averaged bottom bed voidage which is constant with height (in agreement with the above-mentioned bed-pressure drop measurements). This is a consequence of assuming both the bubble fraction and the emulsion voidage constant with height (see Eq. (9)). However, measurements by Shen et al. [36] show a height-dependant bubble density. In addition, Johnsson et al. [17] assumed the voidage in the emulsion phase to equal the minimum fluidization voidage, which is a classical assumption used in this type of modeling (cf. above equations) although part of the throughflow passes the bottom bed through the emulsion phase, yielding an interstitial gas velocity higher than the minimum fluidization velocity. It is uncertain to what extent this increased velocity in the emulsion leads to an increase in the voidage of the emulsion. The possibility of an emulsion voidage higher than ε_{mf} is discussed and defended by Gogolek [54] and expressions for the voidage of an expanded emulsion phase are given in literature [51,55], but the gas velocity in the dense phase due to the throughflow is required as input to these models. Also, if there is an increase in voidage due to the throughflow, it is

likely that such an increase would be local, i.e. in-between bubbles.

In addition, the bottom bed voidage of a CFB furnace was found to level out at a certain fluidization velocity [21] which could exceed the terminal velocity of an average sized bed solids provided that enough bed solids are recycled to maintain a bottom bed as can be seen from the experimental data in Fig. 3. In this regime, bubbles are of an exploding type and during eruption they extend all the way from the air distributor to the top of the dense bed. This behaviour provides a large and almost free passage of gas through the dense bed during the time of bubble eruption (i.e. throughflow). Thus, a further increase in primary gas velocity is restricted to an increase mainly in the throughflow gas, u_{tf} , together with a small increase in the visible bubble flow, u_{vis} , due to the increase in the bubble (growth) velocity. This saturation value of the bottom bed voidage, found to depend on the riser pressure drop and the mean particle size, is correlated as [53]

$$\varepsilon_{b,sat} = 0.5352 + 496.5 \Delta p_0^{-1} + 4.9 \times 10^{-6} d_{s,b}^{-1}. \quad (20)$$

The fluidization velocity at which the levelling out of ε_b takes place is taken as that for which the dense bed voidage calculated by means of ψ (Eq. (17)) equals the value obtained by Eq. (20) [53]. A comparison of results by the model given by Eqs. (6)–(17) and (19) and experimental CFB data from Svensson et al. [39] is shown in Fig. 3.

Finally, it should be noticed that the mean particle size in the bottom bed, which should

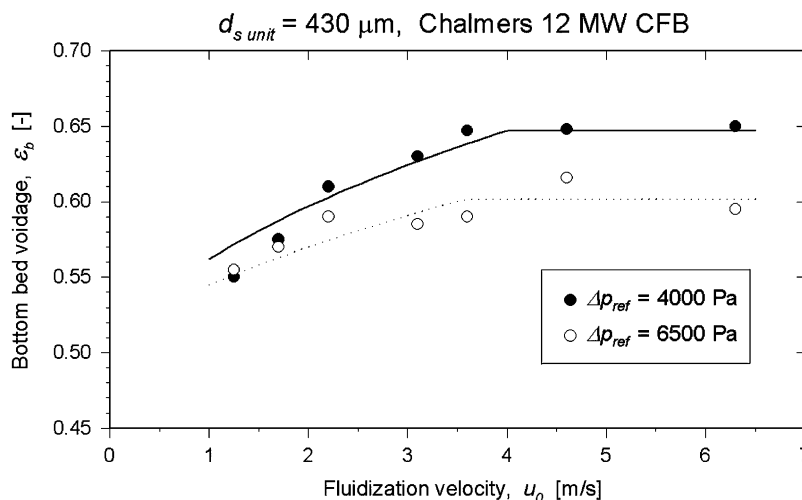


Fig. 3. CFB bottom bed expansion. Experimental data from Svensson et al. [39] compared with results from model calculations.

influence calculations of most of the variables given above, is larger than the particle size as averaged over the entire CFB loop, since fines tend to end up in the return leg and the freeboard, while coarse particles remain in the bottom bed. Thus, when an overall modeling of a CFB is carried out, the size segregation effect can be taken into account and estimated through the formulation of a population balance over the whole CFB loop.

2.2. Modeling of the freeboard

In presence of a dense bottom bed with the characteristics mentioned in the previous section, the freeboard comprises the height interval $H_b < h \leq H_{duct}$ with a solids suspension with a decreasing solids concentration with height. Bed material is elutriated from the bottom bed to the freeboard by the bursting of bubbles at the bottom bed surface ejecting particles into the freeboard. Once in the freeboard, these particles might either fall down again to the bottom bed after reaching different heights or be entrained up through the freeboard and be separated to the solids wall-layers or externally recirculated through the cyclone and return loop after having reached the exit duct height and followed the gas stream through the exit duct.

A division of the flow into two characteristic zones with respect to the backmixing in the freeboard of CFB risers was suggested by Harris et al. [56]: a homogeneous particle clustering flow and a core/annulus flow, with the former dominating the flow pattern in the lower part of the riser and the latter dominating in the upper part of the riser. Following this concept, Johnsson and Leckner [57] identified a splash zone and a transport zone in a fluidized-bed boiler and in cold models operated under conditions similar to those of boilers [57,58]. The splash zone, situated above the bottom bed surface, is characterized by a strong backmixing due to a ballistic-type of movement of clustered solids projected into the freeboard. This behaviour is directly related to the eruption of bubbles, which throw lumps of solids into the splash zone. The clusters are immersed in a more dispersed phase. Few of the clusters reach high up in the freeboard. Instead, the dispersed phase dominates the transport zone, adopting a core-annulus flow structure with upflow in the core and downflow in the annulus in a solids wall layer, with a solids net flux from the core to the solids wall layer all along the transport zone [59]. Local solids flux measurements

in a CFB riser show that the back mixing in the transport zone occurs mainly in the downflowing solids wall-layers, with an average concentration several times higher than the upflowing solids concentration in the core [7]. Furthermore, it has been experimentally determined that most of the parameters in the wall layers have an heterogeneous horizontal distribution in the wall layer, as reported in [7,60,61].

2.2.1. Terminal velocity

The terminal velocity, i.e. the free fall velocity, of a single particle falling in a fluid (terminal velocity), u_t , is derived as

$$u_t = \left(\frac{4d_p(\rho_s - \rho_g)g}{3\rho_g C_D} \right)^{1/2}, \quad (21)$$

where the drag coefficient, C_D , is obtained from experiments. A study on drag coefficients was carried out by Haider and Levenspiel [62], and they propose the following correlation:

$$C_D = \frac{24}{Re} [1 + (8.1716 e^{-4.0655\phi} Re^{0.0964+0.5565\phi})] + \frac{73.69 e^{-5.0784\phi} Re}{Re + 5.378 e^{6.2122\phi}}. \quad (22)$$

However, simpler correlations to estimate the terminal velocity exist in literature (see [62–65]). One such correlation, also provided by Haider and Levenspiel [62], is

$$u_t = u_t^* \left(\frac{\rho_g^2}{\mu_g(\rho_s - \rho_g)g} \right)^{-1/3}, \quad (23)$$

where

$$u_t^* = \frac{1}{18/d_p^{*2} + (2.335 - 1.744\phi)/d_p^{*0.5}}, \quad (24)$$

$$d_p^* = Ar^{1/3} = \left(\frac{\rho_s(\rho_s - \rho_g)g}{\mu_g^2} \right)^{1/3} d_p. \quad (25)$$

Yet these correlations are intended for isolated particles in a fluid. For calculation of the effective terminal velocity of particles in a solids suspension, interactions between particles have to be taken into account as done in the model by Win et al. [66], which was simplified by Palchonok et al. [67] assuming quasi-steady-state conditions applying averaged physical properties of the suspension. These models are based on the momentum conservation during collisions between particles flowing

at their slip velocity, making the effective terminal velocity of a particle different from the single particle terminal velocity, due to the interaction with the neighbouring particles in the solids suspension. Applying the model by Palchonok et al. the effective terminal velocity for a particle p , $u'_{t,p}$, immersed in a disperse solid suspension n is calculated solving the following polynomial:

$$a u'_{t,p}{}^2 + b u'_{t,p} + c = 0, \quad (26)$$

where

$$a = \frac{\pi(d_p + \overline{d_{s,n}})^2 \overline{\rho_{s,n}}(1 - \varepsilon)}{4(1 + (m_p/\overline{m_{s,n}}))} + 0.055 \pi \overline{d_{s,n}}^2 \rho_g \varepsilon^{-4.75}, \quad (27)$$

$$b = \frac{u_{t,p} - \overline{u_{t,n}}}{|u_{t,p} - \overline{u_{t,n}}|} \times \frac{\pi(d_p + \overline{d_{s,n}})^2 \overline{\rho_{s,n}}(1 - \varepsilon)\overline{u_{t,n}}}{2(1 + (m_p/\overline{m_{s,n}}))} + 3 \pi d_p \mu_g \rho_g \varepsilon^{-4.75}, \quad (28)$$

$$c = \frac{u_{t,p} - \overline{u_{t,n}}}{|u_{t,p} - \overline{u_{t,n}}|} \times \frac{\pi(d_p + \overline{d_{s,n}})^2 \overline{\rho_{s,n}}(1 - \varepsilon)\overline{u_{t,n}}^2}{4(1 + m_p/\overline{m_{s,n}})} - \overline{m_{s,n}} g. \quad (29)$$

The effect of considering particle interactions through the use of a modified effective terminal velocity is shown in Fig. 4, where the ratio of effective terminal velocity to single particle terminal velocity, $u'_{t,p}/u_{t,p}$, has been plotted against the

particle size. The figure illustrates the interaction effect for three different average sizes (100, 300 and 500 μm) of the particles forming the solids suspension surrounding a particle with diameter d_p . A value of $\varepsilon = 0.002$ has been taken for the voidage of the suspension surrounding the particle, (corresponding to a particle concentration of 5 kg/m^3). In the example of Fig. 4, the particle density for the suspension is assumed to have the same density as the surrounded particle (i.e. $\rho_{s,n} = \rho_p$).

It can be seen that when a particle is surrounded by a suspension of finer particles of equal density, its effective terminal velocity is lower than the corresponding single particle terminal velocity. In the core region of the freeboard, particles are assumed to flow upwards at a velocity equal to the slip velocity. Thus, a particle within a suspension of finer particles in the core region moves upwards at a higher velocity than in the case when it is surrounded by gas only (i.e. it is pushed up by the momentum of the surrounding particles, which flow upwards at a higher velocity). The opposite effects take place when a particle is surrounded by coarser particles, and the above-mentioned effects are enhanced the higher the suspension density (for example in the wall layers).

In summary, particle interactions can be taken into account through the use of an effective terminal velocity, allowing the solids suspension in the freeboard obtained from modeling to contain

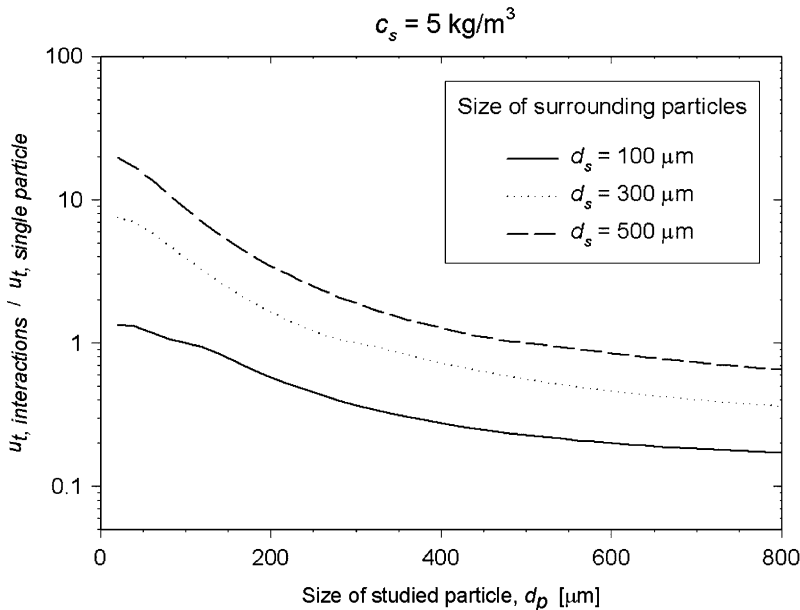


Fig. 4. Effect of particles interactions on terminal velocity values according to Palchonok et al. [67].

particles coarser than the size corresponding to the slip velocity based on the terminal velocity of a single particle which is in agreement with experiments [66].

2.2.2. Wall-layer thickness

The wall-layers thickness, t_{wall} , can be defined as the distance from the wall to the position of zero net local solids flux in the vertical direction. The thickness seems to be fairly independent of solids flux and the fluid dynamics of the unit once circulating conditions are established, but dependant on height in the riser [7,68]. This can be observed in Fig. 5, where data from different units under different fluidization conditions follow the same trend. These experimental data from several large-scale CFB units were summarized by Johnsson et al. [6]. For large CFB units, there is an increase in wall-layer thickness downwards along the riser wall. However, data for large CFB units are only available down to a certain distance from the top of the unit, H_{sat} , which can be defined as a function of the equivalent diameter of the riser, D_{eq}

$$H_{sat} = H_0 - 6D_{eq} \quad (30)$$

with H_{sat} expressed as distance from the bottom of the riser. The reason for the lack of experimental data points for $(H_0 - h)/D_{eq} > 6$ for large CFB units is that the riser height-to-width ratio of these units is typically less than 10 (and available data for this ratio exceeding 6 is only available from small-scale units and these exhibit a different behaviour [6,69]. Thus, under typical operational conditions in large

CFB units, heights for which $(H_0 - h)/D_{eq}$ exceeds 6 are normally within the splash zone. In the splash zone, most of the solids belong to the cluster phase, which, as mentioned above, has different fluid dynamical behaviour than the disperse phase forming the core and wall layers structure. To experimentally investigate the behaviour of the disperse phase in the splash zone is difficult since measurements are disturbed by the cluster phase. However, from a modeling point of view exact knowledge on the dispersed phase in the splash zone should be of less importance since, in this zone, its concentration is low compared to that of the cluster phase.

On the other hand, modeling of the disperse phase (and the core-annulus structure formed by the separation of solids to the walls) in the splash zone can be carried out based on experimental data from laboratory CFB units, which (having in mind that they may present different flow patterns than those of large CFB units) cover this missing range of data [6].

From Fig. 5, it can be observed that the reduced wall-layer thickness levels out for $(H_0 - h)/D_{eq} > 6$ (although the data scatter considerably which can be expected since they were obtained in different units under different operating conditions with respect to type of solids and gas velocity). Thus, a height-independent value of t_{wall} is assumed for $(H_0 - h)/D_{eq} > 6$ (this assumption has little influence on the results, since the cluster phase is highly predominant in this height interval and for this work the focus is on large-scale CFBs for which the ratio is often less than 6). The expression for the

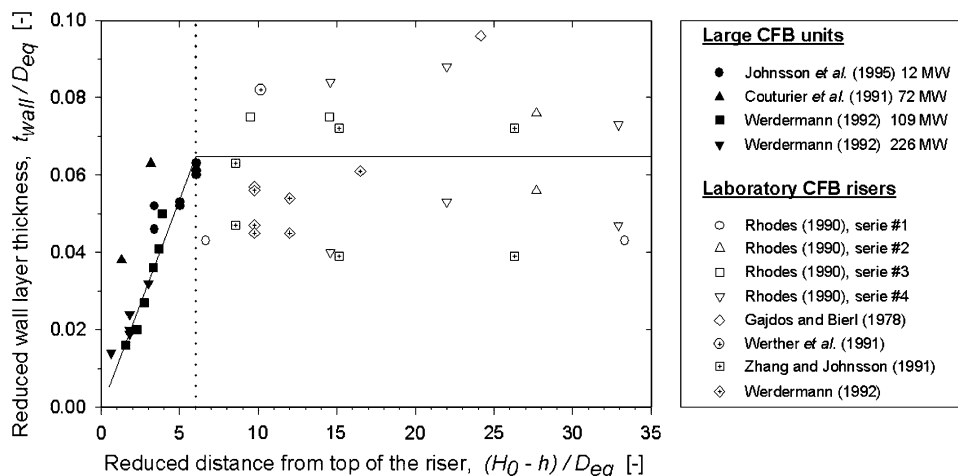


Fig. 5. Dependence of wall layer thickness on height in the riser. Measured data compared with results from model calculations with Eqs. (31) and (32).

wall-layer thickness is written as

$$t_{wall}(h) = 0.0108(H_0 - h) \quad \text{for} \quad H_{sat} < h \leq H_{duct}, \quad (31a)$$

$$t_{wall,sat} = 0.0648 D_{eq} \quad \text{for} \quad H_b < h \leq H_{sat}. \quad (31b)$$

Werther [1] also presented a correlation to estimate the thickness of the wall layer, reading

$$\frac{t_{wall}}{D_{eq}} = 0.55 \times Re_t^{-0.22} \left(\frac{H_0}{D_{eq}} \right)^{0.21} \left(\frac{H_0 - h}{D_{eq}} \right)^{0.73}. \quad (32)$$

Another expression was derived by Johansson et al. [70] under the assumptions that $t_{wall} \ll D_e$ and that the solids downflow in the wall layers at the exit duct height small enough to be neglected:

$$t_{wall} = \frac{D_{eq}}{4} k \times \exp\left(\frac{H_0 - h}{H_0}\right). \quad (33)$$

Note that a value for the backflow ratio, k , is required to apply this expression (see Section 2.3 for a detailed analysis and estimation of this ratio).

With the wall-layer thickness determined along the entire freeboard, the cross-sectional area of the core and the wall layer region at any height in the riser, $A_{i \text{ core}}$ and $A_{i \text{ wall}}$, can be determined.

2.2.3. Gas flow

Zhang et al. [7] measured velocities of down-flowing solids in the wall layer for different particle sizes and fluidization conditions. The results obtained are close to the values of the average terminal velocities of the particle suspension, which supports the assumption of no or low gas flow in the annular region of the freeboard (wall layers). Measurements of vertical gas dispersion in CFB wall layers by Sternéus et al. [71] show vertical dispersion both in upward and downward direction. This supports that the net (time averaged) gas velocity within the wall layers is zero or near zero, but that the gas velocity may fluctuate in the vertical direction due to the time dependant character of the downward flowing wall-layer solids. The effect will depend on operational conditions, but the data of Sternéus et al. were obtained under typical CFB conditions in the Chalmers 12 MW_{th} CFB boiler.

Concerning the core region, measured (horizontal) solids flux profiles are almost flat all over the core (i.e. the solids flux [kg/m²s] is more or less independent of spatial location [1,68,72]). Thus, the gas can be assumed to follow a plug-flow in the core region.

Additional air is usually injected in the freeboard (secondary or even tertiary air injections) with the purpose to burn volatile matter released by the fuel in the freeboard and to improve the gas mixing above the bottom bed [73] and to lower NO_x formation. Despite the importance of the additional air injections, no model in literature can reliably predict their penetration and mixing with the main flow in the riser [74]. Two difficulties can be observed: the influence of the particular design of the injector on the local gas flow, and the influence of the downflowing solids wall layer through which the air jet has to flow (which varies with fluidization parameters as well as riser geometry). Obviously, in an SFB there are hardly any solids wall layers and these can be neglected in terms of influencing the secondary air penetration as done in [75]. In CFB modeling one approach is to model air injections as discretized in the horizontal plane assuming horizontal diffusion of the injected air in a vertical plug flow [76]. This does not account for the momentum of the gas injected and the solution has to be experimentally adjusted. In the present work, since no gas flow is assumed in the wall layers and the core region is not discretized in the horizontal direction, all gas injected is assumed to join the plug flow at the injection height, as also assumed in other similar works [77,78]. This assumption becomes critical in terms of mixing and combustion modeling for units with large cross sections, but, from a macroscopical point of view, it should be a reasonable assumption with respect to fluid-dynamics.

2.2.4. Solids concentration

In the literature, simple models are given for the backmixing and decay in solids concentration above bubbling beds as well as along CFB risers [79–84]. These models assume a constant backmixing, yielding an exponential decay in solids concentration with height (with decay constant a'). Based on these single solids phase models, a general form to express the vertical solids concentration profile (for a given PSD size interval, d , of any of the solids fractions in the bed, f , at any height in the freeboard, h) can be written as

$$C_h^{f,d} = C_{H_0}^{f,d} + (C_{H_b}^{f,d} - C_{H_0}^{f,d}) \exp(-a_h^{f,d}(h - H_b)). \quad (34)$$

From experiments, the decay constant a' for these models was found to be inversely proportional to the gas velocity as shown in [79,85] for fine and

coarse particles respectively. Thus,

$$a_h^{f,d} \propto \frac{1}{u_{g,h}}. \quad (35)$$

Johnsson and Leckner [57] developed a similar type of model. However, it differs from the above models in that it considers both of the two above-mentioned back-mixing phenomena (back-mixing of clusters dominating in the splash zone and back-mixing at the riser walls, mainly of the disperse phase). Thus, these back-mixing processes are superimposed in the model by Johnsson and Leckner [57].

The back mixing of the cluster phase can be described as a ballistic type of solids back-mixing of clustered solids which gives a high backmixing rate with the clusters originating from the eruptions of bubbles at the dense bed surface. Due to this origin, the cluster phase can be assumed to be equally distributed over the cross section (i.e. not to exhibit a core wall-layer flow structure). In the splash zone formed, not only the solids flux and solids concentration show a strong gradient with height above bed surface, but also the average particle size. The strong gradients make modeling of the entire CFB loop sensitive to the splash zone modeling with respect to pressure and mass balances [53].

The dispersed solids phase occupies most of the height from the upper part of the splash zone to the top of the riser. This zone has been referred to as the transport zone [86,87] and, as mentioned above, exhibits a core-annulus flow structure, with upflow in the core with a net lateral flow to the down-flowing annulus (solids wall-layers). Solids concentration values in the transport zone are much lower than in the splash zone and the decrease with height is less pronounced.

Consequently, the resulting backmixing is not constant with height in the model by Johnsson and Leckner [57], but the result of two back-mixing processes which both give an exponential decay in solids concentration with height with decay factors a for the cluster phase and K for the disperse phase. Thus, if as for Eq. (34) written for a given PSD size interval, d , of any of the solids fractions in the bed, f , the vertical solids concentration profile in the freeboard becomes

$$C_h^{f,d} = C_{clus,h}^{f,d} + C_{disp,h}^{f,d}, \quad (36)$$

$$C_{clus,h}^{f,d} = C_{clus,H_b}^{f,d} \exp(-a_h^{f,d}(h - H_b)), \quad (37)$$

$$C_{disp,h}^{f,d} = C_{disp,H_0}^{f,d} \exp(K_h^{f,d}(H_0 - h)). \quad (38)$$

With the decay constants defined as

$$a_h^{f,d} = 4 \frac{u_t^{f,d}}{u_{g,h}}, \quad (39)$$

$$K_h^{f,d} = \frac{0.23}{u_{g,h} - u_t^{f,d}}. \quad (40)$$

As indicated above, the formation of the splash zone is directly related to the bubbles erupting at the top of the bottom bed, i.e. related to the bottom bed characteristics (fluidization regime and height of bottom bed). However, nor Eq. (39) or any other expression in literature for describing the splash zone solids concentration take into account the bottom bed characteristics. Inclusion of the bottom bed characteristics would most likely improve the modelling of the decay in solids concentration in the splash zone (as expressed by the decay constant a).

The gas velocity can, as a first approximation be taken as $u_g = u_0$. In reality, the gas velocity varies along the riser height even if only considering the time-averaged velocity. The variation is due to variations in riser cross section and in the cross-sectional area of the core region if it is assumed that the gas only flows upward through the core region. In addition, secondary gas injections, gas generation by fuel conversion, and temperature variations along the riser will add changes to the gas velocity. Therefore, the decay constants should vary their values with height in furnace/riser and a discretized approach of the problem is required for an accurate analysis.

Evaluation of the two types of modeling (single and two back-mixing terms) by comparison with experimental data from large CFB units is shown in Figs. 6 and 7. Four models with only one back-mixing term (i.e. a single decay factor) from the literature [28,82,88,89] have been selected and compared with the model by Johnsson and Leckner [57]. As can be seen, the experimental data from a CFBC included in Figs. 6 and 7 yield an exponential decay in solids concentration, but with strongly different decay constants in the two different zones (splash and transport zones) and accounting for the two back-mixing phenomena is required in order to obtain a good agreement between experimental data and model predictions. Although the model by Johnsson and Leckner [57] is also based on assumptions, it can be concluded that any modeling of this type based on a single back-mixing expression (i.e. a single decay constant) cannot fit the experimental data, whatever value for the decay factor a' is applied (see Figs. 6 and 7).

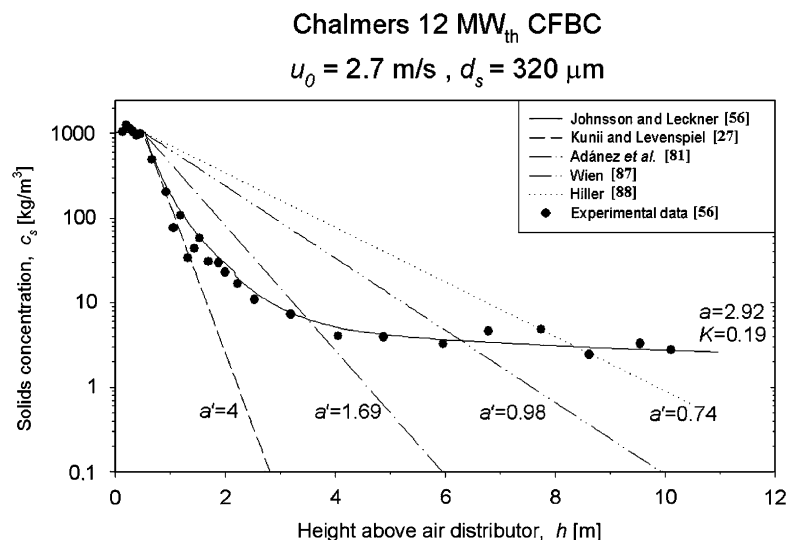


Fig. 6. Solids concentration profile. Experimental data from Johnsson and Leckner [57] vs. modelled data [28,57,82,88,89].

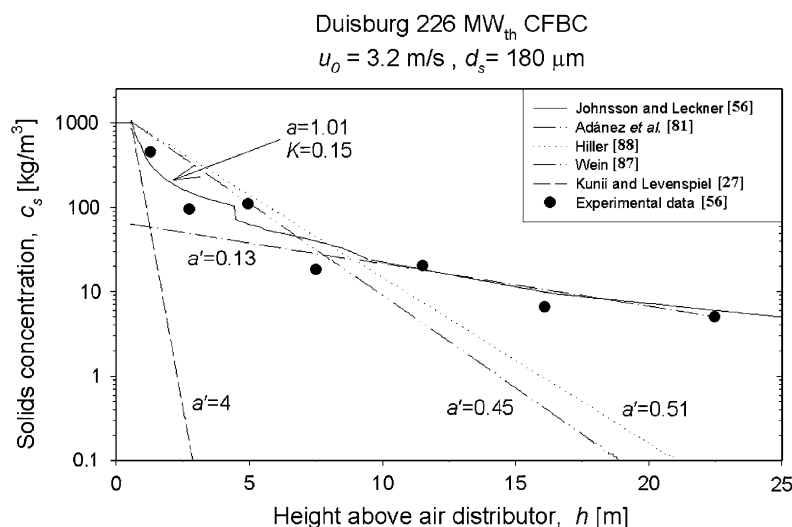


Fig. 7. Solids concentration profile. Experimental data from Werdermann [68] vs. modelled data [28,57,82,88,89].

Unfortunately, for large CFB units there is little experimental data on solids concentration covering both splash and the transport zones. In most cases, there is no experimental data on the splash zone, while measured data on the transport zone is more common [68,90–92]. Single solid phase models are able to fit experimental data either in the transport or the splash zone, and if enough experimental data from any of the two zones is lacking, fitting a one-decay model may lead to that wrong conclusions are drawn on the solids back-mixing process and thereby on the characteristics of the vertical concentration profile. Fig. 7 shows how the model

by Adánez et al. [82] predicts with reasonable accuracy the trend in the transport zone ($h > 5 \text{ m}$) but not in the splash zone ($h < 5 \text{ m}$). Also in this figure it can be seen that a 2-decay modeling is required to reach reasonable agreement with measured solids concentration profile along the entire freeboard, i.e. including both the splash and the transport zones.

2.2.5. Solid flows

The net solids flow out of the furnace (rate of particles leaving the riser towards the cyclone) is assumed to entirely consist of solids belonging to

the disperse phase, since no cluster phase is assumed to reach the upper part of the freeboard. Measurements show that particles in the core region of the transport zone travel at velocities close to their slip velocity [72]. The use of the concept slip velocity is analysed in [93]. Assuming particles to flow upwards at their slip velocity (with the terminal velocity modified in order to account for particle interactions, as explained above) and having calculated the vertical solids concentration profile, the upflow in the core region of the transport region becomes

$$F_{core,h}^{f,d} = c_{core,h}^{f,d} A_{core,h} (u_{g,core,h} - u_{t,core,h}^{f,d}). \quad (41)$$

Davidson [93] gives a detailed discussion on modeling of the transfer of solids from the core to the wall region based on a diffusion process in the core region. Obviously, it is physically not a diffusion process since the solids concentration in the annular region is higher than in the core (but the net transfer of solids is from core towards wall).

There seems to be an agreement in literature on the existence of a net transfer of solids from the core region to the wall layer in the transport zone. This net transfer is the result of a balance where, at a certain height, there are more solids leaving the core towards the wall region than vice versa (thus, there is a flow in both directions). The lateral net solids flow in the transport zone can be calculated by differentiation of the solids flow in the core region of the freeboard

$$F_{lat,h}^{f,d} = F_{core,h}^{f,d} - F_{core,h+dh}^{f,d}. \quad (42)$$

Thus, note that the net lateral flow obtained is the result of the net balance $F_{core \geq wall,h}^{f,d} - F_{wall \geq core,h}^{f,d}$, although the individual values of these terms remain unknown. Knowing that the net solids flow contributes to increase the downward flow in the wall layer, the downflow in the annular region of the transport zone can be calculated as

$$F_{wall,h}^{f,d} = F_{wall,h+dh}^{f,d} + F_{lat,h}^{f,d} \quad (43)$$

with the initial value given at the cell located at $h = H_{duct}$ by means of the definition of the backflow ratio, k_b (see Section 2.3):

$$F_{wall,H_{duct}}^{f,d} = \frac{k^{f,d}}{1 + k^{f,d}} F_{core,H_{duct}}^{f,d}. \quad (44)$$

Finally, with the above-mentioned assumption of zero wall gas-flow, the solids concentration in the

wall region becomes

$$c_{wall,h}^{f,d} = \frac{F_{wall,h}^{f,d}}{u_t^{f,d} A_{wall,h}}. \quad (45)$$

2.3. Modeling of the exit zone

The height interval $H_{duct} < h \leq H_0$ in a fluidized bed riser is here referred to as exit zone. When an FB unit is operated under circulating conditions, the exit zone exhibits a different and more uncertain solids flow mechanism from that in the freeboard (see Section 2.2). The highly dilute conditions in the exit zone make pressure measurements unreliable. Thus, experimental knowledge concerning solids concentration and flow in this zone of a large CFB unit is usually limited to techniques based on visual observations in scale models. Due to the unclear solids flow picture, a proper modeling of the exit zone requires the use of CFD tools [94].

An important fact to point out concerning the solids flow pattern in the exit zone of large CFB units is that its picture differs from that of narrow laboratory units, so literature based on observations in the latter type of units might be misleading.

For narrow laboratory units, it has been shown that different configurations of the exit geometry (i.e. smooth, extended or abrupt) can strongly influence some of the main fluid dynamical parameters of a CFB unit, as the vertical solids concentration profile, the solids net flow and the residence time. On the other hand, studies carried out in large CFB units [58,95] show that the influence of the exit zone geometry is far less important in CFBC and CFBG units (the most common types of exit zone designs in operating units were tested in these works). Zheng and Zhang [96] carried out an analysis of the influence of the exit zone geometry on the performance of CFB combustors, but based on experiments in a riser with an aspect ratio over 50 (i.e. far higher than the typical values below 10). Thus, their observations of a strong influence of the exit geometry on the solids net flow and vertical concentration profile, typical for narrow laboratory risers, are hardly applicable to CFB combustors. The reason that the exit geometry seems to be of less importance in large units than in laboratory units is most likely simply due to that the solids loading is much lower in the exit region in large units than in the small units, with the latter operated with high solids flux.

2.3.1. Backflow effect

Upflowing particles in the core region of the freeboard can follow two paths when reaching the exit zone: they either enter the downflow in the riser wall layers (i.e. be internally recirculated) or they follow the gas flow out of the riser through the exit duct (i.e. be externally recirculated, forming the so-called solids net flow of the unit). The proportions in which these two effects take place are of great importance, since the larger the internal recirculation in the wall-layer downflow (backflow) the greater the particle residence time in the riser. The solids residence time in the riser is an important parameter to adjust when optimizing the performance of CFB units, and this parameter was found to be strongly influenced by the exit configuration chosen, as discussed in [97]. Yet, as stated above, the low solids loadings in the top of industrially sized CFBs makes these less sensitive to exit geometry than small units operated at high recirculation flows.

The relative magnitudes of internal and external recirculation of solids can be expressed through the backflow ratio, k , which, for a given size interval of any solids fraction in the CFB unit is defined as

$$k^{f,d} = \frac{F_{wall,H_{duct}}^{f,d}}{F_{net}^{f,d}}. \quad (46)$$

It has been shown [58,95] that there is little or no difference between an extended, abrupt and enhanced exit with respect to the ratio of internal to external solids flow (k was similar in these three cases) in large CFB units. It was also found that a reduction in the cyclone inlet area (increase in entrance velocity) decreases k , resulting in an increase of the solids flow into the cyclone (i.e. the solids net flow). Addition of internals near the exit duct was—as expected—found to lead to the opposite effect, i.e. resulting in a higher residence time and backmixing rate of the particles.

Despite the importance of k , little information is available on its magnitude and no simple and reliable modeling expressions are available in literature for its calculation. What is more, the backflow effect is often neglected in modeling of fluid dynamics. Experimental correlations for estimating the backflow in standard exit configurations are given in [1,53,68,98]. Only in the latter work by Pallarès and Johnsson [53] k is assumed not to only depend on the vertical location of the exit duct but also on the flow conditions. The Pallarès and Johnsson expression is based on fits to experimental data of solids fluxes from three large CFB units and the correlation is shown in Fig. 8. The correlation relates the probability of entrainment of a particle, p_{ent} , to its slip velocity and the core region flux at the

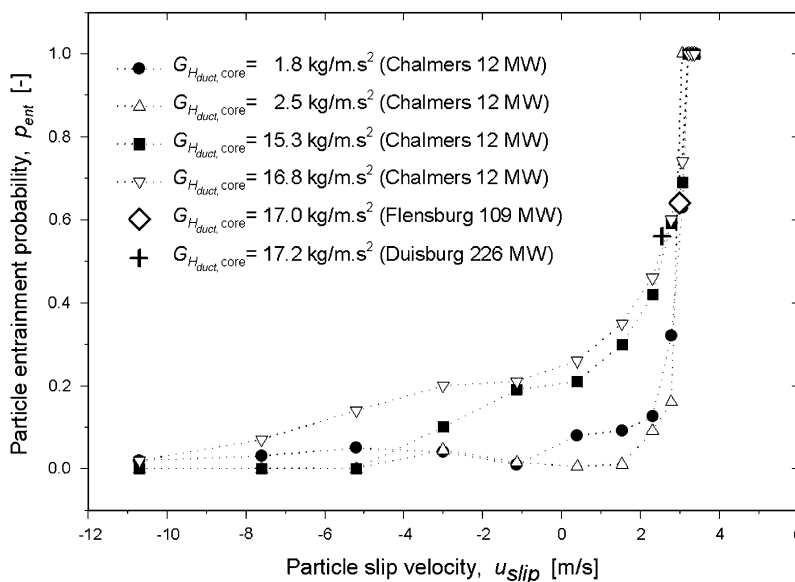


Fig. 8. Entrainment probability of a particle in the exit zone calculated from experimental data found in [68] and [99].

beginning of the exit zone and it is written

$$p_{ent}^{f,d} = \frac{1}{(4.07 - u_{slip,H_{duct}}^{f,d})^{\max\{0.5; 3.057 - 0.129 \cdot G_{s,H_{duct}}\}}} \quad \text{for } u_{slip,H_{duct}}^{f,d} \leq 3.07 \text{ m/s}, \quad (47a)$$

$$p_{ent}^{f,d} = 1 \quad \text{for } u_{slip,H_{duct}}^{f,d} > 3.07 \text{ m/s}. \quad (47b)$$

Unlike previous expressions in literature for evaluation of the backflow effect, the probability of entrainment of a particle in Eq. (47) is not directly correlated to height in the furnace, but to fluid dynamical variables which, however, vary with height in the furnace (thus, indirectly accounting for the dependence on height). The data points in Fig. 8 are taken from [68,99]. However, since the performance of the correlation given by Eq. (47) depends on exit configuration, it should not be used in units with an exit configuration significantly differing in geometry from those units which were used as experimental basis for Eq. (47) (although data taken from three large CFB units, most of the data are from the Chalmers 12 MW CFB unit, cf. Fig. 2 and [58]).

In spite of the complex nature of the backflow effect as well as the fact that available data originate from different units, the resulting data points in Fig. 8 fall on rather continuous curves, which makes it possible to simplify the modeling by identification of trends. The finer the particles, the higher the probability for them to be entrained and to become externally recirculated through the cyclone. There is also a dependence on the superficial solids upflow due to the effect of the particle interaction, i.e. when a particle is surrounded by other particles (high value of $G_{s,H_{duct}}$), its probability to be entrained is lower the more dilute the solids suspension is.

As indicated above, the probability of entrainment is known to depend also on the geometry of the exit configuration [58]. Thus, care has to be taken when extending the present probability values to units with an exit geometry significantly different from those of the three units from which the data were taken.

The solids net flow, F_{net} , can be determined using the definition of entrainment probability

$$F_{net}^{f,d} = \frac{F_{core,H_{duct}}^{f,d}}{p_{entr}^{f,d}}. \quad (48)$$

Finally, the backflow ratio can be expressed as a function of the entrainment probability as

$$k^{f,d} = \frac{F_{H_{duct}}^{f,d}}{F_{net}^{f,d}} = \frac{F_{core,H_{duct}}^{f,d} - F_{net}^{f,d}}{F_{net}^{f,d}} = \frac{F_{core,H_{duct}}^{f,d}}{F_{net}^{f,d}} - 1 = \frac{1}{p_{ent}^{f,d}} - 1. \quad (49)$$

2.3.2. Solids concentration

In contrast to investigations in narrow CFB risers, where the vertical solid concentration profile is observed to increase in the exit zone, solids concentration values in the exit region of CFB combustors are low (as mentioned above). This implies that the solids inventory in the exit zone of a large CFB unit can be neglected, when a global mass balance over the whole CFB unit is formulated.

By means of fibre optical probes Lacknermeier and Werther [95] observed that the exit zone flow exhibits traces of the core-annulus flow structure governing in the transport zone flow of the freeboard, but with a superimposed horizontal velocity component towards the exit duct due to the drag of the gas flow exiting the riser. Furthermore, based on visual observations made in a scale model by Johnsson et al. [58], particles were observed to follow a ballistic movement in the exit zone. Harris et al. [100] justified by means of force balances all of the above-cited behaviours: particles follow the gas flow towards the exit duct until they eventually experience an inertial separation from the gas streamlines, then following a ballistic movement towards the walls, where they join the downflowing solids annulus.

2.4. Modeling of the exit duct

Particles entrained from the riser flow towards the cyclone through the exit duct due to the drag of the gas stream, with the particles experiencing an acceleration that can be further enhanced by a reduction in the cross-sectional area of the duct (increase in velocity).

Several works in literature deal with horizontal conveying of solid particles [101–103], but the conditions in a CFB exit duct (dilute solids suspension, high acceleration and low length-to-height ratio of the duct) are different from the conditions employed in these investigations.

Muschelknautz and Muschelknautz [104] developed a model especially aimed at CFB units, which is used to determine Δp_{duct} and the solids velocity

along the exit duct. These authors calculate the velocity of the solids at any vertical cross section in the exit duct, x , by solving the following differential equation

$$\frac{du_s}{dx} = \frac{g}{u_s} \left(\frac{u_{g,duct} - u_s}{w_s} \right)^{2-z} \quad (50)$$

taking the initial value

$$u_{s,0} \approx \frac{u_{g,duct,0}}{3}, \quad (51)$$

where

$$u_{g,duct}(x) = \frac{u_{g,core,H_{duct}} A_{core,H_{duct}}}{A_{duct}(x)}, \quad (52)$$

$$w_s = \left[\frac{4(\rho_s - \rho_g)g d_s}{3 Z \mu_g^k \rho_g^{1-k}} \right]^{1/2-z} (1 + (0.25 + z)\gamma^{0.25}), \quad (53)$$

$$\gamma = \frac{F_{net}}{u_{g,i=n_{duct\ core}} A_{i=n_{duct\ core}} \rho_g} \quad (54)$$

$z \approx 0.7$; $Z \approx 18$ for $Re_p = 3$ to 100.

Once the differential equation (Eq. (50)) is solved, the solids velocity profile is known. Thus, the pressure drop along the exit duct can be calculated as

$$\Delta p_{duct} = -\rho_g \overline{u_{g,duct}} \left(\frac{\overline{u_{g,duct}}}{2} + \gamma \Delta u_{s,duct} \right). \quad (55)$$

An additional loss of pressure due to the entrance effect might be included in the calculations by taking the value of $\Delta u_{s,duct}$ between the duct entrance ($x_0 = 0$) and a virtually extended length of the duct equal to $x_f = L_{duct} + b$ (being b the entrance width of the duct).

2.5. Modeling of the cyclone

From a fluid dynamical point of view, two phenomena should be of main importance as far as the cyclone is concerned: the pressure drop, Δp_{cycl} , and the separation efficiency for each size interval of each solid fraction present in the CFB unit, $\eta^{f,d}$. The pressure drop across the cyclone is relatively small compared to the pressure drops in the other parts of a CFB unit (see Fig. 15) and the overall collection efficiency of the cyclone is close to 1 under typical operational conditions. Thus, nor the mass nor the pressure balance over the whole CFB unit are sensitive to the modeling of the

cyclone. Furthermore, studies on cyclones are available in literature and available models are able to provide accurate results.

With respect to the pressure drop over the cyclone, several expressions are available in literature, all of them giving similar results [105–107]. The latter expression [107] has been used in several works in the field of large CFB units [77,84,108] and reads:

$$\Delta p_{cycl} = C_{cycl} \frac{\bar{V}_{g\ duct}^2 \rho_g}{A_{cycl\ inlet}^2}. \quad (56)$$

Based on comparison with experimental data [108] the empirical coefficient, C_{cycl} , can be set to 10.0, which yields values for $\Delta p_{cyclone}$ of the order of 100 Pa under typical boiler and gasifier conditions.

With respect to the cyclone separation efficiency, several comprehensive models are available. Some of them restrict their set of inputs to geometrical parameters [109], while more accurate models also account for flow conditions (gas velocity, solid load) [110–112]. With the cyclone separation efficiency determined for each size interval of each solid fraction considered, the rate of solids separated by the cyclone and externally recirculated through the return leg can be expressed as

$$F_{ret\ leg}^{f,d} = \eta_{cycl}^{f,d} F_{net}^{f,d}, \quad (57)$$

where $F_{net}^{f,d}$ is the solids net flow of each size interval. Thus, in the return loop (i.e. downcomer, particle seal and, optionally, particle cooler), the mass fraction of each size interval can be calculated as

$$x_{ret\ leg}^{f,d} = \frac{F_{ret\ leg}^{f,d}}{\sum_f \sum_d F_{ret\ leg}^{f,d}}. \quad (58)$$

With these values, the other parameters required to the model the downcomer and particle seal (e.g. mean particle size and mean solids density) can be calculated. Since the separation efficiency is high (near 1) for the inert solids present in the primary cyclone, the result will have little effect on the overall fluid dynamical modeling presented here. On the other hand, separation efficiency is lower for fuel particles which are at the end of their conversion process (i.e. fine and light). Thus, these fines are to some extent entrained out of the cyclone, reducing the combustion efficiency [76].

2.6. Modeling of the downcomer and particle seal

The system formed by the particle seal and the downcomer has the purpose of allowing the transportation of externally recycled particles through the return loop once they have passed the cyclone, and preventing the fluidization gas to flow backwards through the return loop and into the cyclone. This is usually achieved by inserting the end of the downcomer in a bubbling bed and driving the fluidized particles back to the riser through a return leg. In some CFB units, the bubbling bed acts as particle cooler, extending the range of operating conditions with respect to the heat balance/output power. Some CFB designs, such as the one in Fig. 9, have a particle-cooler bed separated from the particle-seal bed. In addition, the pressure drop in the riser, exit duct and cyclone, is compensated by a column of fluidized solids that is formed in the downcomer.

In order to both ensure solids transportation and avoid gas by-pass flow to the cyclone, the particle-seal bed is normally under bubbling conditions. The fluidization regime in the column of fluidized solids formed in the downcomer should theoretically be as

close as possible to minimum fluidization conditions. This, since it is desired to minimize the gas flow entering the cyclone through the cyclone leg and the formation of bubbles (which may project solid particles into the cyclone). However, in practise a higher gas flow is employed in order to ensure a sufficiently good fluidization both in the downcomer and in the particle seal.

Thus, assuming a dense bubbling bed in the particle seal, models for bed expansion in SFB units can be applied to model the voidage and the gas flow division of the bed in the particle seal and the fluidized solids column in the downcomer. A description of the fluid dynamics of a dense bottom bed including a modeling approach is given in Section 2.1.

Fig. 10 compares experimental data from the dense bottom bed of a 16 MW_{th} SFB boiler with results from the model by Johnsson et al. [17]. A good agreement between experiments and modeling is shown, with the data obtained at different bed pressure drops (Δp_0 from 4 to 8 kPa), showing that the bed pressure drop has no or little influence on the bed expansion (all data points follow the same curve). However, a CFB particle seal will typically operate at lower gas velocities (below 1 m/s) and smaller mean solids size than those corresponding to the conditions in an SFB combustor. At this point, it is important to recall the role played by particle size segregation effects in a CFB unit. Under typical operation conditions, the mean particle size in the dense bed of the particle seal (which is needed in the modeling of the particle seal) may be less than half of the mean particle size of the bed material used. Thus, as in the modeling of the riser bottom bed, modeling the bed in the particle seal by assuming a mean particle size equal to that of the material in the whole CFB unit (which is known) is not realistic and may lead to large errors. Thus, the value of the mean solids size in the particle seal should be obtained through an overall CFB model accounting for the mass balance over the entire unit (see Section 3), considering solids segregation.

Since solids in the downcomer flow downwards at a certain superficial velocity, $u_{s,dc}$, fluidization conditions in the downcomer are defined by the relative gas–solids velocity, $u_{rel,dc}$, which is the gas velocity to be used as input when applying an SFB bed-expansion model. Thus

$$u_{rel,dc} = u_{g,dc} - u_{s,dc}, \quad (59)$$

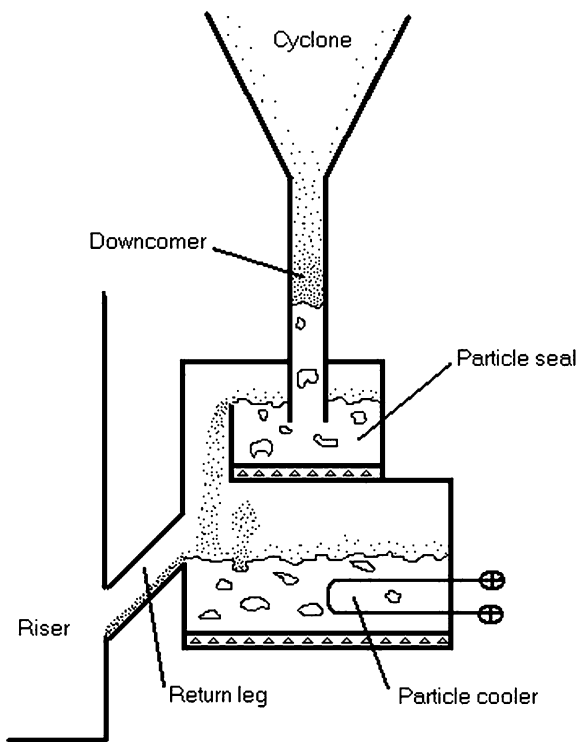


Fig. 9. Overview of a CFB return loop with independent particle cooler.

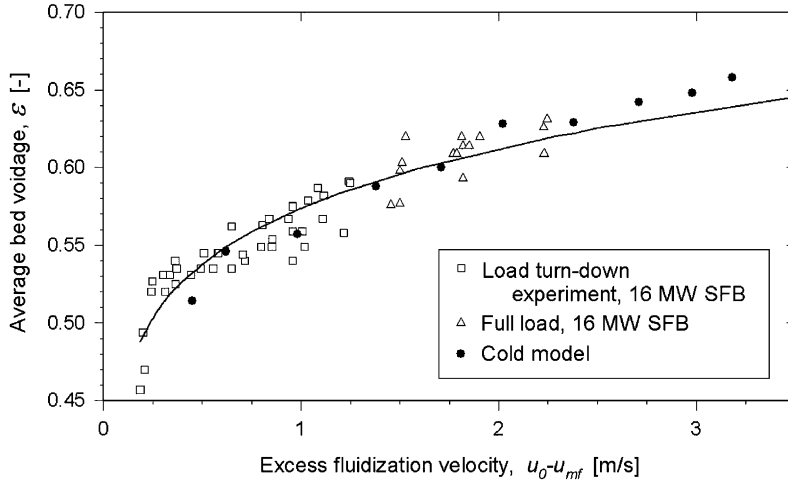


Fig. 10. SFB expansion. Measured data compared to results from model calculations (from [17]).

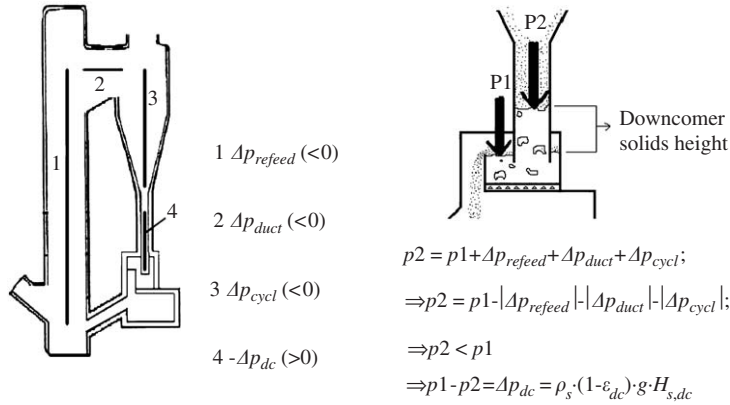


Fig. 11. Pressure balance terms in CFB loop, with focus on downcomer and particle seal.

where

$$u_{s,dc} = -\frac{F_{ret\ leg}}{\rho_s A_{dc}}. \quad (60)$$

The superficial velocity of the gas in the downcomer is assumed to equal that in the bubbling bed of the particle seal. This assumption is supported by the fact that the pressure that the gas has to flow against is the same both through the bubbling bed of the seal and the solids column in the downcomer (since $p_1 > p_2$, see Fig. 11). Thus

$$u_{g,dc} = u_{g,seal}. \quad (61)$$

However, this value of $u_{g,dc}$ is only a valid estimation when the nozzles fluidizing the particle seal are equally distributed over the entire cross section of the particle seal.

2.6.1. Pressure balance

Modeling of the height of the column of fluidized solids formed in the downcomer requires the formulation of a pressure balance over the circulating loop. Rhodes and Geldart [107] and Yang [108] carried out some investigations on the pressure loss in different parts of FB units, and Leckner [3], Lei [78] and Hannes [77] formulated pressure balances over the whole circulating loop in their works.

The value of the pressure drop over the solids column formed in the downcomer, Δp_{dc} , is obtained by formulating the pressure balance all over the circulating loop. Assuming no pressure drop across the return leg (where the particles are assumed to flow back to the riser by gravity), the pressure balance can be written

$$\Delta p_{refeed} + \Delta p_{duct} + \Delta p_{cycl} + \Delta p_{dc} = 0. \quad (62)$$

The meaning of the pressure drop terms in this expression is illustrated in Fig. 11a, where Δp_{refeed} is the pressure drop caused by the solids suspension in the riser between the centerlines of the return leg (inlet of externally recycled solids) and the exit duct (outlet of externally recycled solids). This is calculated as

$$\Delta p_{\text{refeed}} = \int_{H_{\text{retleg}}}^{H_{\text{duct}}} \rho_s g C_s dh. \quad (63)$$

The values of Δp_{duct} and Δp_{cycl} are determined by Eqs. (55) and (56), respectively. Thus, the pressure drop in the downcomer, Δp_{dc} , is obtained from the pressure balance given by Eq. (62). In terms of absolute values, Δp_{duct} and Δp_{cycl} are rather small compared to the terms Δp_{refeed} and Δp_{dc} . The pressure balance over the downcomer and the particle seal is illustrated in Fig. 11b. Hence, the height of solids required in the downcomer solids column, $H_{s,dc}$, to achieve this pressure drop, Δp_{dc} , can be obtained by the balance

$$\Delta p_{dc} = \rho_s (1 - \varepsilon_{dc}) g H_{s,dc}. \quad (64)$$

Generally, the height of the solids column in the downcomer increases as the fluidization velocity in the riser or the particle seal is increased.

3. Overall modeling of a CFB unit

Separate modelling of any of the zones presented in the previous section, schematically illustrated in Fig. 2, might fail in giving satisfactory results, since strong interactions exist between the zones. Interactions exist between the bottom bed and the rest of the riser due to the elutriation of solids from the bed, backmixing of solids from freeboard to bed; between the freeboard and the exit zone due to the backflow effect; between the downcomer and the other zones due to the pressure balance; and between all zones due to the population and pressure balances. Thus, changes in flow pattern in any given zone will to a certain extent affect the features of the flow in the remaining zones. Thus, for proper modelling of each of the six zones given above as well as of the entire CFB unit, an overall model taking into account interactions among the different zones of a CFB unit has to be implemented. Lei [78] provided such an overall CFB model, although expressions found in literature directed towards narrow laboratory units are used in some zones of this model. The model does not account for solids size segregation and has the net solids flux, G_s ,

as an input to be provided to the model. Hannes [77] also presented an overall CFB model, which is not limited to fluid dynamics but included also the other modeling fields given in Section 1.2 (Fig. 1). However, the work by Hannes is restricted to the riser of the CFB unit, and the return loop (exit duct, cyclone and downcomer and particle seal) is not modelled but substituted by a set of boundary conditions in the riser.

Due to the importance of the above-mentioned interaction of the zones of the entire CFB loop, some key features are particularly expected to be included in a fluid dynamical overall CFB model:

- The overall model should exhibit a realistic input scheme. If the model is intended to have a practical meaning and applicability, its input parameters should be such which are both measurable and independently adjustable under operation, i.e. some models require the solids net flow as input, although this parameter is not known under operation and is dependant on the model inputs: geometry of the unit (specially of the riser exit), operational conditions and bed material used. Hence, a reasonable set of inputs to an overall CFB fluid dynamical model can be classified in three categories: geometry of the CFB unit, operational conditions (injected gas flows and pressure drop over the riser) and physical properties of the bed solids and the fluidizing gas.
- Discretization of the riser into a mesh is required to provide an appropriate treatment to geometrical and fluid dynamical discontinuities which may be present due to changes in the riser cross-sectional geometry and secondary air injections, and possible discontinuities as a result of the existence of the above-mentioned (three) fluid dynamical zones in the riser.
- The well-established core-annulus flow structure in the freeboard should be included in the model, which implies a discretization of the freeboard cells not only in the vertical but also in the horizontal direction.
- The particle size segregation is of importance and should be taken into account. This is done by enabling the overall model to handle PSD for each of the solids fractions considered instead of only assuming a mean particle size to represent all solids. This modelling approach forces the inclusion of a population balance over the CFB unit in the calculations. As a result, the PSD of each solid fraction (and thereby the mean particle

size) in all zones of the CFB unit is obtained, i.e. resulting in that particle size segregation is modelled. As mentioned above, the mean particle size in the dense bed of the riser and in the particle seal both usually differ considerably from that of the particle size averaged over the entire CFB loop, and there is also a considerable variation in solids size within the freeboard. The crucial importance of including the return loop in the overall modeling and not just the riser is revealed in the evaluation of the population balance, where two facts can be observed: the return loop contains an amount of bed material that is not negligible (typically from 10% to 30%) and that solids in the return loop have a PSD which typically differs significantly from the average solids size in the CFB unit (i.e. PSD of solids in the return leg is biased towards finer particle size intervals).

An overall CFB model comprising the above features will make it possible to close the pressure balance in order to determine the amount of material contained in the fluidized solids column formed in the downcomer. This amount of solids must also be considered in the population balance.

3.1. Practical example of an overall CFB model

In order to exemplify the possibilities that an overall CFB model can offer, a set of local models have been selected from those presented in the previous section and linked into an overall CFB model through an implementation which takes the four above-listed requirements into account. Details on the implementation itself are considered outside the scope of this paper.

The local models selected are: Pallarès and Johnsson [53] for the expansion of the bottom bed

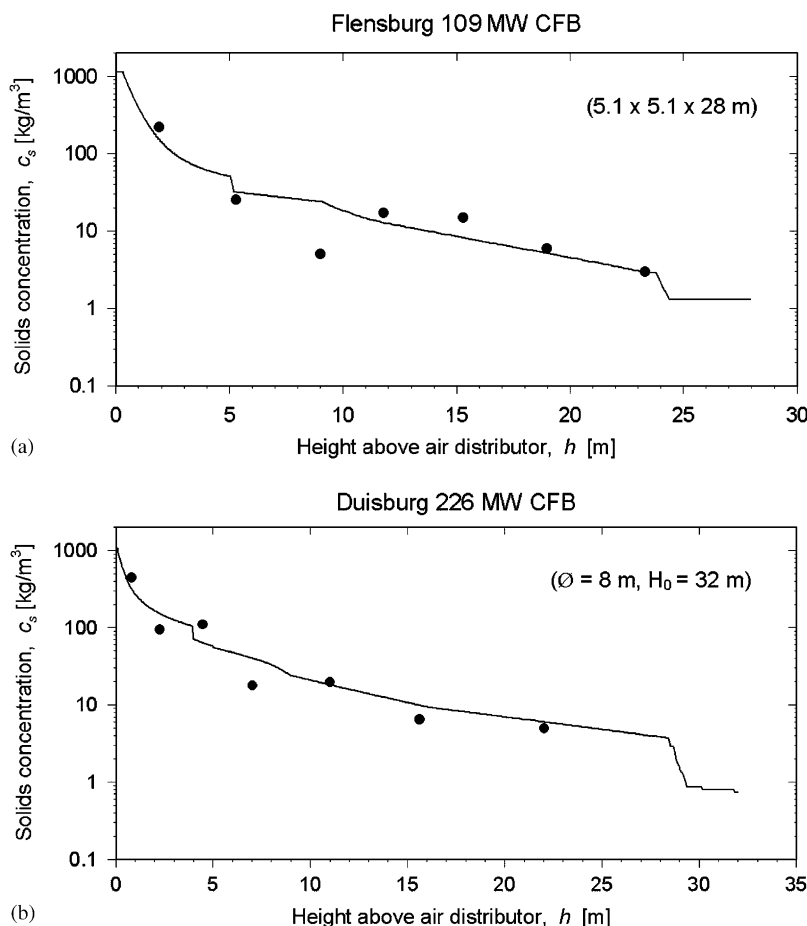


Fig. 12. Vertical profile of solids concentration in cross-section average. Experimental data from Werdermann [68] compared to model results.

in the CFB riser; Johnsson and Leckner [57] for the freeboard; Palchonok et al. [67] for the effect of interactions between particles; the correlation given by Eq. (47) for the back-flow effect in the exit zone; Muschelknautz and Muschelknautz [104] for the riser exit duct; in the cyclone, the models by Dietz [110] for the collection efficiency and by Rhodes and Geldart [107] for the pressure drop; and finally the model by Johnsson et al. [17] for the expansion of the dense bed in the particle seal. In addition, a pressure balance according to what is proposed in Section 2.6 and a population balance all over the CFB unit need to be formulated and fulfilled. Finally, interaction between solids of different size is accounted for according to Eqs. (26)–(29) and the riser has been discretized in a way accounting for what is mentioned in the previous section.

Fig. 12 exemplifies results obtained from the overall CFB model together with experimental data. It should be noted that the experimental data shown in Fig. 12 has not been part of the modeling process of any of the local models used. As mentioned in Section 1.3 the data available from large units is for obvious reasons restricted. Much of the data is from the Chalmers 12 MW_{th} boiler which, although of industrial scale, is considerably smaller than a large power boiler of some 100 MW_{el}. What is important,

however, is that certain key characteristics of solids flow in large-scale CFBs have been identified (see criteria listed in Section 1.1) from which it can be expected that the same characteristics of the flow should be present in all boilers fulfilling the criteria listed in Section 1.1. Fig. 12 shows the vertical profile of solids concentration in the riser of two large CFB combustors (with a cross section of more than 25 and 49 m², respectively) investigated in detail in [68]. As seen, the agreement of the overall CFB model with the experimental data is good. The sudden drops in the solids concentration profiles are due to changes in the secondary air injections or in the cross-sectional geometry of the riser. The drop in solids concentration at the top of the riser is due to the different flow pattern in the freeboard and the exit zone.

The value of the net solids flow, F_{net} , is a valuable output from the overall CFB model, since it governs important features in an operating CFB unit, such as the residence time of the bed material in the riser and the return leg and the thermal stability around the circulating loop. The net solids flow cannot be directly measured in large CFB units, but it can be estimated through rough methods, such as integration of available cross-sectional data on the solids flux in the riser (as was done to obtain the

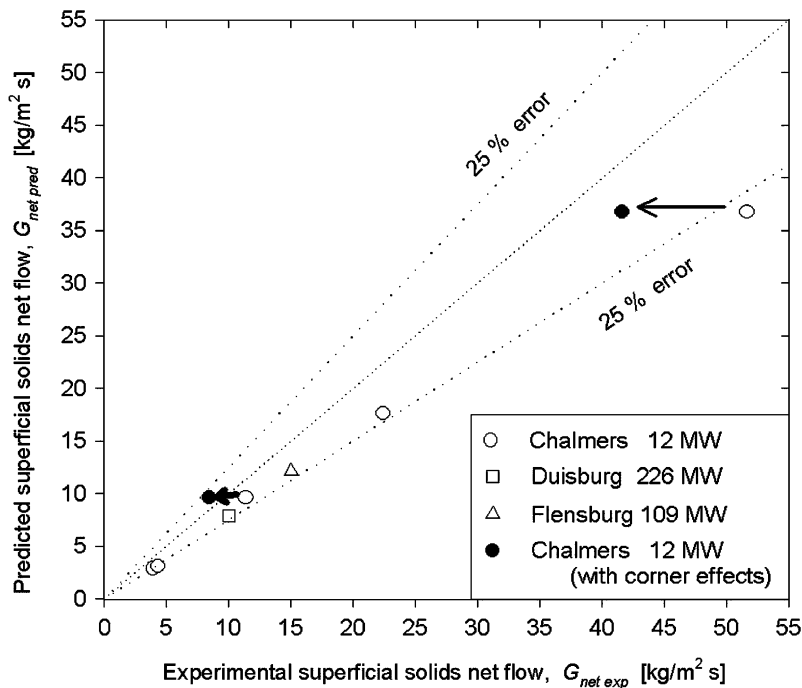


Fig. 13. Comparison between experimental [7,60,113] and modelled values of the superficial solids net flow.

experimental data in Fig. 13) or by using the expression:

$$F_{net} = C_{s,H_{duct}}(u_{g,H_{duct}} - \overline{u}_t)A_{H_{duct}}. \quad (65)$$

Experimental values in Fig. 13 have been taken from [7,60,113] in the case of the Chalmers 12 MW_{th} CFB unit, and from [68] for the other two units. Concerning the empty symbols in Fig. 13, the values predicted by the model tend to be somewhat lower than the corresponding flow values calculated by

integration of experimental data on solids flux. This should be due to the fact that the measured values do not include measurements in the corners of the cross section, which was shown to exhibit strong downflowing flux values [7], i.e. the so-called “corner effect” is not taken into account in the experimental values, leading to an overestimation of the experimental solids flow. This is seen when the corner effect is taken into account, as in the filled symbols plotted in the same figure. The arrows show

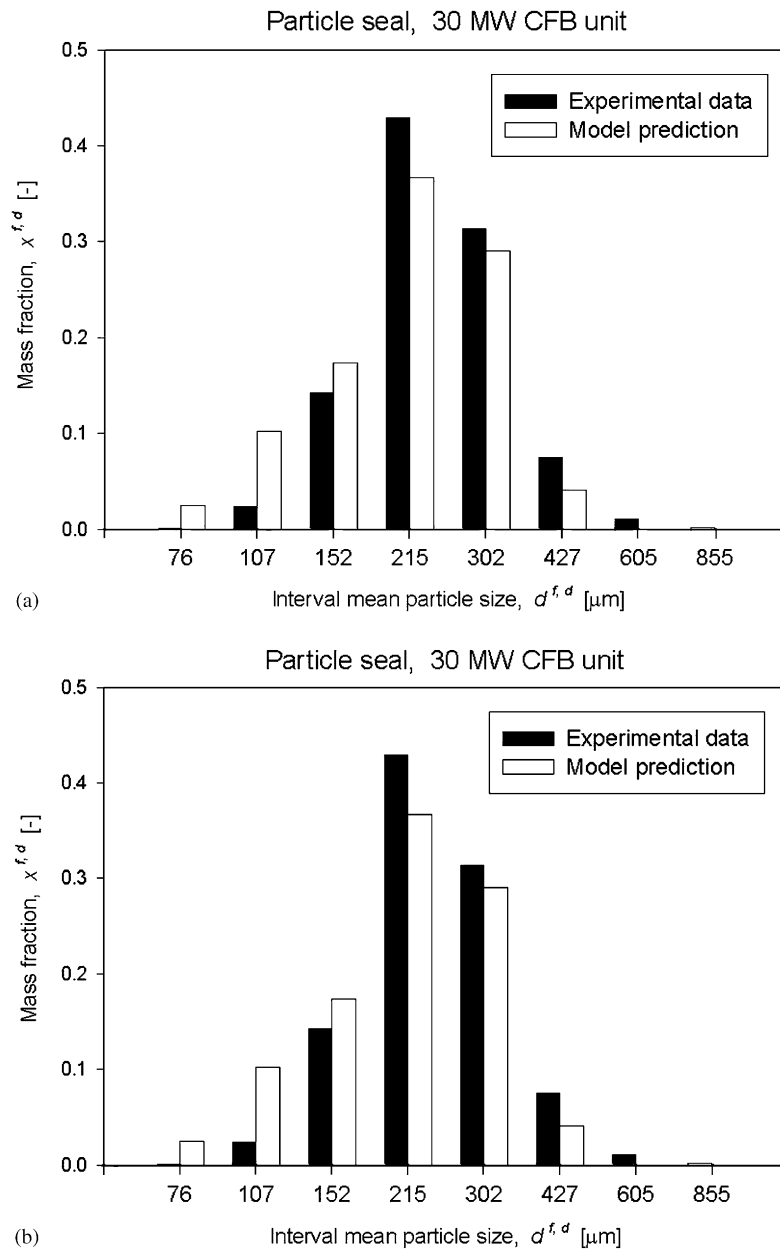


Fig. 14. (a and b) Size segregation. Measured data from a 30 MW_{th} CFB unit (unpublished) compared to results from model calculations.

that such inclusion improves the agreement of the overall CFB model and experimental data.

Concerning the solids PSD, a good agreement between model results and measured PSD in the bottom bed of the riser and in the bubbling bed of the particle seal is shown in Fig. 14 (a and b, respectively). The measured values are from a 30 MW_{th} CFB boiler. Having the PSD of the inert solids in the CFB unit as input (with an average size of 238 µm in this case), the measured average particle size in the bottom bed is 308 µm and this is estimated by the model to 273 µm (11% error). In the dense bed of the particle seal, the measured value is 226 µm while the model estimates an average particle size of 193 µm (16% error). Considering the likely scatter in the data this should be regarded as a satisfactory result.

Finally, the predicted pressure distribution around the CFB loop for a run representing the Chalmers CFB unit (with $u_0 = 4$ m/s, $d_s = 250$ µm and $\Delta p_0 = 7$ kPa as main input parameters) is shown in Fig. 15. As can be seen, most of the riser pressure drop takes place over the first metres of the riser (i.e. bottom bed and the splash zone). The point corresponding to the bottom bed surface is marked with an arrow in the pressure diagram (the bottom bed height, H_b , is estimated by the model to 0.27 m). The pressure drop gradient (which corre-

sponds to the average solids concentration) is much lower in the upper part of the riser (transport zone and exit zone) than in the lower part of the riser (bottom bed and splash zone). The pressure drop along the exit duct is low compared to all other pressure drops in the loop. Two parts of the downcomer can be identified in the pressure diagram: an upper part, with almost no solids and characterized by a loss of height at a constant pressure value, and a lower part, occupied by the fluidized solids column which maintains the pressure balance along the circulating loop (see Section 2.6.1). Finally, the pressure loop is closed by the return leg recirculating the particles back into the riser.

4. Closure

This paper highlights the major features to take into account in semi-empirical modeling of macroscopic fluid dynamics in a large CFB unit. The CFB unit is divided into six zones, and models appropriate for the modeling of each zone are described and discussed. Special emphasis has been made in pointing out to the reader the differences in the flow pattern between large CFB units directed towards combustion or gasification applications (which are the scope of the present work) and narrow CFB

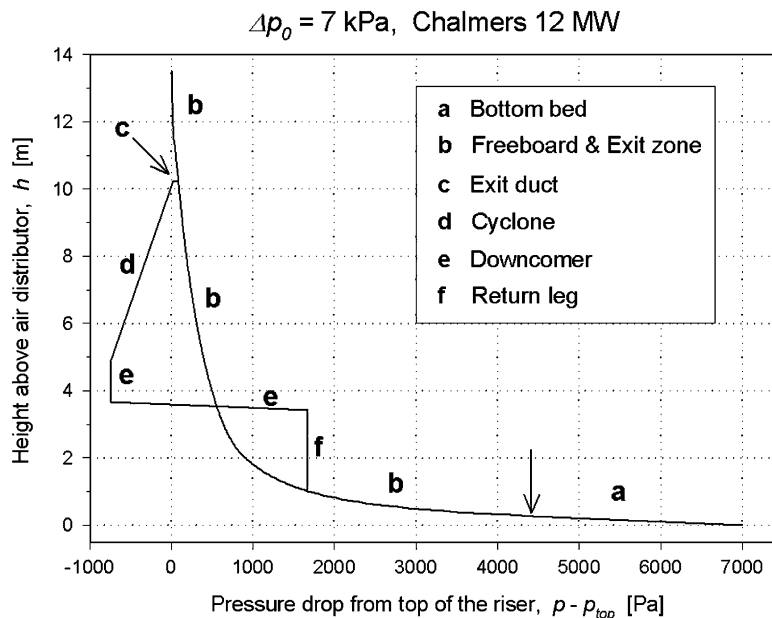


Fig. 15. Pressure diagram predicted by the overall CFB model for a standard run in the Chalmers CFB boiler (a—bottom bed, b—freeboard and exit zone, c—exit duct, d—cyclone, e—downcomer, f—return leg). The arrow indicates the location of the bottom bed surface.

units used in many of the investigations given in literature. Literature for the latter is abundant but hardly useful for modeling purposes for large CFB units, for which, on the other hand, literature is more limited.

The paper shows that integration of the local models into an overall CFB model for the entire CFB loop is possible, but requires that the population balance of the solids is taken into account in order for each model to have a sound link to the underlying physics of the fluid dynamics. The overall model given here is shown to exhibit good agreement with experimental data and give reasonable calculation times (in the order of a few minutes). Aspects known by experience to be key features in the establishment of an overall CFB model are: a set of inputs consisting only of parameters that are known and independently adjustable under operation, a discretized approach of the model in the riser (both in the vertical and horizontal directions) and consideration of the size segregation effect by including the entire circulating loop in the modeling.

Acknowledgements

The work presented is a continuation of a work originally funded by the EU Non Nuclear Energy Programme JOULE III (JOR3CT980306). Current funding from the Swedish Energy Agency is greatly appreciated.

References

- [1] Werther J. Fluid Mechanics of large-scale CFB units. *Circul Fluid Bed Technol* 1993;IV:1–14.
- [2] Anthony EJ. Fluidized bed combustion of alternative solid fuels; status, successes and problems of the technology. *Prog Energy Combust Sci* 1995;21:239–68.
- [3] Leckner B. Fluidized bed combustion: mixing and pollutant limitation. *Prog Energy Combust Sci* 1998;24(1):31–61.
- [4] Longwell JP, Rubint ES, Wilson J. Coal: energy for the future. *Prog Energy Combust Sci* 1995;21:269–360.
- [5] Issangya AS, Grace JR, Bai D, Zhu J. Further measurements of flow dynamics in a high-density circulating fluidized bed riser. *Powder Technol* 2000;111(1–2):104–13.
- [6] Johnsson F, Zhang W, Leckner B. Characteristics of the formation of particle wall layers in CFB boilers. *Proceedings of the second international conference on multiphase flow*, 1995. p. 25–32.
- [7] Zhang W, Johnsson F, Leckner B. Fluid-dynamic boundary layers in CFB boilers. *Chem Eng Sci* 1995;50(2):201–10.
- [8] Le Guevel T, Thomas P. Fuel flexibility and petroleum coke combustion at Provence 250 MW CFB. *Proceedings of the international conference on fluidized bed combustion* 2003:643–9.
- [9] Jaud P, Piedfer O, Jacquet L, Jestin L. Provence 250 MWe unit: the largest CFB boiler ready for operation. *Proceedings of the 13th international conference on fluidized bed combustion* 1995:721–8.
- [10] Goidich SJ, Hyppänen J. Foster wheeler compact cfb boilers for utility scale. In: *Proceedings of the 16th International conference on fluidized bed combustion*. Reno, NV; 2001.
- [11] Greil C, Vierrath H. Fuel gas from biomass—utilisation concepts. *DGMK-Fachbereichstagung*; 2000.
- [12] Fitzgerald TJ. Cold modeling of fluidized bed combustors. Report EPRI CS-1476, RP315-1; 1980.
- [13] Svensson A, Johnsson F, Leckner B. Fluid-dynamics of the bottom bed of circulating fluidized bed boilers. *Proceedings of the 12th international conference on fluidized bed combustion* 1993:887–97.
- [14] Rhodes MJ. Modelling the flow structure of upward-flowing gas–solids suspensions. *Powder Technol* 1990;60(1):27–38.
- [15] Zhang Y-F, Arastoopour H. Dilute fluidized cracking catalyst particles—gas flow behavior in the riser of a circulating fluidized bed. *Powder Technol* 1995;84(3):221–9.
- [16] Kim SW, Kirbas G, Bi H, Lim CJ, Grace JR. Flow behavior and regime transition in a high-density circulating fluidized bed riser. *Chem Eng Sci* 2004;59(18):3955–63.
- [17] Johnsson F, Andersson S, Leckner B. Expansion of a freely bubbling fluidized bed. *Powder Technol* 1991;68(2):117–23.
- [18] Zijerveld RC, Johnsson F, Marzocchella A, Schouten JC, van den Bleek CM. Fluidization regimes and transitions from fixed bed to dilute transport flow. *Powder Technol* 1998;95(3):185–204.
- [19] Geldart D. Types of gas fluidization. *Powder Technol* 1973;7(5):285–92.
- [20] Grace JR. High-velocity fluidized bed reactors. *Chem Eng Sci* 1990;45(8):1953–66.
- [21] Svensson A, Johnsson F, Leckner B. Fluidization regimes in non-slugging fluidized beds: the influence of pressure drop across the air distributor. *Powder Technol* 1996;86(3):299–312.
- [22] Avidan AA, Yerushalmi J. Bed expansion in high velocity fluidization. *Powder Technol* 1982;32(2):223–32.
- [23] Bi H, Fan L-S. Existence of turbulent regime in gas–solid fluidization. *AIChE J* 1992:297–301.
- [24] Glicksman LR. Scaling relationships for fluidized beds. *Chem Eng Sci* 1984;39(9):1373–9.
- [25] Wen CY, Yu YH. A generalized method for predicting the minimum fluidization velocity. *AIChE J* 1966;12:610–2.
- [26] Grace JR. Contacting modes and behaviour classification of gas–solid and other two-phase suspensions. *Can J Chem Eng* 1986;64:353–63.
- [27] Ergun S. Fluid flow through packed columns. *Chem Eng Progr* 1952;48:89–94.
- [28] Kunii D, Levenspiel O. *Fluidization engineering*, 2nd ed. Amsterdam: Elsevier; 1991.
- [29] Gogolek PEG, Grace JR. Fundamental hydrodynamics related to pressurized fluidized bed combustion. *Prog Energy Combust Sci* 1995;21(5):419–51.

- [30] Abrahamsen AR, Geldart D. Behaviour of gas-fluidized beds of fine powders part II: voidage of the dense phase in bubbling beds. *Powder Technol* 1980;26(1):47–55.
- [31] Darton RC, LaNauze RD, Davidson JF, Harrison D. Bubble-growth due to coalescence in fluidized beds. *Trans Inst Chem Eng* 1977;55(4):274–80.
- [32] Clift R, Grace JR. Continuous bubbling and slugging. *Fluidization* 1985:73–132.
- [33] Davidson JF, Harrison D. *Fluidised particles*. Cambridge; 1973.
- [34] Rowe PN, Yacono CXR. Bubbling behaviour of fine powders when fluidized. *Chem Eng Sci* 1976;31(12):1179–92.
- [35] Yacono C, Rowe PN, Angelino H. Analysis of the distribution of flow between phases in a gas fluidised bed. *Chem Eng Sci* 1979;34(6):789–800.
- [36] Shen L, Johnsson F, Leckner B. Digital image analysis of hydrodynamics two-dimensional bubbling fluidized beds. *Chem Eng Sci* 2004;59(13):2607–17.
- [37] Hepbasli A. Estimation of bed expansions in a freely-bubbling three-dimensional gas-fluidized bed. *Int J Energy Res* 1998;22(15):1365–80.
- [38] Kobayashi N, Yamazaki R, Mori S. A study on the behavior of bubbles and solids in bubbling fluidized beds. *Powder Technol* 2000;113(3):327–44.
- [39] Svensson A, Johnsson F, Leckner B. Bottom bed regimes in a circulating fluidized bed boiler. *Int J Multiphase Flow* 1996;22(6):1187–204.
- [40] Johnsson F, Stérneus J, Leckner B, Wiesendorf V, Hartge EU, Werther J, et al. Fluid Dynamics of the bottom zone of CFB combustors. Sixth international conference on circulating fluidized beds. Würzburg; 1999. p. 191–8.
- [41] Johnsson F, Zijerveld RC, Leckner B. Air-plenum pressure fluctuations in a circulating fluidized bed boiler. *Proceedings of the second European conference on CFB* 1997: 223–30.
- [42] Johnsson F, Larsson GBL. Pressure and flow fluctuations in a fluidized bed—interaction with the air feed system. *Chem Eng Sci* 2002;57:1379–486.
- [43] Sasic S, Leckner B, Johnsson F. Dynamics of gas-solid fluidized beds—inclusion of the air supply system. In: *Proceedings of the 11th International conference on fluidization*. Ischia, Naples, Italy; 2004. p. 467–74.
- [44] Sasic S, Johnsson F, Leckner B. Fluctuations and waves in fluidized bed systems: the influence of the air-supply system. *Powder Technol* 2005;153(3):176–95.
- [45] Wu SY, Baeyens J. Segregation by size difference in gas fluidized beds. *Powder Technol* 1998;98(2):139–50.
- [46] Toomey RD, Johnstone HF. Gaseous fluidization of solid particles. *Chem Eng Prog* 1952;48(5):220–6.
- [47] Grace JR, Clift R. On the two-phase theory of fluidization. *Chem Eng Sci* 1974;141(70):53–62.
- [48] Werther J. Influence of the bed diameter on the hydrodynamics of gas fluidized beds. *Fluidiz Fluid-particle Syst* 1974;70(141):53–62.
- [49] Olowson PA, Almstedt AE. Influence of pressure and fluidization velocity on the bubble behaviour and gas flow distribution in a fluidized bed. *Chem Eng Sci* 1990;45(7):1733–41.
- [50] Sit SP, Grace JR. Effect of bubble interaction on interphase mass transfer in gas fluidized beds. *Chem Eng Sci* 1981;36(2):327–35.
- [51] Werther J, Wein J. Expansion of gas fluidized beds in the turbulent regime. *AIChE Symp Ser* 1994;90:31–44.
- [52] Zijerveld RC, Koniuta A, Johnsson F, Marzocchella A. Axial solids distribution and bottom bed dynamics for CFBC application. *AIChE Symp Ser* 1997;93:97–102.
- [53] Pallarès DJ, Johnsson F. Fluiddynamic modeling of large CFB units. In: *Proceedings of the seventh international conference on circulating fluidized beds (CFB7)*. Niagara Falls, Ont., Canada; 2002. p. 387–94.
- [54] Gogolek PEG. *Mathematical modelling of fluctuations in fluidized bed combustion*. Kingston, Ont., Canada: Queen's University; 1998.
- [55] Couderc J-P. Incipient fluidization and particulate systems. *Fluidization* 1985:1–46.
- [56] Harris BJ, Davidson JF, Xue Y. Axial and radial variation of flow in circulating fluidized bed risers. *Proceedings of the fourth international conference on circulating fluidized beds* 1993:103–7.
- [57] Johnsson F, Leckner B. Vertical distribution of solids in a CFB-furnace. *Proceedings of the 13th international conference on fluidized bed combustion* 1995:671–9.
- [58] Johnsson F, Vrajer A, Tiikma T, Leckner B. Solids flow pattern in the exit region of a CFB-furnace. Influence of geometry. In: *Proceedings of the 15th international conference on fluidized bed combustion*. Savannah, USA; 1999.
- [59] Johnsson F, Zhang W, Johnsson W, Leckner B. Optical and momentum probe measurements in a CFB furnace. *Circul Fluidiz Bed Technol* 1997:652–7.
- [60] Leckner B, Golriz MR, Zhang W, Andersson BA, Johnsson F. Boundary layers—first measurements in the 12 MW CFB research plant at Chalmers University. *Proceedings of the 11th international conference on fluidized bed combustion* 1991:771–6.
- [61] van der Meer EH, Thorpe RB, Davidson JF. The influence of exit geometry for a CFB with a square sectional riser. *Proceedings of the 5th international conference on CFB* 1996:575–80.
- [62] Haider A, Levenspiel O. Drag coefficient and terminal velocity of spherical and nonspherical particles. *Powder Technol* 1989;58(1):63–70.
- [63] Geldart D. Estimation of basic particle properties for use in fluid-particle process calculations. *Powder Technol* 1990;60(1):1–13.
- [64] Arsenijevic ZL, Grbavcic ZB, Garic-Grulovic RV, Zdanski FK. Determination of non-spherical particle terminal velocity using particulate expansion data. *Powder Technol* 1999;103(3):265–73.
- [65] Gibilaro LG, Di Felice R, Waldram SP, Foscolo PU. Generalized friction factor and drag coefficient correlations for fluid-particle interactions. *Chem Eng Sci* 1985;40(10):1817–23.
- [66] Win K, Nowak W, Matsuda H, Hasatani M, Bis Z, Krzywanski J, et al. Transport velocity of coarse particles in multi-solid fluidized bed. *J Chem Eng Japan* 1995;28(5):535.
- [67] Palchonok GI, Breitholtz C, Thunman H, Leckner B. Impact of heat and mass transfer on combustion of a fuel particle in CFB boilers. *Proceedings of the 14th international conference on FBC* 1997:871–88.
- [68] Werdermann CC. Feststoffbewegung und Wärmeübergang in zirkulierenden Wirbelschichten von Kohlekraftwerken; 1992.

- [69] Johnsson A. PhD. thesis, Chalmers University of Technology, Göteborg, Sweden, 2005.
- [70] Johansson A, Johnsson F, Leckner B, Gadowski J. Solids back-mixing in CFB furnaces. In: Proceedings of the eighth international conference on circulating fluidized beds. China; 2005.
- [71] Stérneus J, Johnsson F. Gas mixing in the wall layer of a CFB boiler. In: Proceedings of the 14th international conference on fluidized bed combustion. Vancouver; 1997. p. 1237–46.
- [72] Zhang W, Johnsson F, Leckner B. Momentum probe and sampling probe for measurement of particle flow properties in CFB boilers. *Chem Eng Sci* 1997;52(4):497–509.
- [73] Koksai M, Hamdullahpur F. Gas mixing in circulating fluidized beds with secondary air injection. *Chem Eng Res Design* 2004;82(8):979–92.
- [74] Savolainen K, Karvinen R. Experimental and numerical studies of particle–turbulence interaction and jet penetration in gas–particle flow. *Adv Fluid Mech* 2001;29: 87–96.
- [75] Karlsson T, Svensson F. Penetration of air injection in the riser of a fluidized bed. Göteborg: Chalmers University of Technology; 1999.
- [76] Lücke K. On the influence of mixing on the performance of large-scale atmospheric circulating fluidized bed combustors. Technical University of Hamburg-Harburg; 2003.
- [77] Hannes JP. Mathematical modelling of circulating fluidized bed combustion. Aachen, Germany: City-Print Verlag GmbH; 1996.
- [78] Lei H. Hydrodynamic modelling of circulating fluidized bed reactors. PhD. thesis, Tokyo University of Agriculture and Technology Koganei, Tokyo, Japan, 1998.
- [79] Lewis WK, Gilliland ER, Lang PM. Entrainment from fluidized beds. *Chem Eng Prog Symp Ser* 1962;58:65–78.
- [80] Kunii D, Levenspiel O. Entrainment and elutriation from fluidized beds. *J Chem Eng Japan* 1969;2:84–8.
- [81] Kunii D, Levenspiel O. Entrainment of solids from fluidized beds. *Powder Technol* 1990;61(2):193–206.
- [82] Adanez J, Gayan P, Garcia-Labiano F, de Diego LF. Axial voidage profiles in fast fluidized beds. *Powder Technol* 1994;81(3):259–68.
- [83] de Diego LF, Gayan P, Adanez J. Modelling of the flow structure in circulating fluidized beds. *Powder Technol* 1995;85(1):19–27.
- [84] Lei H, Horio M. A comprehensive pressure balance model of circulating fluidized beds. *J Chem Eng Japan* 1998;31(1): 83–94.
- [85] Walsh PM, Mayo JE, Beer JM. Refluxing particles in the freeboard of a fluidized bed. *AIChE Symp Ser* 1984;119–28.
- [86] Teplitskiy YS, Ryabov GA. Scaling in a circulating fluidized bed: particle concentration and heat transfer coefficient in a transport zone. *Int J Heat Mass Transfer* 1999;42(21):4065–75.
- [87] Weinell CE, Dam-Johansen K, Johnsson JE. Single-particle behaviour in circulating fluidized beds. *Powder Technol* 1997;92(3):241–52.
- [88] Wein JW. Das Expansionsverhalten von Gas/feststoff-wirbelschichten bei höheren Gasgeschwindigkeiten. Harburg, Germany: Technical University of Hamburg; 1992.
- [89] Hiller R. Mathematische Modellierung der Kohleverbrennung in einer Circofluid-wirbelschichtfeuerungen. Dortmund, Germany: Dortmund University; 1995.
- [90] Horio M, Morishita K, Tachibana O, Murata N. Solid distribution and movement in circulating fluidized beds. In: P.a.L. Basu JF, editor. *Circulating fluidized beds technology II*. New York, USA: Pergamon Press; 1988. p. 147–53.
- [91] Horio M, Ishii H, Nishimura M. On the nature of turbulent and fast fluidized beds. *J Chem Eng Japan* 1992;30:691–7.
- [92] Andersson BÅ. Heat transfer in the Örebro circulating fluidized bed boiler Internal report I. 91–28, Chalmers University of Technology, Department of Energy conversion; 1991.
- [93] Davidson JF. Circulating fluidised bed hydrodynamics. *Powder Technol* 2000;113(3):249–60.
- [94] Peirano E, Begis J, Johnsson F, Leckner B. Gas-solid flow computations applied to circulating fluidized beds. Göteborg, Sweden: Chalmers University of Technology; 1998.
- [95] Lacknermeier U, Werther J. Flow phenomena in the exit zone of a circulating fluidized bed. *Chem Eng Process* 2002;41(9):771–83.
- [96] Zheng Q-Y, Zhang H. Effect of geometry of bed exit (end effect) on hydrodynamic behaviour of gas–solid flow in CFB combustor. *Fluidization VIII*. C. L. E. J.-F. Large. New York, Foundation; 1995. p. 453.
- [97] Brereton CM, Grace JR. End effects in CFB hydrodynamics. *Circulat Fluidiz Bed Technol* 1993;4:137–44.
- [98] Sanderson WE. The separation effect on the CFBC's riser exit. DUP science. TU-Delft. Delft, The Netherlands: Delft University Press; 1994.
- [99] Åmand LE, Lyngfelt A, Karlsson M, Leckner B. The reference case for coal at the 12 MW CFB-boiler at Chalmers. Characterisation of the gas and particle phases in the combustion chamber. Report A97-221. Internal report A97-221; 1995.
- [100] Harris AT, Davidson JF, Thorpe RB. Influence of exit geometry in circulating fluidized-bed risers. *AIChE J* 2003; 49(1):52–64.
- [101] Stoess HA. *Pneumatic conveying*. New York: Wiley Interscience; 1983.
- [102] Thomas D. Transport characteristics of suspensions. *AIChE J* 1961;7(3):423–30.
- [103] Jones PJ, Leung LS. A comparison of correlations for saltation velocity in horizontal pneumatic conveying. *Ind Eng Chem Process* 1978;17(4):571–5.
- [104] Muschelknautz U, Muschelknautz E. Special design of inserts and short entrance ducts to recirculating cyclones. Proceedings of the fourth international conference on circulating fluidized beds 1991:597–602.
- [105] Muschelknautz E. Fundamentals and practical aspects of cyclones. Proceedings of the fifth international conference on circulating fluidized beds 1994:20–7.
- [106] Krambrock W. Modellierung der zeitabhängigen Entgasung von Kohlepartikeln in der zirkulierenden Wirbelschicht. Aachen, Germany: The Aachen University of Technology; 1971.
- [107] Rhodes MJ, Geldart D. A model for the circulating fluidized bed. *Powder Technol* 1987;53(3):155–62.
- [108] Yang WC. A model for the dynamics of a CFB loop. Proceedings of the second international conference on circulating fluidized beds technology 1988:181–91.
- [109] Sundberg RE. The prediction of overall collection efficiency of air pollution control devices from fractional

- efficiency curves. *J Air Pollut Control Assoc* 1974;24(8): 758–64.
- [110] Dietz PW. Collection efficiency of cyclone separators. *AIChE J* 1981;27(6):888–92.
- [111] Avci A, Karagoz I. A mathematical model for the determination of a cyclone performance. *Int Commun Heat Mass Transfer* 2000;27(2):263–72.
- [112] Zhang R, Basu P. A simple model for prediction of solid collection efficiency of a gas-solid separator. *Powder Technol* 2004;147(1–3):86–93.
- [113] Zhang W, Johnsson F. Particle flow pattern in circulating fluidized bed boilers. Thesis for the Degree of Licenciate, Department of Energy Conversion in Engineering, Chalmers University of Technology, Göteborg, Sweden, 1992.

Errata in "Macroscopic modelling of fluid dynamics in large-scale circulating fluidized beds"

Page	Equation	Reads	Shall read
557	48	$F_{net}^{f,d} = \frac{F_{core,H_{duct}}^{f,d}}{P_{entr}^{f,d}}$	$F_{net}^{f,d} = F_{core,H_{duct}}^{f,d} \cdot p_{entr}^{f,d}$
557	49	$k^{f,d} = \frac{F_{H_{duct}}^{f,d}}{F_{net}^{f,d}}$	$k^{f,d} = \frac{F_{wall,H_{duct}}^{f,d}}{F_{net}^{f,d}}$
561	63	$\Delta p_{refeed} = \int_{H_{retleg}}^{H_{duct}} \rho_s \cdot g \cdot C_s \cdot dh$	$\Delta p_{refeed} = \int_{H_{retleg}}^{H_{duct}} g \cdot C_s \cdot dh$

Paper II

Pallarès, D., Johnsson, F. (2008)

"Modeling of fuel mixing in fluidized bed combustors"

Accepted for publication in *Chemical Engineering Science*

Modeling of fuel mixing in fluidized bed combustors

David Pallarès, Filip Johnsson*

Department of Energy and Environment, Chalmers University of Technology, SE-412 96 Göteborg (Sweden)

Abstract

This paper presents a 3-dimensional model for fuel mixing in fluidized bed combustors. The model accounts for mixing patterns which were experimentally shown to govern mixing in risers with geometry and operational conditions representative for furnaces in fluidized-bed combustors. The mixing process is modeled for three different solid phases in the furnace and the model, which includes the return leg, can be applied both under bubbling and circulating regimes. The semi-empirical basis of the model was previously validated in different large-scale fluidized bed combustors and is combined with a model for fuel particle conversion to obtain the fuel concentration field. Model results are compared with experimental data from the Chalmers 12 MW_{th} CFB combustor, yielding reasonable agreement.

Keywords: Modeling; Mixing; Fuel; Combustion; Fluidization; Fluidized bed

1. Introduction

Fuel mixing has a great influence on the overall performance of fluidized bed combustors. The better the horizontal mixing of the fuel the more homogenous is the local stoichiometric ratio over the cross section of the furnace, which in its turn lowers the risk of occurrence of locations with unreacted fuel or oxygen. In the vertical direction a high mixing rate is important in order to secure long enough contact time between the oxygen and the fuel particles. Moreover, good mixing is a prerequisite for an even distribution of heat and gas release from the fuel. Despite the importance of fuel mixing, there is at present a lack of mechanistic models describing this process and research works have so far been limited to calculate experimental values of the dispersion coefficient [1-4] which is occasionally correlated to operational parameters. Neither has there been much work done to incorporate mixing of fuel particles in CFD calculations, excepting the attempt made by Tanskanen [5] which, however, gave unrealistic results in some locations of the calculation domain. Concerning semiempirical modeling, fuel mixing was included in a comprehensive model for a CFB combustor [6-8]. Yet, the fuel mixing process is complex and there is a need to make a focused work on fuel mixing modeling where the fuel model is explicitly validated. Thus, the aim of the work presented in this paper is to provide a model for fuel mixing in fluidized bed combustors validated with experimental data representative for fluidized bed combustion obtained during runs with different fuel types. The aim is to develop a fuel mixing model which can be used in a comprehensive fluidized-bed model as well as to provide experimental basis for verification of CFD modeling.

The continuous physical changes of fuel particles (such as size and density, and thereby terminal velocity) as they undergo conversion (*i.e.* drying, devolatilization and char combustion) lead to constantly changing fuel mixing behaviours. Shortly after the injection into a fluidized bed combustor a fuel particle is likely to occupy the bottom part of the riser (furnace) due to its relatively large size and high density, while it has an increasing tendency to populate the upper freeboard or even being entrained to the return leg as it gets closer to its burn-out time (due to the smaller size and lower density). Thus, in the present work, a fuel particle conversion model is combined with a (3-dimensional) fuel mixing model in order to describe the transient fluid dynamics resulting from the constantly changing physical properties during burnout of a batch of fuel particles. As detailed below the burnout of the fuel batch is then applied in a continuous approach to simulate the effect of continuous fuel feeding.

It is important to stress the role of fragmentation on both fuel mixing and fuel conversion: With respect to fuel mixing, fuel fragmentation enhances fuel concentration at higher levels in the freeboard and the flow of externally recirculated fuel. Concerning fuel conversion, the burnout time of the fuel particles is drastically shortened by fragmentation which thereby lowers the fuel inventory in the unit. Thus, fuel fragmentation will influence modeled and measured results on in-furnace parameters such as temperatures, gas concentration and char distribution. Fuel fragmentation is a complex process which, although is not known in detail, is known to be strongly dependent on the fuel type and it has indeed been investigated in several studies, *e.g.* [9,10]. Since there is not yet any general model

* Corresponding author: filip.johnsson@me.chalmers.se . Tel.: +46 31 772 1449; Fax: +46 31 722 3592

available for any fuel type which has been verified under industrial conditions and since the focus of this work is on fuel mixing, fuel fragmentation is not modeled in this present work. Instead fuel fragmentation is taken as input to the modeling as a given fragmentation pattern. This is done in order to maintain a high degree of transparency in the modeling procedure. A sensitivity analysis on the fuel fragmentation is included.

2. Theory

2.1. Fuel mixing model

In general terms, mixing of fuel particles can be modeled on a semi-empirical basis using the same principles and equations as for the fluid dynamics of the inert (bulk) particles. Literature on macroscopical fluid dynamics of fluidized bed boilers [6-8, 11-13] have roughly the same description of the overall solids pattern in the furnace: in the bottom part a dense bottom bed is established which, by means of bubble explosions, forms a splash zone of erupted solids in the form of clusters (*cluster phase*) which follow a ballistic movement, hence governing the back-mixing of solids in this region. Under circulating conditions, a fraction of the solids (*disperse phase*) is entrained higher up in the furnace creating a core-annulus structure in the freeboard, with upflow in the core, net horizontal flow from the core to the downflowing annulus (*i.e.* most of the solids back-mixing occurs at the furnace walls). Yet, both the cluster and the disperse phase can exist all the way up through the furnace, with the cluster phase dominating in the bottom freeboard (splash zone) and the disperse phase in the upper freeboard (transport zone). Figure 1 illustrates the main solids movements in the furnace. Table 1 lists the assumptions made in this work with respect to the governing mixing mechanisms in the horizontal and vertical directions for the bottom bed and for the two phases of the freeboard (cluster and disperse phase). These fuel mixing mechanisms are further described below.

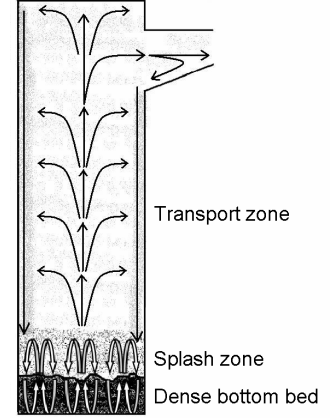


Figure 1: Zones of a CFB riser with corresponding mixing patterns

The 3-dimensional mesh used to discretize the furnace applies a finer mesh in regions known to exhibit large gradients (*e.g.* splash zone). At present, perfect mixing is assumed in the return leg and this is therefore not discretized. Note that, at present stage, the fuel mixing model does not account for interactions with the inert solids flow, *i.e.* fuel mixing is modeled independently from the bulk flow. This results in the same type of error as in

fluid dynamical models which do not take into account interactions between different size intervals of the bed material. Although there might be a general increase of the fuel hold up as a consequence of the interaction with the (mostly finer) inert phase, the extent of this effect is limited and, as will be shown, the proposed model is able to provide reasonable agreement with experimental data. However, further development of the model will include interactions between fuel and bulk particles through a particle interaction model given in [14].

	Mixing mechanism	
	Vertical	Horizontal
Bottom bed	Perfect mixing	Diffusion
Cluster phase	Ballistic	
Disperse phase	Core/annulus	

Table 1: Solids mixing mechanisms in a fluidized bed furnace applied in this work

Despite that the real mixing mechanism behind horizontal mixing in the bottom part of the riser is strongly convective, the experimentally verified existence of toroidal flow structures around each main bubble path [15,16] makes it possible to macroscopically approximate the horizontal mixing in the dense bottom bed as a diffusion process reading:

$$\frac{\partial C_{fuel}(x, y, z_0)}{\partial t} = \nabla \cdot (D_{horiz} \nabla C_{fuel}(x, y, z_0)) + S_{feed} \quad \text{for } z_0 \leq H_b \quad (1)$$

with the source term S_{feed} corresponding to the fuel feeding. This is a common method in literature (see *e.g.* [17]) with several experimental values and correlations for the horizontal diffusion coefficient D_{horiz} available (*cf.* [2]) but differing up to two orders of magnitude between investigations carried out under similar conditions. There is little experimental fuel mixing data from fluidized bed combustors with the exception of the work given in [2,18] where D_{horiz} is estimated to be about $0.1 \text{ m}^2/\text{s}$. Thus, this value is used in the simulations presented in the present work.

This work assumes perfect vertical mixing in the bottom bed. This is a reasonable assumption according to experimental works ([2] and references therein) showing that mixing in this region is at least one order of magnitude faster in the vertical than in the horizontal direction together with the fact that dense bottom beds are usually no higher than a few decimeters compared to several meters in the horizontal direction. In addition, an experimental study [15] providing simulated steady-state fuel concentrations in a 2-dimensional bed showed almost perfect vertical mixing in the dense bed for most types of tracer (fuel) particles and operational conditions, with the only exception being runs for which the fuel-to-emulsion ratio Ar_f/Ar_{em} is higher than 10^4 at low fluidization velocities (under 1.5 m/s). Under these conditions tracer particles show a tendency to float on the dense bed surface, as reported also in [19].

As indicated above, the presence of the fuel in the freeboard is divided into a cluster and a disperse phase. Thus, the total fuel concentration in the freeboard can be expressed as a sum of these phases:

$$C_{fuel} \Big|_{z>H_b} = C_{fuel}^{clust} + C_{fuel}^{disp} \quad (2)$$

The cluster phase consists mainly of non-entrainable particles which are ejected into the freeboard from the bed which then fall back into the dense bed. Thus, this phase corresponds to a vertical mixing phenomenon governed by a ballistic movement, which leads to an exponential decay in vertical concentration of the fuel particles, *i.e.*,

$$C_{fuel}^{clust}(x_o, y_o, z) \Big|_{z>H_b} = C_{fuel}^{clust}(x_o, y_o, H_b) \cdot e^{-a(z-H_b)} \quad (3)$$

Several experimental correlations for the decay constant a have been proposed in literature for fluidized bed combustors operated under bubbling as well as circulating conditions [20-22], most of them adopting the form:

$$a = c \cdot \frac{u_t}{u_g} \quad (4)$$

Based on data from pressure measurements in several large-scale units, the coefficient c was correlated in [23] to a value around 4 m^{-1} (although this value was later found by the authors to slightly increase as the bottom bed height decreases and hosts less vigorous bubbles). Note that (as for the disperse phase decay constant, K , see below) coefficients are obtained from pressure measurements, *i.e.* they represent the sum of all in-bed solids (including inert phase). Under the assumption indicated above (*i.e.* neglecting interaction between phases), these empirical coefficients can be applied also to the fuel phase.

The continuous separation of disperse-phase solids to the furnace walls gives the above-mentioned core-annulus flow structure (*cf.* [24,25]). The thickness of the wall layers defining the border between the core and annulus regions has been studied in several in several works, with the most exhaustive compilation of experimental data given in [26] and correlations from different authors compared in [12].

Modeling the back-flow in terms of a falling film approach (which is widely accepted) where the disperse phase in the core region flows at the slip velocity yields an exponential decay in solids concentration with height in the upflowing core region (see [27] for details), *i.e.*

$$C_{fuel}^{disp}(x_o, y_o, z) \Big|_{z>H_b} = C_{fuel}^{disp}(x_o, y_o, H_b) \cdot e^{-K(z-H_b)} \quad (5)$$

with (x_o, y_o) in the core region and the decay constant, K , taking the form:

$$K = \frac{4 \cdot k}{D_{eq} \cdot (u_g - u_t)} \quad (6)$$

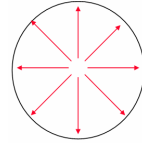
In a study [23] gathering data from four different CFB boilers the mass transfer coefficient, k , in Eq. (6) is found to depend linearly on D_{eq} , which leads to the following correlation for the decay constant, K , in Eq. (5):

$$K = \frac{0.23}{u_g - u_t} \quad (7)$$

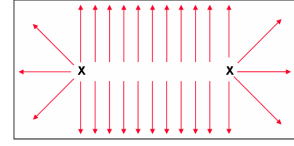
The decreasing fuel upflow with height is due to the net lateral flow from core to wall region, *i.e.* fuel back mixing is assumed to mainly occur at the furnace walls. Thus, in a core cell i with a given height dz , the net differential fuel flow leaving the core cell upflow and joining the wall-layer downflow can be expressed as:

$$F_{lat,i} = -dF_{core,i} = -A_i \cdot (u_g - u_{t,fuel}) \cdot dC_{fuel,i}^{disp} = A_i \cdot (u_g - u_{t,fuel}) \cdot K \cdot e^{-K(z-H_b)} \cdot dz \quad (8)$$

In net terms, this lateral flow at each cross section of the riser freeboard is assumed to follow the patterns illustrated in Fig. 2, for circular and rectangular cross-sectional geometries. The core-to-annulus fuel flow feeds the downflow in the wall region with fuel particles all along the riser. When reaching the bottom bed, this downflow which joins the horizontal diffusive mixing process described above is embodied within the source term S_{feed} in Eq. (1).



a) Circular cross section



b) Rectangular cross section

Figure 2: Horizontal core to wall net solids transfer in the freeboard

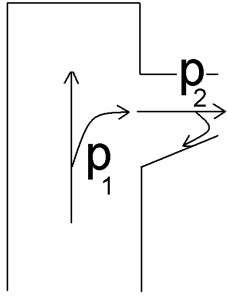


Figure 3: Mechanisms in the backflow effect

Finally, some of the upflowing particles in the core region which reach the height of the exit duct experience a backflow effect, through which only a certain fraction of these particles reaches the cyclone. A proper modeling of this effect requires the use of CFD tools, but experimental correlations for estimating the backflow in standard exit configurations is given in [12,24,25,28]. From any of these correlations, an entrainment probability p can be estimated. Since the correlations were found in CFB combustors with a single exit duct an assumption has to be made in order to handle a more general case where n exit ducts exist, which is represented by Eq.(9.a). Moreover, the backflow effect can be assumed to take place in two steps in series: firstly, some of the upflowing particles in the core follow the gas flow and leave the core upflow towards the exit duct whereas the other part are separated to the walls-layers and secondly, once in the exit duct, some particles follow the gas stream all the way into the cyclone while the rest fall back down into the riser and join the downflow in the wall-layers. These two steps can be expressed as probabilities p_1 and p_2 , as illustrated in Fig. 3. Thus, with the single-exit entrainment probability p given by experimental correlations and knowing that $p^* = p_1 \cdot p_2$, the assumption $p_1 = p_2$, leads to the values of p_1 and p_2 given by Eq. (9.b):

$$p^* = 1 - (1 - p)^n \quad (9.a) \quad \text{with} \quad p_1 = p_2 = \sqrt{p^*} \quad (9.b)$$

As far as the externally recirculated fuel particles are concerned, their residence time in the return leg is calculated as the sum of the residence times in the cyclone, downcomer and particle seal. The residence time of fuel particles in the cyclone can be calculated according to [29]. The fuel residence time in the downcomer and particle seal is easily calculated with the assumption that it equals the residence time of the bulk solids in the return leg according to Eq. (10).

$$\tau_{downcomer \& seal} = \frac{V_{fluidized \text{ in return leg}} \cdot \rho_s \cdot \left(1 - \varepsilon_{return \text{ leg}}\right)}{F_{net,s}} \quad (10)$$

In the present work, the net solids circulating flow required in Eq. (10) has been modeled according to [12]. There are also experimental methods to estimate this value in industrial CFB combustors as listed in [30]. Finally, after flowing through the return leg, fuel particles (if not burned out) are refed into the bottom part of the riser. This is implemented through the source term S_{feed} in Eq. (1).

2.2. Fuel conversion model

In the present work, the fuel conversion model presented in [31] is chosen for modeling the drying and devolatilization processes since this model yields low calculation times and yet is shown to give satisfactory agreement with experimental data. Assuming quasi-steady state, this 1-dimensional fuel conversion model provides an analytical transient solution to the formulation of the energy equation in a fuel particle whose geometry is approximated through a plate, cylinder or sphere ($r=0, 1$ or 2 respectively in Eq. (11)). Thus, defining a dimensionless spatial coordinate, ξ , and temperature, θ , the energy equation for the quasi-steady state reads:

$$\frac{1}{\xi^r} \frac{\partial}{\partial \xi} \left(\xi^r \frac{\partial \theta}{\partial \xi} \right) + \alpha \beta \frac{1}{\xi^r} \frac{\partial \theta}{\partial \xi} = 0 \quad (11)$$

where α and β are constants expressing the magnitude of the convective term (see [31] for details). While the first term represents the heat diffusion from the surroundings into the fuel particle, the convective term describes the heating up of the moisture and volatiles as they flow towards the surface of the fuel particle. When applying Eq. (11) the following boundary conditions (for simplicity not expressed here in dimensionless terms) are imposed:

$$T|_{r=drying\ front} = 100\ ^\circ\text{C} \quad (12)$$

$$-\lambda_{part} \frac{\partial T}{\partial r} \Big|_{r=r_{part}} = h_{eff} \cdot (T|_{r=r_{part}} - T_\infty) \quad (13)$$

where h_{eff} accounts for both convective and radiative heat transfer between the particle and its surrounding. Expressions for the analytical solution of Eq. (11) with the above boundary conditions are listed in [31]. Differentiation of the solution obtained provides temperature gradients which are used to calculate heat fluxes at the drying front and particle surface, providing (once a time step is defined) the displacement of the drying front and the new surface temperature (through Eq. (13)). Thus, this gives an updated set of boundary conditions for solving the next time step.

From the dynamical evolution of the temperature field inside the fuel particle obtained after solving Eq. (11), all of the drying, devolatilization and char combustion rates can be calculated. According to the approach described in [32], the effective char combustion rate, R_{eff} , is modeled through a combination of two processes which, respectively, are governed by the kinetic rate, R_{kin} (determined through an Arrhenius-type correlation) and the mass transfer coefficient, h_m (determined through a Sherwood-type correlation) yielding:

$$R_{eff} = \frac{1}{\frac{1}{R_{kin}} + \frac{1}{h_m}} \quad (14)$$

which is to be used in the general expression for coal combustion (first order reaction is assumed) reading:

$$\frac{d m_C}{dt} = -\Omega \cdot R_{eff} \cdot A_{part} \cdot C_{O_2, \infty} \quad (15)$$

With this, the dynamical mass loss of the fuel particle studied can be obtained (the modeled mass loss for a 10 mm i.d. brown coal particle is exemplified in Fig. 4). Neglecting particle shrinking and thus assuming no changes in particle size due to drying and devolatilization, the progress of the fuel particle size and density during combustion can be calculated and, from these, the terminal velocity is obtained (as shown in normalized values in Fig. 5). As explained below, the progress of the fuel particle terminal velocity shown in Fig. 5 enables the mixing model given in the previous section to account for the continuous change in the fluid-dynamical properties of the fuel particle. Depending on the fuel type, fuel fragmentation might play a major role in the conversion kinetics and thereby significantly influence the final results and should be taken into account by the fuel conversion model (the assumed fragmentation patterns applied in this work are given below).

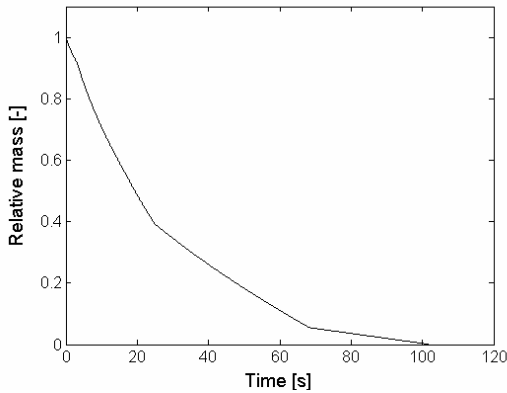


Figure 4: Evolution of the relative mass of a fuel particle

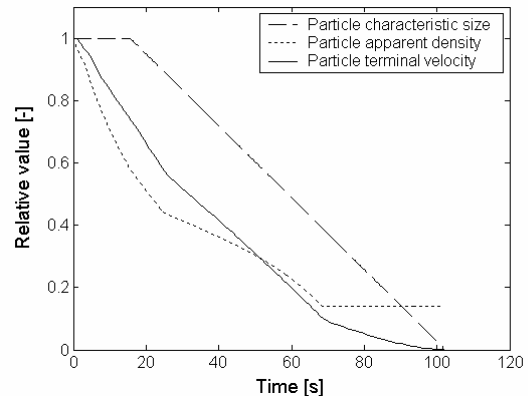


Figure 5: Evolution of the relative size, density and terminal velocity of a fuel particle

2.3. Method for a steady-state solution

Obviously, modeling the behavior of a batch of fuel particles requires a transient simulation during the whole burnout time. An efficient way to proceed for the case of fuel particles in fluidized bed combustion consists in modeling the mixing of a batch of fuel particles during its burn-out time. Applying the above-described model for fuel mixing, the fuel distribution (expressed in [particles/m³]) at each time step can be calculated using the corresponding value of the terminal velocity calculated from the fuel particle conversion model. Applying then the pertinent value for the fuel particle mass, the concentration field can be converted to [kg/m³]. Thus, the spatial distribution of the fuel concentration C originated by the fuel batch at any time step t_i is known (given in the first row in Fig. 6). Having this, a continuous feeding of fuel into a combustor can be simulated by a ‘continuous batch’ approach, in which a new batch is fed to the unit at each time step. This procedure is illustrated in Fig. 6 and leads to a resulting total fuel concentration in each time step equal to the sum of the values in the corresponding column. Thus, a stationary concentration field is obtained after a time interval equal to the burnout time of the fuel particles, and this value is equal to the sum of all intermediate values in each time step.

	$t=t_0$	$t=t_1$	$t=t_2$	$t=t_3$...	$t=t_{\text{burnout}}$	$t>t_{\text{burnout}}$
Batch #1	$C_0(x,y,z)$	$C_1(x,y,z)$	$C_2(x,y,z)$	$C_3(x,y,z)$...	$C_{\text{burnout}}(x,y,z)$	0
Batch #2		$C_0(x,y,z)$	$C_1(x,y,z)$	$C_2(x,y,z)$	$C_3(x,y,z)$...	$C_{\text{burnout}}(x,y,z)$
Batch #3			$C_0(x,y,z)$	$C_1(x,y,z)$	$C_2(x,y,z)$	$C_3(x,y,z)$...
Batch #4				$C_0(x,y,z)$	$C_1(x,y,z)$	$C_2(x,y,z)$	$C_3(x,y,z)$
...					$C_0(x,y,z)$	$C_1(x,y,z)$	$C_2(x,y,z)$
...						$C_0(x,y,z)$	$C_1(x,y,z)$
...							$C_0(x,y,z)$

Figure 6: The scheme applied to calculate the steady state distribution of fuel concentration

It must be noted that the use of this approach is only suitable to problems where the influence of a certain batch on the previous batches can be neglected, which is considered reasonable for fuel in fluidized bed combustors (where it typically represents only between 1 and 5% of the total amount of solids in the combustor).

3. Experiments

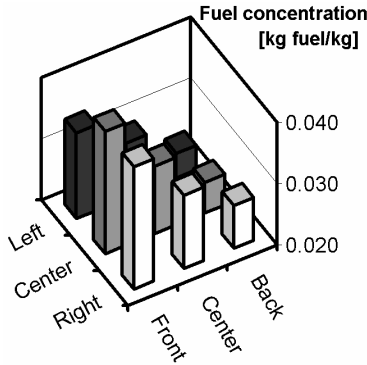
The experimental data used for model validation in this work is taken from the Chalmers 12 MW_{th} CFB combustor. The size of the combustion chamber is 1.7×1.7×13.5 m with two of the walls covered with refractory lining (0.11 m thick) up to 2 m above the air distributor and the other two covered all along their height. The fuel is fed by gravity from the fuel chute at a height of 1.1 m above the air distributor (see [33] for a detailed description of the unit). The mean size of the inert bed material is 320 μm and the average height of the dense bottom bed during the tests was estimated (from pressure drop) to be about 0.5 m. The present work contains experimental data from runs with four different fuel types: two Polish bituminous coals, wood chips and peat (fuel analysis for these fuels are given in Table 2). Operational conditions were kept as similar as possible for all runs: a fluidization gas velocity of 3.7 m/s, secondary air injection at a rate of 1.3 kg/s through 13 ports located in the rear and front walls at a height of 2.1 m above the gas distributor and a heat flow supplied with fuel of 9.4 MW_{th}. This corresponds to an air ratio of about 1.2, with a measured oxygen concentration on wet flue gases of approximately 3.3%. The temperature in the bottom of the furnace was kept at 850°C. Part of the data sampled during these runs (including part of the experimental data used in this work) has been previously published in other studies (see [34-36]).

		Coal	Peat	Wood
Proximate (%)	Moisture	14.80	25.00	43.10
	Volatiles	31.36	49.97	46.10
	Char	47.24	22.03	10.40
	Ash	6.60	3.00	0.40
Ultimate daf (%)	C	79.8	59.5	50.6
	O	12.6	31.5	43.2
	H	5.3	6.4	5.9
	N	1.56	2.1	0.22
	S	0.72	0.53	0.04
LHV [MJ/kg ar]		29.0	20.8	17.6

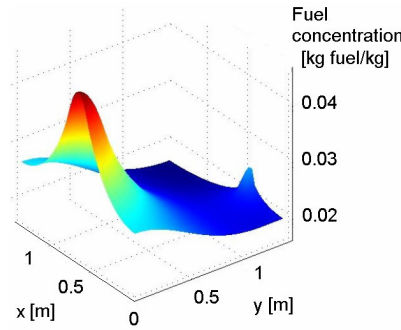
Table 2: Analyses of fuels used in runs shown in Figures 11 to 13

4. Results

Figure 7a shows measured values from 9 points distributed across the cross-section at a low level ($h=0.52$ m) in the furnace. Fuel is Polish coal with a mean size of 8 mm, with moisture, volatiles, char and ash contents (as received) of 17%, 30%, 44% and 9%, respectively. The fuel was fed at a rate of 0.43 kg/s from the fuel chute, placed at the center of the front wall (Fig. 7a), while the inlet of the return leg (fuel re-feed) is located to the right of the rear wall. The data yield fuel concentration values from 2.3% to 4.3%, with a cross-sectional average of 3.2%. The distribution of the fuel concentration given by the model in the same cross section is shown in Fig. 7b. In the model, fuel particles are assumed to undergo fragmentation after 75% of the devolatilization time, yielding 10 pieces, which is the pattern found in [37] for coal (although it should be emphasized that fragmentation is strongly fuel dependent and difficult to generalize).



a) Experimental data



b) Modeled data

Figure 7: Fuel concentration at bottom region of the Chalmers combustor

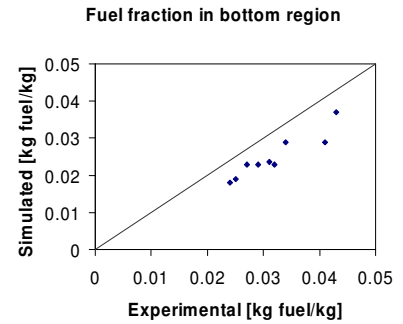


Figure 8: Comparison between modeled and experimental data on fuel concentration

In the modeled fuel distribution, fuel concentration values range from 1.7 to 3.7 %, with a cross-sectional averaged value of 2.5 %. The average error between modeled and experimental values is 19%. A comparison between experimental and simulated values at the 9 sampling points is shown in Fig. 8, where a general tendency of the model to slightly underestimate fuel concentration values is observed for all points. There may be several reasons for this (or a combination of them). One probable explanation is an overestimation of the fragmentation leading to an overestimation of the fuel conversion rate and thereby resulting in a lower fuel inventory.

Figure 9 shows the modeled fuel concentration values for the same test at a height of 7 m above the air distributor. As seen, the fuel concentration in the core is much lower than in the walls (in agreement with literature, *e.g.* [38]), where corner effects are significant. It is also seen that the wall with the fuel chute (to the left) gives higher fuel concentration values than at the other walls, also this is an expected result.

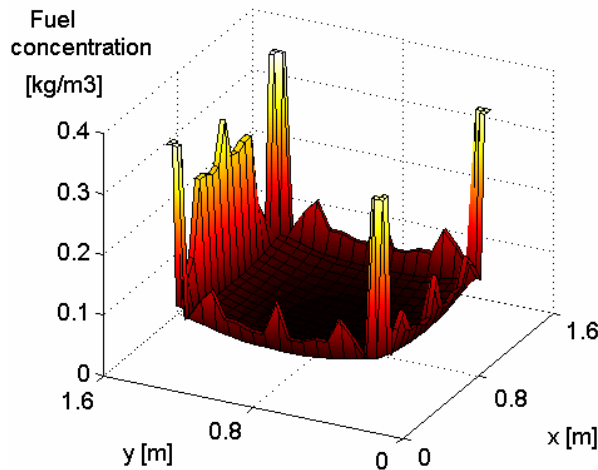


Figure 9: Modeled fuel concentration at a height of 7m

Modeled data from a case burning wet wood chips (with an assumed proximate analysis of 45% moisture, 45% volatiles, 9% char, 1% ash) is chosen to exemplify the importance of accounting for the changes in the size and density of fuel particles during their conversion. During the first seconds in the furnace the wet wood particles are relatively dense and remain mostly in the bottom region of the riser while releasing their moisture. As conversion progresses the wood particles become lighter and dryer and volatiles and later on char combustion products are released at the same time that fuel particles tend to occupy higher locations in the riser. This is seen in Fig. 10, which shows the modeled cumulative releases of moisture, volatiles and char combustion products. It can be observed that, in this simulated example, 95% of the moisture and 79% of the volatiles are expected to be released below a height of 4 m in the riser whereas only 60% of the char combustion products are produced below this level. As far as coal is concerned, its much lower moisture and volatile contents make physical changes in the fuel particles due to drying and devolatilization of lower significance compared to those in wood, leading to a less pronounced effect than that shown in Fig. 10.

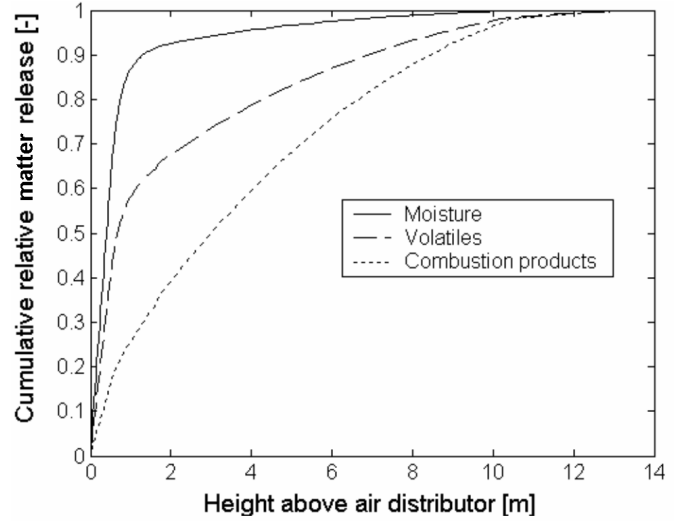


Figure 10: Modeled cumulative fuel field releases

Experimental data in Figs 11 and 12 (represented by symbols) were sampled under runs in the Chalmers 12 MW_{th} CFB boiler with different fuel types (with proximate and ultimate analyses as listed in Table 2). In all runs, the load was kept around 8 MW_{th} and bed material samples were taken at different heights in the riser and analyzed with respect to their char content. In addition, the vertical pressure profile was measured along the furnace height with denser spacing between the pressure taps in the lower region of the furnace where the strongest gradients in the solids

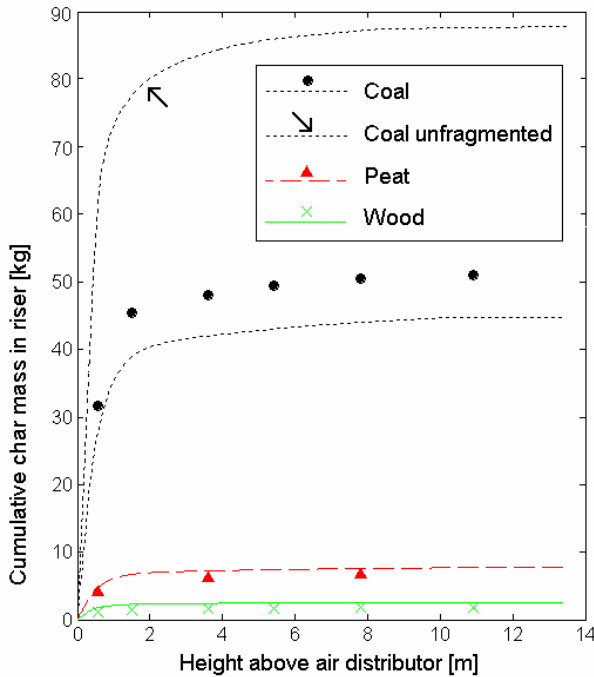


Figure 11: Comparison between modeled and experimental data on vertical cumulative char mass

concentration are expected. Combining the results of the bed samples and the pressure drop profile (*i.e.* the vertical solids concentration) gives the experimental cumulative mass of char in the vertical direction of the riser shown in Fig. 11. The modeled data show a satisfactory agreement with these data and follow the trend which, as expected, gives coal-firing the largest char inventory in the riser (about 51 kg measured and 44 kg modeled), much larger than that found under peat- and wood-firing (with the latter yielding the lowest char inventory: approximately 2 kg in both experiments and simulations). Two main reasons lie behind this large difference: the higher char content in coal compared to wood (see Table 2) and the lower reactivity of coal char compared to wood char (due to the higher activation energy and lower particle voidage and intrinsic area of coal char) which together make the burnout time of coal char particles significantly longer than that of wood char. The peat char content and reactivity are between those of wood and coal (although closer to wood), thus leading to an intermediate inventory between those of wood and coal in Fig. 11. As mentioned above, modeled data vary strongly depending on the fragmentation pattern used, so a fragmentation pattern could be used as fitting parameter between simulated data and experiments for

each particular run/fuel type. Thus, a high level of agreement would be obtained for all fuel types if such a fitting exercise is applied separately to each run. Instead, the procedure has been based on using a common (*i.e.* regardless of the type of fuel) fragmentation pattern as fitting parameter for all simulations shown in Figs 11, 12 and 13. The obtained fragmentation pattern consists of the fuel particle falling apart into 5 equal pieces after 20 seconds (*i.e.* when the fuel particle still undergoes devolatilization), which is a realistic pattern according to those found experimentally (*e.g.* [37, 39]). For comparison and illustration of the sensitivity of the results to the fragmentation pattern fed to the model, model results from the case burning coal are compared in Figs. 11 to 13 with modeled data in which fragmentation of the fuel particle is assumed not to occur. As seen in the non-fragmented data curve (marked by an arrow in Fig. 11), the char inventory in the unit increases substantially when fragmentation is not included (almost 100% increase in the case shown). This is due to that without fragmentation the burnout time predicted by the fuel particle conversion increases as a consequence of the decreased char surface. Thus, since char combustion rate is proportional to the char surface in the model, fragmentation (increased char surface) results in an enhanced conversion rate and thereby to a decreased char inventory for a given fuel and operational conditions.

Figure 12 shows the dependency of the mean size of the char particles on height in furnace. As seen, the size distribution of wood particles shows a strong difference between those in the dense bottom bed which are close to the size at the feeding point (about 1 cm) and those much smaller populating the freeboard. This difference is well predicted by the model but can only be confirmed by one experimental data point (4.2 mm at a height of 0.56 m) and is not observed in the same proportions under peat- or coal-firing (in this sense, the model also follows the experimental data correctly). Before analyzing the three curves presented, it must first be noted that particle size is mainly decreased due to fragmentation and char combustion, assuming char combustion takes place on surface of the char particle (which is the usual case in fluidized bed combustion) and not inside the whole particle. Thus, fuel particle size (which is largest for wood chips) does not notably decrease under the drying and devolatilization processes, but the fuel particle density does (see Fig. 5). Bearing in mind this and the high moisture content in the wood chips (see Table 2) for which there is a significant increase in density, wood fuel occupies the bottom part of the riser until its size and density has decreased enough to be entrained up into the freeboard. On the other hand, coal and peat particles have a lower terminal velocity than the large wood chips used and occupy both the bottom bed and the freeboard directly from the feeding stage, leading to a more homogeneous fuel particle size distribution. As seen in Fig. 12, when fuel fragmentation is not included, the fuel particle size increases at all heights in the furnace compared to the case with fragmentation included, with the highest increase taking place in the dense bed. This is an expected result, since without fuel fragmentation fuel particles remain relatively large for a longer time in the dense bed. Concerning the freeboard, without fuel fragmentation the largest fuel particles are those with terminal velocities not much below the gas velocity, which are larger than those found when accounting for fuel fragmentation. For the case shown, omitting the fuel fragmentation results in a 36% increase in the average fuel size in the furnace.

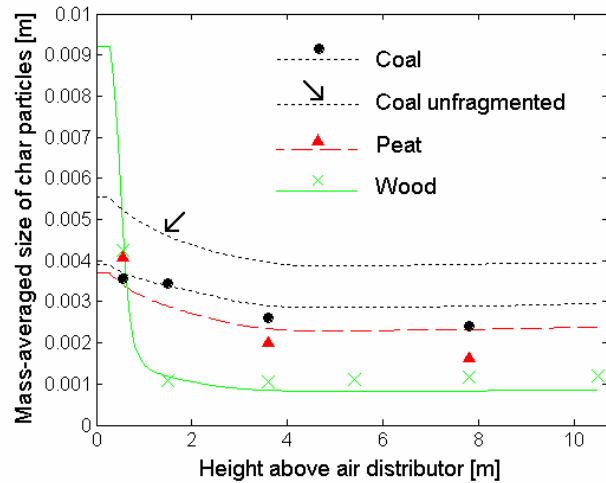


Figure 12: Comparison between modeled and experimental data on vertical distribution of char particle size

Finally, Fig. 13 shows the normalized cumulative char surface along the height of the furnace of the Chalmers 12 MW CFB boiler, with experimental data taken from [36]. Bituminous coal with 40% of volatiles and a mean particle size around 1 cm was used as fuel. Combining experimental data on fuel concentration (see above) and fuel mean size at several heights, the cumulative char particle surface can be obtained. This variable, together with the oxygen concentration gives information on how the char combustion is distributed along the riser. As seen in Fig. 13, a good agreement is obtained between normalized experimental and simulated data for the fragmented coal case. When no fragmentation is accounted for the curve becomes steeper, meaning that more char surface is located in the bottom region which implies that the model predicts a higher proportion of the combustion taking place in the bottom region (provided enough oxygen is available). While only about half (52%) of the total char surface is located in the dense bottom bed when fragmentation is accounted for, omitting fragmentation results in that this value increases to 82%.

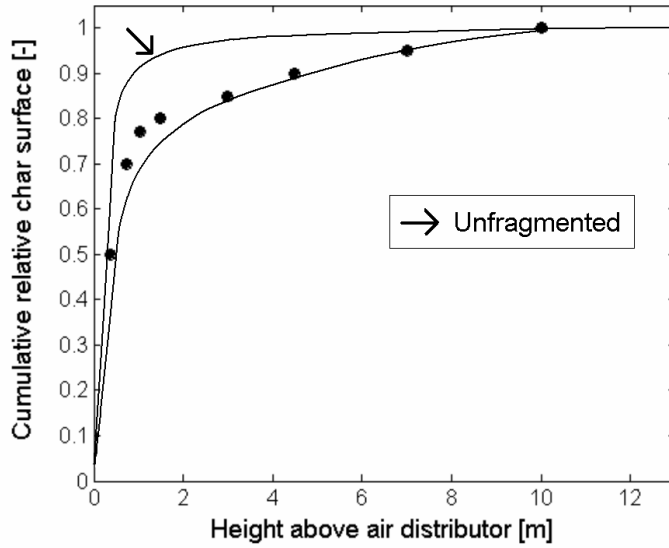


Figure 13: Comparison between modeled and experimental data on vertical cumulative char surface

provided similar overall burnout in the furnace. In addition, it should be noted that the dynamics of the inert solids are not taken into account in the model either than within the bottom bed. A further development of this model should allow interaction between the fuel and inert solid fractions.

5. Conclusions

A model for solids mixing in a fluidized has been applied to fuel particles in combination with a fuel conversion model in order to account for physical changes that fuel particles undergo during conversion. The modeled fuel concentration values differ around 20% compared to experimental data and a common fragmentation pattern can be adjusted so that simulated distributions of fuel particles size show also a good agreement to measured values for 3 different fuel types. Fuel fragmentation (which is not modeled but is an input in the form of a given empirical pattern from experiments) is found to have a large influence on the results and its proper modeling is thereby crucial for a more accurate modeling of the spatial distribution of the fuel inventory within the unit. Yet, the importance of fuel fragmentation on the overall CFB process may be less than the one on fuel inventory and distribution which this paper focuses on.

Acknowledgments

The authors gratefully acknowledge financial support from the Swedish Energy Agency, the EU Research Fund for Coal and Heat under contract RFC-CR-03001 and Metso Power Oy.

Notation

a	Splash zone's decay constant [m^{-1}]	F	Solids flow [kg/m^3]
A	Area [m^2]	h_m	Mass transfer coefficient [m/s]
Ar	Archimedes number [-]	H_b	Dense bed height
c	Proportionality constant [-]	k	Mass transfer coefficient [m/s]
C	Concentration [kg/m^3]	K	Transport zone's decay constant [m^{-1}]
D_{eq}	Equivalent diameter [m]	m	Mass [kg]
D_{horiz}	Diffusion coefficient [m^2/s]	n	No. of exit ducts [-]

p	Entrainment probability with 1 exit duct	T	Temperature [C]
p^*	Entrainment probability with n exit ducts	u_g	Gas velocity [m/s]
p_1	Disengagement probability at the riser	u_t	Terminal velocity [m/s]
p_2	Entrainment probability at the duct	V	Volume [m ³]
r	Geometrical scalar in Eq. (11) [-]	α	Constant in Eq. (11)
R	Rate [m/s]	β	Constant in Eq. (11)
S_{feed}	Source term [kg/m ³ s]		

Greek letters

ε	Voidage	ζ	Dimensionless spatial coordinate
λ	Conductivity [W/m·s]	ρ_s	Solids density [kg/m ³]
τ	Residence time [s]	θ	Dimensionless temperature
Ω	Conversion factor [kg C/mole O]		

Subscripts and superscripts

$clust$	Cluster phase	i	Cell index
$core$	Core region	kin	Kinetical
$disp$	Disperse phase	lat	Lateral
eff	Effective	$part$	Particle
$fuel$	Fuel	∞	Surrounding

References

- Schlichthaerle, P., Werther, J. 2001. "Solids mixing in the bottom zone of a circulating fluidized bed". *Powder Technology*, 120 (1-2), pp. 21-33.
- Niklasson, F., Thunman, H., Johnsson, F., Leckner, B. 2002. "Estimation of solids mixing in a fluidized bed combustor". *Industrial and Engineering Chemistry Research*, 41 (18), pp. 4663-4673.
- Xiang, Q., Huang, G., Ni, M., Cen, K., Tao, T. 1987. "Lateral dispersion of large coal particles in an industrial-scale fluidized bed combustor". *Proc. of the 9th Int. Conf. on FBC, Montreal*, pp. 771-776.
- Xiao, P., Yan, G., Wang, D. 1998. "Investigation on horizontal mixing of particles in dense bed in circulating fluidized bed". *Journal of Thermal Science*, 7 (2), pp. 78-84
- Tanskanen, V. 2005. "CFD study of penetration and mixing of fuel in a CFB furnace". *Master Thesis, Dept. of Energy and Environment, Lappeenranta Univ. of Tech.* (Finland).
- Knöbig, T. 1998. "Three-dimensional modeling of circulating fluidized bed combustion". *PhD Thesis, Tech. Univ. of Hamburg-Harburg (Germany). Shaker Verlag, Aachen (Germany)*. ISBN 3-8265-4480-3.
- Hartge, E.-U., Luecke, K., Werther, J. 1999. "The role of mixing in the performance of CFB reactors". *Chemical Engineering Science*, 54 (22), pp. 5393-5407.
- Luecke, K., Hartge, E.-U., Werther, J. 2004. "A 3D model of combustion in large-scale circulating fluidized bed boilers". *International Journal of Chemical Reactor Engineering*, 2, A11.
- Chirone, R., Massimilla, L., Salatino, P. 1991. "Comminution of carbons in fluidized bed combustion". *Progress in Energy and Combustion Science*, 17 (4), pp. 297-326.

10. Salatino, P., Massimilla, L. 1989. "A predictive model of carbon attrition in fluidized bed combustion and gasification of a graphite". *Chemical Engineering Science*, 44 (5), pp. 1091-1099.
11. Hannes, J. 1996. "Mathematical Modelling of Circulating Fluidized Bed Combustion". *City-Print Verlag GmbH*, Aachen (Germany). ISBN 3-88817-002-8.
12. Pallarès, D., Johnsson, F. 2006. "Macroscopic modeling of fluid dynamics in large-scale circulating fluidized beds". *Progress in Energy and Combustion Science*, 32 (5), pp. 539-569.
13. Lei, H. 1998. "Hydrodynamic modelling of circulating fluidized bed reactors". *PhD Thesis, Tokyo Univ. of Agric. and Tech.* (Japan).
14. Palchonok, G., Breitholtz, C., Thunman, H., Leckner, B. 1997. "Impact of heat and mass transfer on combustion of a fuel particle in CFB boilers". *Proc. of the 14th Int. Conf. on FBC, Vancouver*, pp. 871-888.
15. Pallarès, D., Johnsson, F. 2006. "A novel technique for particle tracking in cold 2-dimensional fluidized bed - simulating fuel dispersion". *Chemical Engineering Science*, 61, pp. 2710-2720.
16. Xiao, P., Yan, G., Wang, D. 1998. "Investigation on horizontal mixing of particles in dense bed in CFB units". *Journal of Thermal Science*, 7 (2), pp. 78-84.
17. Berruti, F., Scott, D.S., Rhodes, E. "Measuring and modelling lateral solid mixing in a 3-D batch gas-solid fluidized bed reactor". *Canadian Journal of Chemical Engineering*, 64 (1), pp. 48-56.
18. Xiang, Q., Huang, G., Ni, M., Cen, K., Tao, T. 1987. "Lateral dispersion of large coal particles in an industrial-scale fluidized bed combustor". *Proc. of the 9th Int. Conf. on FBC, Boston*, pp. 546-553.
19. Stubington, J.F., Chan, S.W., Clough, S.J. 1990. "A model for volatile release into a bubbling fluidized bed combustor". *AIChE Journal*, 36, pp. 75-83.
20. Lewis, W.K., Gilliland, E.R., Lang, P.M. 1962. "Entrainment from fluidized beds". *Chemical Engineering Progress Symposium Series* 58, pp. 65-78.
21. Kunii, D., Levenspiel, O. 1990. "Entrainment of solids from fluidized beds". *Powder Technology*, 61 (2), pp. 193-206.
22. Lei, H., Horio, M. 1998. "A comprehensive pressure balance model of circulating fluidized beds". *Journal of Chemical Engineering of Japan*, 31 (1), pp. 83-94.
23. Johnsson, F., Leckner, B., 1995. "Vertical distribution of solids in a CFB furnace". *Proc. of the 13th Int. Conf. on FBC, Orlando*, pp. 671-679.
24. Werther J. 1993. "Fluid Mechanics of Large-Scale CFB Units". *Circulating Fluidized Bed Technology IV*, pp. 1-14.
25. Sanderson, W.E. 1994. "The separation effect on the CFBC's riser exit". *Delft University Press Science*, TU-Delft (The Netherlands).
26. Johnsson, F., Zhang, W., Leckner, B. 1995. "Characteristics of the formation of particle wall-layers in CFB boilers". *Proc. of the 2nd Int. Conf. on Multiphase Flow*, pp. 25-32.
27. Davidson, J.F. 2000. "Circulating fluidised bed hydrodynamics". *Powder Technology*, 113 (3), pp. 249-260.
28. Werdermann, C.C. 1993. "Feststoffbewegung und Wärmeübergang in zirkulierenden Wirbelschichten von Kohlekraftwerken". *PhD Thesis, Tech. Univ. Hamburg-Harburg (Germany)*.
29. Kang, S.K., Kwon, T.W., Kim, S.D. 1998. "Hydrodynamic characteristics of cyclone reactors". *Powder Technology*, 58 (3), pp. 211-220.
30. Edvardsson, E., Åmand, L.-E., Thunman, H., Leckner, B., Johnsson, F. 2006. "Measuring the external solids flux in a CFB boiler", *Proc. of the 19th Int. Conf. on FBC, Vienna*.
31. Thunman, H., Davidsson, K., Leckner, B. 2004. "Separation of drying and devolatilization during conversion of solid fuels". *Combustion and flame*, 137 (1-2), pp. 242-250.
32. Field, M.A., Gill, D.W., Morgan, B.B., Hawksley, P.G.W. 1967. "Combustion of pulverized coal". *The British Coal Utilization Research Association, Surrey (England)*.

33. Leckner, B., Golriz, M.R., Zhang, W., Andersson, B.Å., Johnsson, F. 1991. "Boundary layers - first measurements in the 12 MW CFB research plant at Chalmers University". *Proc. of the 11th Int. Conf. on FBC, Montreal*, pp. 771-776.
34. Åmand, L.-E. 1996. "Nitrous oxide emission from circulating fluidized bed combustion". *PhD Thesis, Chalmers Univ. of Tech. (Sweden)*.
35. Lyngfelt, A., Åmand, L.-E., Leckner, B. 1995. "Low N₂O and SO₂ emissions from circulating fluidized bed boilers". *Proc. of the 13th Int. Conf. on FBC, Orlando*, pp. 1049-1057.
36. Lyngfelt, A., Åmand, L.-E., Leckner, B. 1996. "Progress of combustion in the furnace of a circulating fluidized bed boiler". *Proc. of the 26th Int. Symp. on Combustion, Naples*, pp. 3253-3259.
37. Zhang, H., Cen, K., Yan, J., Ni, M. 2002. "The fragmentation of coal particles during the coal combustion in a fluidized bed". *Fuel*, 81 (14), pp. 1835-1840 .
38. Zhang, W., Johnsson, F., Leckner, B. 1995. "Fluid-dynamic boundary layers in CFB boilers". *Chemical Engineering Science*, 50 (2), pp. 201-210.
39. Sreekanth, M., Kolar, A. and Leckner, B. 2006. "Effect of shape and size of wood on primary fragmentation in a laboratory scale fluidized bed combustor". *Proc. of the 19th Int. Conf. on FBC, Vienna*.

Paper III

Pallarès, D., Johnsson, F. (2008)

"Macroscopic modeling of the gas phase in fluidized bed combustion"

Submitted for publication

Macroscopic modeling of the gas phase in fluidized bed combustion

David Pallarès*, Filip Johnsson

Department of Energy and Environment, Chalmers University of Technology, SE-412 96 Göteborg (Sweden)

Abstract

A model for gas phase mixing in fluidized bed boiler furnaces (risers) is presented. The model takes its basis in a description of the dynamics of the dense bottom bed which strongly govern the gas mixing up through the furnace. Thus it is the opinion of the authors that a time-resolved approach is required to link the modeling to the physics of the underlying processes determining the gas mixing. As output, the model gives the fluctuating flux of gas species, in contrast to the classical modeling approach which is limited to time-averaged gas fluxes.

The dynamical approach allows assumption of the volatile combustion system as transport-controlled but at the same time avoids complete consumption of either oxygen or combustible gases in each modeled cell. Instead, time-resolved analysis enables application of a realistic criterion for the mixing: reactants must coincide in both space and time in order to react. While fitted kinetics is strongly system and operational dependent, the present model integrates key system variables, such as the bottom bed height and the characteristic pressure drop constant over the primary-air distributor.

The model divides the gas flow into two phases, a throughflow and an emulsion gas, and calculates their respective fluctuations in velocity and composition. Having these, in-furnace gas probe measurements can be simulated and compared with in-situ gas suction probe measurements (*i.e.* the probe is modeled). Such an approach is crucial in fluidized bed-boilers furnaces since in-situ gas probe measurements in regions with high fluctuations in gas velocity are known to give results which are biased towards reducing conditions. These bias results from the significant velocity differences between oxidizing (throughflow) and reducing (emulsion) gas fluxes, with the latter flowing at a lower velocity. This effect is especially pronounced in the lower part of the furnace, as differences in gas velocities decrease with height in furnace.

Model results, including simulation of the gas suction probe, are analyzed and compared with experimental data from the Chalmers 12 MW_{th} CFB boiler and a good agreement is obtained.

Keywords: Modeling; Gas; Fluidization; Fluidized bed; Fluctuations; Dynamics

1. Introduction

A thorough understanding of combustion applications requires knowledge on the behaviour of the gas phase, which brings oxygen in contact with the fuel to be oxidized. As far as fluidized bed combustion is concerned solid fuels (such as coal, peat, biomass or waste) is the usual fuel type, for which the combustion process is characterized by the release of volatile gas species (part of which are combustible) and by char burn out. Oxygen is mainly supplied to the fluidized bed furnace through gas injection in the lower part of the furnace, often divided into primary and secondary air with primary air entering through a primary air distributor. Under typical operating conditions there is a relatively dense bed directly above the primary air distributor. Due to the limited pressure drop across the primary air distributor, the gas flow through the air distributor is highly intermittent with strong fluctuations in gas velocity both in time and space, as shown by Svensson *et al.* (1996). Thus, the gas supplied through the primary air distributor is responsible for the highly fluctuating dense bed dynamics which strongly influence how oxygen is brought into contact with the fuel, both with respect to the char (which to a large extent remains in the bottom region of the furnace during burnout) and the combustible volatile species.

There is a rather limited amount of experimental work with extensive gas concentration data in industrial boilers. The work by Åmand (1994) provides the experimental data in Fig. 1, which shows vertical profiles of oxygen and methane measured with a gas suction probe in the Chalmers CFB boiler.

Figure 1 shows that oxygen and a combustible gas such as methane seem to coexist at different heights despite the high furnace temperature which should make kinetics for methane oxidation fast enough for this not to occur. The values shown are time-averaged values from gas suction probe measurements over a certain period of time (typically 20 minutes). Also, such probe measurements make cannot give information on the time scale corresponding to typical times for mixing and reaction in the furnace, *i.e.* the response time of the gas sampling probe with gas conveying lines is of the order of 10 s or more for the probe system used. The explanation for the

* Corresponding author: david.pallares@chalmers.se ; Telf: (+46)317721435 ; Fax: (+46)317723592

coexistence of oxygen and methane on a time-averaged basis is found in the rapid fluctuations between oxidizing and reducing conditions at the points of measurement.

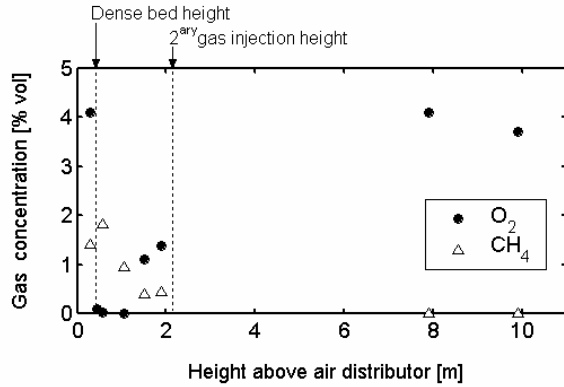


Figure 1: Vertical gas concentration profiles in the Chalmers 12 MW_{th} CFB boiler. From Åmand (1994).

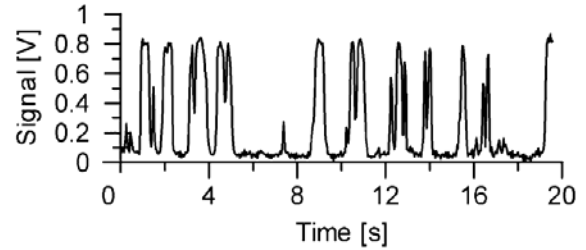


Figure 2: Time series of voltage signal from a zirconia cell probe. From Niklasson *et al.* (2003)

This can be illustrated by time-resolved experimental data, such as the measurements with zirconia cell probe shown in Fig. 2. The output signal from a zirconia cell is an indicator of the oxidizing or reducing condition (low and high values respectively) of the sampled environment. Studies on time series of signals from zirconia cells inserted in a fluidized bed furnace can be found in Niklasson *et al.* (2003) and Stubington and Chan (1990). The rapid fluctuations between oxidizing and reducing conditions seen in Fig. 2 indicate that there is no coexistence of oxygen and combustible gases on a time-resolved basis. Yet, also the zirconia cell has a limited response time and the measurements only give a qualitative illustration of these fluctuations, see Niklasson *et al.* (2003).

The fluctuating character of the gas phase concentration makes it difficult to apply the classical approach used in macroscopic modeling of the gas phase in fluidized bed boilers (see *e.g.* Hannes (1996), Knöbig (1998) and Okasha (2007)), namely a time-averaged modeling. This since time-averaged modeling will obviously not allow for coexistence of combustion reactants with fast reaction kinetics in the same point (cell). This is usually solved by fitting the combustion kinetics in the modeling to experimental data, which is an indirect way to account for the fluctuating nature of the gas concentration. This fitting is strongly dependent on operational conditions, nozzle characteristics and other parameters influencing gas fluctuations. This classical model approach is illustrated in Fig. 3a, in which r represents empirically-fitted combustion kinetics while k represents inter-cell gas mixing mechanisms.

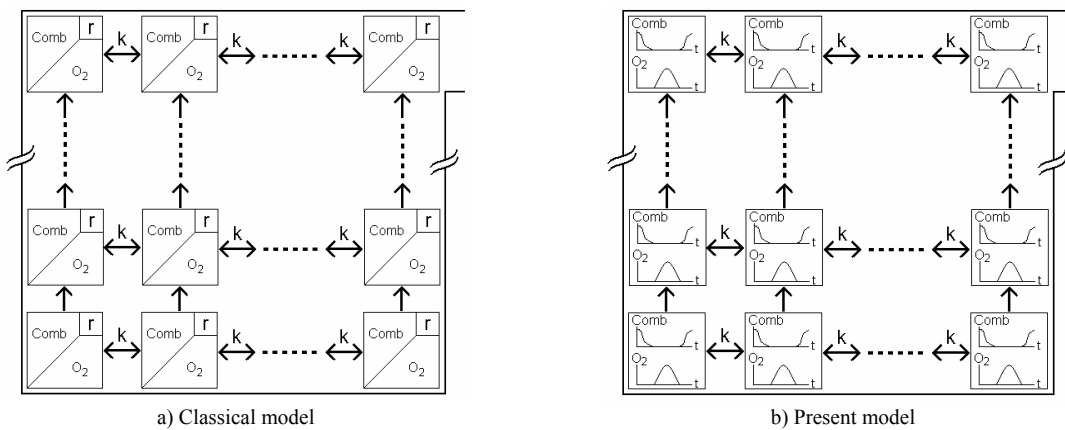


Figure 3: Schemes for macroscopic modeling of the gas phase. Inter-cell gas mixing mechanisms are represented by k and empirically-fitted combustion kinetics are represented by r .

The present model is time-resolved and assumes volatile combustion to be transport-controlled and thus does not allow coexistence of combustion reactants at the same cell and time step. The model describes fluctuations in the flux and species concentrations of the gas phases considered. Thus, comparison with time-averaged experimental data requires the modeled values to be first time-averaged.

A second phenomenon shown in Fig. 1 is the apparent contradiction in that oxygen concentration increases with height in the region between the dense bed surface and the secondary air injection height. This is a consequence of that gas flowing through the bubbles in the bottom bed region finds a low pressure drop path through the bubbles and thus has a higher velocity (often called throughflow) than gas flowing through the dense bed emulsion (called emulsion-only gas in this work). This is illustrated in Fig. 4, which shows a captured videoframe from a cold 2-dimensional unit where two high velocity through flow areas can be seen: one with a moderately high velocity to the left and one with a high velocity to the right creating what has been described as an exploding-type bubble by Svensson *et al.* (1996). An experimental study evaluating this increased gas velocity of the throughflow gas was carried out by Olowson and Almstedt (1990).

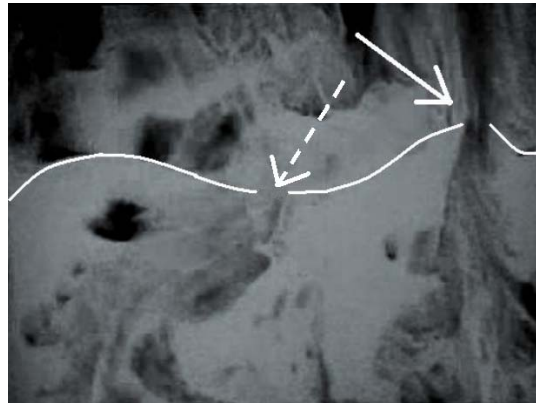


Figure 4: A videoframe from a 2-dimensional cold unit (1.2 x 0.02 x 2 m operated with Group B solids). The white curve indicates the bed surface, the solid arrow the ejection of high-velocity throughflow gas from an exploding type bubble and the dashed arrow a throughflow region with a lower gas velocity.

The pattern illustrated in Fig. 4 results in large fluctuations in gas velocity in and above the dense bottom bed. The throughflow is characterized by a higher oxygen content due to the limited contact with char particles, which predominantly stay and burn in the dense (low velocity) phase of the bed. This means that a gas suction probe measurement in regions with such fluctuating gas flow conditions will be exposed to an environment which alters between high-velocity oxygen rich gas flow and low-velocity oxygen lean flow. The flow fluctuations will decrease gradually up through the splash zone (located above the dense bed), eventually yielding a fairly homogeneous gas velocity distribution in the upper freeboard. The degree of bias in gas suction probe measurements depends on the difference in velocity and gas concentration between the high and low velocity gas phases, which, thus, is highest within the dense bed and decreases up through the splash zone (*i.e.* the bias is reduced along the splash zone). The reduced velocity difference between the two phases up through the splash zone explains the increase in oxygen concentration with height between the dense bed surface and the secondary air injection height observed in Fig. 1. Thus, these effects prevent a proper evaluation of gas concentration measurements (by suction probe) in the bottom region of fluidized bed furnaces. Lyngfelt *et al.* (1996) proposed an empirical method to correct measured gas concentration values. Since the bias in measured gas concentration values as well as the gas mixing in general are strongly influenced by the dynamics of the flow in the bottom of the furnace a dynamic approach seems inevitable when modeling the gas mixing.

In the bottom region of the furnace, the model presented in this work describes the gas phase behavior in both the throughflow and the emulsion phase of a fluidized bed with emphasis on circulating fluidized bed boilers, *i.e.* for high velocity conditions with entrainment of solids from the bed. The model allows for simulation of local gas concentration values as seen by a gas sampling probe in order to compare them with *in-situ* gas probe measurements in line with the above given discussion. Description of the gas fluctuations takes into account key parameters such as the pressure drop across the air distributor and dense bed height.

Finally, the list of inputs for the model presented contains the mass rate, composition and location of the injected flows to the furnace and the penetrating length and width of the secondary air injections. Besides these, it must be noted that the model presented is part of a comprehensive model for large-scale fluidized bed units and requires additional input data (*e.g.* dense bed height, char concentration field, volatile release field) from other submodels, but modeling of these are outside the scope of the present work. In summary, the model of gas mixing presented in this work is combined with input data from other models (*i.e.* the fuel moisture and volatile release and the char concentration fields, modeled according to Pallarès and Johnsson (2007) and, as a result, the fields of gas species concentration and flux in the furnace are obtained.

In order to allow for comparison of modeled results with *in-situ* measurements, the modeled data are transformed by means of a model of the gas suction probe used for the sampling.

2. Theory

The bottom region of a fluidized bed boiler furnace is typically occupied by a so-called dense (or bottom) bed, which exhibits a linear drop in the vertical profile of the time-averaged pressure (see Johnsson *et al.* (1991)). The dense bed is characterized by the presence of gas bubbles which become larger as they rise up through the bed. Several authors have contributed with semi-empirical correlations for the bubble size, with the expression proposed by Darton *et al.* (1977) accounting for bubble coalescence being amongst the most widely used:

$$D_{bub} = 0.54 \cdot (u_0 - u_{mf})^{0.4} \cdot (h + 4\sqrt{A_0})^{0.8} \cdot g^{-0.2} \quad (1)$$

Based on a survey of experimental data from several authors, Clift and Grace (1985) proposed the following correlation for the rise velocity of a single bubble through an infinitely wide bed:

$$v_{bub} = 0.71 \cdot \sqrt{g \cdot D_{bub}} \quad (2)$$

Combining Eqs. (1) and (2) on a time-discretized basis provides a description of the size and location of the bubble as it raises through the bed.

The formulation of the present model is made for simplicity in a portion of the bed containing one single bubble but which can be considered representative for the entire bed. Thus, the width of the part of the bed which is analyzed, L^* , is adjusted so that its bubble fraction will equal the bubble fraction, δ , in the entire bed. This local value of the bubble fraction in the entire bed can be easily calculated assuming the dense bed emulsion to remain under minimum fluidization conditions, which implies:

$$\delta = \frac{\varepsilon_b - \varepsilon_{mf}}{1 - \varepsilon_{mf}} \quad (3)$$

and estimating the voidages ε_b and ε_{mf} from some of the several submodels available in literature (see Pallarès and Johnsson (2006) for the ones used in the present model). With this, having the modeled bubble size and the width of the bed portion analyzed, the relative cross section of the throughflow gas phase can be defined as (*cf.* Fig. 5):

$$\sigma_{tf} = \frac{D_{bub}}{L^*} \quad (4)$$

From this follows the relative cross section for the emulsion-only gas phase, $\sigma_{em} = 1 - \sigma_{tf}$. Note that σ_{tf} increases as the bubble grows, while σ_{em} decreases.

The gas bubble rising in the representative bed portion analyzed represents a preferred low pressure-drop path for a fraction of the fluidization gas (as illustrated in Fig. 4). This fraction is here called throughflow phase. The gas flowing through the emulsion is called emulsion-only phase. In the model, it is assumed that there is no mass transfer between these two gas phases. This should be a reasonable assumption since the throughflow phase has been shown to be of high velocity whereas the emulsion phase flows at much lower velocity (see Olowson and Almstedt (1990)). The regions of throughflow phase and emulsion-only gas phase are indicated in Figure 5 with gray and dotted fields, respectively.

A dynamic pressure balance accounting for the above division between the two gas phases (the throughflow and emulsion-only phase) is the basis of the modeling in this work, illustrated in Fig. 5. For each time step of the rise of the bubble, the cross section of each gas phase is updated according to the calculated bubble size and a pressure balance is applied which considers the same total pressure loss across the gas distributor and the dense bed ($\Delta P_{bot} = P_{plenum} - P_{freeb}$) for both gas phases. Thus, at each time step the total pressure drop is:

$$\Delta P_{bot} = \Delta P_{dist}(u_{em,t}) + \frac{dP_{emul}(u_{em,t})}{dh} \cdot H_b = \Delta P_{dist}(u_{tf,t}) + \frac{dP_{emul}(u_{tf,t})}{dh} \cdot H_{emul\,tf,t} \quad (5)$$

where H_b represents the dense bed height (an input to the present model) and $H_{emul\,tf}$ the emulsion path length seen by the throughflow gas phase (which is obtained from combination of the dense bed height and the bubble size). The pressure loss across the gas distributor is a function of gas velocity (the so-called characteristic curve) and takes the form:

$$\Delta P_{dist}(u) = a \cdot u^2 \quad (6)$$

The coefficient a in Eq. (6) is known from experiments and thus an input to the model. The pressure loss across the emulsion can be determined through the well-known Ergun equation (see Ergun (1952)), *i.e.*,

$$\frac{dP_{emul}(u)}{dh} = 150 \frac{\mu \cdot (1-\varepsilon)^2}{d_p^2 \cdot \phi^2 \cdot \varepsilon^3} \cdot u + 1.75 \frac{\rho_g \cdot (1-\varepsilon)}{d_p \cdot \phi \cdot \varepsilon^3} \cdot u^2 \quad (7)$$

Thus, assuming an initial value for the total pressure loss, ΔP_{bot} , the pressure balance can be solved at each time step, providing the evolution of the velocities of each gas phase during the bubble rise. Integration over time of the gas flows corresponding to these velocities gives the time-averaged gas velocity, \bar{u} , resulting from the chosen ΔP_{bot} .

$$\bar{u} = \sum_t u_{em,t} \cdot \sigma_{em,t} + u_{tf,t} \cdot \sigma_{tf,t} \quad (8)$$

Having this, an iterative procedure is used to find the value for ΔP_{bot} giving a time-averaged modeled gas velocity equal to the fluidization velocity set as input.

It should be mentioned that for simplicity the model applies a constant value for the bottom region pressure drop, ΔP_{bot} . Indeed, this value is known to oscillate depending on several parameters related to not only the operational conditions but also the air feeding system (*e.g.* pipe lengths, valve system), as studied by Sasic *et al.* (2005). Yet, for typical boiler conditions (*i.e.* rather high velocities) these fluctuations should be limited.

To illustrate the feature of the dynamic pressure balance modeling an example is here taken of operation with a 0.42 m-high dense bed fluidized by primary air at 850 °C with a superficial gas velocity of 3.1 m/s and two different gas distributors (with values of a in Eq. (6) of 120 and 800 Pa·s²/m², respectively). Figure 6 shows the calculated flow dynamics in the part of the bed which is analyzed for the two gas phases (emulsion and throughflow) obtained from the pressure balance expressed by Eqs (5) to (7).

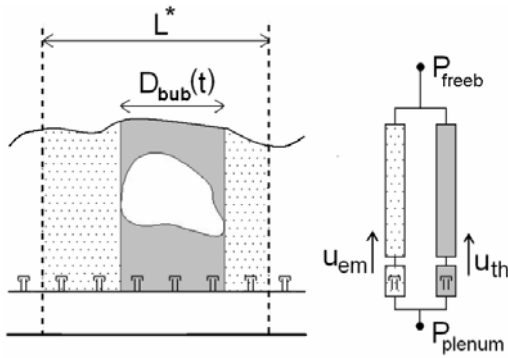


Figure 5: Scheme of the pressure balance for the emulsion-only gas phase and the through flow gas phase.

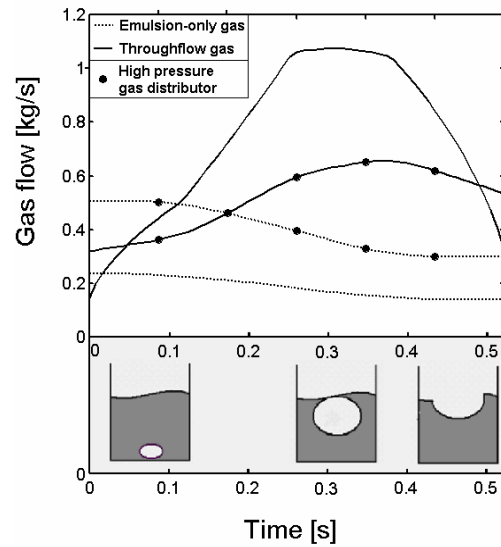


Figure 6: Modeled flows of the emulsion-only and throughflow gas phases in a single bubble bed. Lines with bullets (•) are for the high pressure-drop gas distributor whereas lines without bullets are for low pressure-drop distributor.

Figure 6 shows the gas flow division between the throughflow phase and emulsion-only phase during one bubble cycle. The lines without bullets represent the case with the low-pressure gas distributor ($a=120$ Pa·s²/m²), which is representative for large-scale CFB boilers and predicts that a large part of the fluidization gas crosses the dense bed as throughflow (solid line) whereas the emulsion gas flow (dotted line) is much lower and more constant over time. These model results agree with what has been experimentally observed by Olowson and Almstedt (1990). The throughflow gas flow reaches a maximum as the gas bubble reaches the dense bed surface. The dotted curves for the high-pressure drop gas distributor ($a=800$ Pa·s²/m²) reveal a more even distribution of the gas between the throughflow and emulsion-only phases than with the low-pressure drop gas distributor.

Indeed, during a considerable part of the bubble-rise cycle more gas joins the emulsion-only phase than the throughflow (since emulsion-only phase has a larger cross section as long as the gas bubble is relatively small, although gas velocity is always higher in the throughflow phase). In addition, it can be seen from Fig. 6 that a higher pressure drop across the air distributor dampens the magnitude of the total gas flow fluctuations (the amplitude of the total flow fluctuations for the low high-pressure distributor is 21% compared to the low-pressure drop distributor). Thus, the air-distributor pressure drop has a large influence on the gas flow division into a throughflow and emulsion-only phases, with lower pressure drops accentuating fluctuations and the differences in gas velocity between these phases. The dense bed height plays a similar role, in the sense that higher dense beds having an analogous effect to that of lower pressure drops across the gas distributor.

In the model, gas has the same statistical distribution between emulsion-only and throughflow phases at all locations in the dense bed, namely the one obtained from the dynamic pressure balance. Thus, the so-called “preferred bubble paths” (zones where the probability of presence of gas throughflow is higher than in the rest of the bed, typical for fluidization with very low distributor pressure drop at low gas velocities) are not accounted for in the present model. Thus, the gas phase division obtained from the above-described dynamic pressure balance and exemplified in Fig. 6 can be applied as boundary condition for the entering primary air at the bottom cells in the riser mesh. The data line for oxygen at $h=0$ m in Fig. 7 illustrates this showing the modeled flow of oxygen injected with the primary gas in the emulsion-only gas phase of a bottom cell in the riser mesh.

The present model requires as input the spatial distribution of fuel release rates (*i.e.* moisture and volatile species) and size and concentration of char (providing char surface), which in the present simulations are provided by a fuel mixing submodel (see Pallarès and Johnsson (2008)). Thus, in each cell the fuel release fields, $r(x,y,z)$, are added to each gas phase proportionally to the relative cross section of the gas phase concerned. Released moisture and non-combustible volatiles will increase the volumetric flow and thus the velocity of the gas phase, while released combustible volatiles react with oxygen available at each time step (infinitely fast kinetics are assumed) generating product gases (CO_2 and H_2O) which add to the gas phase flow.

In an analogous way, char particles in a given cell are assumed to get in contact with each gas phase in a fraction proportional to the relative cross section of the two gas phases. Thus, together with the given average char size this will provide the char surface as seen by the two gas phases (emulsion-only and throughflow) at each time step in the cell studied (*i.e.* A_c in Eq.(9)). Thus, the char combustion rate in a specific cell can be calculated as (first order reaction is assumed):

$$\frac{dm_c}{dt} = -\Omega \cdot R_{\text{eff}} \cdot A_c \cdot c_{\text{O}_2} \quad (9)$$

where, according to Field *et al.* (1967), the so-called effective combustion rate, R_{eff} , can be expressed as a combination of two processes governed by respectively the kinetic rate, R_{kin} (determined through an Arrhenius-type correlation, see Field *et al.* (1967)) and the mass transfer coefficient, h_m (determined through a Sherwood-type correlation, see Field *et al.* 1967)), yielding:

$$R_{\text{eff}} = \frac{1}{\frac{1}{R_{\text{kin}}} + \frac{1}{h_m}} \quad (10)$$

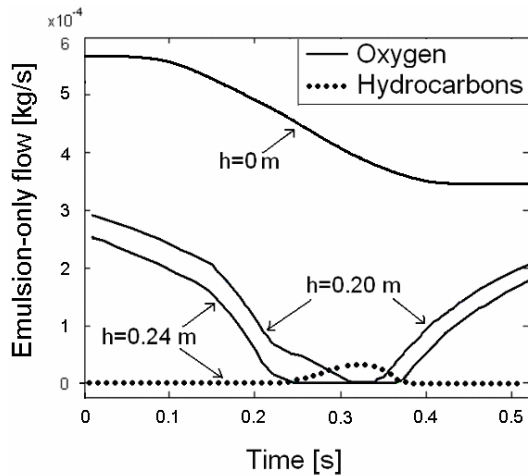


Figure 7: Modeled gas species flows in the emulsion-only phase at different heights in the furnace centerline.

Thus, combustion of volatile species and char can be combined with the fluidynamical inlet boundary conditions for both gas phases provided by the above-described pressure balance, yielding a model for the transport-controlled oxygen consumption in the dense bed. Modeled data showing the evolution of the oxygen consumption with height during a bubble cycle is shown in Fig. 7. Figure 7 shows that, along the furnace centerline, the lowest height above the gas distributor for which no oxygen is available in the emulsion-only gas flow at some point during a bubble cycle is 0.2 m. Above this height, the duration of emulsion-only gas flow with a zero oxygen concentration lasts for longer periods. During absence of oxygen released volatile hydrocarbons will remain unburned and add to the gas flow, as observed in the data line corresponding to $h=0.24$ m.

However, it should be noted that, on a time-averaged basis, the cell corresponding to a height of 0.24 m at the furnace centerline has non-zero concentrations of both oxygen and hydrocarbons, although coexistence of these is not allowed in the time-resolved modeling.

While combustion in the freeboard is modeled in the same way as in the dense bed, modeling of the gas phase mixing above the dense bed applies a widely-used concept of division of a CFB freeboard into two regions: a splash zone and a transport zone. The solids flow of the splash zone, which is located immediately above the dense bed surface, is dominated by cluster formations which are ejected into the freeboard as bubbles burst and, following a ballistic movement, fall back to the dense bed. The transport zone is dominated by dispersed solids suspension flowing more steadily in a core-annulus structure (*i.e.* back-mixing of solids mainly at furnace walls). The height of the splash zone can be defined as the vertical position where the concentrations of the cluster phase and the dispersed phase are equal, as proposed by Johnsson and Leckner (1995).

In the splash zone, the difference in gas velocity between gas phases and the gas velocity fluctuations decrease with height until gas velocity becomes eventually fairly constant over the cross section at the interface with the transport zone. In terms of modeling, this is approached through a gradual damping of the gas flow fluctuations (so that both gas phases considered reach constant velocity values) together with an adjustment of the relative cross section of the gas phases. This is done so that both gas phases reach the same constant velocity. The expressions used for these model calculations implemented in a hexahedral mesh are summarized below.

Firstly, a damping factor is defined at each cell which indicates how much of the gas velocity fluctuations within each gas phase will be damped in the present cell and how much the difference in gas velocity between phases will decrease. In the present model, this damping factor is calculated in each cell as the height of the present cell divided by the distance from the bottom of the present cell up to the end of the splash zone:

$$f = \frac{h_{cell, top} - h_{cell, bot}}{h_{splash, top} - h_{cell, bot}} \quad (11)$$

With this, damping of the gas velocity fluctuations across a splash zone cell in the two gas phases can be expressed as:

$$u_{top} = u_{bot} - f \cdot u'_{bot} \quad (12)$$

where u' is the fluctuating component of the gas velocity, u . Damping of the gas velocity fluctuations implies a rearrangement of the gas flow with mass transfer between the different time steps. However, if only damping of the gas velocity fluctuations for each gas phase was considered, the time-independent gas velocity reached at the top of the splash zone for the gas phases would differ. Thus, there is also a need to model the fade out in velocity difference between the fast-throughflow and the slow-flowing emulsion-only gas. This is done knowing that the phase-averaged velocity for a certain time step is:

$$u_{phase-avg} = \frac{u_{em} \cdot \sigma_{em} + u_{tf} \cdot \sigma_{tf}}{\sigma_{em} + \sigma_{tf}} \quad (13)$$

which is the aimed velocity for both gas phases at the upper limit of the splash zone, where the relative cross section for the gas phases then becomes (emulsion-only phase shown) :

$$\sigma_{em, aim} = \sigma_{em} \frac{u_{em}}{u_{phase-avg}} \quad (14)$$

Thus, making use of the damping factor defined by Eq. (11), the variation of the relative cross section of the emulsion-gas phase through one splash zone cell is expressed as:

$$\sigma_{em, top} = \sigma_{em, bot} + f \cdot (\sigma_{em, goal} - \sigma_{em, bot}) \quad (15)$$

Finally, the relative cross section for the throughflow gas phase is calculated knowing that $\sigma_{tf} = 1 - \sigma_{em}$.

With these two damping mechanisms for the gas velocity fluctuations within each gas phase (Eq.(12)) and for the difference in gas velocity between the two gas phases (Eq.(15)), a constant gas velocity value common to both gas phases is reached for cells at the top of the splash zone. Note that gas mixing associated to the damping

of the gas velocity fluctuations in the splash zone occurs on an intra-cell level, *i.e.* there is a rearrangement of the dynamics of the gas flow within each cell (expressed by Eq.(12)), but no lateral gas mass transfer between cells.

In the transport zone extending from the top of the splash zone to the riser exit, the gas flows more steadily and solids develop a core-annulus structure with upflow in the core region and downflow in so-called wall layers. While gas upflow in the core region is clear, measurements in the wall layer region of the Chalmers 12 MW_{th} CFB boiler by Stern  s and Johnsson (1997) indicate low gas velocity and both occasional upflow and downflow of gas within the wall layer. Thus, in the present model, zero gas flow is assumed in the wall layers of the transport zone. In the core region, gas mixing between cells is modeled by means of lateral diffusion of the mass flux G of each gas species i considered, *i.e.*,

$$\frac{\partial G_i}{\partial t} = \alpha_{g,diff} \cdot \nabla^2 G_i \quad (16)$$

Note that the mass flux is taken as transport variable in Eq.(16) instead of the concentration (which is the traditional approach). Both formulations are equivalent in a homogeneous gas velocity field. However, in presence of gas velocity gradients, Eq.(16) is able to model the lateral gas flows which lead to a flattening of the gas velocity. This flattening of the gas velocity field with height in the furnace is reported in the experimental work by Kruse and Werther (1995). Generally, the main reason for the existence of gas velocity gradients in the transport zone is secondary gas injection (which in the present model is handled by having as input the penetration length and width of the injected gas jet at the injection height).

Values of the gas lateral dispersion coefficient, $\alpha_{g,diff}$, have been studied in several experimental studies in literature (see *e.g.* Werther *et al.* (1992), Gay  n *et al.* (1997) and Stern  s *et al.* (2000)). This study applies the Peclet number-based expression proposed by Kruse *et al.* (1995):

$$Pe = \frac{u \cdot D_{eq}}{\alpha_{g,diff}} = 387 \quad (17)$$

With this final expression, a dynamical model for the gas mixing in fluidized bed boilers is formulated which allows for introduction of transport-controlled combustion. In summary, the model presented above divides the gas into two phases and is based on different assumptions and approaches for the dense bottom bed, the splash zone and the transport zone.

2.1. Gas probe simulation

As explained above in relation to Figure 1, the velocity differences between the throughflow and emulsion-only gas phases prevent proper evaluation of *in-situ* gas probe measurements in the bottom region (*i.e.* dense bed and splash zone) of a fluidized bed boiler. However, since the model accounts for the gas phase division which is the reason for this effect and provides the velocity variations and relative cross sections of both gas phases, simulation of the values measured by a gas probe is possible.

The time-averaged mass concentration for a certain gas species, i , in any cell is defined as the ratio between the mass flow of the gas species i and the total gas mass flow, namely:

$$\bar{C}_i = \frac{F_i}{F_{TOT}} = \frac{\sum_t (u_{em}^t C_{em,i}^t \sigma_{em,i}^t + u_{tf}^t C_{tf,i}^t \sigma_{tf,i}^t)}{\sum_i \sum_t (u_{em}^t C_{em,i}^t \sigma_{em,i}^t + u_{tf}^t C_{tf,i}^t \sigma_{tf,i}^t)} \quad (18)$$

However, the time-averaged mass concentration of the gas species seen by a gas probe does not take into account the effect of gas-velocity difference between the gas phases. Thus, the mass concentration of a gas species i seen by a gas probe can be simulated by the following expression:

$$\bar{C}_{i,probe} = \frac{\sum_t (C_{em,i}^t \sigma_{em,i}^t + C_{tf,i}^t \sigma_{tf,i}^t)}{\sum_i \sum_t (C_{em,i}^t \sigma_{em,i}^t + C_{tf,i}^t \sigma_{tf,i}^t)} \quad (19)$$

Note that in locations where $u'_{em} = u'_{tf}$ (which is the case in the transport zone) the expressions in Eqs.(18) and (19) give the same value. In such case, an in-situ gas probe measurement gives a representative value of the gas species concentration. On the other hand, it is found in the dense bed and the splash zone that $u'_{em} < u'_{tf}$, which, in accordance to Eqs (18) and (19), implies an under-representation of the throughflow gas-phase in the gas concentration measured by a gas probe.

3. Experiments

The experimental part in this work consists of detailed in-situ measurements taken at the Chalmers 12 MW_{th} CFB boiler outlined in Fig. 8a. The riser (furnace) of the Chalmers CFB boiler is 13.5 m.-high with a top cross section of 1.62×1.42 m. The location of the key parts of the riser is illustrated in Fig. 8b. There is a single fuel feeding point located in the front wall and secondary air injection ports in both front and rear walls. The boiler walls are membrane tube walls (water-tubes) and the boiler is a heat only boiler. The front and rear walls are refractory lined all the way from bottom to top of furnace whereas the side walls are bare membrane walls except for the heights below 2.2 m which are refractory lined. The air is introduced as primary air through the bottom gas distributor and secondary air at 2.1 meters above the primary air distributor. Gas coming from the seal and the particle classifier enter the riser through the rear wall at 0.99 and 1.29 m above the distributor respectively. Further details on the geometry of the unit are given in Leckner *et al.* (1991). For the calculations in the present work, the mesh discretizing the furnace contains about 100.000 cells (10% of which are plotted in Fig. 8.c).

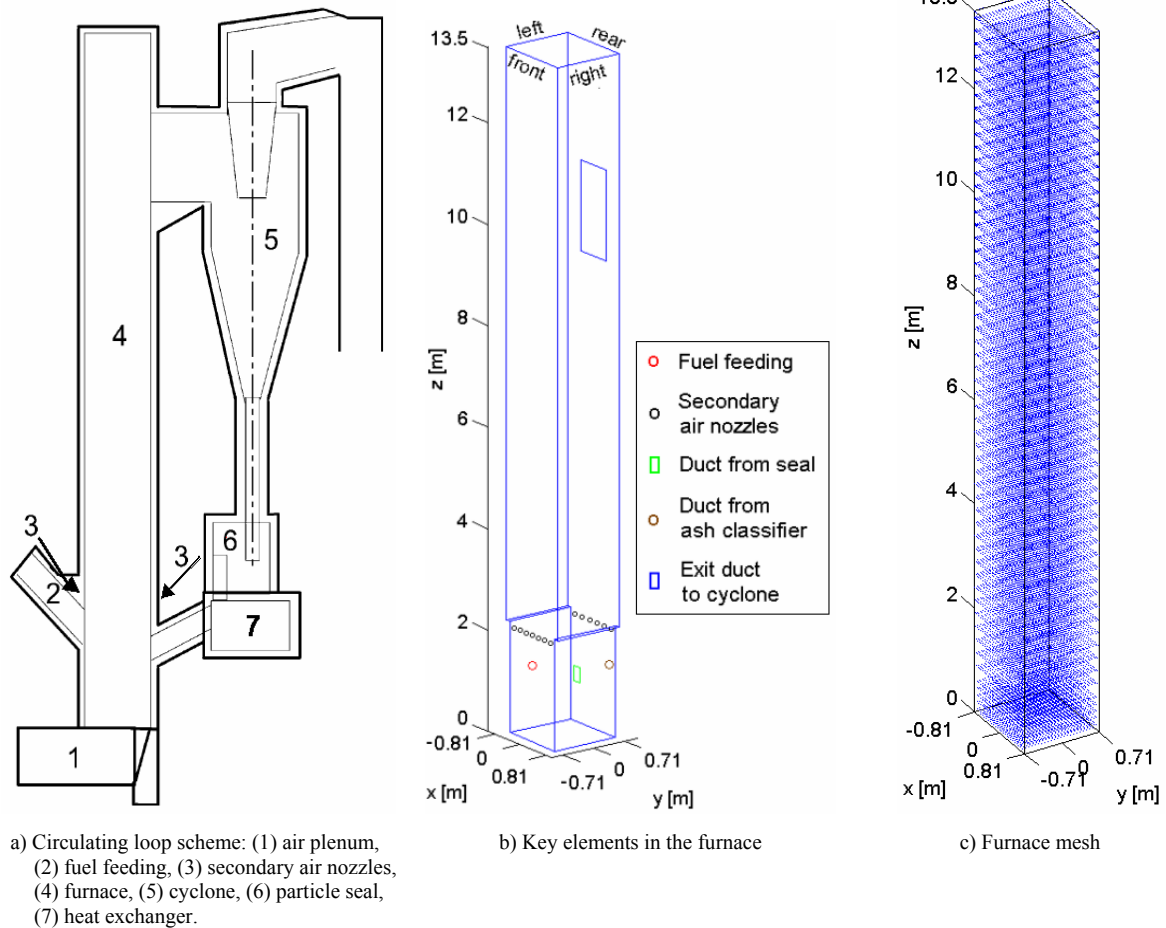


Figure 8: The Chalmers 12 MW_{th} CFB boiler

Two runs are analyzed in this work, both using coal as a fuel. Burning similar coal types (but at a higher fuel feeding rate for Run B), the air-to-fuel ratio is similar for both cases (around 1.2) and so does the air staging ratio (around 58% of the air directly injected to the riser was supplied as primary air). The higher fuel feeding rate in Run B represents a higher fluidization velocity and thus a higher operational pressure drop over the furnace was

established for this run in order to ensure a stable dense bed. Table 1 lists the experimental conditions applied in this work and Table 2 gives the fuel analyses.

Table 1: Operational conditions

		Run A	Run B
Fluidization velocity	m/s	2.22	2.90
Primary air	kg/s	1.39	1.81
Secondary air	kg/s	1.06	1.24
Air injection height	m	2.1	
Classifier air	kg/s	0.14	0.15
Seal air	kg/s	0.10	0.15
Fuel rate	kg/s	0.30	0.43
Fuel type		Coal A	Coal B
Solids size	μm	300	320
Solids density	kg/m^3	2600	
Bed temperature	$^{\circ}\text{C}$	850	
Riser pressure drop	Pa	5110	7950

Table 2: Fuel analyses

		Coal A	Coal B
Moisture	%, ar	8.5	16.9
Volatiles	%, daf	34.2	40.2
Ash	%, df	9.7	10.7
LHV	MJ/kg, df	29.1	28.4
C	%, daf	80.7	78.4
O	%, daf	12.4	12.7
H	%, daf	4.8	5.5
N	%, daf	1.5	1.6
S	%, daf	0.6	0.7

ar - as received, daf - dry and ash-free, df - dry fuel

4. Results

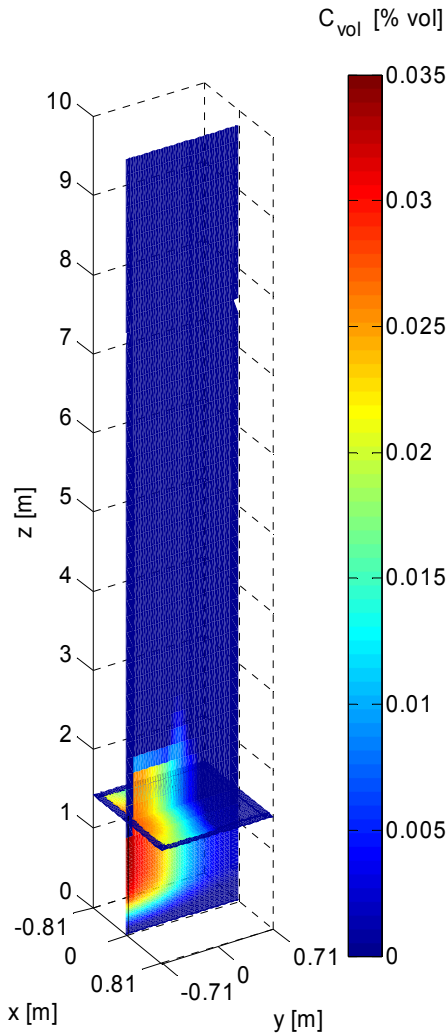


Figure 9: Modeled volumetric concentration of combustible volatiles (sum of hydrocarbons, H₂ and CO) for Run B.

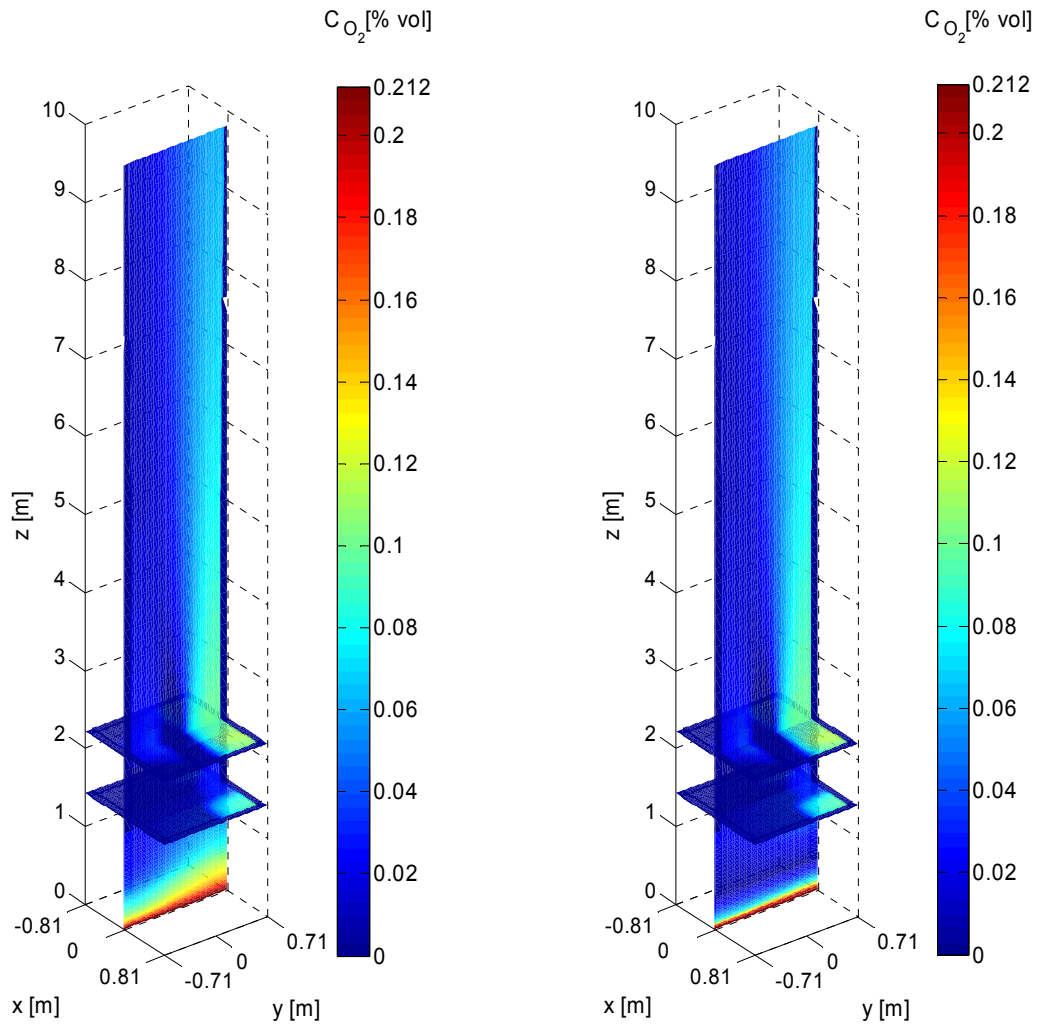
As mentioned above, the model of gas mixing and char combustion of this work (Eqs (1) to (17)) are combined with input data from other models (*i.e.* the fuel moisture and volatile release and the char concentration fields, modeled according to Pallarès and Johnsson (2007)) and the calculated oxygen concentration field in the furnace is modeled and compared to the *in-situ* measurements. For the calculations in this work, the penetration length of all gas jets injected in the freeboard (*i.e.* secondary air and gas from seal and classifier) is set to 0.35 m.

Figure 9 shows the modeled volumetric concentration of combustible volatile matter for Run B. As seen, all combustible volatiles released immediately above the air distributor are fully consumed and it is not until a few centimeters above the distributor that some of the released volatile matter remains unburned due to the lack of oxygen in some periods of the gas fluctuations, as explained above in relation to Fig. 7. This effect takes place mainly close to the fuel feeding point, where the volatile release rates are much higher than close to the rear wall, due to the kinetic rate of volatile release, which is fast compared to the horizontal fuel mixing rate. Thus, close to the fuel feeding point, the model predicts a build up of concentration in combustible volatiles with height. According to the model, these unburned volatiles are combusted by the secondary air flow injected from the front wall at a height of 2.1 m.

Figure 10 shows the modeled oxygen volumetric concentration for Run B. As observed, in the bottom region oxygen concentration decreases slightly faster with height closer to the front wall, which is due to the higher release of both volatile matter and moisture close to the fuel feeding point. The high volatile release implies a higher volatile combustion and thus oxygen consumption and the high moisture release leads to a more dilute, less concentrated oxygen flow. The lower horizontal slice in Fig. 10 shows the effect of the injection of gas coming from the ash classifier

(which is located at the rear wall, 0.2 m from the right wall). An increase in oxygen concentration is predicted also close to the corner between the back wall and the left wall due to injection of gas coming from the particle seal, although this is located in a dead angle in Fig. 10 and thus cannot be seen. The upper horizontal slice in Fig. 10 shows the modeled oxygen concentration immediately above the secondary air injections. Secondary air at a height of 2.1 m above the distributor is injected through the front and rear walls. As seen in the figure, oxygen injected from the front wall is mostly consumed (by combustion of unburned volatiles, as seen in Fig. 9) while oxygen from injected from the back wall hardly meets any unburned volatile matter (see Fig. 9) and therefore remains mostly unconsumed (although some oxygen consumption through char combustion takes place). Along the freeboard, horizontal convective mixing of the gas takes place due to the disturbance of the velocity field created by the secondary air injection at the same time as horizontal diffusion of gas species occurs. Both these phenomena lead to a significantly more homogeneous oxygen concentration in the upper freeboard than immediately above the secondary air injection.

As explained above, gas concentration measurements sampled with a gas probe can be simulated through Eq.(19). This has been done for the result data from the simulation of Run B and the obtained field is shown in Fig. 10b. It can be observed how values in the upper heights of the furnace (*i.e.* in the transport region) are the same as those shown in Fig. 10a, since both gas phases considered are assumed in the model to flow at the same velocity in this region, which leads to the same outcome from the use of Eqs.(18) and (19). However, concentration values for the simulated gas probe differ strongly from those in Fig. 10a in the bottom region of the furnace. As seen in Fig. 10b the probe-measured oxygen concentration presents a much more accentuated vertical gradient which leads to a bias in the results towards more oxygen-poor values.



a) Time-averaged oxygen concentration.

b) Oxygen concentration in Figure 10a as measured by a gas suction probe.

Figure 10: Modeled oxygen volumetric concentration for Run B.

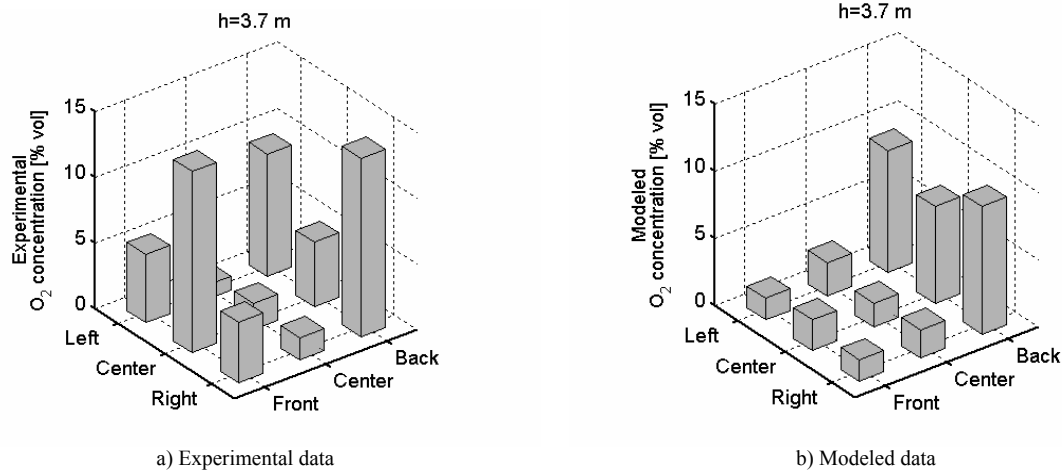


Figure 11: Comparison between measured and modeled cross-sectional data on oxygen volumetric concentration for Run B at $h=3.7$ m.

Figures 11 and 13 give comparisons between modeled and measured cross-sectional data on oxygen concentration available from Run B, with nine experimental values sampled (with a gas suction probe) over furnace cross sections at heights of 3.7 and 9.9 m respectively. Both these cross sections belong to the transport zone, where both gas phases are modeled to have the same gas velocity, so the modeled gas concentration takes the same values whether it is calculated through a true mass balance (*i.e.* Eq.(18)) or as seen by a gas suction probe (Eq.(19)).

It can be seen that there is a relatively good agreement between modeled and measured data, except for the value in the center of the front wall. The likely reason for this discrepancy is most likely related to blocking of secondary air nozzles. In the Chalmers CFB boiler, the secondary air ports (13 active nozzles for the present run: 7 in the front wall and 6 in the back wall) should in principle all provide the same air flow (which is also the assumption made in the modeling). However, partial and total plugging of the secondary air nozzles is a phenomenon often occurring in the boiler. The picture in Fig. 12 is taken at the furnace of the Chalmers boiler and shows partial plugging of a secondary air nozzle.



Figure 12: Partial blocking of a secondary air nozzle. Photo taken from inside the Chalmers CFB boiler.

A rather severe partial plugging is shown in the picture, but the different secondary air nozzles are affected by plugging to rather different extent, from no plugging to total plugging. This redistributes the injected secondary air between the different nozzles in a fashion which cannot be measured and, thus, remains unknown during operation. Measured values in Fig. 11a could indicate that there is such a redistribution between the nozzles. This, since the oxygen concentration in the front wall varies strongly with the highest value at the center of the wall. This pattern was observed in other runs, which supports the suggestion on the existence of plugging/partial plugging of some of the secondary air nozzles.

Figure 13 gives a corresponding comparison in the upper cross section ($h=9.9$ m). As seen from the measured values (Fig. 13a), oxygen is more uniformly distributed at upper locations in the furnace due to lateral mixing occurring along the transport zone and modeled by means of gas species mass flux diffusion. However, note that at this height (almost 8 meters above the secondary air injection) the consequence of the presumed effect of secondary air plugging is still seen: the highest oxygen concentration value is found at the center of the front wall (where, theoretically, this value should be low due to the locally high volatile release close to the fuel feeding point, in agreement with the modeled values in Fig. 13b).

Figure 13 gives a corresponding comparison in the upper cross section ($h=9.9$ m). As seen from the measured values (Fig. 13a), oxygen is more uniformly distributed at upper locations in the furnace due to lateral mixing occurring along the transport zone and modeled by means of gas species mass flux diffusion. However, note that at this height (almost 8 meters above the secondary air injection) the consequence of the presumed effect of secondary air plugging is still seen: the highest oxygen concentration value is found at the center of the front wall (where, theoretically, this value should be low due to the locally high volatile release close to the fuel feeding point, in agreement with the modeled values in Fig. 13b).

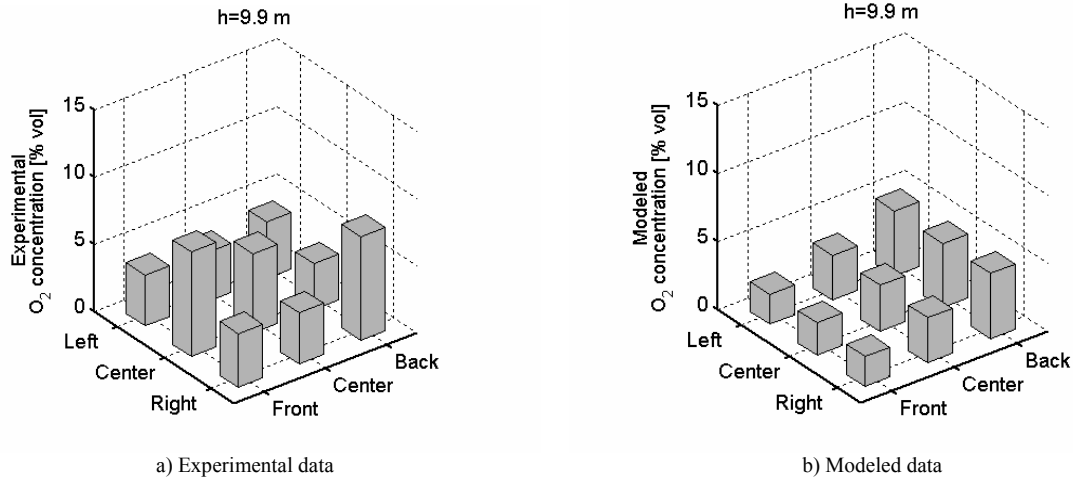


Figure 13: Comparison between measured and modeled cross-sectional data on oxygen volumetric concentration for Run B at $h=9.9$ m

Comparisons between modeled data and axial gas probe measurements from Runs A and B are shown in Fig. 14. The comparisons are carried out along the centerline of the back wall, at 0.37 m from the back wall). As seen from the experimental data for both plots, measured oxygen concentration increases along the splash zone (*i.e.* approximately in the height interval between 0.5 and 2 m). The modeled oxygen concentration (represented by a solid line) decreases steadily along the dense bottom bed and the splash zone, mainly due to volatile and char combustion. A sudden increase in oxygen concentration is observed at a height of 2.1 m due to secondary air injection followed by a decrease due to both char combustion and (mostly) horizontal dispersion of the oxygen. As seen, the modeled data which includes simulation of the gas probe (represented by a dashed curve) differs strongly from the modeled concentration curve in the bottom region of the furnace, showing lower values of the oxygen concentration. It is also seen that the gas probe simulation agrees with the measurement data in the bottom region, where there is a disagreement between experiments and raw (*i.e.* gas probe modeling not included) modeled data, in analogy with the above given discussion.

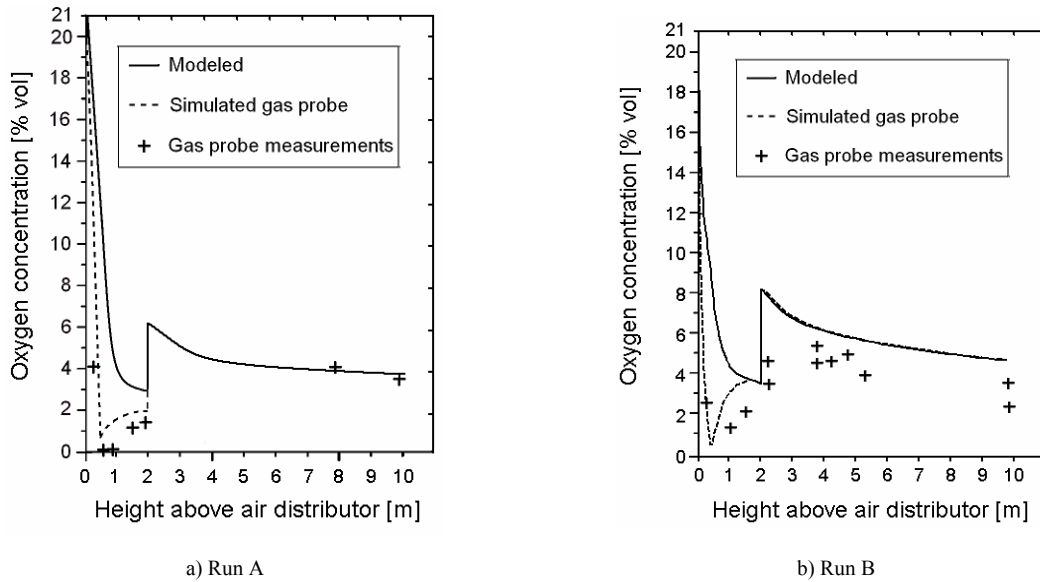


Figure 14: Comparison of measured and modeled vertical profiles of oxygen volumetric concentration at 0.37 m from the center of the back wall.

As observed, the curve corresponding to the probe simulation through Eq.(19) gives the expected lower oxygen concentration values (although it does not reach the almost zero values observed in Fig. 14 for Run A). Note that the curves in Figs 14a and 14b approach a common value as the differences in gas velocity decrease with height in the splash zone. In summary, it is shown that inclusion of a model for the gas sampling probe accounting for the gas phase division expressed in this paper is crucial in order to compare with in-situ measurements in the lower regions of a FB combustor, *i.e.* in regions where there are considerable fluctuations in gas velocities.

5. Conclusions

A modeling approach for the gas phase mixing in fluidized beds is presented. The model has been implemented and validated with experimental data from the Chalmers 12 MW CFB boiler. The model accounts for both the fluctuating nature of the gas flow and the existence of two different gas phases with different dynamics and composition, features which are necessary if the modeling should have a realistic coupling to the underlying physics of the gas mixing. The present approach allows a formulation of the gas combustion reactions as transport-controlled and thus, there is no need for an empirical fit of the kinetics. Good agreement between modeled data and experiments is observed.

In addition, the gas phase division employed by the model allows the simulation of gas probe measurements in the bottom region of the furnace, characterized by strongly varying gas velocities.

References

- Clift, R., Grace, J.-R. 1985. "Fluidization". Davidson, Harrison and Clift Eds., Academic Press Inc., London (UK).
- Darton, R., LaNauze, R., Davidson, J., Harrison, D. 1977. "Bubble-growth due to coalescence in fluidized beds". *Transactions of the Institution of Chemical Engineers*, 55, pp. 274-80.
- Ergun, S. 1952. "Fluid flow through packed columns". *Chemical Engineering Progress*, 48, pp. 89-94.
- Field, M.A., Gill, D.W., Morgan, B.B., Hawksley, P.G.W. 1967. "Combustion of pulverized coal". The British Coal Utilization Research Association, Surrey (England).
- Gayán, P., de Diego, L.F., Adánez, J. 1997. "Radial gas mixing in a fast fluidized bed". *Powder Technology*, 94 (2), pp. 163-171.
- Hannes, J.-P. 1996. "Mathematical modelling of circulating fluidized bed combustion". City-Print Verlag GmbH, Aachen (Germany). ISBN 3-88817-002-8.
- Johnsson, F., Leckner, B., 1995. "Vertical distribution of solids in a CFB furnace". *Proc. of the 13th Int. Conf. on FBC (Orlando, USA)*, pp. 671-679.
- Johnsson, F., Andersson, S., Leckner, B. 1991. "Expansion of a freely bubbling fluidized bed". *Powder Technology*, 68 (2), pp. 117-123.
- Knöbig, T. 1998. "Three-dimensional modeling of circulating fluidized bed combustion". PhD Thesis, Tech. Univ. of Hamburg-Harburg (Germany). Shaker Verlag, Aachen (Germany). ISBN 3-8265-4480-3.
- Kruse, M., Werther, J. 1995. "2D gas and solids flow prediction in circulating fluidized beds based on suction probe and pressure profile measurements". *Chemical engineering and processing*, 34 (3), pp. 185-203.
- Kruse, M., Schoenfelder, H., Werther, J. 1995. "Two-dimensional model for gas mixing in the upper dilute zone of a circulating fluidized bed". *Canadian Journal of Chemical Engineering*, 73 (5), pp. 620-634.
- Leckner, B., Golriz, M.R., Zhang, W., Andersson, B.Å., Johnsson, F. 1991. "Boundary layers - first measurements in the 12 MW CFB research plant at Chalmers University". *Proc. of the 11th Int. Conf. on FBC (Montreal, Canada)*, pp. 771-776.
- Lyngfelt, A., Åmand, L.-E., Leckner, B. 1996. "Progress of combustion in the furnace of a circulating fluidized bed boiler". *Proc. of the 26th Int. Symp. on Combustion (Naples, Italy)*, pp. 3253-3259.
- Niklasson, F., Pallarès, D., Johnsson, F. 2007. "Biomass co-firing in a CFB boiler – The influences of fuel and bed properties on in-furnace gas-concentration profiles". *Proc. of the 19th Int. Conf. on Fluidized Bed Combustion (Vienna, Austria)*.
- Niklasson, F., Johnsson, F., Leckner, B. 2003. "Local air ratio measured by zirconia cell in a circulating fluidised bed furnace". *Chemical Engineering Journal*, 96 (1-3), pp. 145-155.
- Okasha, F. 2007. "Modeling combustion of straw-bitumen pellets in a fluidized bed". *Fuel Processing Technology*, 88 (3), pp. 281-293.

- Olowson, P.A., Almstedt, A.-E. 1990. "Influence of pressure and fluidization velocity on the bubble behaviour and gas flow distribution in a fluidized bed". *Chemical Engineering Science* 45 (7), pp. 1733-1743.
- Pallarès, D., Johnsson, F. 2006. "Macroscopic modeling of fluid dynamics in large-scale circulating fluidized beds". *Progress in Energy and Combustion Science*, 32 (5), pp. 539-569.
- Pallarès, D., Johnsson, F. 2008. "Modeling fuel mixing in a fluidized bed combustor". *Accpeted for publication in Chemical Engineering Science*.
- Sasic, S., Leckner, B., Johnsson, F. 2005. "Fluctuations and waves in fluidized bed systems: the influence of the air-supply system". *Powder Technology*, 153 (3), pp. 176-195.
- Sternéus, J., Johnsson, F., Leckner, B. 2000. "Gas mixing in circulating fluidised-bed risers". *Chemical Engineering Science*, 55 (1), pp. 129-148.
- Sternéus, J., Johnsson, F. 1997. "Gas mixing in the wall layer of a CFB boiler". *Proc. of the 14th Int. Conf. on Fluidized Bed Combustion (Vancouver, Canada)*, pp. 1237-46.
- Stubington, J.F., Chan, S.W. 1990. "Interpretation of oxygen-probe measurements in fluidised-bed combustors". *Journal of the Institute of Energy*, 63 (456), pp. 136-142.
- Svensson, A., Johnsson, F., Leckner, B. 1996. "Bottom bed regimes in a circulating fluidized bed boiler". *International Journal of Multiphase Flow*, 22 (6), pp. 1187-1204.
- Werther, J., Hartge, E.U., Kruse, M. 1992. "Radial gas mixing in the upper dilute core of a circulating fluidized bed". *Powder Technology*, 70, pp. 293-301.
- Åmand, L-E. 1994. "Nitrous oxide emission from circulating fluidized bed combustion". PhD Thesis, Chalmers Univ. of Tech. (Sweden).

Acknowledgements

Financially support by the Swedish Energy Agency and Metso Power Oy is gratefully acknowledged.

Notation

A_0	Nozzle density, m ⁻²	H	Height interval, m
A_c	Char surface, m ²	h	Height, m
a	Decay constant, m ⁻¹	h_m	Mass transfer coefficient, m/s
c	Gas molar concentration, mole/m ³	m_c	Char mass, kg
C	Gas mass concentration, kg/m ³	P	Pressure, Pa
D_{bub}	Bubble diameter, m	R_{eff}	Effective combustion rate, m/s
D_{eq}	Equivalent diameter, m	R_{kin}	Kinetic combustion rate, m/s
d_p	Particle size, m	u	Gas velocity, m/s
f	Damp factor, -	u_0	Fluidization velocity, m/s
G	Mass flux, kg/m ² s	u_{mf}	Minimum fluidization velocity, m/s
g	Gravitational acceleration, m/s ²	v_{bub}	Bubble velocity, m/s

Greek letters

α	Gas dispersion coefficient, m ² /s	μ	Gas viscosity, kg/m·s
δ	Bubble fraction, -	σ	Relative cross section, -
ε_b	Dense bed voidage, -	ρ	Apparent density, kg/m ³
ε_{mf}	Minimum fluidization voidage, -	Ω	Conversion factor, kg C/mole O
Φ	Sphericity, -		

Subscripts

em	Emulsion-only gas phase
tf	Throughflow gas phase

Paper IV

Pallarès, D., Johnsson, F. (2006)

"A novel technique for particle tracking in cold 2-dimensional
fluidized beds - simulating fuel dispersion"

Chemical Engineering Science, 61 (8), pp. 2710-2720

A novel technique for particle tracking in cold 2-dimensional fluidized beds—simulating fuel dispersion

David Pallarès, Filip Johnsson*

Department of Energy and Environment, Energy Conversion, Chalmers University of Technology, SE-412 96 Göteborg, Sweden

Received 1 April 2005; received in revised form 29 September 2005; accepted 16 November 2005

Available online 18 January 2006

Abstract

This paper presents a novel technique for particle tracking in 2-dimensional fluidized beds operated under ambient conditions. The method is applied to study the mixing mechanisms of fuel particles in fluidized beds and is based on tracking a phosphorescent tracer particle by means of video recording with subsequent digital image analysis. From this, concentration, velocity and dispersion fields of the tracer particle can be obtained with high accuracy. Although the method is restricted to 2-dimensional, it can be applied under flow conditions qualitatively resembling a fluidized-bed combustor. Thus, the experiments cover ranges of bed heights, gas velocities and fuel-to-bed material density and size ratios typical for fluidized-bed combustors. Also, several fluidization regimes (bubbling, turbulent, circulating and pneumatic) are included in the runs.

A pattern found in all runs is that the mixing pattern of the tracer (fuel) solids is structured in horizontally aligned vortexes induced by the bubble flow. The main bubble paths always give a low concentration of tracer solids and with the tracer moving upwards, while the downflow of tracer particles in the dense bottom bed is found to take place in zones with low bubble density and at the sidewalls. The amount of bed material (bed height) has a strong influence on the bottom bed dynamics (development and coalescence of bubbles) and, consequently, on the solids mixing process. Local dispersion coefficients reach maximum values around the locations of bubble eruptions, while, in the presence of a dense bottom bed, an increase in fluidization velocity or amount of bed material enhances dispersion. Dispersion is found to be larger in the vertical than in the horizontal direction, confirming the critical character of lateral fuel dispersion in fluidized-bed combustors of large cross section.

© 2005 Elsevier Ltd. All rights reserved.

Keywords: Fluidization; Mixing; Dispersion; Fuel; Combustion; Digital image analysis

1. Introduction

In fluidized-bed combustion, a high enough fuel dispersion is crucial in order to ensure good mixing of fuel and combustion air (i.e., to obtain a satisfactory burnout while keeping the excess air ratio as low as possible), at the same time as the number of fuel feed points must be kept small. Consequently, fuel mixing is known to be critical in large fluidized-bed units which may have cross sectional areas up to several hundreds of square meters.

Evaluating fuel mixing requires modelling of both fuel dispersion and conversion (drying, devolatilization and char burnout). With respect to fuel conversion, literature gives a number of particle combustion models shown to give satisfactory results (Agarwal et al., 1986; Palchonok et al., 1997;

Peters and Bruch, 2001; Thunman et al., 2002). On the other hand, no models of practical application based on the underlying physics are available for particle mixing, since numerical modeling (CFD simulations) from first principles (e.g. Enwald et al., 1996; van Wachem et al., 2001; Peirano et al., 2002) yield long calculation times and still give uncertain results for conditions applicable to fluidized-bed combustors. In addition, such simulations are still more or less restricted to beds with solids of one size and density. Some semiempirical models express the solids mixing in form of dispersion coefficients (Lin and Chyang, 2003; Du and Wei, 2002). These models focus mainly on modeling the vertical mixing in laboratory fluidized-bed units where, due to their narrow geometry, this is the critical direction for solids mixing, although horizontal solids dispersion coefficients have also been measured in narrow units (Mostoufi and Chaouki, 2001; Fan et al., 1986). However, as mentioned above, in large fluidized-bed units such as boilers solids mixing is critical in the horizontal direction, due to the low bed-height

* Corresponding author. Tel.: +46 31 772 1449; fax: +46 31 722 3592.

E-mail address: filip.johnsson@me.chalmers.se (F. Johnsson).

to bed-width ratio. There is some work on horizontal solids mixing in large fluidized-bed units which is based on estimating an effective horizontal dispersion coefficient (Highley and Merrick, 1971; Xiang et al., 1987; Schlichthaerle and Werther, 2001; Niklasson et al., 2002) showing that such large units give dispersion coefficients which are an order of magnitude larger than those found in the above-mentioned narrow laboratory CFB units. In summary, modeling of the mixing of fuel particles in a large fluidized bed based on the phenomenology behind the process is not available at present. In fact, little is known about the basic physics behind the mixing process, since it is experimentally difficult to study the mixing with the process obviously being highly dynamic, the latter especially valid under industrial conditions. Thus, there is need to apply experimental techniques which can resolve the particle mixing in both space and time.

Particle tracking techniques can provide valuable information on the governing mechanisms of solids mixing. In the case of fluidized beds, several particle tracking techniques have been used to investigate solids mixing. Although non-tracking techniques providing local data, such as Laser Doppler Anemometry (Ibsen et al., 2002) or the use of radio transmitters (van Barneveld et al., 1987) exist, these are not able to provide information on the trajectory of a single particle. For 3-dimensional units, various tomography-tracking techniques have been applied both in narrow laboratory units and in scale models of large fluidized beds. In the latter case, works are available based on γ -ray emission (Parker et al., 1993; Larachi et al., 1994; Dudukovic, 2002), X-ray (Grassler and Wirth, 2000) and electrical capacitance (Du et al., 2002). In scale models of large fluidized beds, scaling relationships (see Glicksman, 1984, and references therein) have to be applied if the conditions should resemble those of a fluidized-bed combustor. Stein et al. (2002) applied γ -ray-based particle-tracking tomography to validate a simplified set of scaling laws in the viscous limit. In 2-dimensional units, solids mixing have been studied using optical techniques (Guo et al., 2001; Bokkers et al., 2004; Shen et al., 2004) which enable direct observation of the bed dynamics simultaneously with measurements, but these 2-dimensional studies are obviously limited to qualitative analyses.

The above experimental investigations are mostly directed towards studies on flow and mixing of the bed material itself, using a tracer particle that mimes the bed material. When mixing of a fuel particle is to be studied, as in the works by Lim and Agarwal (1994) and Rios et al. (1986), the tracer particle should typically have larger size and lower density than the bed material.

There is a need to investigate the phenomenology of solids mixing under conditions relevant for fluidized-bed combustors, covering a large range of operational conditions and focusing on the fuel mixing. This work introduces a novel particle tracking method for 2-dimensional fluidized beds, with the tracer particle simulating a fuel particle and the operational conditions employed qualitatively resembling the dynamics of fluidized-bed combustors. The method is robust in that the dynamics of the mixing can be studied over a wide range of operational parameters allowing for a fundamental study on the phenomenology

of solids mixing. However, the results are limited to qualitative interpretation, since quantitative analysis would require measurements in a real combustor or a 3-dimensional unit operated according to scaling laws. Still, the present work is motivated by the low level of knowledge on the fundamentals behind the fuel mixing process.

2. Experiments and image analysis

The particle-tracking technique is based on capturing the phosphorescence of a single particle in a 2-dimensional fluidized bed with a transparent front wall. To maximize phosphorescence, the riser is placed in a dark chamber. In addition, a special digital camera equipped with an enhanced digital gain circuitry is used (up to -24 dB at a shutter speed of 4×10^{-2} s). This technique presents two main advantages compared to tracking of pigmented particles as was applied in a first step of this work (Shen et al., 2004): the contrast between a phosphorescent particle and its dark surrounding is much sharper than between a colored particle and the bed material, and the use of glass beads as bed material allows phosphorescence to be seen also in cases where the tracer particle is behind the bed material. Both of these facts increase the percentage of videoframes in which the tracer particle is detected in the digital image analysis (95% compared to around 65% when using pigmented particles in the same unit, c.f. Shen et al., 2004). A recording time of 20 min per run (yielding around 30,000 videoframes to be used in the subsequent digital image analysis) was chosen based on an analysis of three 40-min runs at three different fluidization regimes which showed that recordings longer than 15 min provided no significant additional information.

The experimental facility used (shown in Fig. 1) is a 2-dimensional cold riser with a cross-section of $0.02 \text{ m} \times 0.4 \text{ m}$ and a height of 2.15 m, having a perforated plate as air distributor. The front side of the riser is made of transparent Perspex, which enables visual observation and videorecording of the flow. Since the solids mixing in the bottom region is the focus of this work, only the first 0.85 m of the riser is video recorded.

Glass beads with size and density values similar to those of sand particles typically used in fluidized-bed boilers are used as bed material; $d_{s,\text{bed}} = 330 \mu\text{m}$ and $\rho_{s,\text{bed}} = 2600 \text{ kg/m}^3$ (belonging to the Group B in the Geldart classification and having a minimum fluidization velocity $u_{mf} = 0.12 \text{ m/s}$ and a terminal velocity $u_t = 1.76 \text{ m/s}$ under ambient conditions). Hence, the bed solids are not scaled but the operational conditions (fluidization velocity, bed height and bed-height to bed-width ratio and air-distributor pressure drop) cover conditions with an overall flow pattern similar to that in bubbling fluidized-bed boilers as well as in the bottom bed of circulating fluidized-bed boilers.

Tracer particles used are cylindrical capsules made of transparent plastic filled with a self-phosphorescent solution. The so-called *reference* tracer particle (used in most of the experimental runs) has a larger size and a lower density compared with the bed solids, making it suitable for simulating a fuel particle in a fluidized-bed boiler. In order to study the influence

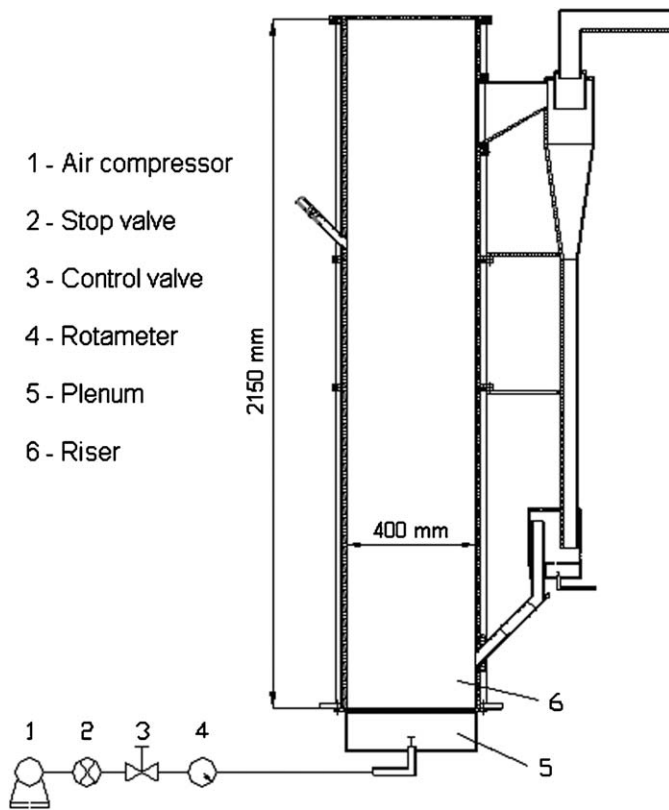


Fig. 1. Experimental facility. The riser has a cross section of $0.02 \text{ m} \times 0.4 \text{ m}$ and a height of 2.15 m.

Table 1
Properties of tracer particles used

Tracked particle	Height (mm)	Diameter (mm)	Density (kg/m^3)	Terminal velocity (m/s)
Reference	12	10	985	10.9
SS	6	5	985	7.5
HD	12	10	2760	19.2

of size and density of the tracer particle, two additional types of tracer particles were used: one type smaller in size (type “SS”) and one with higher density, similar to that of the bed solids (type “HD”). Table 1 summarizes sizes and densities of the tracer particles used in the experiments.

The method of evaluation is based on tracking a single particle in each experimental run, so interactions between fuel particles are assumed not to influence their mixing process, which is reasonable knowing that the fuel fraction represents only between 1% and 3% of the total bed material in fluidized-bed boilers. With this assumption, the probability of presence of a single tracer particle can be seen as concentration value at steady state, C_{fuel} , normalized so that:

$$\int_A C_{\text{fuel}} dA = 1. \quad (1)$$

Table 2
Conditions in experimental runs

Run	Fluidization velocity (m/s)	material (kg)	Tracked particle	Height of dense bottom bed (m)
1	0.40	1.5	Reference	0.15
2	1.11	1.5	Reference	0
3	1.74	1.5	Reference	0
4	1.11	4.0	Reference	0.25
5	0.40	5.0	Reference	0.48
6	0.54	5.0	Reference	0.49
7	0.95	5.0	Reference	0.50
8	1.11	5.0	Reference	0
9	0.40	7.0	Reference	0.69
10	0.95	7.0	Reference	0
11	0.40	1.5	SS	0.15
12	1.11	1.5	SS	0
13	0.40	4.0	SS	0.32
14	1.11	4.0	SS	0.25
15	0.40	1.5	HD	0.15
16	0.40	4.0	HD	0.32

Or, expressed in the discrete form employed in digital image analysis by using a total of N pixels:

$$\sum_{i=1}^N C_{\text{fuel},n} A_n = 1 \quad \text{with } n = 1, \dots, N. \quad (2)$$

A total of 4 parameters have been varied in the experiments in order to study their influence on the mixing process: the fluidization velocity, u_0 , the amount of bed material, m_{bed} , and the size and density of the tracer particle, $d_{s,\text{fuel}}$ and $\rho_{s,\text{fuel}}$, respectively. Table 2 lists the combinations of these parameters applied in the experimental runs.

The time-averaged height of the dense bottom bed is obtained from an analysis of the video frames and the values are included in Table 2 (a value of “0” indicates absence of a dense bottom bed, i.e., pneumatic transport regime). The fluidization velocity, u_0 , was always lower than the terminal velocity of the average size of the bed particles forming the bed material ($u_{t,\text{bed}} = 1.76 \text{ m/s}$). Still, circulating conditions or even pneumatic transport regime could be reached already at a fluidization velocity of around 1 m/s. This can be explained by the parabolic gas velocity profile established along the narrow dimension of the cross section, with local velocities in the center of the cross section considerably higher than the average velocity. This is one reason why results from 2-dimensional units can only be qualitatively interpreted.

With respect to the representation of the results, the velocity field is given in form of a vector plot with the normalized concentration field plotted in the background. The height of the dense bottom bed, if existing, is indicated by a horizontal black line.

Local values of the solids dispersion coefficients (at each pixel) have been calculated as

$$D_{k,n} = \frac{\Delta t_{k,n}^2}{2 \cdot \Delta t_n} \quad \text{with } k = x, y \quad \text{and} \quad \text{for } n = 1, \dots, N. \quad (3)$$

Methods for calculation of the local dispersion coefficients from experiments vary widely in literature. By setting Δt_n equal to the shutter time of the videocamera (i.e., very low, generally in the order of 10^{-2} s or lower) and thus taking $\Delta l_{k,n}$ as the displacement occurred from one videoframe to the following implies values of the dispersion coefficient that do not account for the history of the trajectory. On the other hand, setting large values of Δt_n in such a small unit as the one applied in this work increases the risk of a value of Δt_n larger than the characteristic time for solids mixing in the unit, resulting in an underestimation of the dispersion coefficient. A more robust and reliable calculation strategy is to set the distance $\Delta l_{k,n}$ instead of Δt_n . For eminently convective flows (as the present case), $\Delta l_{k,n}$ has to be given relatively high values in order to capture the history of the trajectory and minimize the dependence of the result on the election of $\Delta l_{k,n}$. Thus, in the present work $\Delta l_{k,n}$ is therefore set to 0.1 m for all cases analyzed. Thus, Δt_n is defined as the time it takes for the tracer particle at each point on its trajectory to reach the distance of 0.1 m.

The global dispersion coefficient of a given run is calculated by weighting the local dispersion coefficients with respect to concentration of tracer particle, i.e.,

$$\overline{D_k} = \sum_{n=1}^N C_{\text{fuel},n} \cdot A_n \cdot D_{k,n} \quad \text{with } k = x, y \quad \text{and} \quad \text{for } n = 1, \dots, N. \quad (4)$$

3. Results

3.1. General pattern

In all runs having a dense bottom bed, preferred bubble paths were observed as schematically illustrated in Fig. 2. This phenomenon is typical for units with low pressure drop across the air distributor, such as the present unit and also large industrial fluidized-bed units (Werther, 1977). These bubble paths, which can easily be identified by visual observations, exhibit in all runs the lowest tracer particle concentration values in the dense bottom bed as well as ascending velocities of the tracer particle. This is exemplified in Figs. 3 and 4, which, respectively show frames from the video recordings and corresponding results from the digital image analysis. In Fig. 4a (corresponding to Run 1 in Table 2), two preferred bubble paths can be identified as vertical channels through the bottom bed, with low concentration and upward velocities. A video frame for the corresponding run is given in Fig. 3a in which these two bubble paths can be seen.

All runs exhibit flow pattern of the tracer particle which can be characterized by horizontally aligned vortices with alternated rotational direction, as indicated in Fig. 2. This vortex structure is induced by the fact that preferred bubble paths act as ascending channels for the tracer particle through the dense bottom bed. After reaching the bottom bed surface, the tracer particle is thrown into the splash zone, where it exhibits a fast horizontal displacement before sinking again in the bottom bed through the emulsion phase. In a 3-dimensional case, this pattern presumably leads to the formation of a toroidal flow

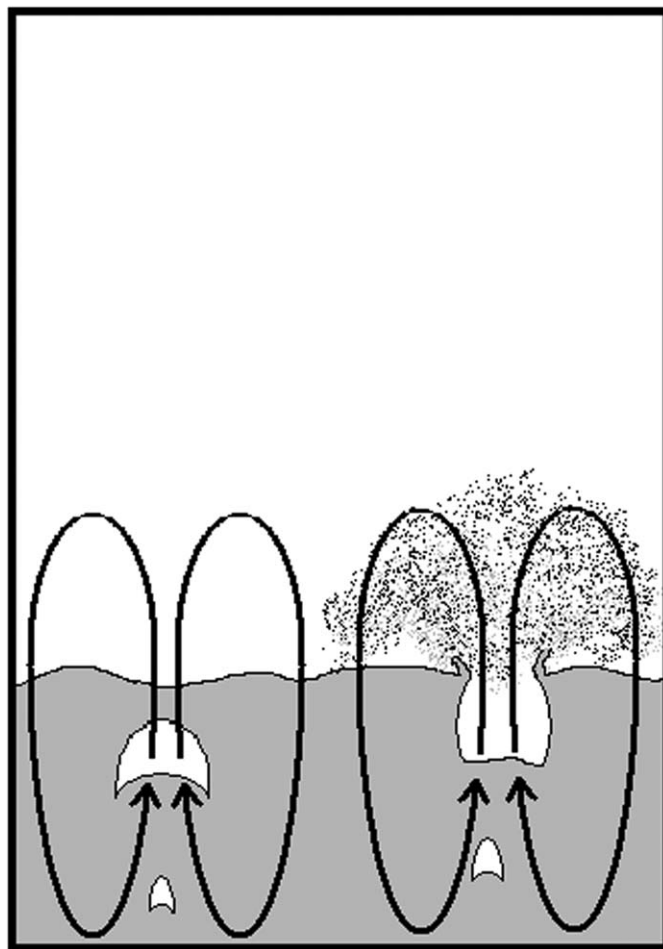


Fig. 2. Schematic illustration of the flow structure of the tracer particle as obtained from the experiments in this work.

structure around each preferred bubble path, whose cut section in form of two vortices along each preferred bubble path can be identified in the present 2-dimensional observations. From this, the number of vortices in the presence of a dense bottom bed is even and depends on the amount of main bubble paths, as can be seen in Fig. 4a (two main bubble paths and four vortices) and Fig. 4b (one main bubble path and two vortices).

Highest concentration values are found at the rotational centerpoints (or centerlines) of the vortices. The centerpoint (or upper end of the vertical centerline) is located close to the dense bottom bed surface (see Fig. 8 below). Another general observation is that neighboring vortices sharing downflowing parts do not have their points of highest tracer particle concentration in their respective rotational centers but in their common interface. This is for example seen in Fig. 4a, with a total of 4 vortices, where the second and third ones share a single high concentration zone (centerline of bed).

3.2. Influence of amount of bed material

One of the main operational parameters in fluidized-bed units is the pressure drop over the riser, which can be increased or decreased by, respectively, adding or subtracting bed material.

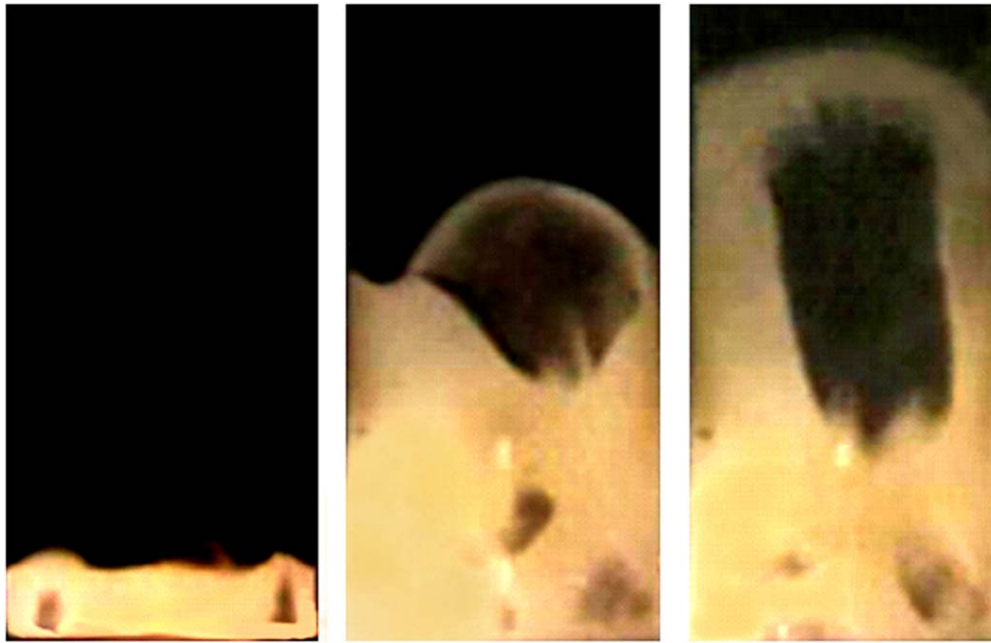


Fig. 3. Videoframes showing the development in the flow pattern with an increase in amount of bed material.

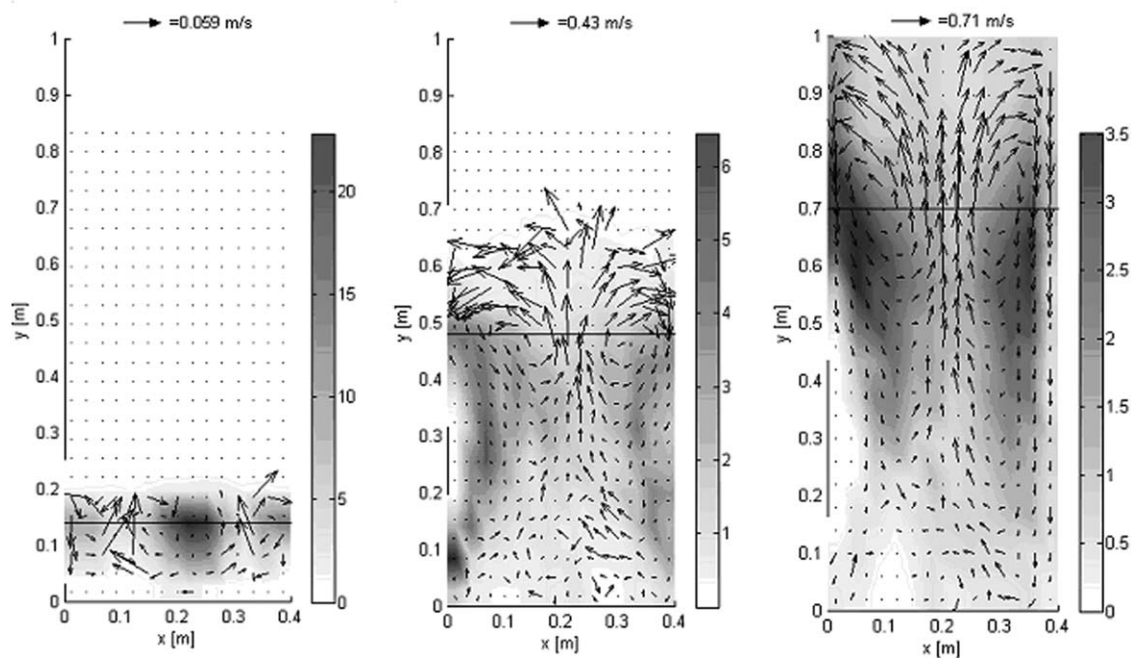


Fig. 4. Development of normalized concentration (m^{-2}) and velocity of tracer particle (m/s) with an increase in amount of bed material (note the different scales in the velocity vector plots). The horizontal line indicates the level of the time-averaged bottom bed height.

In practical terms, this has a direct effect on the dense bottom bed height, which becomes higher as bed material is added (see Fig. 3) provided the fluidization velocity is below the terminal velocity of the bed material. The value of the dense bottom bed height in each run is given in Table 2.

Bubble coalescence is known to be enhanced by increasing the dense bottom bed height (Darton et al., 1977; de Korte

et al., 2001). Thus, adding bed material lowers, by means of bubble coalescence, the number of preferred vertical bubbles paths, and, consequently, the number of vortices in the flow structure. All cases shown in Figs. 3 and 4 are characterized by a bubbling regime. Data from Runs 1, 5 and 9 (shown in Figs. 4a–c), for which the amount of bed material is varied at a constant fluidization velocity, exemplify a change from a

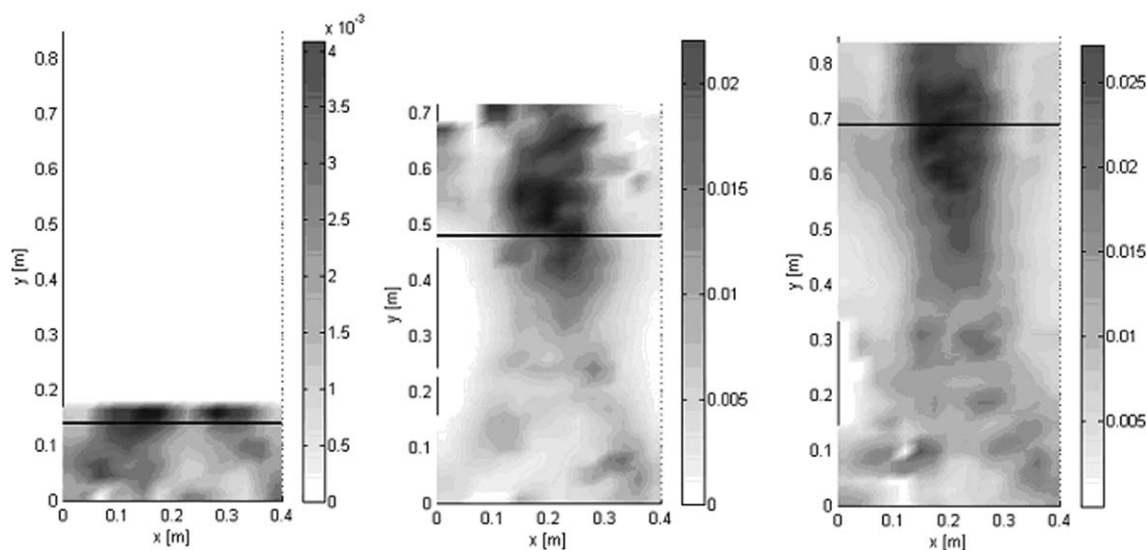


Fig. 5. Development of local horizontal dispersion coefficients (m^2/s) with an increase in amount of bed material. The horizontal line indicates the level of the time-averaged bottom bed height.

4-vortexes structure with 2 main bubble paths (Run 1) to a 2-vortexes structure with one main bubble path (Runs 5 and 9).

Through the operational range covered by all runs, the number of vortexes forming the flow structure was found to depend only on the amount of bed material and not on the regime or the fluidization velocity. However, this behavior might not prevail beyond the operational ranges tested and, therefore, cannot be taken as a general statement. In the presence of a dense bottom bed, this behavior is expected, since it is known (Darton et al., 1977) that the amount of main bubble paths (and thereby, of vortexes in the flow pattern of the tracer particle) has a higher dependence on the dense bottom bed height (strongly related to the amount of bed material) than on fluidization velocity. On the other hand, observation of this behavior in the absence of a dense bottom bed (as seen in Runs 2, 3 and 12, for which tracer particle flow patterns are all governed by a 4-vortexes structure) is not available in literature and, as mentioned above, this behavior might not prevail at higher fluidization velocities.

In addition to the number of vortexes in the flow structure, the amount of bed material is also found to have a strong influence on the concentration and velocity fields of the tracer particle. The results shown in Figs. 4a–c show how the highest concentration values of the tracer particle decrease drastically as the bed mass is increased, resulting in a considerable increase in the velocity of the tracer particle although the fluidization velocity is kept constant (note the change in scales between the figures). An increase in bed height results in bubbles growing larger (from coalescence as well as from inflow from the dense phase) and reaching a higher velocity and, as a result, the tracer particle dragged upwards by the bubble flow reaches higher velocities. Bubbles from Runs 1, 5 and 9 shown in Fig. 3 show a large difference in size. As expected, bursts of the larger and faster bubbles in Fig. 3c throw the tracer particle higher up in the freeboard than what is obtained from smaller bubbles in Run 1, indicating a more vigorous splash zone than for the low bed mass case (Fig. 3a).

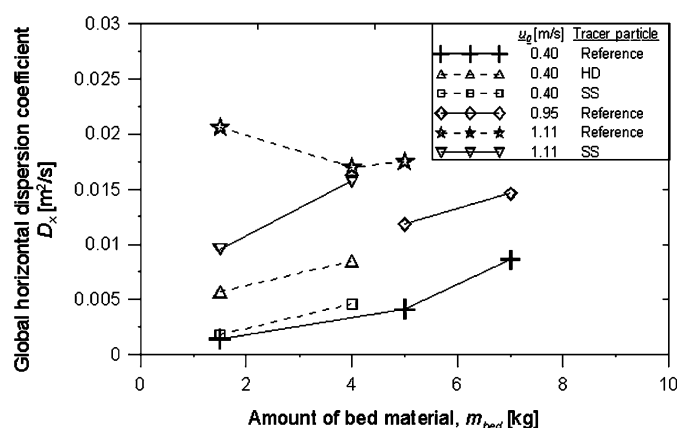


Fig. 6. Global horizontal dispersion coefficients (as obtained from Eq. (4)) for different amount of bed material.

Fig. 5 shows the distribution of the local horizontal dispersion coefficient as obtained from Eq. (3). It can be seen for all three runs (Figs. 5a–c) that the highest dispersion values coincide with the locations of bubble bursting (two main bubble paths are identified in Run 1 and bubble coalescence leads to a single main bubble path in Runs 5 and 9). Also, the lowest values of the horizontal dispersion are obtained near the bottom bed surface close to the sidewalls, i.e., where the fuel particles are most likely to end up after being fed into the unit (with over bed feed) if no special measures against this are taken. Thus, these results may motivate installations of equipment avoiding fuel particles to end up in these zones after injection into the riser from the fuel feeder.

Fig. 6 shows the dependence of the global horizontal dispersion coefficient (Eq. (4)) on the amount of bed material, with values corresponding to the above mentioned runs (Nos. 1, 5 and 9) marked with crosses. A complete list of values of the global dispersion coefficients obtained for all runs is given in

Table 3
Global dispersion coefficients

Run	$D_x \times 10^2 \text{ (m}^2/\text{s)}$	$D_y \times 10^2 \text{ (m}^2/\text{s)}$
1	0.14	0.04
2	2.06	2.93
3	0.93	1.77
4	1.70	4.19
5	0.41	0.83
6	0.89	2.18
7	1.18	3.89
8	1.75	4.62
9	0.86	2.51
10	1.46	4.22
11	0.18	0.21
12	0.96	2.58
13	0.46	0.89
14	1.57	6.74
15	0.57	0.61
16	0.85	1.27

Table 3. Data in Fig. 6 correspond to runs under different fluidization regimes, and interconnected symbols correspond to runs with the same fluidization velocity and type of tracer particle. An increased amount of bed mass results in an increased global horizontal dispersion coefficient, except in one particular case. Thus, the higher the dense bottom bed, the higher the overall lateral mixing rate, i.e., a higher bed (with less frequent but more vigorous bubbles) spreads fuel more effectively than a low bed (with more frequent but smaller bubbles). The exception to this trend is represented by Run 2 (corresponding the highest value for D_x in Fig. 6), in which no dense bottom bed is present (no bubbles are observed) but a solids suspension dense enough to displace the “Reference” tracer particle.

3.3. Influence of fluidization velocity

Runs number 5–8 (with typical video frames shown in Fig. 7) correspond to different fluidization regimes which is obtained by gradually increasing the fluidization velocity while all other parameters are kept constant ($m_{\text{bed}} = 5 \text{ kg}$, with “Reference” particle).

Run 5 (Fig. 7a) corresponds to a low velocity bubbling fluidized bed, with clear-cut bubbles rising through the bed and erupting at a rather constant frequency, resulting in a small splash zone above the bed surface. An increase in fluidization velocity (Run 6, Fig. 7b) results in larger, faster and more jet-shaped bubbles that occasionally extend all the way from the air-distributor to the bed surface, creating a low pressure drop channel for the fluidization air during the eruption of the bubbles yielding a high throughflow of gas (see Svensson et al., 1996 for a thorough description of this regime). Under these conditions, bed dynamics are still rather periodic with a low density of solids suspension above the bottom bed surface. With a further increase in fluidization velocity (Run 7, Fig. 7c), the bed enters an exploding bubble regime where throughflow turns from occasional to a main characteristic of the flow pattern, coexisting with erupting jet-shaped bubbles, with no clearcut

periodical pattern in the bubble flow. The solids suspension above the bottom bed surface increases and pronounced downflowing wall layers are formed. This is the typical regime for the dense bottom bed and splash zone of a CFB unit. Finally, with a further increase in fluidization velocity, the transport velocity is reached and a dense bed can no longer be maintained, i.e., these conditions are similar to pneumatic transport (Run 8, Fig. 7d). The flow regime is characterized by a flow structure with a dilute core and denser regions near the riser walls. In the central region the gas and solids flow are primarily directed upwards and, provided the solids suspension is dense enough to drag the tracer particle upwards, the tracer particle is moving upwards in the central part and descending in the denser downflowing solids wall-layers, i.e., there is a net lateral solids flow from the center of the riser to the side walls in the upper part of the riser and in the opposite direction in the bottom part. This structure extends up through the entire riser and results in an increased flow of externally recirculated solids.

Results from the digital image analysis of Runs 5–8 are shown in Fig. 8. Firstly, it is observed that a 2-vortexes flow structure is kept under all runs (with upflow in the center of the riser and downflow by the sidewalls), which is in agreement with the above conclusion that the number of vortexes depends to a large extent on the amount of bed material. It is also seen that, within the domain studied, the velocity of the tracer particle increases with gas velocity as long as a dense bed exists, but decreases in the freeboard when the dense bed disappears at a sufficiently high fluidization velocity. Thus, existence of a dense bottom bed with fast exploding bubbles (Fig. 8c) gives high initial velocities of the particles projected into the freeboard, i.e., higher than what the dispersed flow without a dense bed (Fig. 8d) can produce even at a higher gas velocity (1.11 m/s compared with 0.92 m/s). This should be expected since the momentum of bed solids is considerably higher than that of the gas, i.e., the higher the concentration of bed solids the higher is the momentum which can act on the tracer particle.

Fig. 9 gives corresponding distribution of local horizontal dispersion coefficients for the above-mentioned series of runs (Runs 5–8). As for the vertical dispersion in the presence of a dense bottom bed, the horizontal dispersion increases with fluidization velocity, with the highest values obtained around the locations of bubble eruptions. Highest dispersion is seen in the dense bottom bed and low values are found in the vicinity of the sidewalls. There is a significant change in the picture as the fluidization velocity is increased further, so that the unit is operated without a dense bottom bed: local horizontal dispersion coefficients are higher and more evenly distributed. However, this high horizontal dispersion observed in Run 8 (note the different scales used in Fig. 9) cannot be considered a general characteristic for pneumatic transport conditions, but decreases as fluidization velocity is further increased. This, since the solid phase becomes more dilute as the fluidization velocity is increased, resulting in a reduction in the momentum exchange between bed material and tracer particle and, as a result, yielding a corresponding reduction in the global dispersion coefficient as fluidization velocity is increased. This can be observed

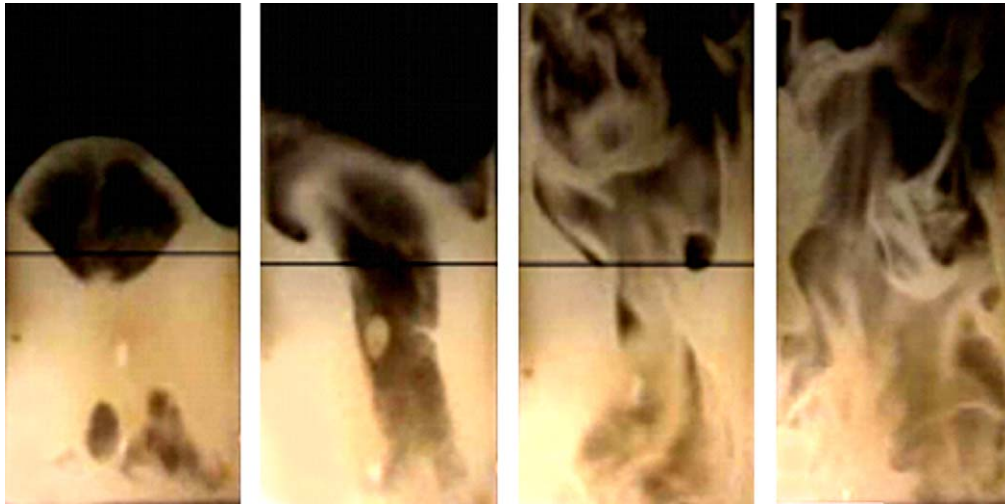


Fig. 7. Videoframes showing the development in the flow pattern with an increase in fluidization velocity. The horizontal line indicates the level of the time-averaged bottom bed height.

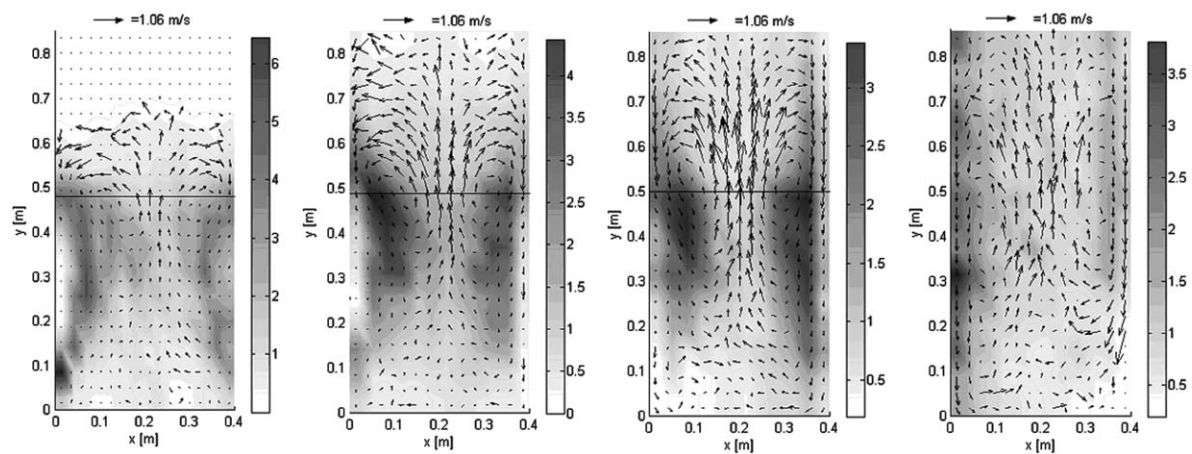


Fig. 8. Development of normalized concentration (m^{-2}) and velocity of tracer particle (m/s) with an increase in fluidization velocity. The horizontal line indicates the level of the time-averaged bottom bed height.

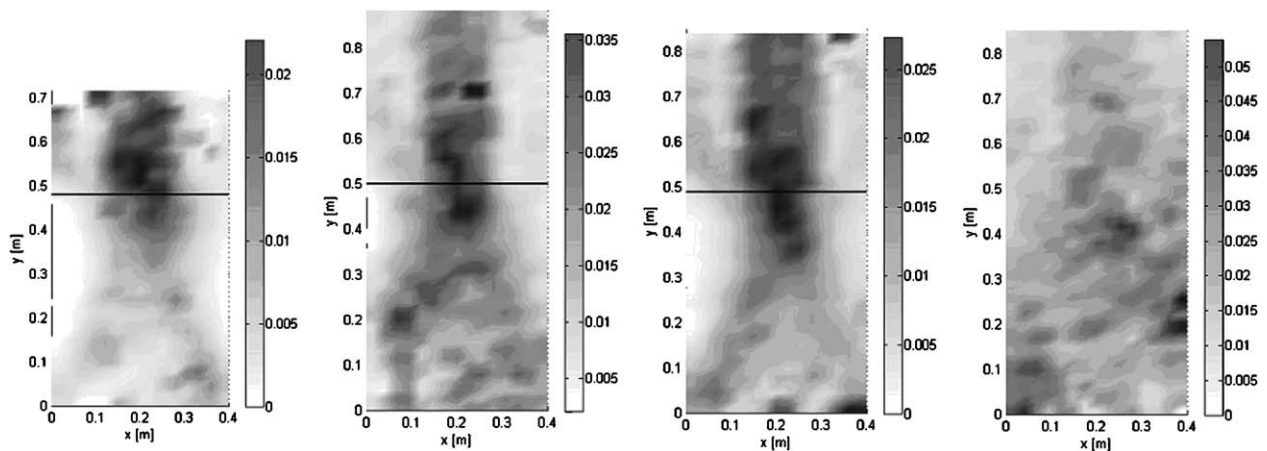


Fig. 9. Development of local horizontal dispersion coefficients (m^2/s) with an increase in fluidization velocity. The horizontal line indicates the level of the time-averaged bottom bed height.

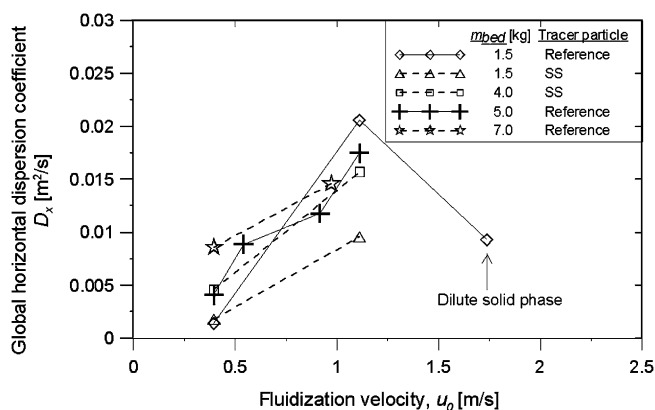


Fig. 10. Global horizontal dispersion coefficients (as obtained from Eq. (4)) for different fluidization velocities.

from a comparison of Runs 2 and 3, both under pneumatic transport regime and with a fluidization velocity of 1.11 m/s and 1.74 m/s, respectively: the highest velocity case gives a reduction of 55% in the global horizontal dispersion coefficient. In all cases where there is no bottom bed, the distribution of the local horizontal dispersion coefficient is rather uniform.

Fig. 10 shows the dependence of the global horizontal dispersion coefficient on fluidization velocity for different amounts of bed material and types of tracer particle. The runs shown in Fig. 9 (Runs 5–8) are marked with crosses. There is a clear trend indicating that the dispersion increases with fluidization velocity as long as a dense bottom bed is maintained. On the other hand, under pneumatic transport conditions and beyond a certain value of the fluidization velocity, dispersion of the tracer particle decreases with an increase in fluidization velocity, as discussed above (see transition from Runs 2 to 3).

3.4. Influence of size of tracer particle

Comparison between the “Reference” and the “SS” tracer particles gives a picture of the influence of the size of the tracer particle, illustrated in Fig. 11 (showing results from Runs 2 and 11, both corresponding to a bubbling regime). There is a significant increase in the velocity of the tracer particle as its size is decreased. As expected, the 4-vortexes flow structure induced by the bed material is maintained. From Fig. 11 it can also be seen that the smaller tracer particle (“SS”) tends to occupy also the lower part of the dense bottom bed (where there are nearly no occurrences of the “Reference” tracer particle), and, consequently, a more homogeneous concentration distribution in the vertical direction is obtained with the smaller tracer particle. Comparison of runs under the exploding bubble regime (Runs 4 and 14) gives a similar observation: a more homogeneous distribution of the concentration field in the vertical direction when the smaller “SS” particle is used. Thus, in presence of a dense bottom bed, global horizontal dispersion coefficients remain nearly unaffected by changes in size of the tracer particle, while vertical dispersion is strongly increased when a tracer particle with a smaller size is used.

For transport conditions (no dense bottom bed) a change in size of the tracer particle gives no significant change in the results (Runs 2 and 12).

3.5. Influence of density of tracer particle

Results from Runs 1 and 15, with identical operational conditions except for different density of the tracer particle, are shown in Fig. 12. An increase in the density of the tracer particle (“HD” particle) leads to a drastic change in the concentration field with high concentration zones replaced from the bottom

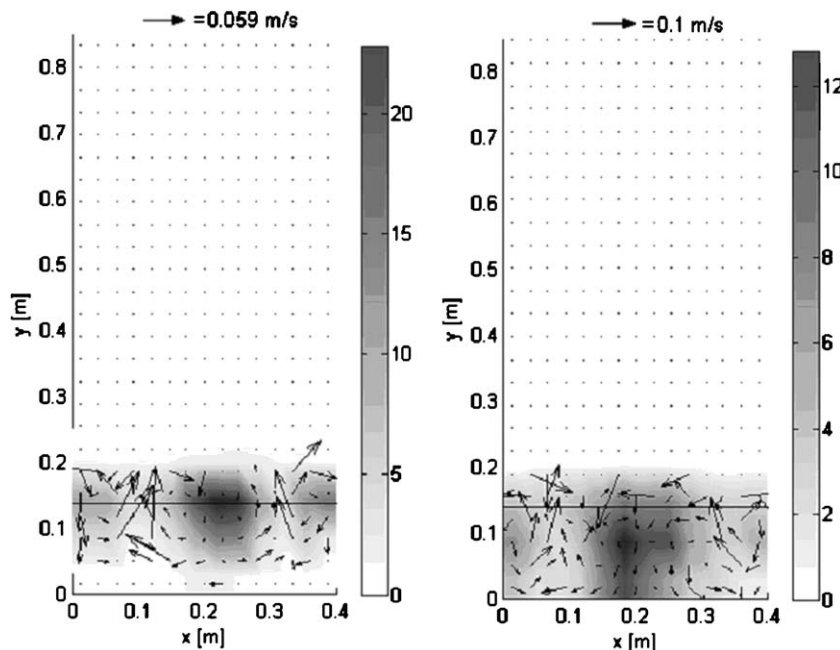


Fig. 11. Development of normalized concentration (m^{-2}) and velocity of tracer particle (m/s) with a decrease in tracer particle size (note the different scales in the velocity vector plots).

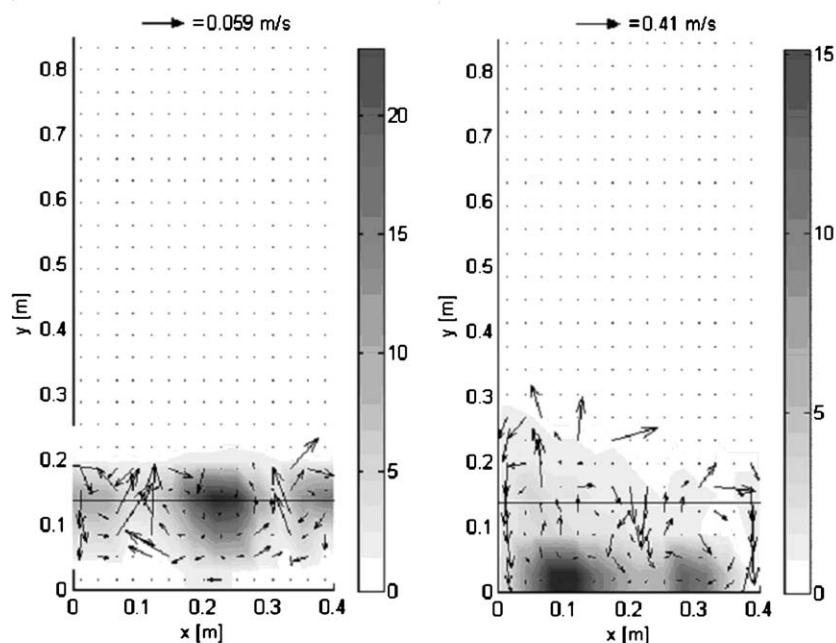


Fig. 12. Development of normalized concentration (m^{-2}) and velocity of tracer particle (m/s) with an increase in tracer particle density (note the different scales in the velocity vector plots).

bed surface to just above the air distributor, coinciding with the preferred bubble paths. Thus, the tracer particle remains near the air-distributor until a bubble is able to drag it up to the dense bed surface and eject it into the splash zone, which is seldom the case according to the low concentration values obtained in the upper zone of the bed. In these occasions, however, the tracer particle is accelerated all along the dense bed height, differing from the low-density “Reference” tracer particle case where the acceleration is typically limited to the upper half of the dense bed (since the particle rarely resides in the lower half of the bed, see Fig. 12a). Thus, the high-density tracer particle has a longer accelerating path and thereby reaches the dense bottom bed surface with a higher velocity, making its occasional trajectories into the freeboard reach higher positions than in the “Reference” tracer particle case. As expected, downflow velocities are considerably higher for the high-density tracer particle than for the low density particle due to gravity.

It should be emphasized that the 4-vortexes flow pattern with three downflowing channels (by the sidewalls and in the central region of the bed) is maintained in both cases.

Runs with a “HD” tracer particle in the absence of a dense bottom bed were carried out, but this only resulted in that the tracer particle ended up resting on the air distributor (i.e., these cases are not reported here). This is expected since the terminal velocity of the “HD” particle significantly exceeds the superficial gas velocity and the low solids suspension density cannot exchange a high enough momentum on the tracer particle for this to be entrained.

4. Conclusions

A novel technique for particle-tracking in 2-dimensional fluidized beds with subsequent digital image analysis is presented

and shown to be an efficient tool for characterization of the particle mixing process. The technique has been used to simulate the mixing of a fuel particle in a fluidized bed, which, as a general result, is found to follow a flow pattern in horizontally aligned vortexes induced by main bubble paths which were characteristic for the conditions investigated.

The influence of four parameters on the solids mixing has been studied and the following conclusions can be drawn:

1. Increasing the amount of bed material is found to reduce, by means of bubble coalescence, the number of vortexes forming the flow picture, increase the homogeneity of the concentration distribution of the tracer particle, increase the velocity of the tracer particle, and increase the global horizontal dispersion coefficient.
2. Increasing the fluidization velocity leads to an increase in tracer-particle velocities and in global dispersion coefficients provided there is a dense bottom bed, while the opposite result is obtained if there is no bottom bed present.
3. Reduction in the size of the tracer particle gives a more homogeneous concentration distribution and increased vertical dispersion, whereas the horizontal dispersion remains nearly unaffected.
4. An increase in density of the tracer particle gives high concentration zones in the lowest part of the bottom bed and high velocities of the tracer particle above these zones.

The dispersion of the tracer particle is generally higher in the vertical than in the horizontal direction. In the presence of a dense bottom bed, the horizontal dispersion coefficient exhibits the highest values around the locations at the bottom bed surface where eruptions of bubbles or jets occur, and low values in the bottom bed surface near the sidewalls. Absence of a

dense bottom bed enhances horizontal dispersion provided the solids suspension is dense enough, but leads to a decrease in dispersion when the solids suspension is dilute. Also, local horizontal dispersion coefficients are more uniformly distributed than in the presence of a dense bottom bed.

Notation

A	area, m^2
C_{fuel}	normalized concentration of tracer particle, m^{-2}
D	dispersion coefficient, m^2/s
N	number of pixels, dimensionless
Δl	reference displacement, m
Δt	time interval, s

Subindexes

n	pixel index
k	dimension index

Acknowledgements

The authors gratefully acknowledge financial support from the Swedish Energy Agency and the EU Research Fund for Coal and Steel under contract RFC-CR-03001.

References

- Agarwal, P.K., Genetti, W.E., Lee, Y.Y., 1986. Coupled drying and devolatilization of wet coal in fluidized beds. *Chemical Engineering Science* 41 (9), 2373–2383.
- Bokkers, G.A., van Sint Annaland, M., Kuipers, J.A.M., 2004. Mixing and segregation in a bidisperse gas–solid fluidized bed: a numerical and experimental study. *Powder Technology* 140 (3), 176–186.
- Darton, R.C., LaNauze, R.D., Davidson, J.F., Harrison, D., 1977. Bubble-growth due to coalescence in fluidized beds. *Transactions of the Institution of Chemical Engineers* 55 (4), 274–280.
- de Korte, R.J., Schouten, J.C., Van den Bleek, C.M., 2001. Controlling bubble coalescence in a fluidized-bed model using bubble injection. *A.I.Ch.E. Journal* 47 (4), 851–860.
- Du, B., Wei, F., 2002. Lateral solids mixing behavior of different particles in a riser with FCC particles as fluidized material. *Chemical Engineering and Processing* 41 (4), 329–335.
- Du, B., Fan, L.-S., Wei, F., Warsito, W., 2002. Gas and solids mixing in a turbulent fluidized bed. *A.I.Ch.E. Journal* 48 (9), 1896–1909.
- Dudukovic, M.P., 2002. Opaque multiphase flows: experiments and modeling. *Experimental Thermal and Fluid Science* 26 (6–7), 747–761.
- Enwald, H., Almstedt, A.-E., Peirano, E., 1996. Eulerian two-phase flow theory applied to fluidization. *International Journal of Multiphase Flow* 22 (Suppl. 1), 21–66.
- Fan, L.T., Song, J.C., Yutani, N., 1986. Radial particle mixing in gas–solids fluidized beds. *Chemical Engineering Science* 41 (1), 117–122.
- Glicksman, L.R., 1984. Scaling relationships for fluidized beds. *Chemical Engineering Science* 39 (9), 1373–1379.
- Grassler, T., Wirth, K.-E., 2000. X-ray computer tomography—potential and limitation for the measurement of local solids distribution in circulating fluidized beds. *Chemical Engineering Journal* 77 (1–2), 65–72.
- Guo, Q., Yue, G., Zhang, J., Liu, Z., 2001. Hydrodynamic characteristics of a two-dimensional jetting fluidized bed with binary mixtures. *Chemical Engineering Science* 56 (15), 4685–4694.
- Highley, J., Merrick, D., 1971. The effects of the spacing between solid feed points on the performance of a large fluidized bed reactor. *A.I.Ch.E. Symposium Series* 67, 219.
- Ibsen, C.H., Solberg, T., Hjertager, B.H., Johnsson, F., 2002. Laser Doppler anemometry measurements in a circulating fluidized bed of metal particles. *Experimental Thermal and Fluid Science* 26 (6–7), 851–859.
- Larachi, F., Kennedy, G., Chaouki, J., 1994. A gamma-ray detection system for 3-D particle tracking in multiphase reactors. *Nuclear Instruments and Methods in Physics Research Section A: Accelerators, Spectrometers, Detectors and Associated Equipment* 338 (2–3), 568–576.
- Lim, K.S., Agarwal, P.K., 1994. Circulatory motion of a large and lighter sphere in a bubbling fluidized bed of smaller and heavier particles. *Chemical Engineering Science* 49 (3), 421–424.
- Lin, Y.-C., Chyang, C.-S., 2003. Radial gas mixing in a fluidized bed using response surface methodology. *Powder Technology* 131 (1), 48–55.
- Mostoufi, N., Chaouki, J., 2001. Local solid mixing in gas–solid fluidized beds. *Powder Technology* 114 (1–3), 23–31.
- Niklasson, F., Thunman, H., Johnsson, F., Leckner, B., 2002. Estimation of solids mixing in a fluidized-bed combustor. *Industrial and Engineering Chemistry Research* 41 (18), 4663–4673.
- Palchonok, G.I., Dikalenko, V.A., Stanchits, L.K., Borodulya, V.A., Werther, J., Leckner, B., 1997. Kinetics of the main stages of fluidized bed combustion of a wet biomass particle. *Proceedings of the 14th International Conference on Fluidized Bed Combustion*, pp. 221–225.
- Parker, D.J., Broadbent, C.J., Fowles, P., Hawkesworth, M.R., McNeil, P., 1993. Positron emission particle tracking a technique for studying flow within engineering equipment. *Nuclear Instruments and Methods in Physics Research, Section A: Accelerators, Spectrometers, Detectors and Associated Equipment* A 326 (3), 592–607.
- Peirano, E., Delloume, V., Johnsson, F., Leckner, B., Simonin, O., 2002. Numerical simulation of the fluid dynamics of a freely bubbling fluidized bed: influence of the air supply system. *Powder Technology* 122 (1), 69–82.
- Peters, B., Bruch, C., 2001. A flexible and stable numerical method for simulating the thermal decomposition of wood particles. *Chemosphere* 42 (5–7), 481–490.
- Rios, G.M., Dang, K., Masson, H., 1986. Free object motion in a gas fluidized bed. *Chemical Engineering Community* 47, 247–272.
- Schlichthaerle, P., Werther, J., 2001. Solids mixing in the bottom zone of a circulating fluidized bed. *Powder Technology* 120 (1–2), 21–33.
- Shen, L., Johnsson, F., Leckner, B., 2004. Digital image analysis of hydrodynamics two-dimensional bubbling fluidized beds. *Chemical Engineering Science* 59 (13), 2607–2617.
- Stein, M., Ding, Y.L., Seville, J.P.K., 2002. Experimental verification of the scaling relationships for bubbling gas–fluidised beds using the PEPT technique. *Chemical Engineering Science* 57 (17), 3649–3658.
- Svensson, A., Johnsson, F., Leckner, B., 1996. Fluidization regimes in non-slugging fluidized beds: the influence of pressure drop across the air distributor. *Powder Technology* 86 (3), 299–312.
- Thunman, H., Leckner, B., Niklasson, F., Johnsson, F., 2002. Combustion of wood particles—a particle model for Eulerian calculations. *Combustion and Flame* 129 (1–2), 30–46.
- van Barneveld, J., Oosterhuis, N.M.G., Pragt, H.J., Smit, W., 1987. Measuring the liquid circulation time in a large gas–liquid contactor by means of a radio pill—1: flow pattern and mean circulation time. *Industrial and Engineering Chemistry Research* 26 (11), 2185–2192.
- van Wachem, B.G.M., van der Schaaf, J., Schouten, J.C., Krishna, R., van den Bleek, C.M., 2001. Experimental validation of Lagrangian–Eulerian simulations of fluidized beds. *Powder Technology* 116 (2–3), 155–165.
- Werther, J., 1977. Bubble chains in large diameter gas fluidized beds. *International Journal of Multiphase Flow* 3 (4), 367–381.
- Xiang, Q., Huang, G., Ni, M., Cen, K., Tao, T., 1987. Lateral dispersion of large coal particles in an industrial-scale fluidized bed combustor. *Proceedings of the Ninth International Conference on Fluidized Bed Combustion*, p. 546.

Paper V

Pallarès, D., Díez, P., Johnsson, F. (2007)

"Experimental analysis of fuel mixing patterns in a fluidized bed"

Proc. of the 12th Int. Conf. on Fluidization (Harrison, Canada)

Experimental analysis of fuel mixing patterns in a fluidized bed

David Pallarès, Pedro A. Díez, Filip Johnsson

Department of Energy and Environment, Chalmers University of Technology, SE-41296 Göteborg (Sweden)
Telf: +46-317721449; E-mail: filip.johnsson@me.chalmers.se

ABSTRACT

The mixing pattern of a tracer particle which simulates a fuel particle is studied in a cold 2-dimensional fluidized bed with respect to the influence of fluidization velocity, bed height, tracer particle size and air-distributor pressure drop under conditions typical for bubbling fluidized bed boilers as well as the bottom region of circulating fluidized bed boilers. The results show that for all conditions studied, the tracer particle follows a flow pattern structured into horizontally-aligned vortices.

INTRODUCTION

Fuel mixing is a key phenomenon for the performance of fluidized bed (FB) boilers (bubbling as well as circulating). In the vertical direction, good fuel mixing is important to ensure sufficient contact time between fuel and combustion air. In the horizontal direction, the fuel dispersion determines to what extent there will be homogeneous cross-sectional fuel distribution which is important for fuel burnout while allowing a low excess air ratio (thus minimizing operational costs). For typical fluidization conditions, horizontal solids mixing in the bottom region of an FB unit was found to be lower than in the vertical direction (1). This, together with the fact that the bed of an FB boiler (where most of the fuel inventory is present) usually has a height-to-width ratio lower than 1, makes the horizontal direction critical in terms of fuel mixing. Moreover, for economical reasons, the number of fuel feeding points should be kept as low as possible (2), which is obviously strongly related to the degree of horizontal fuel mixing.

To what extent a certain fuel mixing behaviour is sufficient or not depends on the fuel conversion time and the characteristic mixing length. A comparison of the characteristic times for fuel dispersion and conversion can be expressed by the Damköhler number:

$$Da = \frac{\tau_{dispersion}}{\tau_{conversion}} = \frac{L^* / r_{dispersion}}{\tau_{conversion}} \quad (1)$$

Thus, the Damköhler number (Da) is a suitable parameter for evaluation of fuel mixing in FB units. The Da number indicates whether the dispersion rate is high enough to ensure a sufficiently homogeneous distribution of the fuel over the entire cross section of the unit (which is the case for low values of the Damköhler number, $Da < 1$). It is seen from Eq. (1) that operational conditions which yield a sufficient fuel mixing rate in a certain FB burning a certain fuel may not be sufficient when changing fuel (*e.g.* to a fuel with a higher volatile content or which is more reactive). It is evident that horizontal fuel mixing becomes a critical issue in large CFB boilers, which may have a cross-sectional area of up to several hundreds of square meters.

To the authors knowledge there are no models on the fuel mixing which give satisfactory agreement with experimental data under conditions applicable to FB boilers and which are based on the underlying physics of the mixing process. Although, there has been significant progress in numerical modelling from first principles, computational fluid dynamics (CFD) is generally limited to a mono-sized solid phase (3-5), while simulating fuel mixing obviously requires accounting for a polydispersed solid phase (bulk particles and fuel particles). There are

some attempts in literature to account for polydispersed solids in CFD simulations (6, 7) but not really concerning fuel mixing, which requires one of the phases (fuel) to have a much smaller fraction (less than 5%) than that of the bulk and to be lighter as well. An attempt to implement conditions corresponding to fuel mixing was made by Tanskanen (8), but more work is required until realistic results can be obtained. Thus, there is a need for semiempirical models expressing the solids mixing as an overall dispersion coefficient to be used as a tool to simulate horizontal fuel dispersion (the word “dispersion” is here used for simplicity since measured and modelled solids mixing is normally expressed as an average dispersion coefficient, although the mixing process is highly convective). Effective horizontal solids dispersion coefficients in FB boilers have been estimated by means of experimental data from boilers (9, 10) and from cold rigs (11). Niklasson *et al.* (9) carried out experiments in the Chalmers 12 MW FB boiler operated under bubbling conditions, obtaining a value of the horizontal fuel dispersion coefficient of around $0.1 \text{ m}^2/\text{s}$, a result which seems to be consistent with the boiler values reported by Xiang *et al.* (10), ranging from 0.01 to $0.1 \text{ m}^2/\text{s}$ for fluidization velocities lower than those applied in (9). However, experimental evaluation of the dispersion only in the form of global dispersion coefficients is a limitation in the sense that this gives no information on the mechanisms governing the mixing process. Application of particle tracking techniques can provide an experimental basis for resolving the particle mixing process in both space and time.

Several particle tracking techniques have been used to investigate solids mixing in FB units (*cf.* 12) for a survey of experimental investigations on fluidized-bed solids mixing). Techniques measuring in a fixed point (Eulerian) exist, such as Laser Doppler Anemometry or the use of radio transmitters, but no information on the trajectory of a single particle can be obtained from such techniques. For tracking in 3-dimensional units, various tomographical techniques have been developed based on X-ray, electrical capacitance or γ -ray emission. The latter was applied by Stein *et al.* (13) in scale models of FB boilers under conditions accounting for fluid-dynamical scaling relationships. Experiments in 2-dimensional rigs have visual access to the dynamics also in dense beds as the main advantage but are obviously limited to qualitative studies. Most experimental works focus on studying the mixing of the bed material itself, *i.e.* using a tracer particle to mimic the bulk bed material. Accordingly, a tracer particle with larger size and lower density than those forming the bulk bed material must be applied when mixing of a fuel particle is studied, as done in (13-16). Yet, none of these works gives the velocity and concentration fields of the tracer particle while varying main operational parameters. The authors of the present work studied the mixing pattern of a tracer particle simulating a fuel particle in a cold 2-dimensional fluidized bed with the wide dimension being 0.4 m (12), finding the flow pattern of the tracer particle to be structured into several horizontally-aligned vortexes with alternated rotational direction. The question is to what extent this is also valid in a wider unit since the limited width of the bed (0.4 m) applied in the previous work may have influenced the horizontal spreading of the tracer particle. Thus, the present work extends the previous work with the aim to further generalize the patterns of the fuel mixing process, with focus on operational conditions typical for fluidized-bed boilers and with the experiments carried out in a 2D bed with the wide dimension about three times (1.2 m) that applied in the previous work.

EXPERIMENTAL SETUP

This work applies the particle tracking technique developed in the previous work (12), which is suitable for tracking particles coarser than the bed material (*i.e.* simulating fuel particles) in cold 2-dimensional fluidized beds and is robust in that the dynamics of the mixing can be studied over a wide range of operational parameters, allowing for a fundamental study on the phenomenology of solids mixing. The particle tracking technique is based on tracking a single tracer particle (a plastic capsule filled with a phosphorescent solution) in a 2-dimensional fluidized bed with a transparent front wall. The mixing process is then analysed and quantified by means of digital image analysis of the trajectory of the capsule. To maximize phosphorescence, the riser is placed in a dark chamber. A special, high-gain CCTV video camera with a time resolution of $4 \times 10^{-2} \text{ s}$ is used for filming the capsule in the bed. In addition, glass beads are used as bed material, allowing phosphorescence to be seen through the bed material as when the tracer particle flows close to the rear wall (opposite camera position). The 2-dimensional unit is illustrated in Figure 1. The riser is 1.2 m wide with a depth of 0.02 m and a height of 2.05 m with a Plexiglas front wall. The gas flow is controlled by a valve located close to the air plenum and the externally recirculated solids flow is refed into the riser through the back wall (see item no. 9 in Figure 1). Two different perforated air-distributor plates are used, both with 2 mm i.d. holes and hole areas of 2% and 9% (called “high- ΔP ” and “low- ΔP ” air distributor, respectively), which yields the ΔP vs u curves given in Figure 2. The glass beads forming the bed have a narrow particle size distribution with an average size of $330 \text{ }\mu\text{m}$ and a density of 2500 kg/m^3 , *i.e.* although no exact scaling is performed, these values

	RUN								
	A	B	C	D	E	F	G	H	I
Fluidization velocity [m/s]	0.7	1.5	2.7	3.5	2.7	2.7	2.7	2.7	3.5
Fixed bed height [m]	0.33	0.33	0.33	0.33	0.33	0.18	0.18	0.18	0.33
Tracer size	Large	Large	Large	Large	Small	Large	Large	Small	Large
Air distributor	High- ΔP	High- ΔP	High- ΔP	High- ΔP	High- ΔP	High- ΔP	Low- ΔP	High- ΔP	Low- ΔP

Table 1: Test matrix

are similar to those of sand or ash particles typically used as bed material in fluidized bed boilers. The glass beads belong to Group B in the Geldart classification with $u_{mf}=0.12$ m/s and $u_t=1.76$ m/s (ambient conditions). For the conditions applied, around 60 minutes of video recording of the tracer particle (providing approximately 90,000 video frames) were shown to give high enough statistical significance in the digital image analysis. Thus, the method requires significant number of data to reach statistical significance.

Table 1 lists the operational conditions for the 9 experimental runs carried out as basis for this work. The runs cover flow conditions qualitatively resembling fluidization regimes typically found in a fluidized-bed boiler. Two sizes of tracer particle were applied both with a size representative for fuels in FB boilers: 15 mm x 6 mm i.d. ("Large") and 10 mm x 4 mm i.d. ("Small"). Although the bed is only 20 mm in depth, analysis of the trajectories of the tracer particles do not indicate any significant influence of wall effects other than the above-mentioned general wall effect which, of course, makes the results qualitative. Both tracers have an apparent particle density of around 650 kg/m³, which is close to that of biomass, somewhat higher than that of coal, and lower than that of waste pellets. The different regimes were reached by changing either operational conditions (fluidization velocity, amount of bed material and tracer particle) or the air distributor.

Since the evaluation method is based on tracking a single particle in each run, interactions between fuel particles are assumed negligible. This should be a reasonable assumption since the fuel fraction usually represents only between 1 and 5% of the total bed material in FB boilers. With this assumption, the probability of presence of the tracer particle at some location can be interpreted as the concentration value at steady state, C_{fuel} , normalized so that:

$$\int_A C_{fuel} \cdot dA = 1 \quad (2)$$

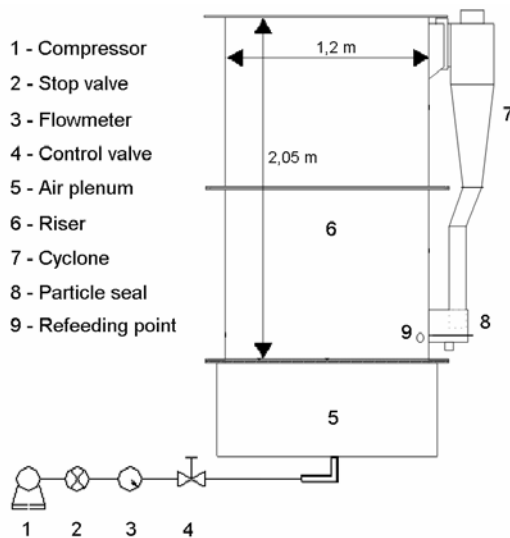


Figure 1: The cold 2-dimensional FB unit used in the experiments.

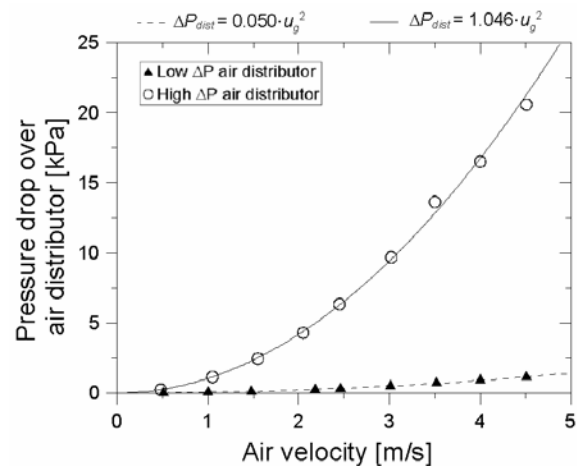


Figure 2: Characteristic curves of the air distributor plates used in the experiments.

Table 2: Average dispersion coefficients as obtained in this work.

	RUN								
	A	B	C	D	E	F	G	H	I
$\overline{D}_x [m^2/s] \cdot 10^2$	0.31	1.11	1.59	2.30	1.48	1.16	1.08	1.20	4.24
$\overline{D}_y [m^2/s] \cdot 10^2$	0.11	0.53	1.67	4.01	2.32	1.14	0.90	1.22	3.00

This can be expressed in discrete form, more suitable for the digital image analysis:

$$\sum_1^N C_{fuel,n} \cdot A_n = 1 \quad \text{with } n=1 \dots N \quad (3)$$

where N corresponds to the total number of pixels of the analyzed videoframe. It should be noted that the probability of not capturing any phosphorescence from the tracer particle at a certain videoframe (around 30% in the present work) is much higher when the tracer particle is immersed in the dense bottom bed than when it is flowing in the freeboard. Thus, this uneven spatial distribution of the phosphorescence capture probability would bias the concentration plots giving the bottom bed region lower concentration values. However, the location of the tracer during the short time intervals (fractions of a second) in which its phosphorescence is not captured can be estimated by linear interpolation. Although the method is restricted to 2D FB units and thereby to qualitative evaluation of the results obtained, tracer particle dispersion is quantified to enable direct comparison of the runs. Thus, the local dispersion coefficient in position n (*i.e.* pixel) in the direction k (horizontal or vertical in our case) at any location can be calculated as:

$$D_{k,n} = \frac{\Delta l_{k,n}^2}{2 \cdot \Delta t_n}; \quad \text{with } k = x, y \quad \text{and} \quad \text{for } n = 1 \dots N \quad (4)$$

As discussed in (12), setting Δt_n equal to a low value and thus taking $\Delta l_{k,n}$ as the displacement occurred in that time interval would imply values of the dispersion coefficient that do not account for the history of the trajectory (which is a prerequisite for defining a dispersion coefficient) and a pseudo-velocity value would be obtained instead. Setting Δt_n to a large value to avoid this effect would increase the risk of having Δt_n larger than the characteristic time for the solids mixing in the unit, also resulting in unrealistic values of the dispersion coefficients. Instead, the method used is to set $\Delta l_{k,n}$ to a relatively high value in order to capture the history of the mixing process, which is shown to be a more robust method for application of Eq (4). Thus, using this approach, Δt_n is defined as the time it takes for the tracer particle to flow a distance equal to $\Delta l_{k,n}$, which has been set to 0.3 m in this work (a fourth of the riser width, as in (12)).

Finally, a global dispersion coefficient can be calculated by weighting the local dispersion coefficients with respect to concentration values, *i.e.*

$$\overline{D}_k = \sum_1^N C_{fuel,n} \cdot A_n \cdot D_{k,n} \quad \text{with } k = x, y \quad \text{and} \quad \text{for } n = 1 \dots N \quad (5)$$

RESULTS

Table 2 lists the average dispersion coefficients obtained for the runs given in Table 1. It should be kept in mind that evaluation of dispersion coefficients in eminently convective flows (as in the present work) has to be done with care, since the values are strongly dependent on the calculation procedure ($\Delta l_{k,n}$ and Equations (4) and (5)), the 2D bed flow and, as indicated above, the convective nature of the flow. Thus, the values in Table 2 have a restricted use only for comparison between runs in this work and shall not be used in, for example, simulations based on a Brownian diffusion process. The calculation procedure (inclusion of a concentration-weighting term in Equation (5) instead of a spatial average) is the reason why the results show vertical and horizontal mixing coefficients in the same order of magnitude (in contrast to (1)). Yet, fuel mixing in FB boilers is critical in the horizontal direction due to the low aspect ratio of the dense bed (where most fuel particles are found). Removing the concentration-weighting term in Equation (5) would significantly increase the values of vertical dispersion coefficient.

When it comes to the appearance of the concentration and velocity fields, the vortex structure of the tracer flow observed in the previous work (in the 0.40 m wide bed) is also found in the present work (1.2 m wide bed) in all runs (A to I), independent of fluidization regime. Thus, it seems to be a general feature that the flow of a tracer particle of the size and density similar to a fuel particle is structured into several horizontally-aligned vortices with alternated rotational direction (*cf.* 12). Figure 3 exemplifies this for Run C, with the ascending channels provided by the bubble paths located at the approximate coordinates $x=0.20$ m and $x=1.0$ m. Thus, the vortex structure is induced by the bubble flow rising through the dense bottom bed, which provides ascending channels for the tracer particle through the dense bottom bed and up to the bottom bed surface, where the tracer particle is projected into the splash zone (experiencing a horizontal displacement) before sinking in the bottom bed through the emulsion phase. This 2D vortex flow structure can be seen as a vertical cross section of what would be a toroidal flow structure around each bubble path in a 3-dimensional case.

An increase in fluidization velocity clearly has a beneficial effect to the solids mixing as can be seen in Figure 4, where the average dispersion coefficient increases in both the vertical and horizontal direction with an increase in velocity, mainly due to the increased bubble flow.

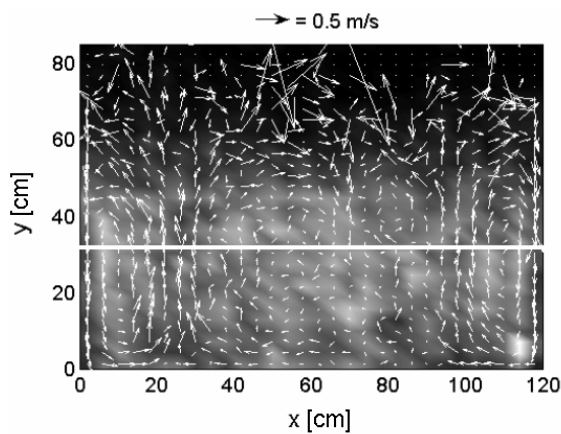


Figure 3: Tracer particle concentration and velocity fields for Run C. White line indicates the bed surface.

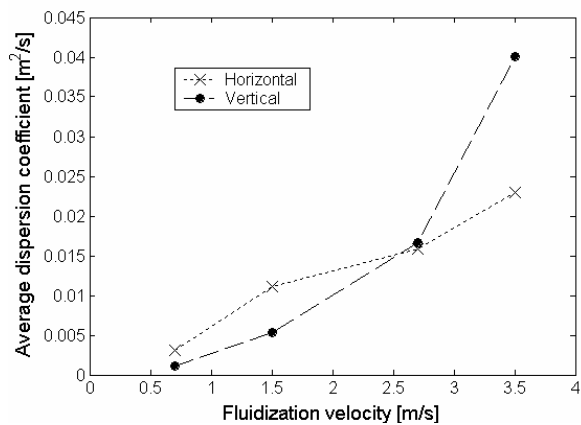


Figure 4: Influence of fluidization velocity on dispersion (Runs A, B, C and D).

The tracer concentration and main velocity fields for Run A are shown in Figure 5, which is characterized by a highly heterogeneous distribution of the tracer concentration field, compared to all other runs. Yet, this regime yields four horizontally aligned vortices induced by two main bubble paths at approximately the same horizontal locations as in Run C in Figure 3 in spite of the fact that the fluidization velocity is four times as high in Run C. Run A gives high-concentration regions at the downflowing interface of the two central vortices, specially at the height equal to the bottom bed height, *i.e.* there is a tendency for the tracer particle to remain most of the time at the dense bed surface while moving horizontally (thus leading to a poor vertical dispersion compared to the other runs, as indicated by the dispersion coefficients). In addition, comparison of runs A and C (and B and D, although not shown here) confirms increasing tendencies of the tracer particle to occupy higher locations in the splash zone as fluidization velocity is increased resulting in more uniform distributions of the concentration and velocity in both directions.

In agreement with the trends shown in the previous work (0.40 m wide bed in (12)) and confirmed in an FB boiler (17), the horizontal dispersion measured is enhanced as the solids inventory in the riser is increased (as seen by comparing the results for runs F and C in Table 2). This is explained by the fact that an increased solids inventory in the riser leads to a higher dense bottom bed, which extends a bit further the bubble rising path, ending in faster and more vigorous bubbles reaching the dense bed surface. Even though a higher solids inventory in the riser of an FB boiler helps homogenizing the fuel concentration over the cross section, thus improving oxygen-fuel contact, it also represents a higher operating (fan power) cost.

The two different tracer particle sizes gave no significant difference in horizontal dispersion (see results for runs C-E and F-H), while the vertical dispersion is enhanced when decreasing tracer particle size in the case with the high- ΔP distributor (runs C-E).

Finally, the low- ΔP distributor gave a significantly different mixing pattern compared to the high- ΔP distributor. This can be seen from Figure 6 corresponding to the low- ΔP distributor in Run G and which shows an asymmetry in the tracer concentration field, with high values in the left side and low ones to the right, specially at $x=1.05$ m (whereas Run F – not shown here - yields an even distribution in tracer concentration over the cross section). The $x=1.05$ m position corresponds to the location of a high throughflow region, although bed was apparently fluidized over the entire cross-section. In repeated experiments, the location of this throughflow channel varies in a random fashion. The location of this intermittent by-pass strongly affects the flow pattern of the tracer particle: when it is located close to the dense bed surface ($y=0.17$ to 0.23 m) it will flow away horizontally from the throughflow location and when the tracer particle is located in the bottom of the bed ($x=0-5$ cm) it will move towards the throughflow location. The large vortex originated by this effect can be seen in Figure 6. In addition, the video recordings show that the tracer moves vertically through the dense bed in locations in the range $x=0.10$ to 0.80 m, but (as also seen in Figure 6) there are no clear “only-rising” or “only-sinking” regions detected in this range, as is the case with the high- ΔP distributor.

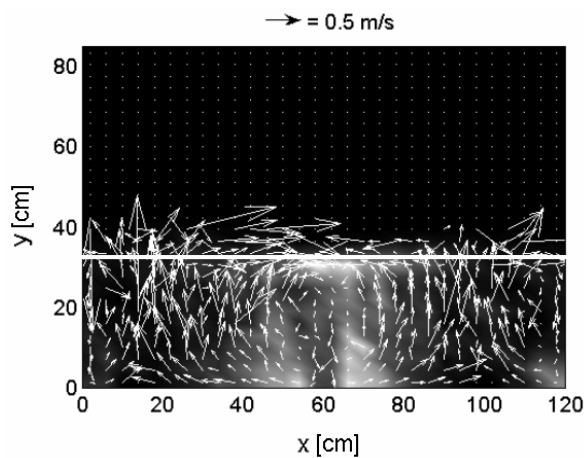


Figure 5: Tracer particle concentration and velocity fields for Run A. White line indicates the bed surface.

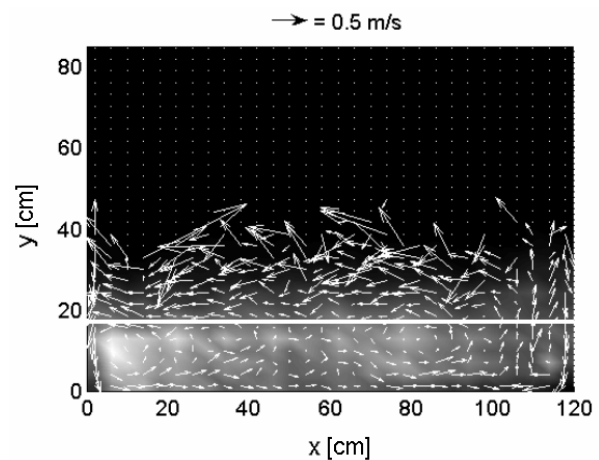


Figure 6: Tracer particle concentration and velocity fields for Run G. White line indicates the bed surface.

Figure 6 shows a rather uniform tracer concentration field when using a low- ΔP distributor. This would support the use of low- ΔP distributors. However, while this leads to that fuel particles get more evenly distributed, the throughflow effects enhance an uneven distribution of the gas flow (and thereby the oxygen). Thus, despite the high horizontal dispersion values found for tests with the low- ΔP distributor (runs G and I), such conditions may still yield insufficient oxygen-fuel contact.

CONCLUSIONS

A simulated fuel particle inserted in a cold 2D FB unit follows a flow pattern structured into horizontally-aligned vortices, which is a 2D equivalent of a toroidal structure in 3 dimensions. From a comparison with previous work in a less wide bed than applied in this work it can be concluded that the vortex pattern is induced by the bubble flow and not affected by the bed width.

Increasing the fluidization velocity enhances solids mixing in both vertical and horizontal directions. When the size of the tracer particle is reduced, it reaches both higher velocities within the dense bed and higher locations in the splash zone, increasing vertical dispersion while horizontal dispersion remains more or less the same. An increase in the amount of bed material (constant velocity) enhances the dispersion coefficients by means of a higher dense bottom bed which allows for the formation of larger and faster bubbles. Finally, lowering the air distributor pressure drop significantly changes the mixing pattern, as a result of the formation of high-throughflow (gas) regions which significantly reduces the solids mixing and the gas-fuel contact.

ACKNOWLEDGMENTS

The authors gratefully acknowledge financial support from the Swedish Energy Agency and the EU Research Fund for Coal and Steel under contract RFC-CR-03001.

NOTATION

A	Area [m ²]	r	Mixing rate [m/s]
C	Normalized concentration [m ⁻²]	u_{mf}	Minimum fluidization velocity [m/s]
D	Local dispersion coefficient [m ² /s]	u_t	Particle terminal velocity [m/s]
\bar{D}	Averaged dispersion coefficient [m ² /s]	k	Subindex for direction
Da	Damköhler number [-]	Δl	Tracer displacement [m]
L^*	Characteristic length [m]	Δt	Time interval [s]
n	Subindex for pixel	τ	Characteristic time [s]
N	No. of pixels		

REFERENCES

1. Ito, O., Kawabe, R., Miyamoto, T., Orita, H., Mizumoto, M., Miyadera, H., Tomuro, J., Hokari, N., Iwase, T. 1999. "Direct measurement of particle motion in a large-scale FBC boiler model". *Proc. 15th FBC Conf, Savannah*, 217.
2. Highley, J., Merrick, D. 1971. "The effects of the spacing between solid feed points on the performance of a large fluidized bed reactor". *AIChE Symposium Series* 67, 219.
3. Enwald, H., Almstedt, A.-E., Peirano, E. 1996. "Eulerian two-phase flow theory applied to fluidization". *International Journal of Multiphase Flow* 22, 21-66.
4. van Wachem, B. G. M., van der Schaaf, J., Schouten, J. C., Krishna, R., van den Bleek, C. M. 2001. "Experimental validation of Lagrangian-Eulerian simulations of fluidized beds". *Powder Technology* 116(2-3), 155-165.
5. Peirano, E., Delloume, V., Johnsson, F., Leckner, B., Simonin, O. 2002. "Numerical simulation of the fluid dynamics of a freely bubbling fluidized bed: influence of the air supply system". *Powder Technology* 122(1), 69-82.
6. Ibsen, C.H., Helland, E., Hjertager, B.H., Solberg, T., Tadriss, L., Occelli, R. 2004. "Comparison of multifluid and discrete particle modelling in numerical predictions of gas particle flow in circulating fluidised beds". *Powder Technology* 149 (1), 29-41.
7. Berres, S., Bürger, R., Tory, E.M. 2005. "On mathematical models and numerical simulation of fluidization of polydisperse suspensions". *Applied Mathematical Modelling* 29, 159-193.
8. Tanskanen, V. 2005. "CFD study of penetration and mixing of fuel in a CFB furnace". Master Thesis, *Dept. of Energy and Environment, Lappeenranta Univ. of Tech. (Finland)*.
9. Niklasson, F., Thunman, H., Johnsson, F., Leckner, B. 2002. "Estimation of solids mixing in a FB combustor". *Industrial and Engineering Chemistry Research* 41(18), 4663-4673.
10. Xiang, Q., Huang, G., Ni, M., Cen, K., Tao, T. 1987. "Lateral dispersion of large coal particles in an industrial-scale fluidized bed combustor". *Proc. 9th FBC Conf, Boston*, 546.
11. Schlichthaerle, P., Werther, J. 2001. "Solids mixing in the bottom zone of a circulating fluidized bed". *Powder Technology* 120(1-2), 21-33.
12. Pallarès, D., Johnsson, F. 2006. "A novel technique for particle tracking in cold 2-dimensional fluidized beds". *Chemical Engineering Science* 61, 2710-2720.

13. Stein, M., Ding, Y. L., Seville, J. P. K., 2002. Experimental verification of the scaling relationships for bubbling gas-fluidised beds using the PEPT technique. *Chemical Engineering Science* 57(17), 3649-3658.
14. Lim, K.S., Agarwal, P.K. 1994. "Circulatory motion of a large and lighter sphere in a BFB of smaller and heavier particles". *Chemical Engineering Science* 49, 421-424.
15. Shen, L., Johnsson, F., Leckner, B. 2004. "Digital image analysis of hydrodynamics two-dimensional bubbling fluidized beds". *Chemical Engineering Science* 59(13), 2607-2617.
16. Rios, G.M., Dang, K., Masson, H. 1986. "Free object motion in a gas fluidized bed". *Chemical Engineering Community* 47, 247-272.
17. Niklasson, F., Pallarès, D., Johnsson, F. 2006. "Biomass co-firing in a CFB boiler–Influence of bed properties on in-furnace gas concentration profiles". *Proc. 19th FBC Conf.*, Vienna.

Appendix A

Macroscopic modeling of heat transfer in circulating fluidized bed units

Macroscopic modeling of heat transfer in circulating fluidized bed units

The heat balance over any control volume in the circulating loop of a CFB unit (*i.e.* riser and return leg) contains enthalpy flow terms related to the in- and outflows of the solid fractions and gas species present, and also terms which account for the loss or gain of heat flow derived from heat transfer mechanisms with the surrounding. In a fluidized bed unit, the main heat transfer mechanisms are assumed to be radiation and convection (where by convection, in this case, is understood the sum of both of gas convection and solids conduction for the gas-solid suspension).

Firstly, some facts with important implications must be beard in mind: the low thermal inertia of the solid particles (due to their size) and the relatively smooth temperature gradients which the gas-solids flow experiences. These, together with the typical gas-particle heat transfer rate of a fluidized bed, support the general and significant assumption of a common local temperature for the solids and gas phases. This assumption significantly simplifies both the investigation of the heat transfer phenomena and the formulation of local heat balances in fluidized beds.

Most experimental works in fluidized bed literature dealing with heat transfer bring the convective and radiative heat mechanisms together to find correlations for effective heat transfer coefficients, which are generally correlated as a function of some fluidodynamical parameter (*e.g.* the suspension density). However, focusing on heat transfer to the heat transfer surfaces (*i.e.* waterwalls or internals), the role of radiation is enhanced in dilute regions (such as the upper freeboard) and lower in dense regions at lower heights (such as the bottom furnace region), due to varying solids absorption effect. The opposite applies to convection (in the sense it is understood here, *i.e.* sum of gas convection and solids conduction), which increases in dense gas-solid suspensions due to higher solids conduction. Considering these differences, the two heat transfer mechanisms should be modeled separately in order to contribute to an improved understanding of the global heat transfer phenomenon.

Breitholtz *et al.* (2001) carried out an experimental work which involved measurements from three large-scale CFB boilers in which radiative and convective heat transfer to the furnace walls were differentiated. This is represented by Fig. 1, which shows the heat transfer coefficients obtained for convective and total heat transfer as a function of the suspension density. As can be seen, both the convective and the total heat transfer increase with an increase in suspension density, while the radiative heat transfer (difference between total and convective radiation) decreases slightly.

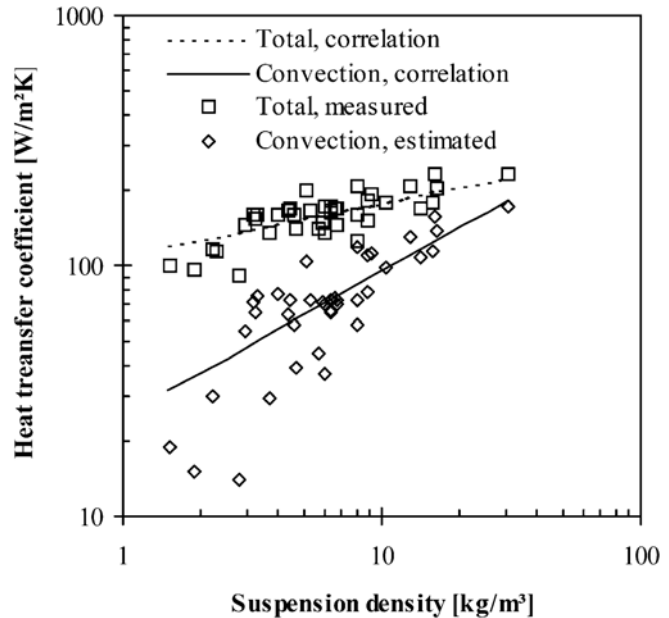


Figure 1: Convective and total heat transfer coefficients as a function of suspension density. From Breitholtz *et al.* (2001).

From the estimated heat convection coefficients shown by the data points in Fig. 1, Breitholtz *et al.* gave the following correlation for the convective heat transfer as a function of the suspension density:

$$h_{conv} = 25 \cdot C_s^{0.58} \quad (1)$$

Concerning radiative heat, the transfer coefficient between a solids-free gas suspension and a surface is directly derived from established radiation theory as:

$$\hat{h}_{rad} = \frac{1}{\frac{1}{\varepsilon_{susp}} + \frac{1}{\varepsilon_{surf}} - 1} \cdot \sigma \cdot (\tilde{T}_{susp}^2 + T_{surf}^2) \cdot (\tilde{T}_{susp} + T_{surf}) \quad (2)$$

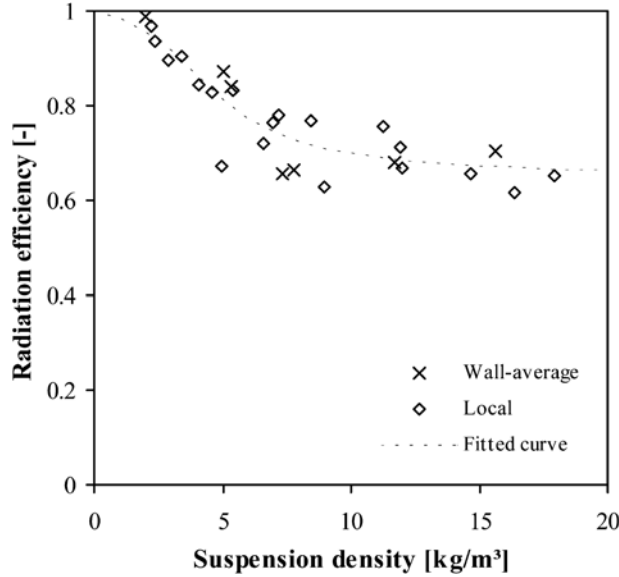


Figure 2: Radiation efficiency as a function of suspension density. From Breitholtz *et al.* (2001).

radiation efficiency are shown in Fig. 2 together with the curve for its correlation, which was given by Breitholtz *et al.* (2001) as:

$$\eta_{rad} = \frac{h_{rad}}{\hat{h}_{rad}} = 0.86 - 0.14 * \operatorname{atg}\left(\frac{\tilde{C}_{s, susp}}{2.6} - 1.6\right) \quad (3)$$

In the calculation of the parameters influencing radiation (such as the suspension density and temperature), an appropriate type of averaging must be applied to the suspension. Due to the absorption by solids, properties in the suspension closer to the surface studied will have a stronger weight in the process than those far away from the surface. This absorption effect in fluidized bed radiative heat transfer was studied by Baskakov and Leckner (1997), who described the absorption effect through the exponential curve proposed by the Bouguer's law for radiative properties of solids suspensions:

$$\alpha = 1 - \exp\left(-\frac{1.5 \cdot C_{v, s} \cdot L}{d_s}\right) \quad (4)$$

Applying the above expression to a mesh allows consideration of the varying values of the solids volumetric concentration and mean size. This has a significant effect in the case of heat transfer to the furnace walls, where wall layers and the core region might present rather different values of the solids concentration and size. A scheme for the application of the Bouguer's law to the radiative heat transfer to the waterwalls in the furnace is seen in Fig. 3. As seen in Fig. 3, the absorption phenomenon leads to that for denser suspensions (such as in the bottom freeboard) the properties of the suspension close to the heat transfer surface dominate the radiation mechanism. On the other hand, the lower absorption in more dilute suspensions makes properties of the suspension relatively far from the surface play a certain role in the radiative heat transfer. Thus, weight coefficients, w_i , for each cell can be calculated according to the relative area below the red curve (*i.e.* the integral

of Eq. 4) in each cell. In a discretized mesh with varying suspension properties, the weight coefficient for a certain cell i is calculated as:

$$w_i = \alpha_i \cdot \prod_{n=1}^{n=i-1} (1 - \alpha_n) \quad (5)$$

with cell index 1 corresponding to the closest cell to the surface studied.

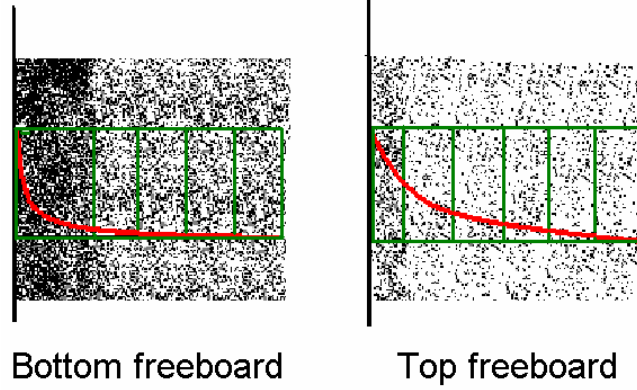


Figure 3: Weight of the local parameters in the Bouguer-averaging used in radiative heat modeling. The green lines represent a mesh at a certain level in the furnace, with the furnace wall (heat transfer surface) to the left.

Thus, the cell weight coefficients are used to calculate the Bouguer-averaged suspension properties in Eqs (2) and (3) and in the general equation for the radiative heat, *i.e.*,

$$q_{rad} = h_{rad} \cdot A \cdot (\tilde{T}_{susp} - T_{surf}) \quad (6)$$

With this, a certain radiative heat flow to the heat transfer surface can be calculated accounting for absorption by the solids. However, what is required in the formulation of the heat balance for each individual cell is the radiative heat flow exchanged between the cell and the heat transfer surface. This heat balance not only depends on optical factor considerations (such as the Bouguer's law) but also on the cell temperature. Cells at higher temperatures obviously will contribute more to the radiative heat transfer than cells with a lower temperature. To account for this, a further weighting coefficient accounting for the temperature effect has to be defined, namely:

$$w'_i = \frac{w_i \cdot (T_i^4 - T_{surf}^4)}{\sum_{i=1}^N w_i \cdot (T_i^4 - T_{surf}^4)} \quad (7)$$

This coefficient is then used in the individual cell heat balances to calculate the cell loss of radiative heat to the heat exchanging surface as:

$$q_{rad\ i} = w'_i \cdot q_{rad} \quad (8)$$

Notation

C	Solids concentration [kg/m ³]	w	Bouguer weight coefficient [-]
d	Particle diameter [m]	w'	Heat flow weight coefficient [-]
h	Heat transfer coefficient [W/m ² K]	α	Bouguer transmissivity [-]
L	Length [m]	ε	Emissivity [-]
q	Heat flow [W]	η	Efficiency [-]
T	Temperature [K]	σ	Stefan–Boltzmann constant [W/m ² K ⁴]

Subscripts

$conv$	Convective	$surf$	Surface
rad	Radiative	$susp$	Suspension
s	Solids	v	Volumetric

References

- Breitholtz, C., Leckner, B., Baskakov, A.P. 2001. "Wall average heat transfer in CFB boilers". *Powder Technology*, 120(1), pp.41-48.
- Baskakov, A.P., Leckner, B. 1997. "Radiative heat transfer in circulating fluidized bed furnaces". *Powder Technology*, 90(3), pp.213-218.